Plasma Physics Reports, Vol. 28, No. 7, 2002, pp. 535–538. Translated from Fizika Plazmy, Vol. 28, No. 7, 2002, pp. 579–583.

TOKAMAKS

Nonmonotonic Spatial Distributions of Charge-Exchange Neutral Fluxes and Optical Radiation from Plasma in the DAMAVAND Tokamak

R. Amrollahy*, E. Farshi, N. N. Brevnov***, Yu. V. Gott***, and V. A. Shurygin*****

**K-N Toosi University of Technology, Tehran, Islamic Republic of Iran*

***National Institute for Fusion Science, Toki-shu, Japan*

****Russian Research Centre Kurchatov Institute, pl. Kurchatova 1, Moscow, 123182 Russia*

Received January 18, 2002

Abstract—Results are presented from investigations of the nonmonotonic spatial distributions of charge-exchange neutral fluxes and optical radiation from plasma in the DAMAVAND tokamak. It is shown that, during ohmic heating of the plasma, the regions with enhanced confinement of both the background plasma particles and heavy impurity ions arise near rational magnetic surfaces with $q = 1$ and 2. These regions are characterized by enhanced emission of accelerated charge-exchange neutrals and optical radiation from impurity ions.

1. INTRODUCTION

One way of prolonging the plasma energy lifetime in tokamaks is to achieve operating conditions favorable for the onset of transport barriers in the plasma, which considerably affect transport processes and trigger transitions to improved confinement regimes (H-modes) [1, 2]. That is why the study of transport barriers and the processes responsible for their formation is important for the development of methods for controlling discharges with long plasma energy lifetimes in a tokamak reactor. In this way, experimental investigations on small tokamaks can also be helpful in solving the related problems.

Experimental results reported in [3] showed that, during MHD activity before current disruption in the TVD tokamak, the ions are accelerated preferentially across the magnetic field lines, in which case the transverse plasma temperature increases by a factor of 1.5 to 2. In studying the processes occurring in the predisruption phase in the DAMAVAND tokamak (Tehran, Islamic Republic of Iran) [4, 5], it was observed that the intensities of charge-exchange neutral fluxes and optical radiation from impurities change nonmonotonically from the plasma core to the periphery. This effect can be interpreted as evidence that the background and impurity ion densities both become elevated in some plasma regions. However, in [4, 5], the related measurements were carried out only at a few radial positions in the plasma column, so that it was impossible to determine the radial profiles of the intensity of charge-exchange neutral fluxes and optical radiation from the plasma with good spatial resolution.

The goal of the present paper is to investigate in more detail regions with enhanced emissivity properties in the predisruption phase and just after the disruption in the DAMAVAND tokamak.

2. EXPERIMENTAL CONDITIONS

The experiments were carried out in the DAMAVAND tokamak [4] with the following main parameters: the major radius is $R = 36$ cm, the minor radius is $a = 7$ cm, the vertical elongation of the plasma column is $k = 1.2$, the toroidal magnetic field is $B_T \le 1$ T, the plasma current is $I_p \le 40$ kA, the plasma density is $n_e \approx (1–2) \times 10^{13}$ cm^{-3}, the electron temperature is $T_e \sim 300–350$ eV, the ion temperature is $T_i \sim 100–150$ eV, and the discharge duration is 15 ms. The elongation k was chosen to be the lowest in order for the vertical instability not to develop.

MHD-driven disruption of the plasma current was initiated by connecting an additional energy supply to the inductor 8 ms after the beginning of the discharge. As a result, the discharge current increased by 10–20% and became disrupted. Experiments were carried out with several different plasma currents [4, 5]. The current was varied consistently with the toroidal magnetic field so as to keep the safety factor at the plasma boundary nearly the same ($q_a \approx 2.3$). Such plasma parameters as the plasma current I_p, the loop voltage V, the time derivative of the oscillating magnetic field component $\tilde{B}$, the intensity of hard X radiation, the intensities of impurity (deuterium, carbon, and oxygen) line radiations in the optical range, and plasma displacements along the major radius and in the vertical direction were measured by a standard tokamak diagnostic complex. The distribution of charge-exchange neutral fluxes and

1063-780X/02/2807-0535$22.00 © 2002 MAIK "Nauka/Interperiodica"

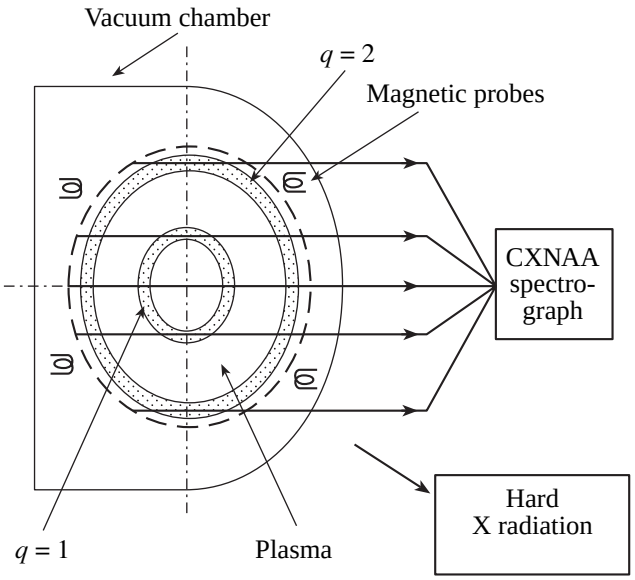

Fig. 1. Schematic of the diagnostic system.

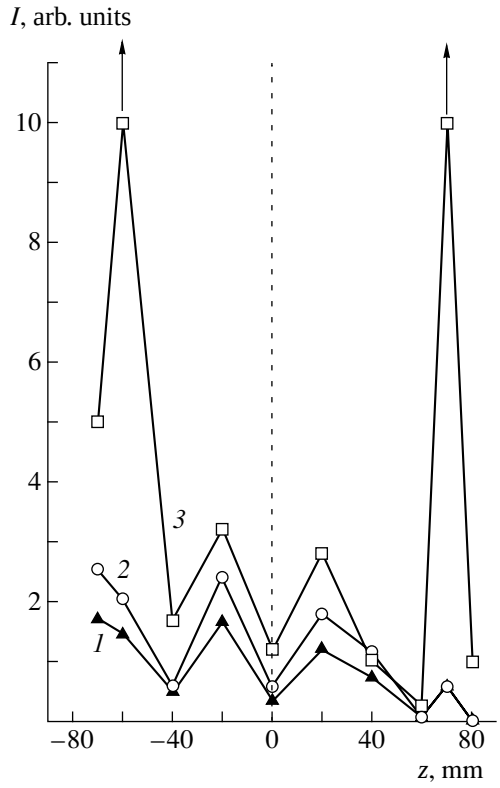

Fig. 2. Intensity of the fluxes of charge-exchange neutrals with an energy of 150 eV, emitted from the plasma in the vertical direction, 1 ms (curve *1*) and 160 μs (curve *2*) before the disruption and 25 μs (curve *3*) after the disruption. The up arrows above the experimental points indicate that the corresponding signal amplitude is much larger than that designated in the figure.

the plasma ion temperature were investigated by a charge-exchange neutral atom analyzer (CXNAA) with a solid target [6], and the plasma electron temperature was measured by an integral photoelectron spectrometer [7]. A layout of the diagnostic components is shown schematically in Fig. 1.

In chord measurements, the spatial resolution Δz of the diagnostic equipment was about 10 mm, the time resolution being about $\Delta t \sim 5$ μs.

A more detailed description of the experimental conditions and diagnostic system is given in [8].

3. EXPERIMENTAL RESULTS

Figure 2 shows representative profiles of the intensities of the fluxes of charge-exchange neutrals with an energy of 150 eV, emitted from the plasma along different chords 1 ms (curve *1*) and 160 μs (curve *2*) before the disruption and 25 μs (curve *3*) after the disruption. Unfortunately, we failed to carry out measurements during the disruption because of technical difficulties. Figure 3 shows the same profiles, but for charge-exchange neutrals with an energy of 700 eV. The profiles are seen to be nonmonotonic: they are highly peaked near the chords corresponding to the vertical displacement at the positions $z \approx \pm 20$ and ± 70 mm with respect to the plasma center. In Fig. 3, this effect is more pronounced. We can also see that the intensity of charge-exchange neutral fluxes, on the average, increases in the negative direction from the plasma center to the periphery. Under the above experimental conditions, the centrifugal drift of the ions and their drift in the nonuniform magnetic field of the device have the same direction.

Figure 4 shows representative profiles of the OV ($\lambda = 2781$ Å) and D_β ($\lambda = 2781$ Å) line intensities. The OV line intensity is seen to be peaked near the same chords as the intensity of charge-exchange neutral fluxes. It is important to note that the positions of the peaks depend neither on the discharge current nor on the magnetic field strength, provided that the safety factor at the plasma boundary is the same in different discharges. The *z*-profile of the D_β line intensity is far more monotonic. It is notable that the intensity of the D_β line increases along the *z* coordinate in the direction of the electron drift.

Figure 5 shows how the plasma ion temperature depends on the distance from the viewing chord to the plasma center. The measurements were carried out 1 ms (curve *1*) before the disruption and 25 μs (curve *2*) after the disruption. The ion temperature profiles are seen to be more monotonic than those of the intensity of charge-exchange neutral fluxes. We note that there are regions with a high temperature gradient near the plasma boundary, i.e., at $|z| > 40$–50 mm. This indicates that the energy lifetime of the ions in these regions is fairly long, which is usually regarded as evidence for the existence of an external transport barrier for the

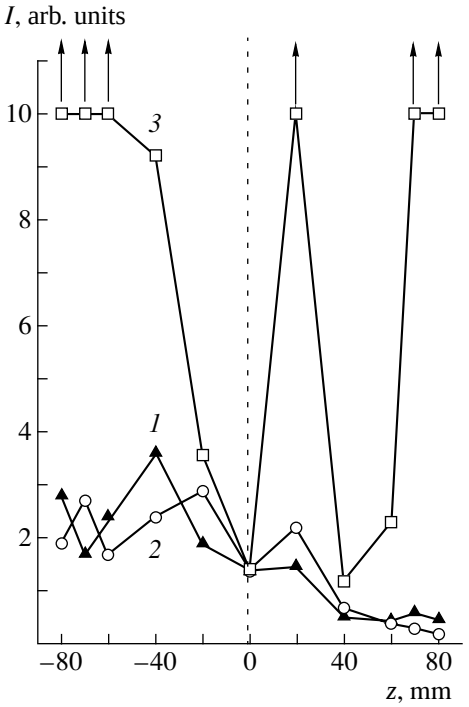

Fig. 3. Same as in Fig. 2, but for charge-exchange neutrals with an energy of 700 eV.

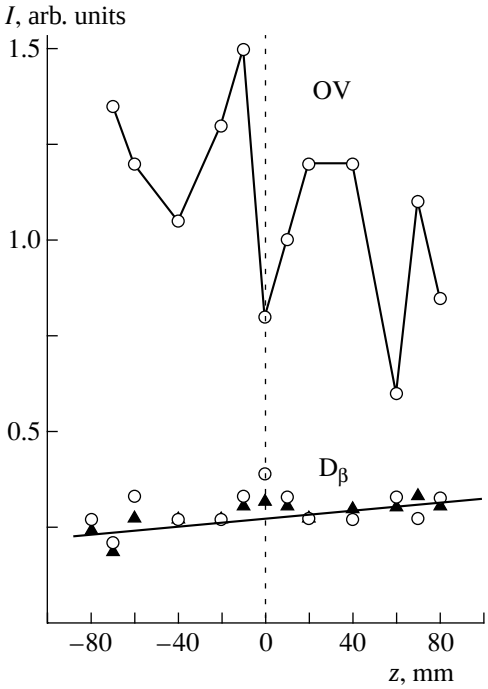

Fig. 4. Intensity of OV and D_β radiation lines emitted from impurities in the vertical direction (▲) 1 ms before and (○) 25 μs after the disruption.

ions. We can see that, during the disruption, the ion temperature (or, more precisely, its transverse component) increases by a factor of approximately 1.5–2. In small tokamaks, the ion temperature determined by analyzing the flux of charge-exchange neutrals emitted from the plasma along a certain chord is close to the maximum plasma temperature over this chord. It should be stressed that the existence of the observed regions with enhanced emission of charge-exchange neutrals and optical radiation from impurity ions may be a source of errors in the measurements of the radial profiles of the ion temperature. Additionally, in tokamaks, errors in the radial ion-temperature profile measured by particle diagnostic techniques may result from banana particles and particles trapped in the local wells of a rippled toroidal magnetic field [9–11]. Since the profiles in Fig. 5 were not corrected for these possible sources of errors, the nonmonotonic character of the ion temperature in the z direction may be less pronounced than that of the charge-exchange neutral fluxes.

4. DISCUSSION OF THE RESULTS

The main distinctive feature of the experimental profiles shown in Figs. 3–5 is that they are peaked near certain chords. Emission of charge-exchange neutrals and radiation from impurities are enhanced in regions near the chords corresponding to the vertical displacement at the positions $z = \pm 20$ mm and $z = \pm 70$ mm with respect to the plasma center. Estimates show that, at such distances from the plasma center in the DAMAVAND tokamak, the safety factor q at $q_a \sim 2.3$ is close to 1 and 2, respectively. This indicates that enhanced emission of charge-exchange neutrals and enhanced

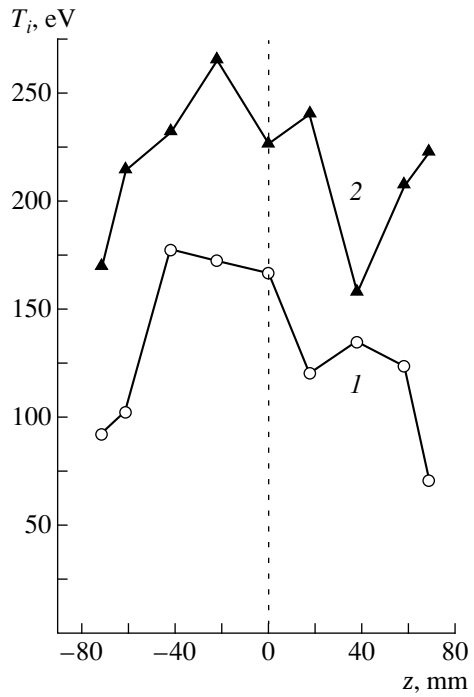

Fig. 5. Profiles of the plasma ion temperature in the vertical direction (*1*) 1 ms before and (*2*) 25 μs after the disruption.

radiation from highly ionized impurities along these chords are largely governed by the regions around rational magnetic surfaces with $m = 1, 2$ and $n = 1$. Summarizing the experimental data presented here and in the cited works makes it possible to conclude that, during the disruption, the ions are accelerated primarily near the rational magnetic surfaces.

The fact that the nonmonotonic character of the z-profile of the OV line intensity is more pronounced than that of the D_β line intensity allows us to suggest that fast electrons accumulate near the rational magnetic surfaces, whereas slow electrons (with energies $E_e < 50$ eV) are distributed more uniformly over the cross section of the plasma column. In fact, the highest ionization rate constant for deuterium atoms corresponds to an electron energy of about 50 eV, while the rate constant of the ionization process OIV $\longrightarrow$ OV is maximum at an electron energy of about several kiloelectronvolts [12]. The nonmonotonic character of the OV line intensity profile can also be regarded as evidence of the accumulation of heavy impurities near the rational magnetic surfaces.

It is known [13, 14] that transport processes near to and far from the rational surfaces differ in properties. This results in the formation of transport barriers near the rational surfaces and the accumulation of background electron and ions, as well as impurity ions, within the barriers. Moreover, the particle temperature in the barrier zones can differ appreciably from that in other plasma regions [13]. Such accumulation of impurity ions (in particular, carbon ions) was observed in experiments on the JT-60U tokamak [14].

Hence, the experimental data obtained from ohmically heated discharges in the DAMAVAND tokamak show that the properties of the regions appearing near the rational magnetic surfaces are characteristic of transport barriers.

For small tokamaks operating in ohmic heating modes, this conclusion, at first glance, seems to be strange. Although the mechanisms for the formation of transport barriers and the physical processes inside them have not yet been studied in detail, it is well known that the formation of transport barriers in large tokamaks is initiated by a sufficiently high auxiliary heating power. It should be emphasized that, in experiments with ohmically heated discharges in the DAMAVAND tokamak, the mean specific power input to the plasma is about 1 W/cm^3, which is nearly the mean specific power input required for the formation of transport barriers in large tokamaks.

5. CONCLUSIONS

(i) The experimental data reported here provide evidence that, in ohmically heated discharges in the DAMAVAND tokamak, local plasma regions appear whose physical properties are typical of transport barriers.

(ii) An analysis of the available database for different plasma currents and different toroidal magnetic fields shows that regions with enhanced emissivity properties arise near rational magnetic surfaces with $q = 1$ ($z = \pm 20$ mm) and $q = 2$ ($z = \pm 70$ mm).

(iii) In these regions, the background and impurity ions both accumulate. Presumably, the electron confinement also improves in these regions.

(iv) The peaks in the profiles of both the intensity of charge-exchange neutral fluxes and the radiation from impurities are observed before and immediately after the disruption of the plasma current. This indicates that the regions with enhanced emissivity properties disappear, if ever, only during the disruption event.

(v) Experimental data show that the radial distribution of the fluxes of charge-exchange neutrals with different energies is fairly sensitive to the presence of transport barriers in the plasma. For this reason, particle diagnostic techniques can be successfully employed to study the formation of transport barriers and their evolution in the plasmas of toroidal devices.

REFERENCES

1. G. M. D. Hogeweij, N. J. López Cardozo, M. R. De Baar, *et al.*, Nucl. Fusion **38**, 1881 (1998).
2. K. Lackner, S. Günter, F. Jenko, *et al.*, Plasma Phys. Controlled Fusion **42**, B37 (2000).
3. A. V. Bortnikov, N. N. Brevnov, Yu. V. Gott, and V. A. Shurygin, Fiz. Plazmy **21**, 672 (1995) [Plasma Phys. Rep. **21**, 634 (1995)].
4. E. Farshi, N. Brevnov, A. Bortnikov, *et al.*, Phys. Plasmas **8**, 3587 (2001).
5. E. Farshi, R. Amrollahy, A. V. Bortnikov, *et al.*, Fiz. Plazmy **27**, 579 (2001) [Plasma Phys. Rep. **27**, 545 (2001)].
6. Yu. V. Gott and A. G. Motlich, Nucl. Instrum. Methods **155**, 443 (1978).
7. Yu. V. Gott and V. A. Shurygin, Fiz. Plazmy **19**, 1075 (1993) [Plasma Phys. Rep. **19**, 559 (1993)].
8. R. Amrollahy, E. Farshi, A. V. Bortnikov, *et al.*, Fiz. Plazmy **23**, 609 (1997) [Plasma Phys. Rep. **23**, 561 (1997)].
9. M. P. Petrov, in *Proceedings of the Conference on Plasma Physics and Controlled Nuclear Fusion Research, Tokyo, 1974* (IAEA, Vienna, 1975), Vol. 1, p. 43.
10. Yu. V. Gott and É. I. Yurchenko, Fiz. Plazmy **9**, 646 (1983) [Sov. J. Plasma Phys. **9**, 377 (1983)].
11. A. V. Gurevich and Ya. S. Dimant, in *Reviews of Plasma Physics*, Ed. by B. B. Kadomtsev (Énergoizdat, Moscow, 1987; Consultants Bureau, New York, 1990), Vol. 16.
12. V. P. Shevelko, H. Tawara, and E. Salzborn, *Multiple-Ionization Cross Section of Atoms and Positive Ions by Electron Impact*, NIFS-DATA-27 (1995).
13. R. D. Hazeltine, Phys. Plasmas **6**, 550 (1999).
14. Y. Koide, T. Takizuka, S. Takeji, *et al.*, Plasma Phys. Controlled Fusion **38**, 1011 (1996).

Translated by G. V. Shepekina

Plasma Physics Reports, Vol. 28, No. 7, 2002, pp. 539–548. Translated from Fizika Plazmy, Vol. 28, No. 7, 2002, pp. 584–593.

MAGNETIC CONFINEMENT SYSTEMS

Kinetic Simulations of EC Plasma Heating and Current Drive in the L-2M Stellarator

A. S. Sakharov and M. A. Tereshchenko

Institute of General Physics, Russian Academy of Sciences, ul. Vavilova 38, Moscow, 119991 Russia

Received February 21, 2002

Abstract—The ECHLAB code, intended for a self-consistent numerical analysis of the evolution of the electron distribution function and the spatial structure of the electromagnetic field during EC plasma heating in a stellarator, is described. The results from calculations of plasma heating and current drive under conditions corresponding to experiments on EC plasma heating by an X2-mode in the L-2M stellarator are presented. It is shown that, at the existing level of microwave power, the energy deposition region displaces only slightly during heating. The energy is mainly absorbed by relatively fast passing electrons. The influence of locally trapped electrons on the efficiency of current drive is insignificant. *© 2002 MAIK "Nauka/Interperiodica".*

1. INTRODUCTION

In present-day plasma confinement experiments, oscillations at the electron cyclotron (EC) frequency and its harmonics are widely used both to heat the plasma and to create and maintain the longitudinal current in toroidal magnetic confinement systems [1–4].

EC oscillations efficiently interact with electrons satisfying the resonant condition $\omega - n\omega_e - k_\| v_\| = 0$. The electric current can be generated due to both direct transfer of the longitudinal momentum from the heating wave to the plasma electrons and collisional relaxation of the perturbed electron distribution function (EDF). The latter mechanism (also called the Fisch–Boozer mechanism [5]) is related to the fact that, at $k_\| \neq 0$, the diffusive flux in velocity space, which reduces the number of electrons with low transverse energies and increases the number of high-energy electrons, is different for electrons with oppositely directed longitudinal velocities. Since the rate of collisional isotropization of low-energy electrons is higher than that of suprathermal electrons ($\nu_{ei} \propto v^{-3}$), there is a relative excess of electrons with $\mathrm{sign}(v_\|) = \mathrm{sign}((\omega - n\omega_e)/k_\|)$; i.e., the longitudinal electric current is generated. This mechanism for current drive is usually dominant; hence, in kinetic simulations of EC heating, it is necessary to take into account both particle collisions and the interaction of electrons with the microwave field. The presence of electrons trapped in the local minima of the magnetic field results in two additional current drive mechanisms. First, trapped electrons, executing fast longitudinal oscillations, immediately lose the acquired longitudinal momentum; as a result, the friction between trapped and passing electrons reduces the current carried by the latter. Second, when "barely passing" electrons acquire transverse energy due to resonant absorption, they can pass into the trapped state; this results in the generation of a current (the so-called Ohkawa current [6]) directed oppositely to the Fisch–Boozer current.

The problem of current drive in closed plasma confinement systems is very challenging from the standpoint of creating and maintaining the optimum current profiles (e.g., for suppressing MHD instabilities or compensating the bootstrap current). A specific feature of EC heating is that the microwave energy is deposited (and, accordingly, the current is driven) in a narrow spatial region, whose position and shape depend substantially on both the magnetic field structure and the EDF. The increase in the electron energy and the attenuation of the microwave beam as it propagates in the plasma are determined by the local efficiency of the resonant EC interaction on each of the magnetic field lines crossed by the beam. These processes are self-consistently taken into account in the codes CQL3D [7], BANDIT-3D [8], and OGRAY [9, 10] (see also [11]), designed for the simulations of EC heating in tokamaks.

Similar numerical codes used to simulate EC heating in stellarators have the following specific features. On the one hand, the majority of modern codes [12–15] take into account radial transport related to uncompensated drift of the trapped particles. On the other hand, the spatial distribution of the microwave field amplitude is usually found by using the local damping coefficients calculated under the assumption that the EDF is Maxwellian and the magnetic field is uniform. This means that, when calculating the interaction of electrons with a microwave beam, the finite beam aperture and the nonuniformity of electron motion in the resonance region are not actually taken into account. For stellarators, such an approach seems to be even less justified than for tokamaks, first of all, because of the considerable longitudinal magnetic field gradient, which varies the efficiency of the resonant interaction. The

1063-780X/02/2807-0539$22.00

importance of a self-consistent analysis is associated not only with the possible influence of the modification of the EDF on the microwave field absorption, but also with the fact that, in the presence of the longitudinal nonuniformity of the magnetic field, the conventional method for computing the damping rate can result in considerable errors in calculating the power absorbed by electrons.

This paper is aimed at simulating EC plasma heating and current drive in stellarators and studying the influence of the change in the EDF on the profiles of energy deposition and current drive during EC heating. For this purpose, the numerical code ECHLAB, designed by us, is applied. The underlying principles of the code are described below.

2. KINETIC EQUATION

The interaction of electrons with an electromagnetic wave results in the time evolution of the EDF on the magnetic surfaces crossed by the microwave beam. To study this process, we use a kinetic equation describing electron diffusion in velocity space under the action of microwave oscillations and Coulomb collisions:

$$\frac{\partial F}{\partial t} + \mathbf{v}_{dr}\nabla F = (\hat{Q} + \hat{S})F. \tag{1}$$

Here, $F = F(V, U, r, \vartheta)$ is the EDF averaged over longitudinal motion, r is the mean radius of a magnetic surface, ϑ is the poloidal angle, $\mathbf{v}_{dr}$ is the drift velocity, $V = p/(m_e c)$, $U = p_{\|0}/p$, p is the absolute value of the electron momentum, and $p_{\|0}$ is the longitudinal momentum of an electron in the minimum of the magnetic field on the given field line. The averaging over longitudinal motion makes sense if the characteristic frequency of this motion (the bounce frequency for trapped particles or the reciprocal of the period of circulation along the torus for passing particles) substantially exceeds the collision frequency. Under conditions typical of EC heating in stellarators, this requirement is satisfied for the majority of electrons. In the variables V and U, the operator of quasilinear diffusion for the resonance heating at the nth harmonic of the electron gyrofrequency has the form [10]

$$\hat{Q}F = \omega_b \hat{L}_n \omega_b^{-1} D_n \hat{L}_n F, \tag{2}$$

where

$$\hat{L}_n = \frac{\gamma}{V}\left(\frac{\partial}{\partial V} + \frac{1 - U^2 - n\omega_{e0}/\omega}{VU}\frac{\partial}{\partial U}\right), \tag{3}$$

$\omega_b = 2\pi/\oint v_\|^{-1} d\ell = 2\pi c V \gamma^{-1}/\oint (1 - b + bU^2)^{-1/2} d\ell$ is the characteristic frequency of longitudinal motion of an electron, ℓ is the longitudinal coordinate, ω_{e0} is the relativistic electronic gyrofrequency in the minimum of the magnetic field on a given field line, $\gamma = (1 + V^2)^{1/2}$ is the relativistic factor, and b is the local value of the magnetic field normalized to its minimum value on the electron trajectory (the mirror ratio). In the so-called "shove" approximation [16], the local value of the quasilinear diffusion coefficient is determined as

$$D_n(V, U, r, \vartheta) = \frac{\omega_t}{4\pi}|\Delta\gamma|^2, \tag{4}$$

where $\Delta\gamma$ corresponds to the increment in the electron energy during one passage through the resonance region and ω_t is the passage rate, which coincides with ω_b for passing electrons and is equal to $\omega_t = \omega_b/M$ for trapped electrons (here, M is the number of the minima of the magnetic field on a given field line). The linearized operator of Coulomb collisions (averaged over longitudinal motion) has the form

$$\hat{S}F = \frac{2\pi e^4 n_e \Lambda}{m_e^2 c^3}\gamma^2 \left\{ u_e^{-2}\frac{\partial}{\partial V}\frac{\gamma}{V} \times \left[\frac{A_e}{\kappa_e}\frac{\partial}{\partial V}(\kappa_e F) + Z_{\text{eff}}\frac{v_{Ti}^2}{v_{Te}^2}\frac{A_i}{\kappa_i}\frac{\partial}{\partial V}(\kappa_i F)\right] + \frac{\omega_b (C_e + Z_{\text{eff}} C_i)}{2\pi c V^4 U}\frac{\partial}{\partial U}\frac{1 - U^2}{U}\oint \frac{(1 - b + bU^2)^{1/2}}{b} d\ell \frac{\partial F}{\partial U}\right\}, \tag{5}$$

where Λ is the Coulomb logarithm, $u_\alpha = V\frac{c}{v_{T\alpha}}$, $v_{T\alpha}^2 = \frac{2T_\alpha}{m_\alpha}$, $\kappa_\alpha = \exp\left(u_\alpha^2 \frac{m_e}{m_\alpha}\right)$, $A_\alpha = \frac{4}{\sqrt{\pi}}\int_0^{u_\alpha} x^2 \exp(-x^2) dx$, $C_\alpha = \frac{2u_\alpha}{\sqrt{\pi}}\exp(-u_\alpha^2) + \left(1 - \frac{1}{2u_\alpha^2}\right)A_\alpha$, $Z_{\text{eff}} = n_e^{-1}\sum_i Z_i^2 n_i$ is the effective ion charge number, and $\alpha = e, i$; the other notation is standard.

Almost all specific features of EC interaction are described by the expression for the quasilinear diffusion coefficient D_n. If the electron Larmor radius is small as compared to the transverse wavelength, then the equations of electron motion (averaged over Larmor rotation) in a microwave field [16] result in the following expression:

$$D_n = \frac{1}{2c}\frac{\omega_t}{\omega_b}\left[\frac{(n/2)^n}{n!}\frac{e|E_-|}{m_e\omega}(N_\perp b^*)^{n-1}\right]^2 \times \frac{V^{2n+1}(1 - U^2)^n}{\gamma^3 \oint (1 - b + bU^2)^{-1/2} d\ell}|G|^2, \tag{6}$$

where $E_\pm = E_x \pm iE_y$ is the circularly polarized components of the microwave electric field (x and y are the coordinates in the minor cross section of a torus); the

amplitude values are taken in the plane $\ell = \ell_0$, corresponding to the beam axis; $b^* \equiv \dfrac{m_e c\omega}{n|e|B_{\min}}$ is the resonant value of b;

$$G = \omega\int_{-\infty}^{+\infty}\zeta b^{1-n/2}a(\ell(t))\exp(-i\Psi(t))dt; \qquad (7)$$

$$\zeta = 1 + N_\perp V\frac{|E_\parallel|}{|E_-|}\frac{b^*}{b}(1 - b + bU^2)^{1/2};$$

$$\Psi = \int_0^t [k_\parallel v_\parallel(\ell(t')) + n\omega_e(\ell(t')) - \omega]dt';$$

and $a(\ell)$ is the profile of the microwave beam amplitude along a magnetic field line. The quantity G is the dimensionless time of resonant interaction (in the given model, the limits of integration can be considered infinite).

3. CODE ECHLAB

Kinetic processes in toroidal devices are simulated by using equation (1), averaged over a magnetic surface. For passing particles, whose energy is rapidly redistributed over the magnetic surface, the averaging is performed over the entire range of poloidal angles. For locally trapped particles, the averaging is performed over the ϑ interval corresponding to their banana trajectories. In the kinetic equation, we use the quasilinear diffusion coefficient $D_n(V, U, r)$, averaged over ϑ with a weight function accounting for the nonuniformity of the magnetic field over ϑ (in particular, for a magnetic surface with a circular cross section, the weight function has the form $(1 + \varepsilon_t\cos\vartheta)^{-1}$).

In this study, we ignore the effects related to the processes of cross-field transport of particles and energy in order to ensure an unambiguous interpretation of the computation results. Accordingly, the kinetic equation does not contain gradient terms describing neoclassical diffusion, so that the electron density $n_e = \dfrac{2\pi m_e^3 c^3}{\int b^{-1}d\ell}\iiint FV^2\left(\dfrac{1-b}{U^2} + b\right)^{-1/2}dVdUd\ell$ on a magnetic surface is conserved. In fact, this means that the residence time of a particle in a trapped state $t_{tr} \sim \nu_e^{-1}\Delta b$, which is determined by the modulation depth of the magnetic field Δb and the collision frequency, is assumed to be so small that, over this time, the trapped particle practically does not shift from the magnetic surface. For the problem of simulating EC heating and current drive in the axial region of a stellarator under conditions when the energy deposited in the locally trapped electrons is relatively low, such a model seems to be quite satisfactory. The contribution of the high-energy tails of the locally trapped electrons to energy transport under conditions typical of L-2M was considered in [17].

Since we are interested, first of all, in the distribution of passing electrons, we will assume that all the trapped electrons are described by a unified distribution function, irrespective of their localization along a torus. As a result, instead of a set of kinetic equations for passing electrons and, in general, for electrons trapped in each magnetic well with boundary conditions corresponding to the continuity of the EDF at the boundaries of the trapping regions and to the conservation of the particle fluxes, we are dealing with one equation describing both trapped and passing electrons.

For many stellarators, the magnetic field near the magnetic axis can be represented by one helical harmonic:

$$B(r, \vartheta, \varphi) \approx [1 - \varepsilon_t\cos\vartheta - \varepsilon_h\cos(l\vartheta - m\varphi)]B_0. \qquad (8)$$

This representation is characteristic of classical stellarators (such as L-2M and U-3M), as well as torsatron (heliotron) devices (LHD, ATF, CHS, and Heliotron-E). For these systems, the longitudinal profile of the magnetic field in the region where electrons interact with a microwave beam can be represented as

$$b = 1 + \xi\sin^2\chi, \qquad (9)$$

where $\xi = 2\varepsilon_h(1 - \varepsilon_t\cos\vartheta - \varepsilon_h)^{-1}$, $\chi = \pi\ell/L$, and L is the spatial (along the torus) period of a helical magnetic field. The unperturbed longitudinal motion of an electron is described by the expression

$$\chi(t) = \mathrm{am}\left(\frac{\pi cVU}{L\gamma}t, \lambda\right), \qquad (10)$$

where the wave phase on the electron trajectory is equal to

$$\Psi(t) = \Psi(0) + \omega[(b^*\gamma)^{-1} - 1]t + \frac{\omega L}{\pi c}\left[N_\parallel\chi(t) + \frac{\xi}{b^*VU}D(\chi(t), \lambda)\right]. \qquad (11)$$

Here, $D(\chi, \lambda) = \int_0^\chi \sin^2\varphi\,(1 - \lambda^2\sin^2\varphi)^{-1/2}d\varphi$ is the Legendre elliptic integral, $\mathrm{am}(\tau, \lambda)$ is the amplitude of the Jacobi elliptic function, and the quantity $\lambda^2 = \xi(1 - U^2)/U^2$ characterizes the degree to which an electron is trapped in the magnetic well. Note that the expressions for $\chi(t)$ and $\Psi(t)$ can also be obtained for magnetic configurations more complicated than those described by formulas (8) and (9) by approximating the dependence $\sqrt{b(\chi) - 1}$ by a piecewise-sinusoidal function with a varying amplitude. This may be needed when the rotational transform over one period of the magnetic field is not small (in the theory of neoclassical transport, a similar approach was used in [18]).

The transverse intensity profile of the microwave beam launched into a plasma is usually close to Gaussian. Therefore, at small angles between the propagation direction of the beam and the magnetic field gradient, the amplitude of the microwave field on the electron trajectory can be described by

$$a(t) = \exp\left(-\frac{L^2}{\pi^2\rho^2}(\chi(t)-\chi_0)^2\right), \quad (12)$$

where ρ and χ_0 are functions of x and y. Integration in formula (7) is performed numerically, because the approximate analytical methods [19, 20], based on keeping the terms $\sim t^3$ and $\sim t^2$ in the expansions of $\Psi(t)$ and $a(t)$, respectively (or taking into account the $a(t)$ dependence parametrically), do not provide the necessary accuracy for certain groups of electrons.

To calculate the distribution of the electromagnetic field in a microwave beam, we used the following model. In the direction perpendicular to both the wave vector **k** and the magnetic field **B**, the beam was split into plane layers. In each of these layers, the profile of the electromagnetic field along the toroidal coordinate was described by expression (12). To find the distribution of the microwave field amplitude in an individual layer along the propagation direction of the beam, we used one-dimensional equations obtained from a set of algebraic equations [16, 21] by the replacement $N_\perp \longrightarrow i\frac{c}{\omega}\frac{\partial}{\partial x}$. In the case $|\omega - n\omega_e| \ll \omega$, $k_\perp v_{Te} \ll |\omega_e|$, and $n \geq 2$, this set takes the form

$$\begin{pmatrix} 2-N^2-N_\parallel^2-\frac{2nq_e}{n-1}+i\eta & N_\perp^2 & N_\perp N_\parallel \\ N_\perp^2 & 2-N^2-N_\parallel^2-\frac{2nq_e}{n+1} & N_\perp N_\parallel \\ N_\perp N_\parallel & N_\perp N_\parallel & 1-N_\perp^2-q_e \end{pmatrix} \begin{pmatrix} E_- \\ E_+ \\ 2E_\parallel \end{pmatrix} = 0, \quad (13)$$

where $q_e = \omega_{pe}^2/\omega^2$. The boundary conditions for an electromagnetic field were imposed in a vacuum and corresponded to an incident and reflected waves on the side where the microwave beam was launched into the plasma and to a transmitted wave on the opposite side. Such an approach allowed us, e.g., to adequately describe the strong damping of the wave in the resonance region (as well as the reflection from this region) for a characteristic damping length on the order of or smaller than the wavelength of microwave oscillations. In this situation, the geometric-optics approximation is inapplicable. We note that, in set (13), we only retain the imaginary component $\eta \equiv \mathrm{Im}\varepsilon_{--}$, because, for $k_\perp v_{Te} \ll |\omega_e|$, the hierarchy of the imaginary parts of the matrix elements is as follows: $\eta \gg \mathrm{Im}\varepsilon_{-\parallel} \gg \mathrm{Im}\varepsilon_{\parallel\parallel} \gg \mathrm{Im}\varepsilon_{+\parallel} \gg \mathrm{Im}\varepsilon_{++}$. To describe the problem self-consistently, the η value should be found from the energy balance between the absorption of the microwave field and the quasilinear heating of electrons:

$$\frac{2\,\mathrm{Im}\,\mathrm{Det}}{\partial(\mathrm{Re}\,\mathrm{Det})/\partial k} = -\frac{\int w_{abs}\,d\ell}{\int P\,d\ell}. \quad (14)$$

Here, Det is the determinant of the matrix in set (13); P is the energy flux density of the wave; and w_{abs} is the specific power density acquired by electrons in the course of quasilinear diffusion, described by Eq. (2):

$$w_{abs} = -\frac{2\pi m_e^4 c^5}{\int b^{-1}\,d\ell}\iiint V\gamma^2 D_n\left(\frac{1-b}{U^2}+b\right)^{-1/2} \times\left[\frac{\partial F}{\partial V}+\frac{1-U^2-(b^*\gamma)^{-1}}{VU}\frac{\partial F}{\partial U}\right]dV\,dU\,d\ell. \quad (15)$$

It follows from Eq. (14) that, for the heating at the second harmonic of the electron gyrofrequency and for quasi-transverse wave propagation, the η value can be calculated by the formula

$$\eta(x,y) = \frac{8\sqrt{2\pi}R_0 w_{abs}(x,y)}{k\rho P_{\chi_0}(x,y)}N^2\left(\frac{3-4q_e}{3-2q_e}\right)^2. \quad (16)$$

The procedures for solving the wave equations and averaging the quasilinear diffusion coefficients over a set of magnetic surfaces (whose coordinates were calculated in advance) require a numerical grid with a rather small step along the x coordinate (no larger than 1/10 of the wavelength). However, the kinetic equation itself can be solved with a relatively large step in r, and the local values of the EDF, required to calculate the specific power density (15), can be found by interpolation.

4. RESULTS OF SIMULATIONS

In calculations, the parameters of the plasma and the magnetic field corresponded to the conditions of experiments on plasma heating by an extraordinary wave at

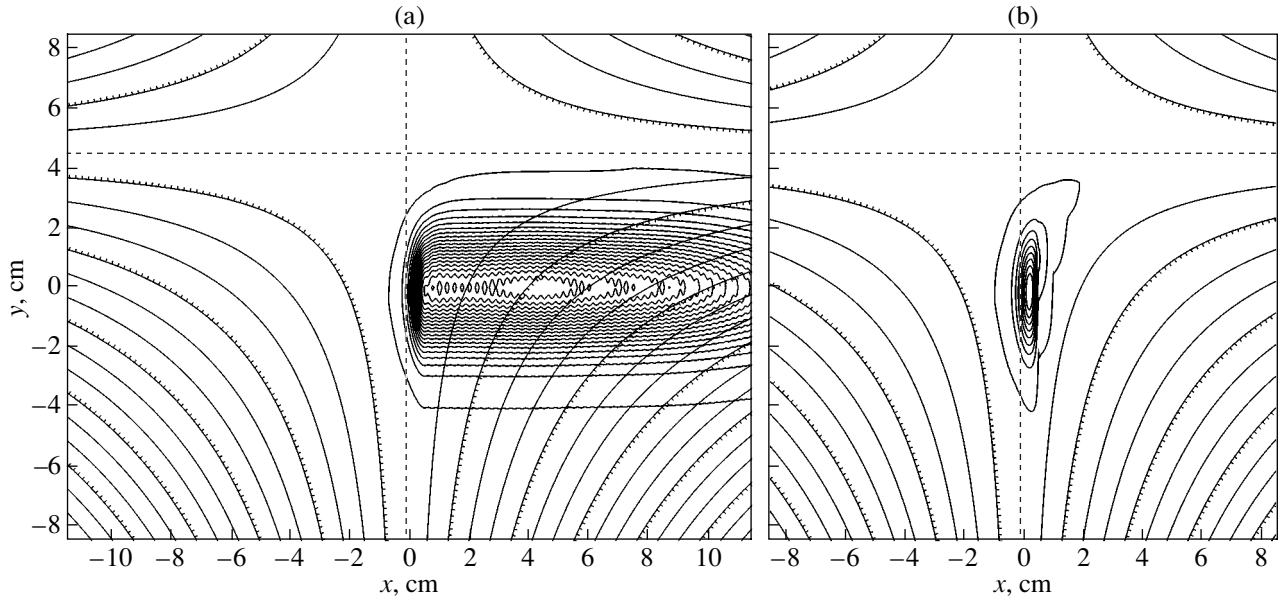

Fig. 1. Distributions of (a) $|E_-|^2$ and (b) w_{abs} in the cross section at which the microwave beam is launched into the plasma for $B_{res}/B_0 = 1$ and $\varphi = 0$ (on-axis heating). The ticks on the contours B = const are directed to the lower B values.

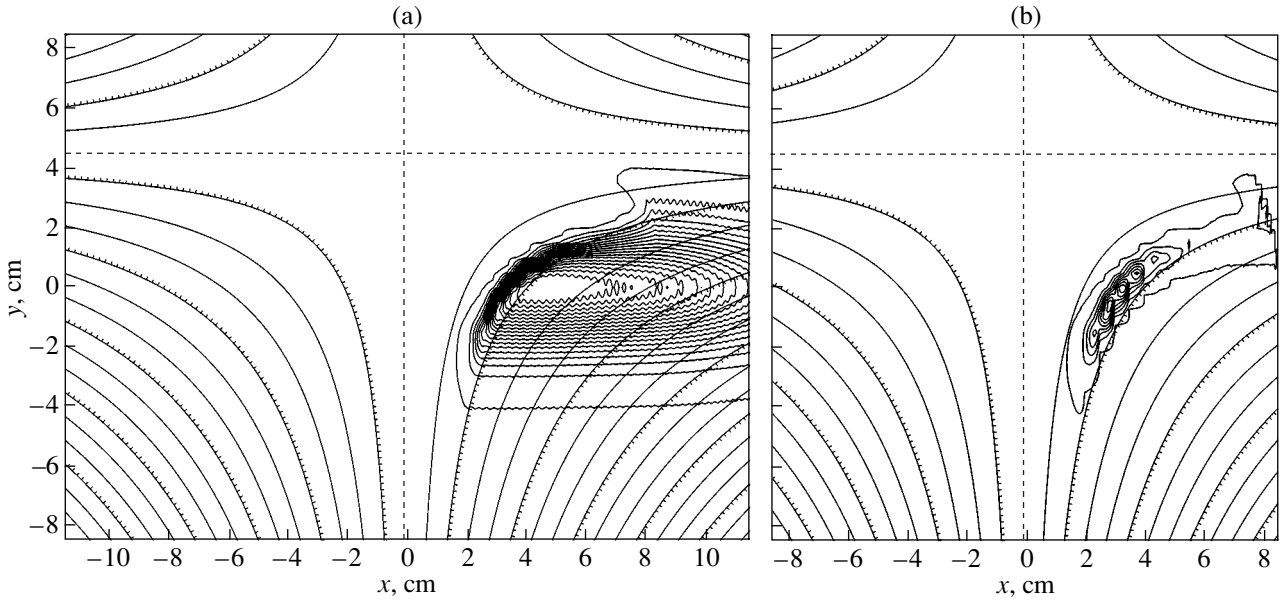

Fig. 2. Same as in Fig. 1 for $B_{res}/B_0 = 0.97$ and $\varphi = 0$ (off-axis heating, the middle of the slope of the magnetic well).

the second harmonic of the electron gyrofrequency in the L-2M stellarator [22–25]: $n_{e0} = 1.7 \times 10^{13}$ cm^{-3}, $T_{e0} = 1$ keV, $T_{i0} \ll T_{e0}$, $Z_{eff} = 2$, the major radius is $R_0 = 100$ cm, and $B_0 = 1.34$ T. The profile of the electron density and the initial profile of the electron temperature were taken to be $n_e = n_{e0}[1 - (r/a_0)^6]$ and $T_e = T_{e0}[1 - (r/a_0)^2]$, where $a_0 = 11.5$ cm is the mean radius of the plasma column and r is the effective radius of a magnetic surface. It is assumed that a microwave beam with the radius $\rho_0 = 2.5$ cm, frequency $f = 75$ GHz, and power $W_0 = 230$ kW is launched from the low-field side. The beam axis lies in the horizontal plane and is quasi-perpendicular to the magnetic field ($N_\parallel = 0.1$). The spatial structure of the magnetic field was described in the

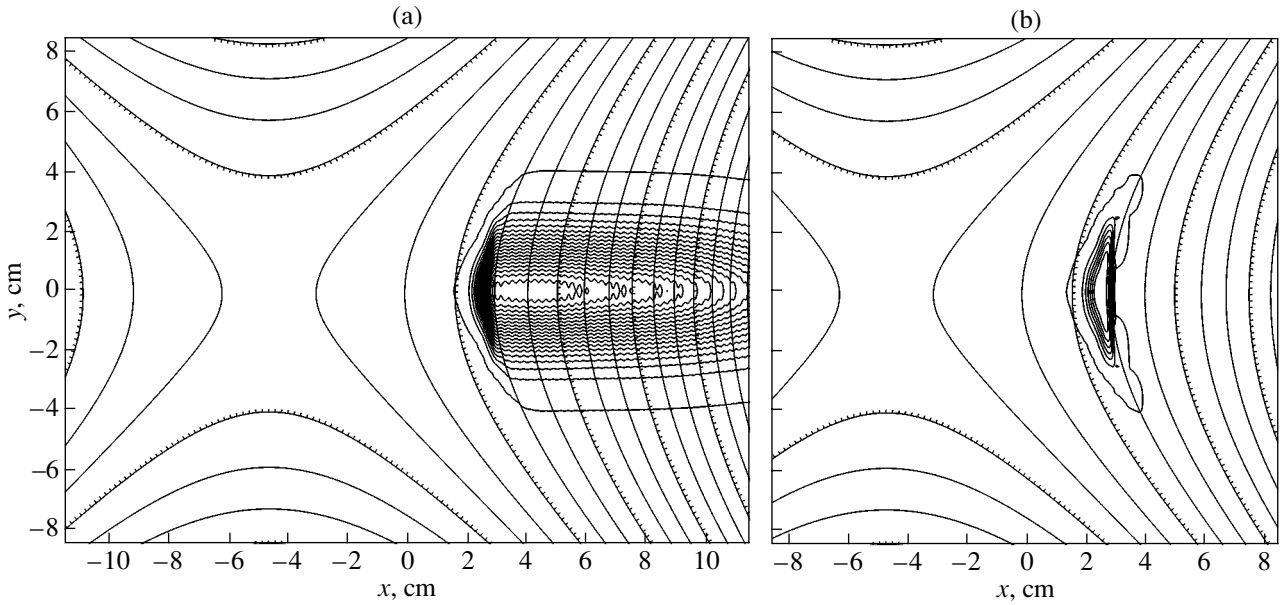

Fig. 3. Same as in Fig. 1 for $B_{res}/B_0 = 0.97$ and $\varphi = -\pi/2M$ (off-axis heating, the bottom of the magnetic well).

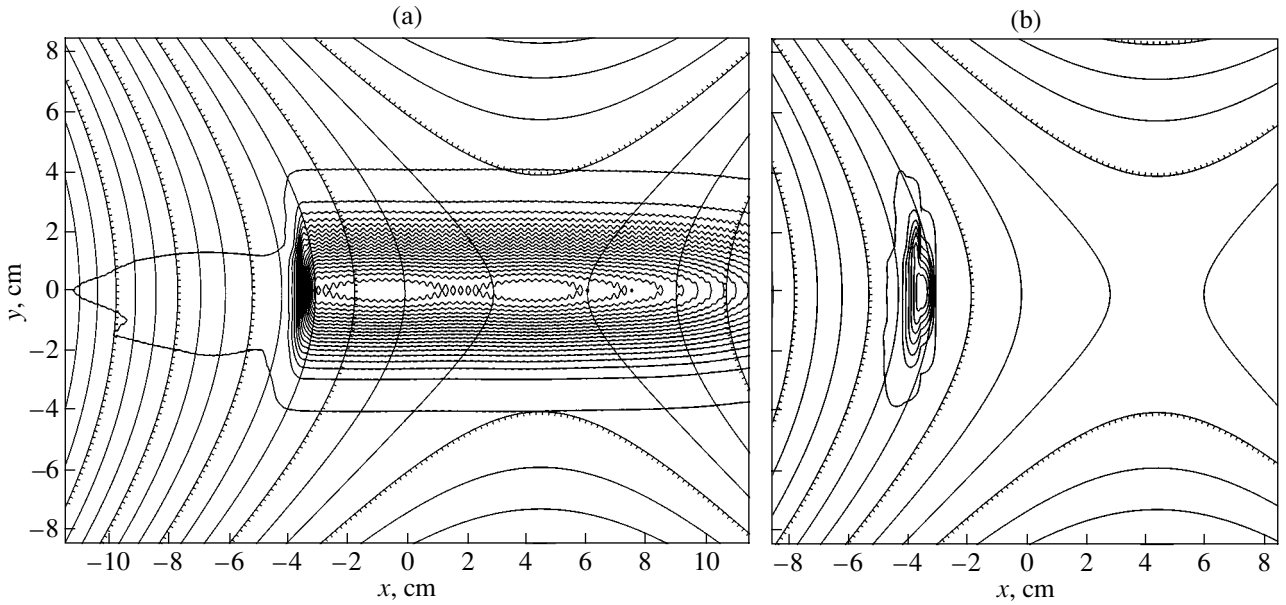

Fig. 4. Same as in Fig. 1 for $B_{res}/B_0 = 1.05$ and $\varphi = \pi/2M$ (off-axis heating, the top of the magnetic hump).

lowest order stellarator approximation by an expression similar to expression (8):

$$B = \left(1 - \frac{r}{R_0}\cos\vartheta + 0.227\left(\frac{Mr}{2R_0}\right)^2 \sin(2\vartheta + M\varphi)\right)B_0, \quad (17)$$

where $M = 14$ is the number of the stellarator field periods.

Calculations were performed for the following schemes of microwave beam launching:

1. $B_{res}/B_0 = 1$ and $\varphi = 0$ (on-axis heating);

2. $B_{res}/B_0 = 0.97$ and $\varphi = 0$ (off-axis heating, the middle of the slope of the magnetic well);

3. $B_{res}/B_0 = 0.97$ and $\varphi = -\pi/2M$ (off-axis heating, the bottom of the magnetic well); and

4. $B_{res}/B_0 = 1.05$ and $\varphi = \pi/2M$ (off-axis heating, the top of the magnetic hump).

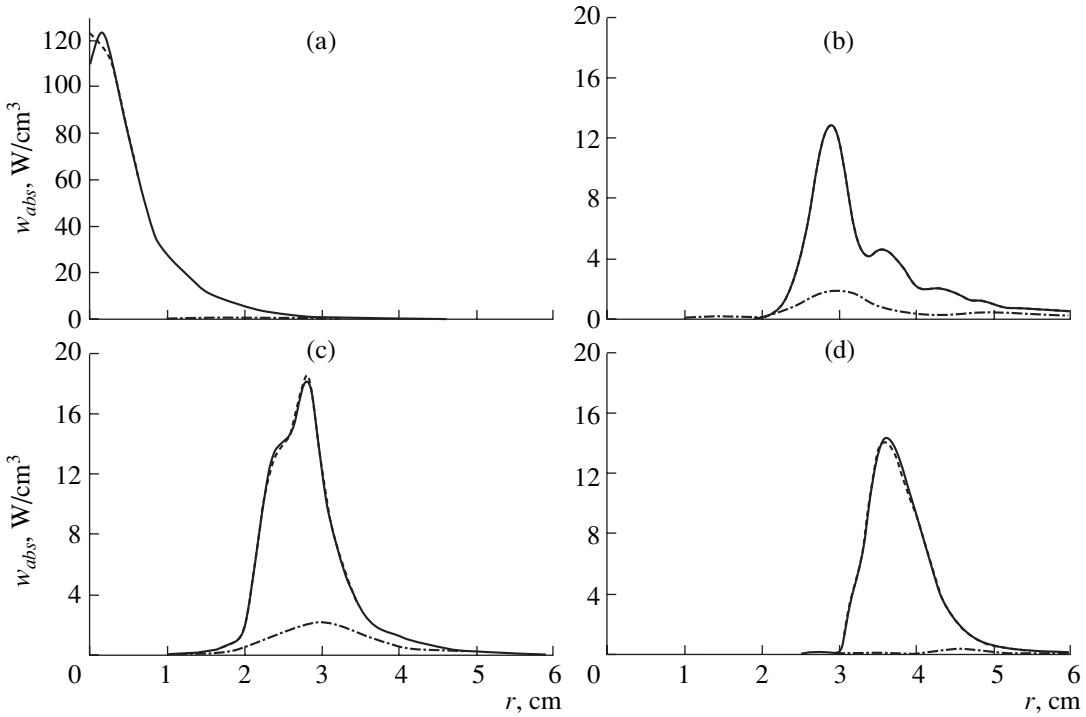

Fig. 5. Radial profiles of the power deposition density w_{abs} at $t = 0$ (dashed curves) and $t = 12\tau_{e0}$ (solid curves): (a) $B_{res}/B_0 = 1$ and $\varphi = 0$ (on-axis heating), (b) $B_{res}/B_0 = 0.97$ and $\varphi = 0$ (off-axis heating, the middle of the slope of the magnetic well), (c) $B_{res}/B_0 = 0.97$ and $\varphi = -\pi/2M$ (off-axis heating, the bottom of the magnetic well), and (d) $B_{res}/B_0 = 1.05$ and $\varphi = \pi/2M$ (off-axis heating, the top of the magnetic hump). The power density deposited in the locally trapped electrons is shown by the dashed-and-dotted line.

Here, $B_{res} = m_e c\omega/2|e|$ is the resonant value of the magnetic field, which determines the position and the general structure of the energy deposition region. Note that, in the existing system of EC plasma heating in the L-2M stellarator, the microwave beam is launched into the plasma in the cross section $\varphi = 0$; therefore, schemes 3 and 4 cannot presently be realized in experiments.

Figures 1–4 show the contour lines of $|E_-|^2$ and w_{abs} in the launching cross section for all of the above schemes. For clarity, the contours $B = \text{const}$ are also shown in the figures. We note that, in the given model, the cross sections of the magnetic surfaces are concentric circles with the center at $x = 0$ and $y = 0$. A somewhat wavy structure of the $|E_-|^2$ contour lines is related to the partial reflection of the wave from the narrow region of resonant absorption, the reflection coefficient being about 1%. It is seen that the energy is deposited in the plasma in a relatively narrow spatial region ($\Delta x \leq \lambda_0$) close to the "cold" resonance ($B = B_{res}$). Calculations show that, at the given microwave power, the spatial distribution of the microwave amplitude changes only slightly in the course of EC heating. Only in the case of on-axis heating, we can see a minor (≈ 2 mm) displacement of the energy deposition region toward the higher magnetic field. A fraction of the microwave power, which is launched into the plasma as an s-polarized wave ($E = E_y$), is transferred to the ordinary mode;

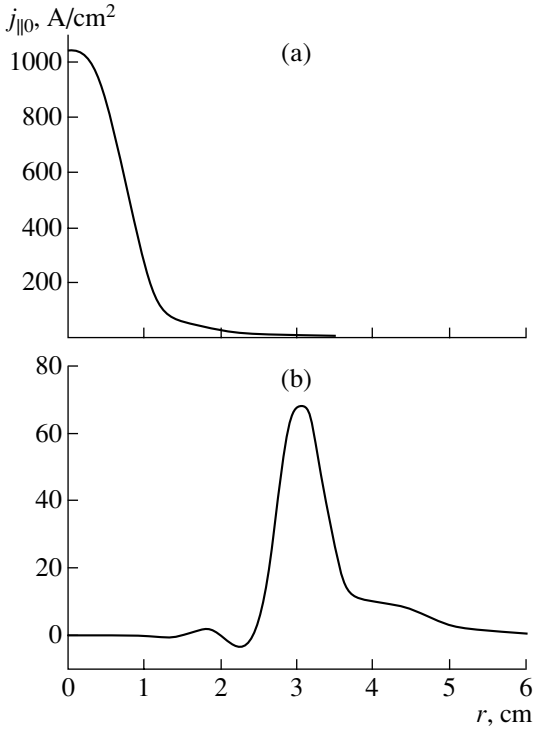

Fig. 6. Radial profiles of the generated current density $j_{\|0}$ at $t = 12\tau_{e0}$: (a) $B_{res}/B_0 = 1$ and $\varphi = 0$ (on-axis heating) and (b) $B_{res}/B_0 = 0.97$ and $\varphi = 0$ (off-axis heating, the middle of the slope of the magnetic well).

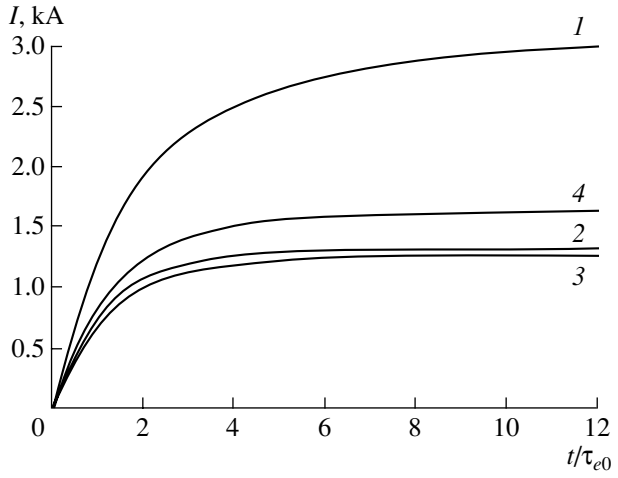

Fig. 7. Time evolution of the total current at (*1*) $B_{res}/B_0 = 1$ and $\varphi = 0$, (*2*) $B_{res}/B_0 = 0.97$ and $\varphi = 0$, (*3*) $B_{res}/B_0 = 0.97$ and $\varphi = -\pi/2M$, and (*4*) $B_{res}/B_0 = 1.05$ and $\varphi = \pi/2M$.

this is related to the mode splitting at the plasma–vacuum interface. As a result, the microwave beam is incompletely absorbed during one passage through the resonance region: for all of the above launching schemes, the absorption factor amounts to 87–92%.

Figure 5 shows the radial profiles of the power deposition density w_{abs} (averaged over magnetic surfaces) in the beginning of EC heating and at $t = 12\tau_{e0}$, when a steady state has been almost established (the characteristic time of Coulomb collisions is $\tau_{e0} \equiv m_e^{1/2} T_{e0}^{3/2} (2\pi n_{e0} e^4 \Lambda)^{-1} = 20$ μs). Naturally, the largest $w_{abs}(r)$ values are attained for on-axis heating, because the plasma volume in which the microwave energy is deposited increases with increasing radius of the magnetic surface. The figure also shows the profiles of the power density deposited in the locally trapped electrons (dashed-and-dotted line). It is seen that, in the region where the power deposition density is maximum, the fraction of energy absorbed by the trapped electrons is no larger than 20% for schemes 2 and 3 and is negligible for schemes 1 and 4. However, at magnetic surfaces distant from the "cold" resonance, the fraction of energy deposited in the locally trapped electrons can substantially increase.

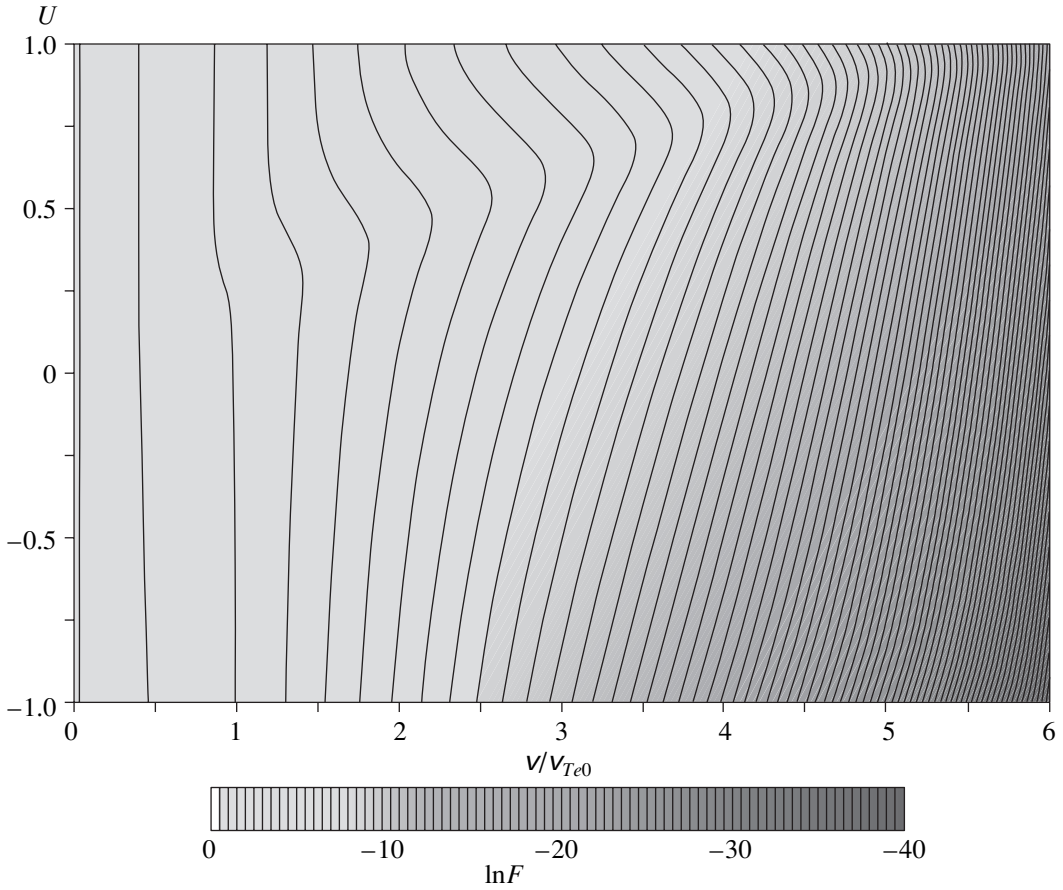

Fig. 8. EDF on the (v/v_{Te0}, $U = p_{\|0}/p$) plane for $B_{res}/B_0 = 1$ and $\varphi = 0$ (on-axis heating) at $t = 12\tau_{e0}$ and $r = 0$.

The radial profiles of the current density $j_{\|0} = -2\pi|e|m_e^3 c^4 \iint F\gamma^{-1}V^3 U dV dU$ in the steady state for schemes 1 and 2 are shown in Fig. 6. It is seen that the current is driven most efficiently in the region where the power deposition density is maximum. The radial profile of the current density for schemes 3 and 4 is approximately the same as for scheme 2. Figure 7 shows the time evolution of the total current for all of the above launching schemes. It is seen that the characteristic time during which the current saturates at a quasi-steady value amounts to several collisional times. The largest current is generated in the case of on-axis heating (≈3 kA), which is explained, first, by the higher value of w_{abs} (and, hence, the larger number of suprathermal electrons) and, second, by the small number of trapped electrons in the axial region.

The anisotropy of electron heating is illustrated in Fig. 8, which shows the relief of the EDF at $t = 12\tau_{e0}$ for the case of on-axis heating (scheme 1). In this case, the effective electron temperature $T_{\text{eff}} = \left\langle \frac{p^2}{2m_e} \right\rangle = \frac{2\pi m_e^4 c^5}{3n_e \int b^{-1} d\ell} \times \iiint FV^4 \left(\frac{1-b}{U^2} + b \right)^{-1/2} dV dU d\ell$ at $r = 0$ and $t = 12\tau_{e0}$ amounts to 2.3 keV, which corresponds to the increase in the temperature by a factor more than 2. We can see the high-energy tail of the EDF in the range of positive longitudinal velocities corresponding to resonant interaction. For the other launching schemes, T_{eff} increases during EC heating by no more than 10% and the tails of the EDF are not so pronounced.

5. CONCLUSION

In this study, we have investigated EC plasma heating and current drive in the L-2M stellarator by using the newly developed numerical code ECHLAB. The code self-consistently takes into account the energy acquired by electrons on a magnetic field line and the damping of the microwave beam. The kinetics of the EC resonant interaction was calculated by using a model that accounts for the nonuniformity of electron motion in a magnetic field with one helical harmonic. The distribution of the electromagnetic field along the propagation direction of the microwave beam was calculated by solving the wave equation, which allowed us, in particular, to take into account the reflection of radiation from the region of resonant absorption. However, at this stage, a number of important effects, such as the refraction of a microwave beam and radial particle transport, as well as the complicated dynamics of transitional (intermediate between trapped and passing) electrons were ignored. When considering Coulomb collisions, the background EDF was assumed to be Maxwellian with the temperature equal to the initial temperature. The calculations were performed without allowance for an additional vertical magnetic field, usually applied to a plasma in real experiments in order to displace the magnetic axis in the horizontal direction. In the presence of such a field, the modulation of the magnetic field on the axis is nonzero, which can substantially increase the role of trapped electrons in the case of on-axis heating.

Nevertheless, the model used, on the whole, satisfactorily describes the main characteristics of the EC interaction for the above schemes of microwave launching. The results obtained demonstrate that, in the case of EC plasma heating by an X2-wave under conditions typical of experiments in L-2M, the energy deposited in the locally trapped electrons is low (as was predicted by analytical estimates [17]). The effect of the reflection of microwave radiation from the region of resonant absorption under the given conditions is also insignificant.

Further simulations of EC plasma heating and current drive will require, on the one hand, improving the numerical code and, on the other hand, combining it with the ray tracing method and the existing transport codes.

ACKNOWLEDGMENTS

This study was supported by the Russian Foundation for Basic Research under the program “Leading Scientific Schools” (grant no. 00-15-96676).

REFERENCES

1. V. E. Golant and V. I. Fedorov, *High-frequency Methods for Plasma Heating in Toroidal Fusion Devices* (Énergoatomizdat, Moscow, 1986).
2. V. Erckmann and U. Gasparino, Plasma Phys. Controlled Fusion **36**, 1869 (1994).
3. T. Watari, Plasma Phys. Controlled Fusion **40**, A13 (1998).
4. B. Lloyd, Plasma Phys. Controlled Fusion **40**, A119 (1998).
5. N. J. Fisch and A. M. Boozer, Phys. Rev. Lett. **45**, 720 (1980).
6. T. Ohkawa, General Atomics Report no. GA-A13847 (1976).
7. R. W. Harvey and M. G. McCoy, in *Proceedings of IAEA 1992 Technical Committee Meeting on Advances in Simulation and Modeling of Thermonuclear Plasmas, Montreal, 1993*, p. 498.
8. M. R. O’Brien, M. Cox, C. D. Warrick, and F. S. Zaitsev, in *Proceedings of IAEA 1992 Technical Committee Meeting on Advances in Simulation and Modeling of Thermonuclear Plasmas, Montreal, 1993*, p. 527.
9. A. V. Zvonkov, A. Yu. Kuyanov, A. A. Skovoroda, and A. V. Timofeev, Fiz. Plazmy **24**, 424 (1998) [Plasma Phys. Rep. **24**, 389 (1998)].
10. A. Yu. Kuyanov, A. A. Skovoroda, A. V. Timofeev, and A. V. Zvonkov, Preprint No. 5790/6, IAE (RRC Kurchatov Institute, Moscow, 1994).

11. E. Westerhof, in *Proceedings of the 9th Joint Workshop on ECE and ECRH, Borrego Springs, 1995*, p. 3.
12. M. Romé, V. Erckmann, U. Gasparino, *et al.*, Plasma Phys. Controlled Fusion **39**, 117 (1997).
13. N. Marushchenko, U. Gasparino, H. Maassberg, and M. Romé, Comput. Phys. Commun. **103**, 145 (1997).
14. S. Kasilov, W. Kernbichler, V. Nemov, and M. Heyn, in *Proceedings of the 26th EPS Conference on Controlled Fusion and Plasma Physics, Maastricht, 1999*, ECA, Vol. 23J, p. 1629.
15. S. Murakami, U. Gasparino, H. Idei, *et al.*, Nucl. Fusion **40**, 693 (2000).
16. A. V. Timofeev, in *Reviews of Plasma Physics*, Ed. by B. B. Kadomtsev (Énergoatomizdat, Moscow, 1985; Consultants Bureau, New York, 1987), Vol. 14.
17. A. S. Sakharov and M. A. Tereshchenko, Fiz. Plazmy **21**, 99 (1995) [Plasma Phys. Rep. **21**, 93 (1995)].
18. C. Beidler and H. Maassberg, Plasma Phys. Controlled Fusion **43**, 1131 (2001).
19. A. Yu. Kuyanov, A. A. Skovoroda, and A. V. Timofeev, Fiz. Plazmy **19**, 1299 (1993) [Plasma Phys. Rep. **19**, 683 (1993)].
20. M. A. Tereshchenko, Krat. Soobshch. Fiz., Nos. 11–12, 44 (1994).
21. A. V. Timofeev and G. N. Chulkov, Fiz. Plazmy **5**, 1271 (1979) [Sov. J. Plasma Phys. **5**, 712 (1979)].
22. S. E. Grebenshchikov, Tr. Inst. Obshch. Fiz. Akad. Nauk SSSR **31**, 37 (1991).
23. V. V. Abrakov, D. K. Akulina, E. D. Andryukhina, *et al.*, Nucl. Fusion **37**, 233 (1997).
24. D. Akulina, G. Batanov, M. Berezhetskii, *et al.*, Fusion Eng. Des. **53**, 321 (2001).
25. D. K. Akulina, G. M. Batanov, M. S. Berezhetskiĭ, *et al.*, Fiz. Plazmy **28**, 9 (2002) [Plasma Phys. Rep. **28**, 7 (2002)].

Translated by the authors

Plasma Physics Reports, Vol. 28, No. 7, 2002, pp. 549–558. Translated from Fizika Plazmy, Vol. 28, No. 7, 2002, pp. 594–604.

PLASMA DYNAMICS

Study of Current Sheets in Three-Dimensional Magnetic Fields with an X-Line by Holographic Interferometry

S. Yu. Bogdanov*, V. S. Markov*, A. G. Frank*, G. V. Dreiden, I. I. Komissarova**, G. V. Ostrovskaya**, and E. N. Shedova****

**Institute of General Physics, Russian Academy of Sciences, ul. Vavilova 38, Moscow, 119991 Russia*

***Ioffe Physicotechnical Institute, Russian Academy of Sciences, Politekhnicheskaya ul. 26, St. Petersburg, 194021 Russia*

Received December 27, 2001; in final form, January 20, 2002

Abstract—Results are presented from experimental studies of the spatial electron density distribution in current sheets formed in three-dimensional magnetic configurations with X-lines. The electron density is measured by using two-exposure holographic interferometry. It is shown that plasma sheets can form in a magnetic configuration with an X-line in the presence of a sufficiently strong longitudinal magnetic-field component $B_\parallel$ when the electric current is excited along the X-line. As the longitudinal magnetic-field component increases, the electron density decreases and the plasma sheet thickness increases; i.e., the plasma is compressed into a sheet less efficiently. *© 2002 MAIK "Nauka/Interperiodica".*

1. INTRODUCTION

According to present notion, the origin of flare phenomena that occur in astrophysical and laboratory plasmas lies in a fundamental physical process—the reconnection of magnetic field lines ("magnetic reconnection") in a high-conductivity magnetized plasma [1–3]. By flare phenomena is usually meant a local, sudden, and rapid (i.e., explosive in character) conversion of magnetic energy into the energy of plasma and accelerated particles. Among flare phenomena, we can mention solar and stellar flares, substorms in the magnetospheres of the Earth and other planets, disruption instabilities in tokamak plasmas, and the fast restructuring of magnetic fields in reversed-field pinches, compact tori, and Z- and Θ-pinches. Magnetic reconnection results in a rapid change of the magnetic-field topology, which is accompanied by the conversion of magnetic energy into the thermal and kinetic energy of the plasma, as well as into accelerated particles and radiation. According to B.B. Kadomtsev, magnetic reconnection is of particular importance as "a fundamental plasma process responsible for many active plasma phenomena. To adequately describe the plasma dynamics in a magnetic field, an understanding of this effect is of no less importance than the frozen-in magnetic field concept" [4].

Magnetic reconnection can occur in plasma regions where oppositely (or differently) directed magnetic field lines lie at a short distance from each other. These regions are characterized by the high current density and small scale length; as a result, dissipative processes begin to play an important role even in high-conductivity plasmas and the condition that the magnetic field be frozen in the plasma can be violated. Plasma regions that separate differently directed magnetic fields and where the current is concentrated usually take the form of a current sheet [1, 2]. In this sheet, the reconnection of oppositely directed magnetic field lines, as well as the efficient conversion of magnetic energy is into other types of energy, can occur.

In real situations, e.g., in the solar corona or plasma confinement systems, magnetic reconnection usually occurs in three-dimensional (3D) magnetic configurations that have topological singularities. Therefore, the study of the current sheet formation in 3D magnetic configurations is of great importance for the magnetic reconnection problem as a whole.

Among a variety of 3D magnetic configurations, configurations with X-lines are of particular interest. Such configurations, which often occur in nature (active solar regions) and in laboratory experiments (closed magnetic confinement systems, etc.), play an important role in effects related to magnetic reconnection. Previously, magnetic reconnection in configurations with null lines [5–9] and null points [10–16] was studied both theoretically and experimentally. It is well known that, in the vicinity of a null line, there are two-dimensional (2D) magnetic fields, which vanish at this line. In 3D configurations, all of the three components of the magnetic field can vanish at isolated null points. In a 3D configuration with an X-line, the total magnetic field can be nonzero everywhere; however, both of the transverse components of the magnetic field vanish at the X-line (as in the case of configurations with a null line), whereas the magnetic field component $B_\parallel$, directed along the X-line, is nonzero. It is the presence

1063-780X/02/2807-0549$22.00

of the longitudinal component that distinguishes the X-line from a null line. In other words, a magnetic configuration with an X-line is a more general structure as compared to configurations with a null line or null point. Note that, in the latter configurations, the singular X-line is present both in the zero-field region and far from it.

According to theoretical predictions, in the vicinity of X-lines, cumulative effects can occur and current sheets can form; i.e., magnetic reconnection in the vicinity of an X-line can play a governing role [1]. Therefore, it is very important to clarify the possibility of the current sheet formation in magnetic configurations with X-lines and to determine the spatial structure of the magnetic field and the plasma parameters in the vicinities of these lines.

The simplest magnetic field configuration with an X-line can be represented in the form

$$\mathbf{B} = \{B_x; B_y; B_z\} = \{-hy; -hx; B_\parallel\}. \quad (1)$$

Here, the X-line coincides with the z-axis and $B_\parallel \simeq$ const is the uniform longitudinal component directed along the X-line. In the (x, y) plane, the magnetic field vanishes at the z-axis and is characterized by a constant gradient $h \simeq$ const; i.e., it increases linearly with distance from the z-axis. Obviously, all three components of magnetic field (1) are independent of the z coordinate.

Recently, it was found that current sheets can actually be formed in a magnetic configuration with an X-line when the electric current is excited along the singular line and the longitudinal component of the magnetic field $B_\parallel$ is sufficiently strong [16–18]. Furthermore, it was established that, throughout the entire region occupied by the plasma (or within the major part of this region), the longitudinal component of the magnetic field can be larger than the transverse component. These results were obtained by analyzing the spatial distributions of HeI and HeII plasma emission. The spatial distributions of plasma emission adequately represent the plasma configuration as a whole; however, they fail to provide quantitative information. At the same time, our previous studies demonstrated that holographic interferometry can be efficient in obtaining quantitative data on the spatial plasma density distributions in current sheets produced in 2D magnetic fields [9, 19–21]. In connection with this, we have recently started investigations of the spatiotemporal characteristics of the plasma in current sheets formed in magnetic configurations with X-lines. These studies are based on two-exposure holographic interferometry. Here, we present the first results obtained by this technique. Most attention is concentrated on the determination of structural features of plasma sheets and their dependence on the initial conditions, including the topology of the initial magnetic configuration. We note that some evidence of decreasing the plasma density in the central region of the sheet in the presence of the longitudinal component $B_\parallel$ were previously obtained from spectral measurements [17].

It is well known that interferometric measurements yield the parameter values averaged over the line of sight (in our case, along the z-axis). For this reason, magnetic configuration (1) with $h \simeq$ const and $B_\parallel \simeq$ const, (i.e., a configuration in which none of the three magnetic field components depend on the z coordinate) is very attractive from the diagnostic standpoint. This also refers to measurements of the spatial distributions of plasma emission [16–18]. In this paper, we compare these methods.

It should be emphasized that magnetic reconnection depends substantially on the magnetic structure of the current sheet, as well as on the plasma parameters inside the current sheet and in its vicinity. Hence, besides the fundamental importance for plasma physics, these studies can be of great importance for a number of applications, in particular, for analyzing various magnetoplasma phenomena in the solar atmosphere and in closed magnetic confinement systems.

2. EXPERIMENTAL DEVICE AND DIAGNOSTIC TECHNIQUES

Magnetic reconnection in configurations with singular X-lines was studied experimentally with the CS-3D device [14–18], shown schematically in Fig. 1. Various initial 3D magnetic configurations were formed by superposing two magnetic fields [22] characterized by different types of symmetry—the translational and axial ones. To form magnetic configuration (1) with an X-line, we used a 2D field $\mathbf{B}_\perp = \{-hy; -hx; 0\}$ with a null line on the z-axis and with the gradient $h \leq 600$ G/cm in combination with an almost uniform field $B_\parallel \leq 6$ kG aligned with the null line. Since $B_\parallel$ in the vacuum chamber somewhat decreases near the electrodes, the magnitude of the longitudinal field averaged over z amounted to $\simeq 90\%$ of the $B_\parallel$ value in the midplane of the device. The ripples of the longitudinal magnetic field far from the ends of the system did not exceed $\simeq 2\%$ in the 4-cm-radius region around the axis.

The magnetic fields were produced with the help of separate electrotechnical systems, so that the parameters of each field could be varied independently. This allowed us to form various configurations with different ratios between the longitudinal and transverse components and also to pass gradually from one configuration to another. Both magnetic fields were quasi-steady on the time scale of plasma processes.

To produce a plasma in the initial 3D magnetic field and to excite the electric current through the plasma, we also used two independent electrotechnical systems, which allowed us to vary the plasma parameters over a wide range. The preevacuated vacuum chamber was filled with a gas under study, specifically, helium at an initial pressure of 300 mtorr. At this relatively high ini-

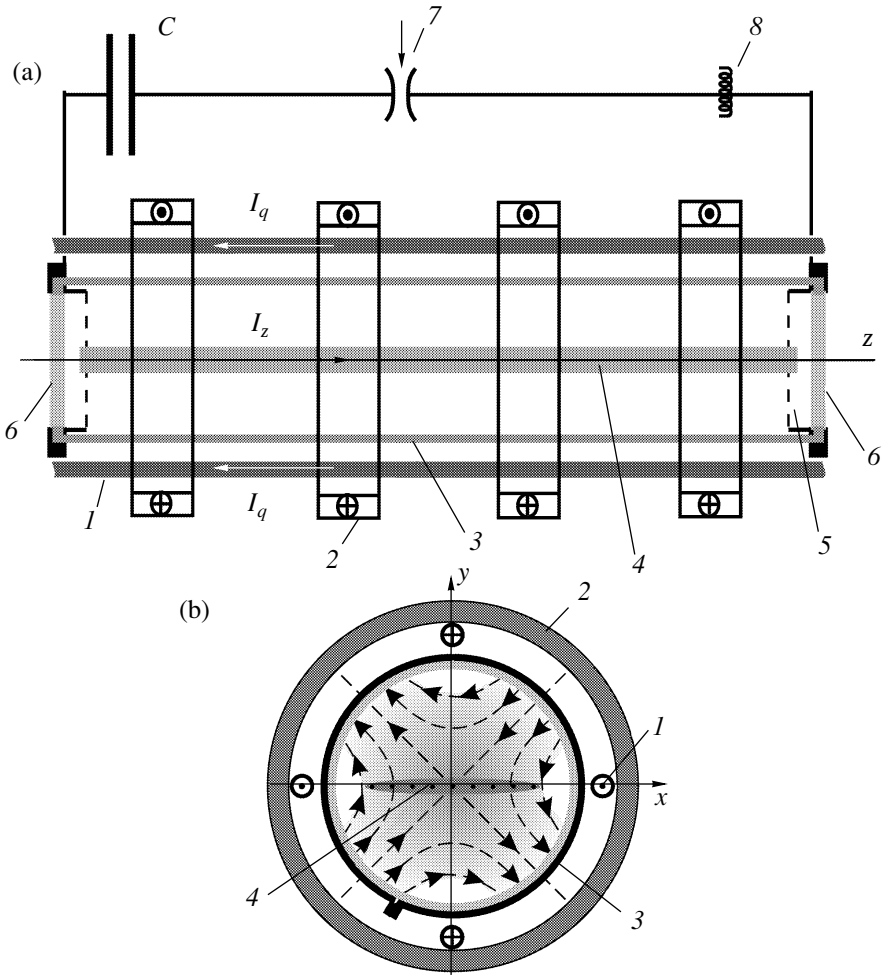

Fig. 1. (a) Longitudinal and (b) transverse cross sections of the CS-3D experimental device: (*1*) conductors producing the transverse 2D magnetic field with a null line; (*2*) coils producing the uniform longitudinal magnetic field $B_{||}$; (*3*) vacuum chamber 18 cm in diameter, $L = 100$ cm; (*4*) current sheet; (*5*) grid electrodes; (*6*) transparent end flanges; (*7*) controllable spark gap for switching the longitudinal electric current I_z; and (*8*) Rogowski coil.

tial pressure, the role of hydrodynamic processes increases (against the background magnetohydrodynamic processes), the sheet forms over a relatively long time, and the dissipative processes become more important [23, 24]. All these features distinguish the high-pressure operating conditions from the previous experiments conducted under the "strong-magnetic-field" conditions, when the plasma pressure was negligibly small [7–9, 19–21].

The initial plasma in the 3D magnetic field was produced by the breakdown of the gas filling the chamber with the help of an auxiliary Θ-discharge with a strong preliminary preionization produced by a set of spark injectors. Then, a pulsed voltage of $\simeq 10$ kV was applied between two grid electrodes inserted into the vacuum chamber from the ends. This voltage excited the electric current I_z in the plasma and initiated the plasma flows in the magnetic field, which resulted in the formation of a current sheet. The half-period of the plasma current was $T/2 = 5$ μs, and its maximum value in this experiment was $I_z^{\max} \simeq 50$ kA.

Experiments carried out with different ratios between the longitudinal and transverse components of the magnetic field allowed us to determine the main characteristics of current sheets and find out how the specific features of their fine structure depend on the topology of the initial magnetic configuration with an X-line.

Conventional diagnostic techniques used in CS-3D included electric measurements, magnetic measurements outside the vacuum chamber [25], time-resolved recording of plasma images in isolated spectral lines [26], and spectral measurements in the visible spectral

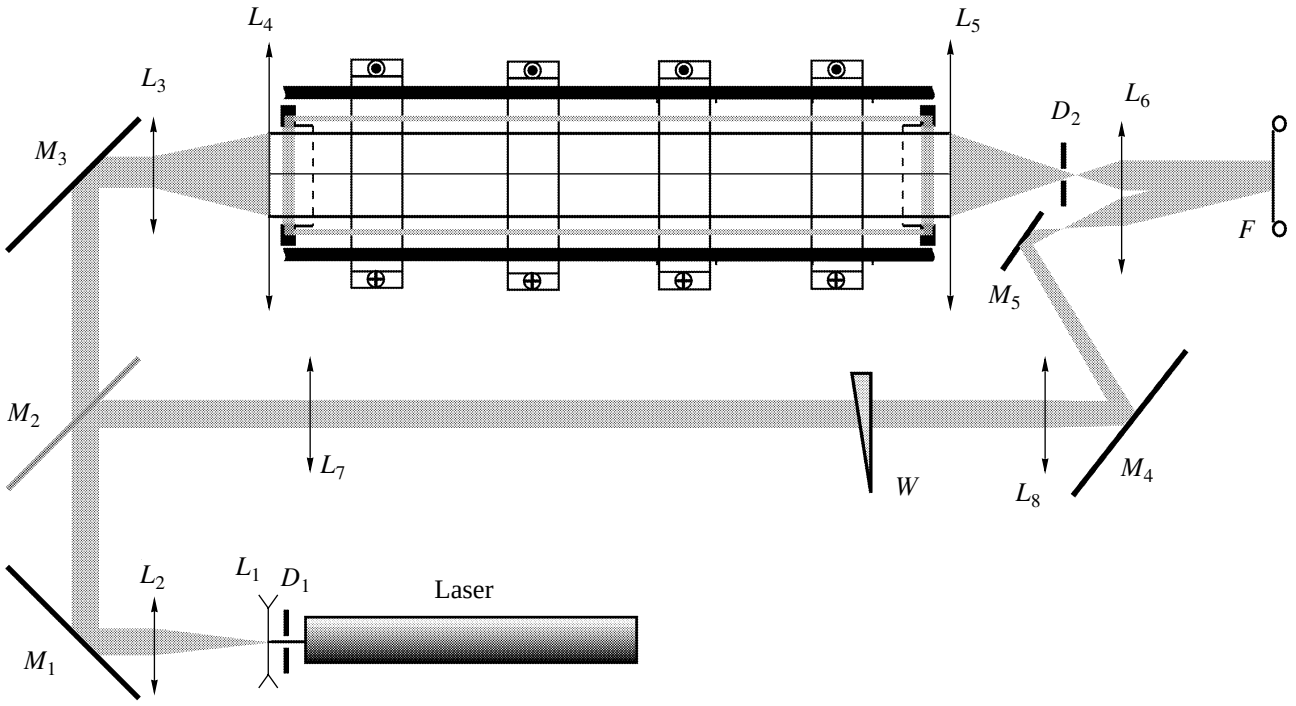

Fig. 2. Schematic of the holographic interferometer: (*L*) lenses, (*M*) mirrors, (*W*) wedge, (*D*) aperture, and (*F*) film.

region [27]. From these data, we obtained information on the plasma configurations and the current distributions [14–18], determined the electron and ion temperatures [28] and, in some cases, the plasma density [27, 29] and the strength of nonequilibrium electric fields [30, 31].

In the present study, most attention was given to the use of two-exposure holographic interferometry [32] to determine the spatial electron-density distributions in current sheets. For this purpose, we created a special setup for hologram recording (Fig. 2) and also modified the CS-3D device.

A holographic procedure, which yields interferograms characterizing the plasma density distributions, is performed in two stages. In the first stage, two holograms are successively recorded: one with a plasma and another without it. In the reconstruction stage, this two-exposure hologram allows one to obtain the fringe pattern of two waves that have passed the same way in successive instants. In view of a differential character of holographic interferometry, this method had a number of advantages over other interferometric methods. In particular, it is insensitive to the quality of optical components and windows through which the radiation passes, which makes it possible to study plasma objects with large cross sections.

The setup for obtaining holograms (Fig. 2) is analogous to that used previously by us when studying a current-sheet plasma in 2D magnetic fields [19–21]. The main distinction of this setup from that described in [19] consists in that we can obtain holograms by using the image holography scheme [33]. One of the advantages of this scheme is that it is possible to eliminate aberrations in the object image at any configuration and wavelength of the reconstructing beam, in particular, in the white light.

The holograms were recorded in the light from an OGM-20 multimode ruby laser (λ = 694.3 nm, τ = 25 ns, and W = 20 MW). The aperture D_1 of diameter $\simeq$1.5 mm separated the central part of the laser beam, where the intensity was almost uniform. Then, the beam diameter was enlarged to $\simeq$20 mm with a telescopic system consisting of a negative (L_1) and a positive (L_2) lens. In this stage, the radiation was divided into an object and a reference beams with the help of a semitransparent mirror M_2.

A telescopic lens system L_3–L_4 served to enlarge the object-beam diameter to $\approx$150 mm. This beam was directed along the axis of the vacuum chamber by mirrors M_1 and M_3. With a lens system L_5–L_6 placed behind the output window of the chamber, a reduced image ($\approx$25 mm in diameter) of the middle cross section of the chamber was formed in the plane *F*, where

holograms were recorded. When passing through grid electrodes located inside the vacuum chamber, the object beam diffracted on these grids, which resulted in the mixing of the beam mode structure. To separate out the zeroth diffraction order, we employed a spatial filtration of radiation. For this purpose, an aperture D_2 positioned in the focal plane of the lens L_5 was used. The aperture diameter was chosen to match the period of the electrode grid structure and was usually equal to $\approx$1.5 mm.

In order to substantially improve the quality of holograms, the CS-3D device was modified. For this purpose, the vacuum chamber electrodes through which the object holographic beam passed were metal grids with a relatively short period $\simeq$0.26 mm. As a result, the angles of the object-beam diffraction on the electrodes increased substantially, so that it became easier to filter the zeroth-order wave in the focal plane of the lens L_5.

The reference beam in the holographic setup was formed by the lenses L_7–L_8. The beam was directed onto the lens L_6 by mirrors M_4–M_5 and was superimposed on the object beam in the plane *F*.

Holograms were recorded on a Mikrat-500 film. To obtain fringes in the holographic interferograms, a glass wedge *W* was placed in the path of the reference beam. This wedge was turned by a small angle between the first and second exposures. Changing the orientation of the wedge, we could change the orientation of fringes; in particular, we could obtain vertical or horizontal fringes. The optical scheme was adjusted with the help of a helium–neon laser whose beam was preliminarily aligned with the ruby laser beam.

The interferograms obtained by reconstructing two-exposure holograms were digitized with an Epson FilmScan 200 slide-scanner. To process the data obtained, we created a special computer program. The data processing includes noise filtering, the determination of fringe orientation, the compensation of the distortion of the optical system, and, finally, the construction of the 2D electron-density distribution. The use of this program made calculations less laborious and allowed us to increase the accuracy of interferogram processing.

An interferogram obtained by reconstructing the two-exposure hologram yields the 2D electron density distribution in the plane orthogonal to the X-line. In other words, the interferogram provides information about the configuration of the region where the plasma is concentrated, as well as about the plasma density at different points in this plane. The values of the electron density at each point are averaged over the X-line, i.e., over a distance of ~60 cm between the electrodes of the vacuum chamber.

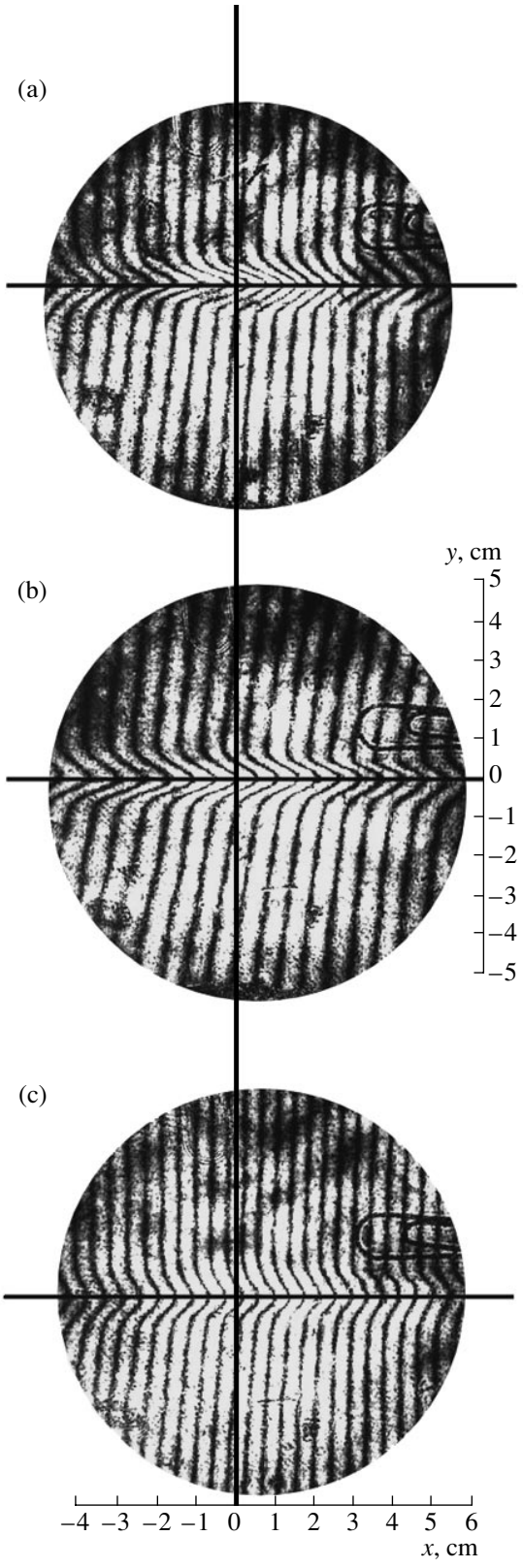

Fig. 3. Interferograms of the current sheets formed in He at a pressure of 300 mtorr for the longitudinal magnetic field $B_{||}$ = (a) 0, (b) 2.9, and (c) 5.8 kG. The gradient of the quadrupole magnetic field is h = 0.43 kG/cm.

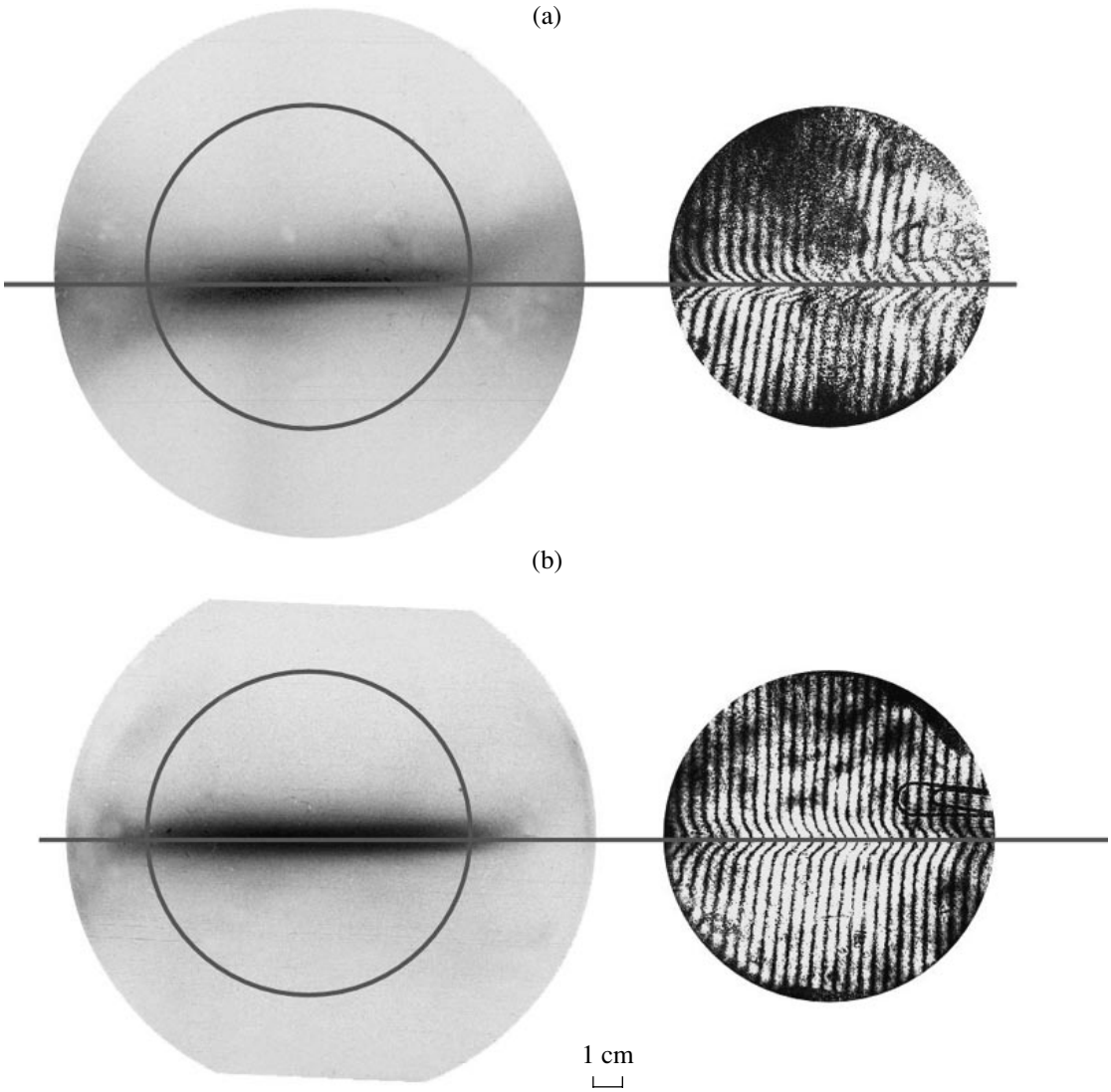

Fig. 4. 2D distributions of the plasma emission intensity in the HeII spectral line (on the left) and the interferograms of the current sheet plasma (on the right) for the longitudinal magnetic field $B_{||}$= (a) 0 and (b) 5.8 kG. The discharge is excited in He at a pressure of 300 mtorr. The gradient of the quadrupole magnetic field is h = 0.43 kG/cm. The circle indicates the viewing field of the holographic interferometer.

3. EXPERIMENTAL RESULTS

3.1. Spatial Plasma Density Distributions in Current Sheets Formed in 2D Magnetic Configurations with a Null Line

In our previous studies, it was found that current sheets in 2D magnetic configurations with null lines could be formed at relatively high initial gas pressures (helium, 300 mtorr) [23, 24]. The results from measurements of plasma emission in different spectral lines indicated that the plasma was also concentrated within a plane sheet. However, the quantitative data on the plasma density in the sheet were obtained for the first time in this study. The interferogram shown in Fig. 3a represents the *z*-averaged distribution of the electron density N_e in the (x, y) plane. In the figure, the deflection of fringes from straight lines is proportional to the electron density N_e. The fringe shift equal to the distance between neighboring fringes corresponds to $N_e \simeq 5.33 \times 10^{15}$ cm^{-3}. It is seen in Fig. 3a that the plasma is shaped as a plane sheet and the electron density inside the sheet is substantially higher than in the surrounding plasma.

A similar interferogram presented in Fig. 4a allows us to compare two diagnostic techniques used by us: the measurements of the spatial distributions of plasma emission in different spectral lines [16–18] and the method of holographic interferometry. Comparing the

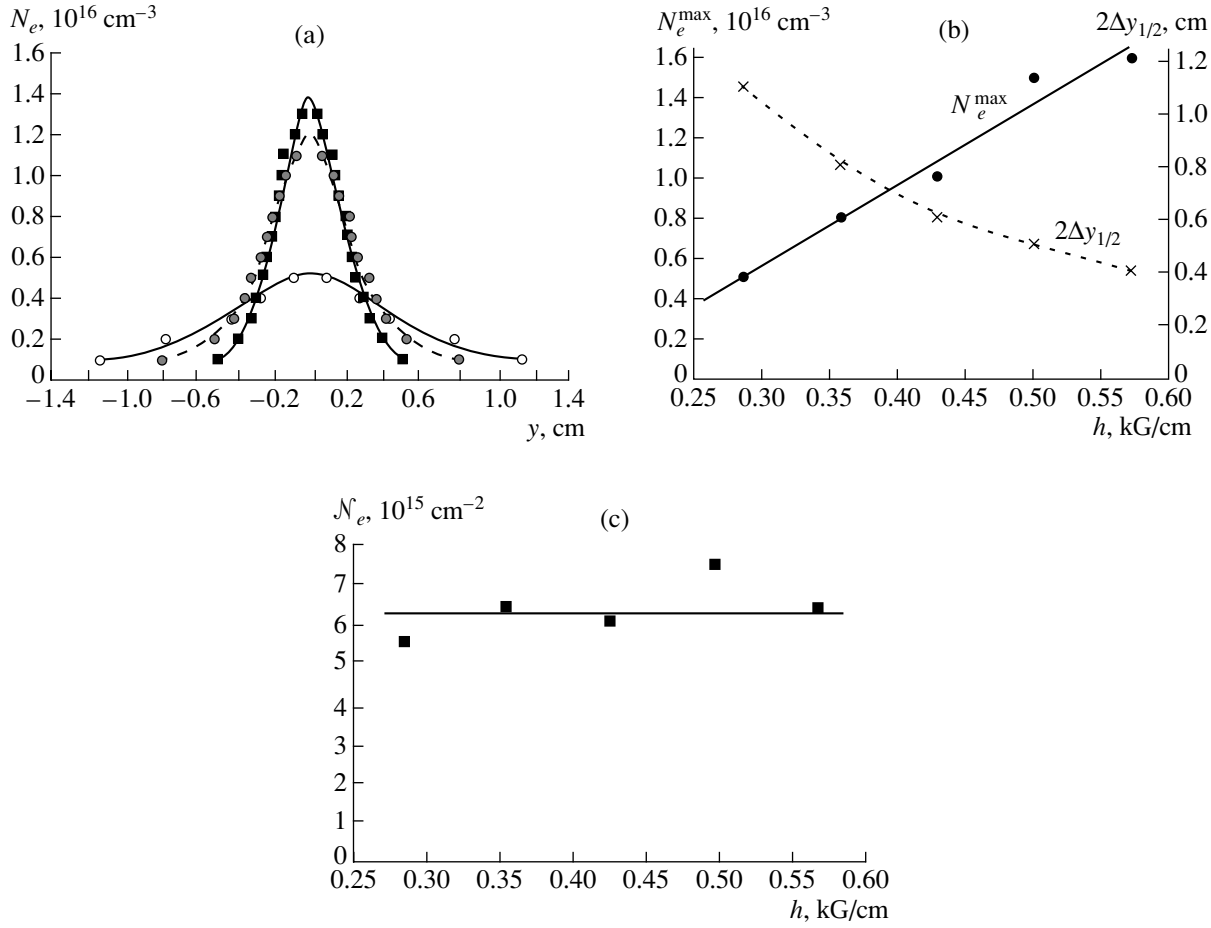

Fig. 5. (a) Electron density distributions across the current sheet $N_e(y)$ in 2D magnetic fields with different gradients: h = (■) 0.57, (●) 0.43, and (○) 0.29 kG/cm; (b) the maximum electron density in the current sheet N_e^{max} and the plasma sheet thickness $2\Delta y_{1/2}$ at a level of $0.5N_e^{max}$ as functions of h; and (c) the number of electrons in the plasma sheet $\mathcal{N}_e$ per centimeter of its width. The discharge is excited in He at a pressure of 300 mtorr.

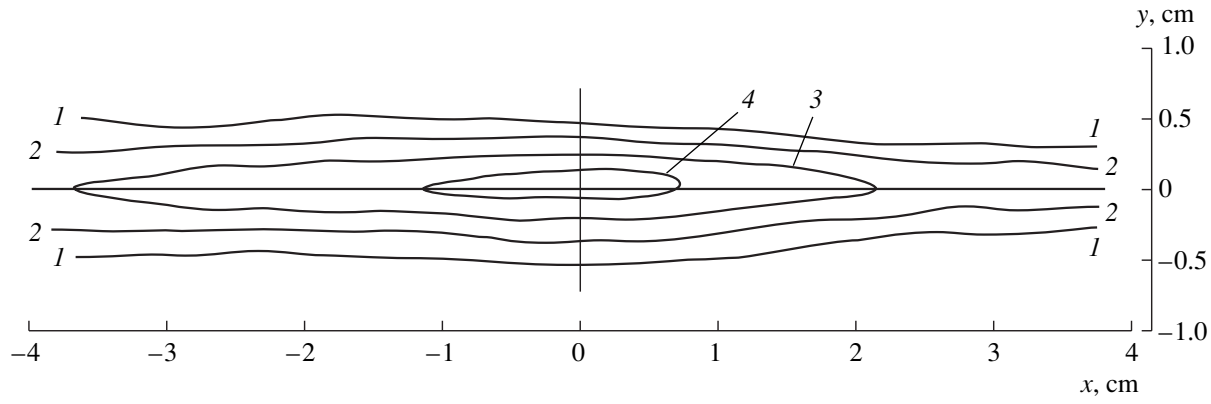

Fig. 6. Contour lines of the electron density in the current sheet produced in He at a pressure of 300 mtorr for N_e = (*1*) 0.25×10^{16}, (*2*) 0.5×10^{16}, (*3*) 0.75×10^{16}, and (*4*) 10^{16} cm^{-3}. The gradient of the quadrupole magnetic field is h = 0.43 kG/cm; the longitudinal magnetic field is $B_{\|}$ = 1.4 kG.

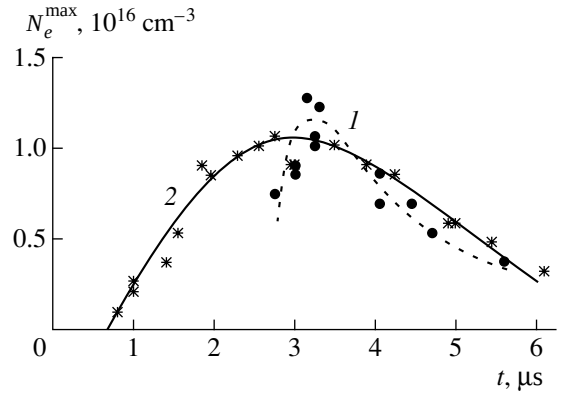

Fig. 7. Time evolution of the maximum electron density in the sheet for the longitudinal magnetic field $B_\parallel$ = (*1*) 0 and (*2*) 2.9 kG. The discharge is excited in He at a pressure of 300 mtorr. The gradient of the quadrupole magnetic field is h = 0.43 kG/cm.

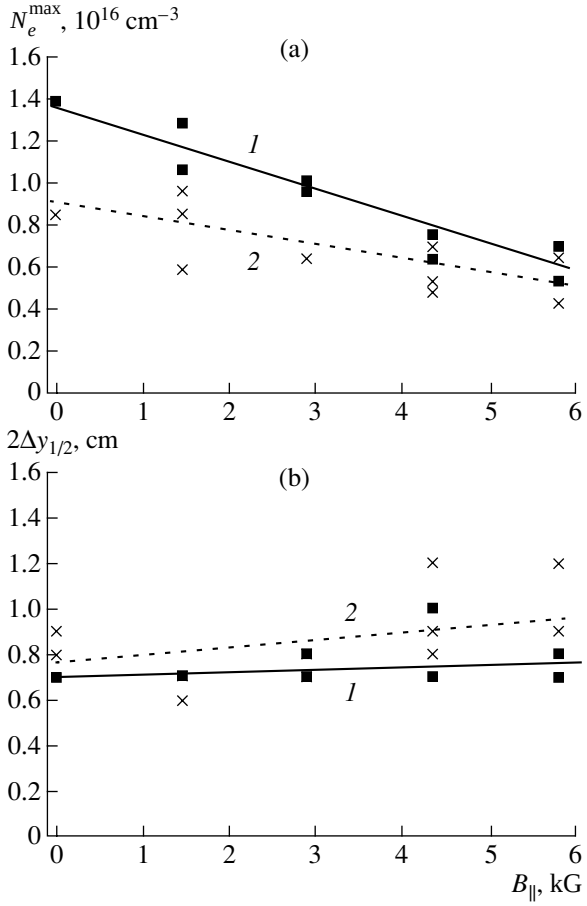

Fig. 8. (a) Maximum electron density in the current sheet N_e^{max} and (b) the plasma-sheet thickness $2\Delta y_{1/2}$ at a level of $0.5\,N_e^{max}$ as functions of the longitudinal magnetic field $B_\parallel$ (*1*) in the center of the current sheet (x = 0) and (*2*) at its periphery ($x \cong 3$ cm). The discharge is excited in He at a pressure of 300 mtorr. The gradient of the quadrupole magnetic field is h = 0.43 kG/cm.

interferogram and the profile of plasma emission in the HeII spectral line measured under the same conditions, we can conclude that both methods agree satisfactorily.

Figure 5 shows the profiles $N_e(y)$ at $x \simeq 0$ for different values of the gradient h, characterizing the 2D magnetic configuration; the maximum electron density N_e^{max} in the sheet and the FWHM sheet thickness $2\Delta y_{1/2}$ as functions of h; and the total number of particles $\mathcal{N}_e$ per centimeter of the sheet width. It is seen that, as the gradient of the 2D magnetic field increases, the plasma is more efficiently compressed into the sheet, which manifests itself as an increase in the maximum plasma density and a decrease in the plasma sheet thickness. Note that similar dependences of plasma evolution on the gradient of the 2D magnetic filed were previously demonstrated by us in [23–24].

3.2. Spatial Plasma Density Distributions in Current Sheets Formed in 3D Magnetic Configurations with an X-line

Of particular interest are the spatial electron density distributions in current sheets formed in magnetic configurations with an X-line, i.e., in the presence of the longitudinal magnetic field component $B_\parallel$. The data on the electron density distributions are presented in Figs. 3b and 3c in the form of interferograms. The longitudinal component was $B_\parallel$ = 2.9 and 5.8 kG for Figs. 3b and 3c, respectively. In all cases presented in Fig. 3, the plasma was shaped as a plane sheet and the sheet width (the size in the x direction) was 10–15 times larger than the sheet thickness (the size in the y direction). As in the 2D case, the electron density in the sheet was substantially higher than in the surrounding plasma and varied relatively slowly along the sheet width. In the direction normal to the sheet, the density gradient was fairly high. This gradient somewhat decreased with increasing $B_\parallel$. In Fig. 6, the plasma density distribution $N_e(x, y)$ is presented by the density contour lines. One can see that the maximum density in the center of the sheet attained a value of $N_e \simeq 10^{16}$ cm^{-3}.

Thus, experiments carried out with a helium plasma show that, when the current sheet is formed in a magnetic configuration with an X-line (including configurations with a sufficiently strong longitudinal component $B_\parallel$ directed along the X-line and along the electric current flowing in the plasma), the plasma also evolves into a plane sheet.

The time evolution of the maximum electron density in the center of the sheet is demonstrated in Fig. 7, which presents the data from processing ≈30 holographic interferograms recorded under identical conditions, but at different instants. Curve *1* shows the density evolution in a plasma sheet formed in a 2D magnetic configuration with a null line ($B_\parallel$ = 0), and curve *2* corresponds to a 3D magnetic configuration with an X-line at $B_\parallel$ = 2.9 kG. It is seen in Fig. 7 that the elec-

tron density grows over 2–3 μs; then, the current sheet seems to be destroyed. This effect requires a further study.

Figure 8 shows how the change in the spatial plasma density distribution depends on the longitudinal magnetic field component $B_\parallel$. The figure presents the maximum electron density and the sheet thickness in the center of the sheet ($x \simeq 0$) and at its periphery ($x \simeq \pm 3$ cm). As the longitudinal component increases, the plasma density decreases and the sheet thickness at the periphery increases. Note that the total number of electrons in the sheet changes insignificantly. Hence, the compression of the plasma within a well-defined sheet becomes less efficient. Most likely, this is because the longitudinal component of the magnetic field in the sheet increases as compared with its initial value, as was suggested previously in [1].

4. CONCLUSIONS

(i) The spatiotemporal characteristics of the current sheet plasma in magnetic configurations with singular X-lines have been studied for the first time by the method of two-exposure holographic interferometry, which made it possible to determine how the main plasma characteristics depend on the structure of the initial magnetic configuration.

(ii) In experiments carried out with a helium plasma, convincing evidence has been obtained that, when the current sheet is formed in a magnetic configuration with an X-line, the plasma also evolves into a plane sheet. The width of the plasma sheet is usually a factor of 10–15 larger than its thickness. It has been demonstrated that plasma sheets can form in the presence of a sufficiently strong longitudinal magnetic-field component $B_\parallel$ directed along the X-line and along the electric current flowing in the plasma.

(iii) It has been shown that, in the absence of the longitudinal component $B_\parallel$ (i.e., in a 2D magnetic field with a null-line), the plasma is compressed into the sheet more efficiently as the gradient of the transverse magnetic field h increases. The more efficient compression manifests itself in an increase in the maximum plasma density and a decrease in the plasma sheet thickness.

(iv) In magnetic configurations with an X-line, the increase in the longitudinal component $B_\parallel$ leads to a decrease in the plasma density and an increase in the plasma sheet thickness; as a result, the total number of electrons in the sheet changes insignificantly. Hence, the plasma compression within a well-defined sheet becomes less efficient. Most likely, this is because the longitudinal component of the magnetic field in the sheet increases as compared with its initial value.

ACKNOWLEDGMENTS

This work was supported in part by the Russian Foundation for Basic Research (project no. 99-02-18351) and the Federal Program "Leading Scientific Schools" (project nos. 00-15-96676 and 00-15-96771).

REFERENCES

1. S. I. Syrovatskii, Annu. Rev. Astron. Astrophys. **19**, 163 (1981).
2. D. Biscamp, *Nonlinear Magnetohydrodynamics* (Cambridge Univ. Press, Cambridge, 1993).
3. E. R. Priest and T. Forbes, *Magnetic Reconnection. MHD Theory and Applications* (Cambridge Univ. Press, Cambridge, 2000).
4. B. B. Kadomtsev, Usp. Fiz. Nauk **151**, 3 (1987).
5. S. I. Syrovatskii, Astron. Zh. **43**, 340 (1966) [Sov. Astron. **10**, 270 (1966)].
6. S. I. Syrovatskii, Zh. Éksp. Teor. Fiz. **60**, 1727 (1971) [Sov. Phys. JETP **33**, 933 (1971)].
7. S. I. Syrovatskii, A. G. Frank, and A. Z. Khodzhaev, Pis'ma Zh. Éksp. Teor. Fiz. **15**, 138 (1972) [JETP Lett. **15**, 94 (1972)].
8. S. Yu. Bogdanov, V. S. Markov, and A. G. Frank, Pis'ma Zh. Éksp. Teor. Fiz. **35**, 232 (1982) [JETP Lett. **35**, 290 (1982)].
9. A. G. Frank, in *Problems of Plasma Physics and Plasma Electronics* (Nauka, Moscow, 1985), Tr. Fiz. Inst. Akad. Nauk SSSR **160**, 93 (1985) [*Plasma Physics and Plasma Electronics* (Nova Science, Commack, 1989), p. 131].
10. P. Rosenau, Phys. Fluids **22**, 849 (1979).
11. S. V. Bulanov and M. A. Ol'shanetskiĭ, Fiz. Plazmy **11**, 727 (1985) [Sov. J. Plasma Phys. **11**, 425 (1985)].
12. Y.-T. Lau and J. M. Finn, Astrophys. J. **350**, 672 (1990).
13. J. M. Green, Phys. Fluids B **5**, 2355 (1993).
14. S. Yu. Bogdanov, V. B. Burilina, V. S. Markov, and A. G. Frank, Pis'ma Zh. Éksp. Teor. Fiz. **59**, 510 (1994) [JETP Lett. **59**, 537 (1994)].
15. A. G. Frank, S. Yu. Bogdanov, and V. B. Burilina, Izv. Akad. Nauk, Ser. Fiz. **59** (8), 41 (1995) [Bull. Russ. Acad. Sci. (Physics) **59**, 1331 (1995)].
16. A. G. Frank, Plasma Phys. Controlled Fusion **41**, A687 (1999).
17. S. Yu. Bogdanov, N. P. Kyrie, V. S. Markov, and A. G. Frank, Pis'ma Zh. Éksp. Teor. Fiz. **71**, 72 (2000) [JETP Lett. **71**, 53 (2000)].
18. A. G. Frank and S. Yu. Bogdanov, Earth, Planets Space **53**, 531 (2001).
19. G. V. Dreiden, N. P. Kyrie, V. S. Markov, *et al.*, Fiz. Plazmy **3**, 45 (1977) [Sov. J. Plasma Phys. **3**, 26 (1977)].
20. S. Yu. Bogdanov, G. V. Dreiden, A. G. Frank, *et al.*, Phys. Scr. **30**, 282 (1984).
21. S. Yu. Bogdanov, G. V. Dreiden, N. P. Kyrie, *et al.*, Fiz. Plazmy **18**, 1269 (1992) [Sov. J. Plasma Phys. **18**, 654 (1992)].
22. S. V. Bulanov and A. G. Frank, Fiz. Plazmy **18**, 1535 (1992) [Sov. J. Plasma Phys. **18**, 795 (1992)].

23. S. Yu. Bogdanov, V. B. Burilina, and A. G. Frank, Zh. Éksp. Teor. Fiz. **114**, 1202 (1998) [JETP **87**, 655 (1998)].

24. A. G. Frank, S. Yu. Bogdanov, V. B. Burilina, *et al.*, Contrib. Plasma Phys. **40**, 106 (2000).

25. V. B. Burilina, V. S. Markov, and A. G. Frank, Fiz. Plazmy **21**, 36 (1995) [Plasma Phys. Rep. **21**, 33 (1995)].

26. S. Yu. Bogdanov, Yu. F. Bondar', V. B. Burilina, *et al.*, Zh. Tekh. Fiz. **64** (9), 30 (1994) [Tech. Phys. **39**, 877 (1994)].

27. S. Büscher, N. P. Kyrie, H. J. Kunze, and A. G. Frank, Fiz. Plazmy **25**, 185 (1999) [Plasma Phys. Rep. **25**, 164 (1999)].

28. S. Yu. Bogdanov, V. B. Burilina, N. P. Kyrie, *et al.*, Fiz. Plazmy **24**, 467 (1998) [Plasma Phys. Rep. **24**, 427 (1998)].

29. A. G. Frank, V. P. Gavrilenko, N. P. Kyrie, and V. S. Markov, Contrib. Plasma Phys. **41**, 85 (2001).

30. A. G. Frank, V. P. Gavrilenko, Ya. O. Ispolatov, *et al.*, Contrib. Plasma Phys. **36**, 667 (1996).

31. V. P. Gavrilenko, N. P. Kyrie, and A. G. Frank, Opt. Spektrosk. **87**, 916 (1999) [Opt. Spectrosc. **87**, 834 (1999)].

32. Yu. I. Ostrovskiĭ, M. M. Butusov, and G. V. Ostrovskaya, *Interferometry by Holography* (Nauka, Moscow, 1977; Springer-Verlag, New York, 1980).

33. I. S. Klimenko, *Image Holography and Speckle Interferometry* (Nauka, Moscow, 1985).

Translated by N. F. Larionova

Plasma Physics Reports, Vol. 28, No. 7, 2002, pp. 559–564. Translated from Fizika Plazmy, Vol. 28, No. 7, 2002, pp. 605–610.

ISOTOPE SEPARATION

Some Features of ICR Heating by a Solenoidal Antenna

V. I. Volosov, V. V. Demenev, A. G. Steshov, and I. N. Churkin

Budker Institute of Nuclear Physics, Siberian Division, Russian Academy of Sciences, pr. Akademika Lavrent'eva 11, Novosibirsk, 630090 Russia

Received January 9, 2002; in final form, January 25, 2002

Abstract—A study is made of some characteristic features of ion cyclotron resonance (ICR) heating in plasma-based isotope separators. The effects associated with ion drift in the RF field of a solenoidal antenna are considered in the single-particle approximation. Estimates are obtained and numerical calculations are carried out for ICR heating in the case of a "narrow" ($\rho/r \sim 1$, where ρ is the ion gyroradius) plasma flow. © *2002 MAIK "Nauka/Interperiodica".*

1. INTRODUCTION

One of the methods of isotope separation is based on selective ion cyclotron resonance (ICR) plasma heating [1–4]. This method may serve as a basis for the development of highly efficient technological devices for isotope separation, because a quasineutral plasma is free from the effects associated with the ion space charge. The problem of choosing an optimum antenna system for ion heating in ICR isotope separators has been discussed in a number of papers [2, 4–6]. A possible candidate for ICR heating of the ions in projected separators is a solenoidal antenna [4, 7]. This type of antenna has a number of advantages:

(i) sufficiently small values of $k_\parallel$ (this makes it possible to heat ions in such a way that they always remain within the resonance region),

(ii) the absence of longitudinal components in the excited electric fields, and

(iii) a simple design.

The obvious drawbacks of solenoidal antennas are:

(i) a high Q-factor [5];

(ii) the weak RF electric field near the antenna axis; and

(iii) a decrease in the ICR heating efficiency because of the opposite polarities of the electric field at the ends of a solenoidal antenna in the presence of a dense ($n \sim 10^{18}$ m^{-3}) plasma (in which case it is necessary to optimize the positions of the plasma source and the extraction system with respect to the antenna [7–9]).

In this paper, we consider one more feature of ICR heating by a solenoidal antenna, namely, the one associated with ion drift in both the radial and azimuthal directions. This drift not only restricts the energy acquired by resonant ions but also leads to the mixing of ions in both coordinate and energy spaces. As a result, the energy spectra of resonant and nonresonant ions at the exit from the antenna region are close to one another.

2. ICR HEATING BY A SOLENOIDAL ANTENNA

A solenoidal antenna produces a solenoidal azimuthal RF electric field whose amplitude is proportional to the radius, $E_\phi(r) = -\pi f_{hf} B_a r \cos(2\pi f_{hf} t)$, where B_a is the amplitude of the RF magnetic field excited by the antenna. In moving along a Larmor orbit in the gradient vortex electric field of a solenoidal antenna, an ion drifts in both the radial and azimuthal directions. Thus, the radial drift of a resonant ion moving in phase ($\Delta\varphi = 0$) with the RF antenna field stems from the fact that, far from the antenna axis, the ion experiences a stronger RF electric field than near the axis. As a result, the ion deviates more and more from its initial trajectory, acquiring a component of drift velocity toward the antenna axis (Fig. 1).

The radial displacement of the ion per Larmor revolution is independent of its position r and can be estimated as

$$\Delta r \approx -\frac{G_a}{B_0}\left(r + \frac{\rho}{2}\right)\frac{T}{2} + \frac{G_a}{B_0}\left(r - \frac{\rho}{2}\right)\frac{T}{2} \approx -\frac{G_a}{B_0}\frac{\rho}{2}T,$$

where r is the distance from the antenna axis to the guiding center of the Larmor orbit, ρ is the ion gyroradius (in the approximation at hand, ρ = const during each Larmor revolution), B_0 is the axial magnetic field in the ICR region, T is the period of ion gyration in the magnetic field, $G_a = \pi f_{hf} B_a$ is the radius-independent gradient of the vortex electric field of the antenna, f_{hf} is the frequency of the RF field, and B_a is the antenna magnetic field.

The radial drift velocity is also independent of the ion position r and increases with ion gyroradius: $V_r \approx \Delta r/T \approx -G_a\rho/2B_0$. The mean energy acquired by an ion during each Larmor revolution is equal to

$$\Delta W \approx \frac{1}{2} q \times 2\pi\rho E_\phi(r) = \pi q B_a f_{hf} r\rho = \pi q G_a r\rho,$$

1063-780X/02/2807-0559$22.00 © 2002 MAIK "Nauka/Interperiodica"

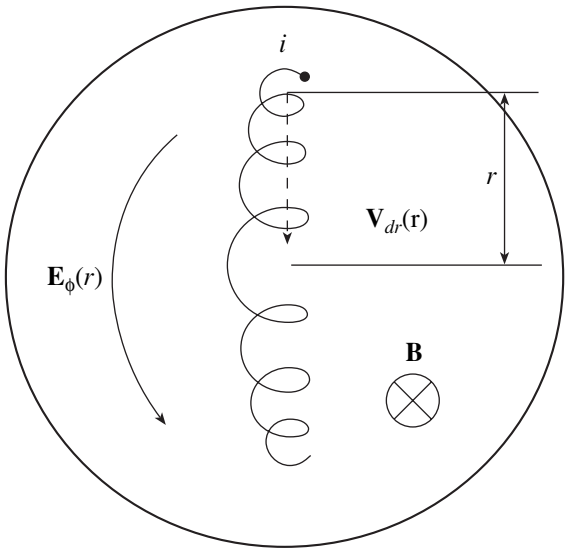

Fig. 1. Drift motion of a resonant ion in the field of a solenoidal antenna.

where q is the ion charge. This energy is a linear function of the radial position of the ion (the guiding center of the Larmor orbit):

$$\frac{\Delta W}{\Delta r} \approx \frac{\pi q G_a r \rho}{\frac{G_a}{B_0}\frac{\rho}{2}T} \approx q\omega B_0 r.$$

The closer the ion to the antenna axis, the lower the rate at which the ion acquires energy. After the guiding center of the ion Larmor orbit intersects the antenna axis, the ion experiences an RF field of opposite sign and thus is decelerated. The maximum energy is acquired by a resonant ion drifting from its initial radial position r_0 to the antenna axis:

$$W_{\max} \approx \left|\int_{r_0}^{0} \frac{2\pi q B_0 r}{T} dr\right| = \frac{\pi q B_0 (\bar{r})^2}{T}$$
$$= \frac{q B_0 \omega}{2}(\bar{r})^2 \approx \frac{q B_0 \omega}{8} r_0^2,$$

where $\bar{r}$ is the mean distance from the antenna axis to the guiding center of the Larmor orbit, $\bar{r} \approx r_0/2$.

The maximum energies acquired by resonant ^{157}Gd ions starting from the initial radial positions $r_0 = 0.03$ m and $r_0 = 0.01$ m in the field of a solenoidal antenna (the amplitude of the axial magnetic field being $B_0 = 1$ T) can be estimated as $W_{\max} \approx 275$ and 30 eV, respectively. Here and below, the energy is expressed in eV (for the benefit of readers), but all of the formulas and estimates are written in SI units.

In an RF field, the ions start to gyrate at arbitrary initial phases and drift in both the radial and azimuthal directions with the velocities

$$V_r \approx \frac{\pi}{\omega}\frac{G_a}{B_0}\frac{\rho}{T}\cos(\Delta\varphi) = \frac{G_a}{B_0}\frac{\rho}{2}\cos(\Delta\varphi),$$

$$V_\phi \approx \frac{\pi}{\phi}\frac{G_a}{B_0}\frac{\rho}{T}\sin(\Delta\varphi) = \frac{G_a}{B_0}\frac{\rho}{2}\sin(\Delta\varphi),$$

where $\Delta\varphi$ is the difference between the phase of the RF field and the phase of an ion at the entrance to the antenna.

The above expressions qualitatively characterize the regular features of the motion of resonant ions. In the gradient RF field of a solenoidal antenna, nonresonant ions behave in essentially the same manner: they also drift in both the radial and azimuthal directions.

The estimates illustrated in Figs. 2 and 3 agree with the results from numerical calculations (carried out in the single-particle approximation) of ICR heating of the ions by a solenoidal antenna. A resonant ion acquires and loses energy several times during its passage through the ICR heating region (Figs. 2a, 3a). The energy of nonresonant ions changes in essentially the same manner (Figs. 2b, 3b). The lower the gradient of the vortex electric field of the antenna, the lower the radial ion drift velocity and the higher the ion gyrofrequency (Figs. 2, 4).

The selective ICR heating method implies that an ion should complete at least $N = A$ Larmor revolutions when passing through the ICR heating region [2]. Here, A is the mass number. In this case, the energy acquired by an ion is $W \sim N\Delta W \sim 2qAG_a\bar{r}\bar{\rho} \leq W_{\max}$, where $\bar{r}$ is the mean distance from the guiding center of the Larmor orbit to the antenna axis and $\bar{\rho}$ is the mean ion Larmor radius.

With an antenna optimally adapted to ICR heating, a resonant ion has enough time to acquire the maximum energy ($W \approx W_{\max}$). The optimal use of the antenna requires that the longitudinal (along the antenna) velocity of the ion be optimum; i.e., the longitudinal ion velocity should be such that the ion completes $N = A$ Larmor revolutions along the antenna length. This yields the following requirement on the gradient of the RF field of a solenoidal antenna: $G_a \approx \omega B_0 \bar{r}/(4A\bar{\rho})$. For a ^{157}Gd ion with a mean gyroradius of about $\rho \sim 0.01$ m at the initial radial position $r_0 = 0.01$ m, we have $G_a \sim 1000$ V/m^2. According to the results shown in Fig. 2, which were obtained for a G_a value larger than that just presented, resonant ^{157}Gd ions are on the average heated to higher energies than nonresonant ^{158}Gd ions and have a small spread in energies at the exit from the antenna region.

Since the optimum parameters of a solenoidal antenna depend on both the initial phases and initial radial positions of the ions, it is difficult to choose the

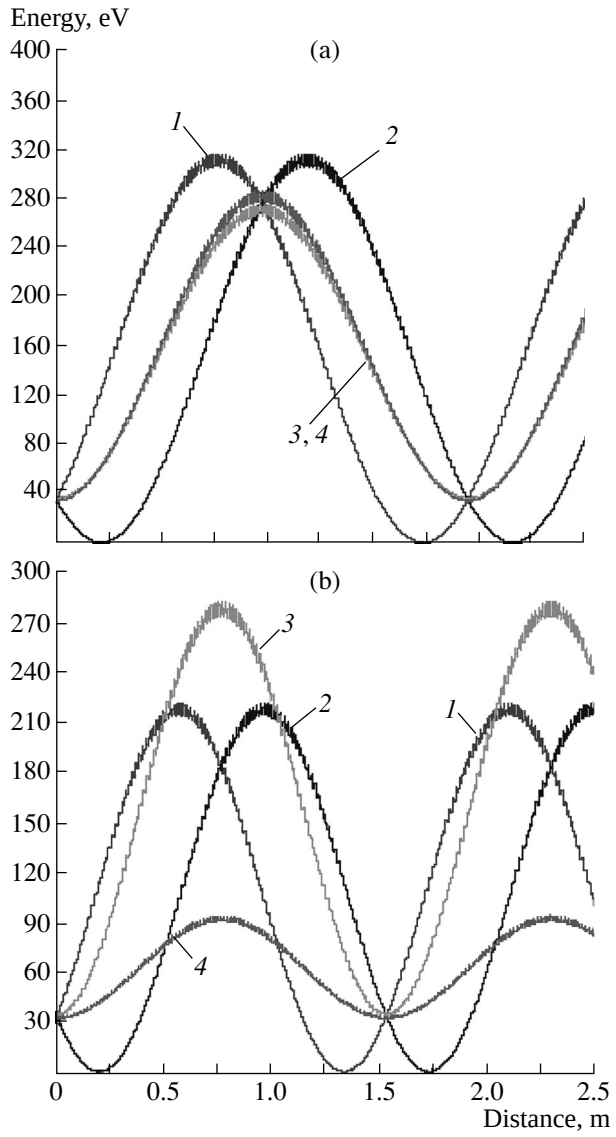

Fig. 2. Change in the transverse energies of (a) resonant ^{157}Gd ions and (b) nonresonant ^{158}Gd ions moving at optimum longitudinal velocities in a heating region with the length L = 2.5 m along the antenna for B_0 = 1 T, G_a = 5000 V/m^2, and r_0 = 0.03 m, the initial ion energy at the entrance to the antenna being W_0 = 35 eV. The relative phases $\Delta\varphi$ of the ions to the phase of the RF field are (*1*) 0°, (*2*) 180°, (*3*) 90°, and (*4*) 270°.

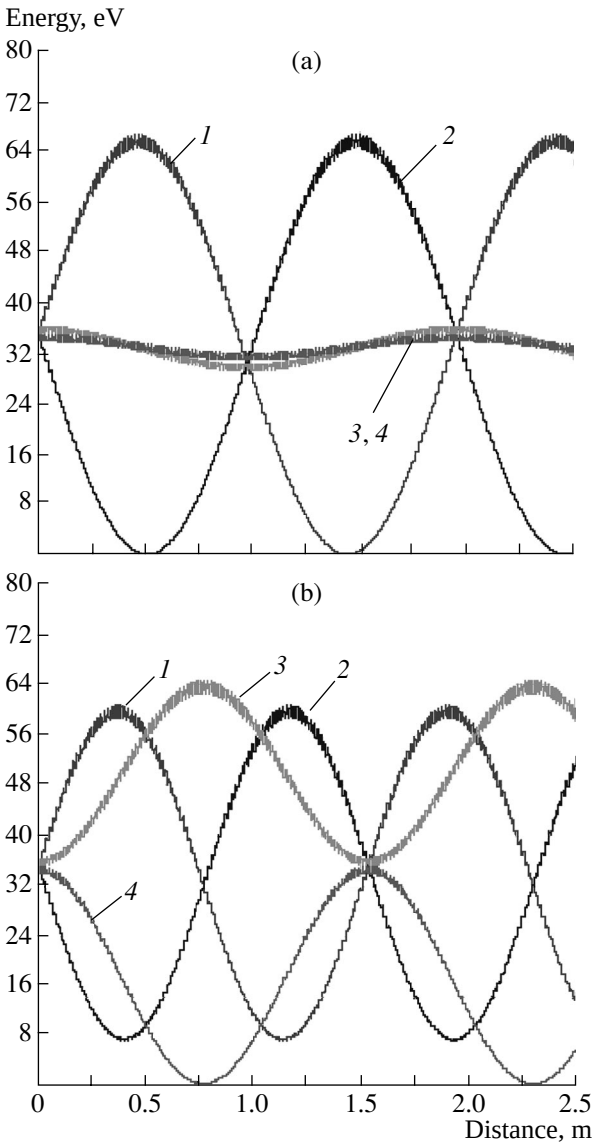

Fig. 3. Change in the transverse energies of (a) resonant ^{157}Gd ions and (b) nonresonant ^{158}Gd ions moving at optimum longitudinal velocities in a heating region with the length L = 2.5 m along the antenna for B_0 = 1 T, G_a = 5000 V/m^2, W_0 = 35 eV, and r_0 = 0.01 m. The relative phases $\Delta\varphi$ of the ions to the phase of the RF field are (*1*) 0°, (*2*) 180°, (*3*) 90°, and (*4*) 270°.

gradient of the RF field so as to satisfy the selective ICR heating conditions for all ions in a plasma flow.

Hence, the results of a qualitative analysis of the features of ion motion in the field of a solenoidal antenna can be summarized as follows.

(i) In the gradient field of a solenoidal antenna, the ions always undergo drift motion and their actual trajectories are complicated curves (Figs. 5, 6).

(ii) ICR heating of the ions depends on their initial phases, on the initial positions of the guiding centers of their Larmor orbits at the entrance to the heating region, and on the RF field amplitude (Figs. 2–4).

In a narrow ($r \sim \rho$) plasma flow, the ions acquire transverse energy in a periodic regime: the larger the amplitude of the RF field, the shorter the period (Figs. 2, 4). Although, along the antenna length, resonant ions are on the average heated to a greater extent

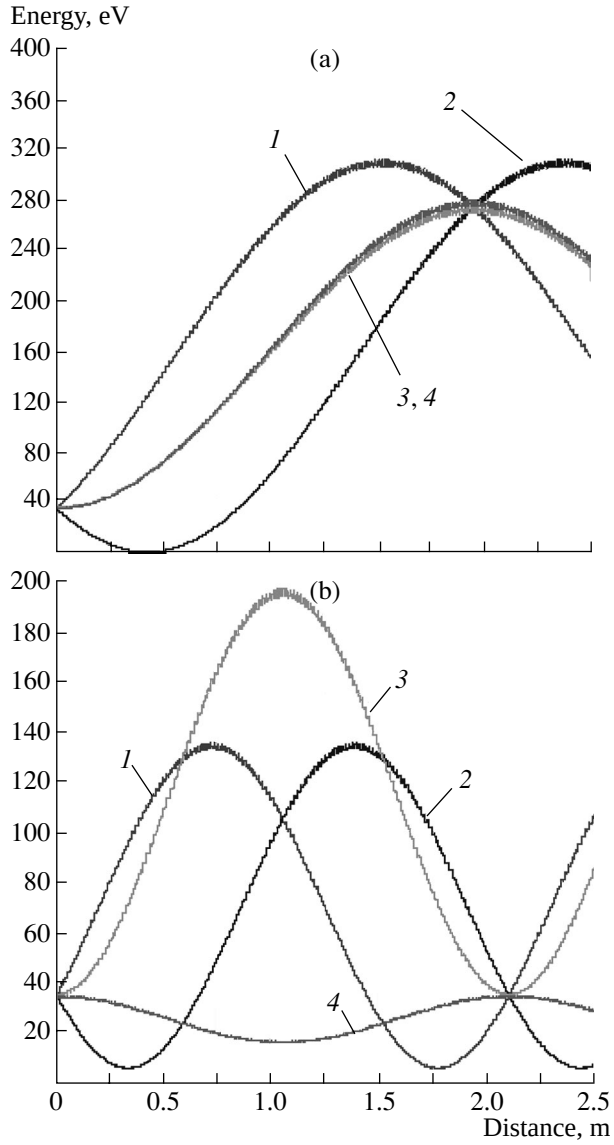

Fig. 4. Change in the transverse energies of (a) resonant ^{157}Gd ions and (b) nonresonant ^{158}Gd ions moving at optimum longitudinal velocities in a heating region with the length L = 2.5 m along the antenna for B_0 = 1 T, G_a = 2500 V/m^2, W_0 = 35 eV, and r_0 = 0.03 m. The relative phases $\Delta\varphi$ of the ions to the phase of the RF field are (*1*) 0°, (*2*) 180°, (*3*) 90°, and (*4*) 270°.

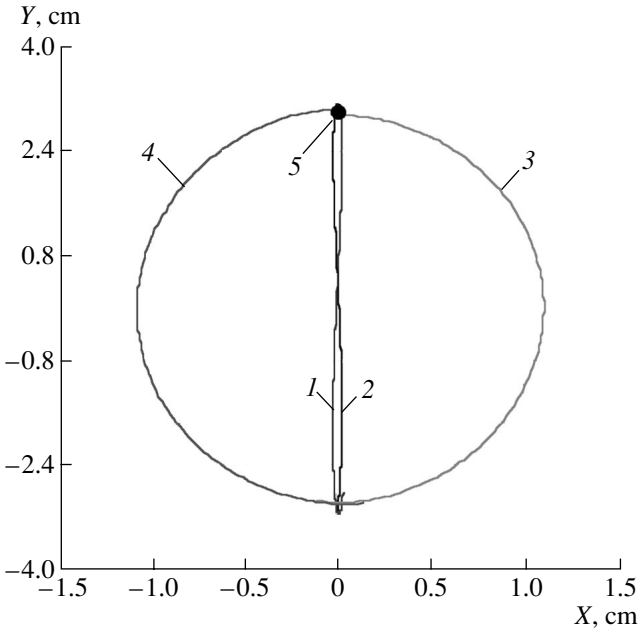

Fig. 5. Displacement of the guiding centers of the Larmor orbits of resonant ^{157}Gd ions moving at optimum longitudinal velocities in a heating region with the length L = 2.5 m along the antenna for B_0 = 1 T, G_a = 5000 V/m^2, W_0 = 35 eV, and r_0 = 0.03 m. The relative phases $\Delta\varphi$ of the ions to the phase of the RF field are (*1*) 0°, (*2*) 180°, (*3*) 90°, and (*4*) 270°. The ions enter the antenna at point *5*.

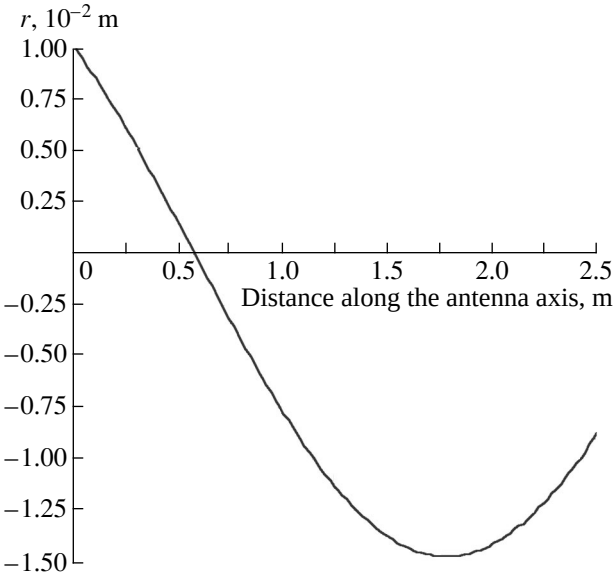

Fig. 6. Displacement of the guiding center of the Larmor orbit of a resonant ^{157}Gd ion moving at an optimum longitudinal velocity in a heating region with the length L = 2.5 m along the antenna for B_0 = 1 T, G_a = 5000 V/m^2, W_0 = 35 eV, and r_0 = 0.01 m. The relative phase $\Delta\varphi$ of the ion to the phase of the RF field is 0°. The displacement changes sign when the guiding center of the Larmor orbit intersects the antenna axis.

than nonresonant ions (Figs. 2–4), the mixing of the ions of different isotopes in both coordinate (Figs. 5, 6) and energy (Figs. 2–4) spaces renders their separation less efficient. In addition, RF fields in the central regions of the plasma flow are too weak to heat the ions therein at the cyclotron resonance.

In a wide ($r \gg \rho$) plasma flow and/or in a strong magnetic field, a resonant ion may drift only slightly when passing through the ICR heating region and thus cannot be heated to the maximum energy. In order for the separation to be efficient, the energy of the resonant

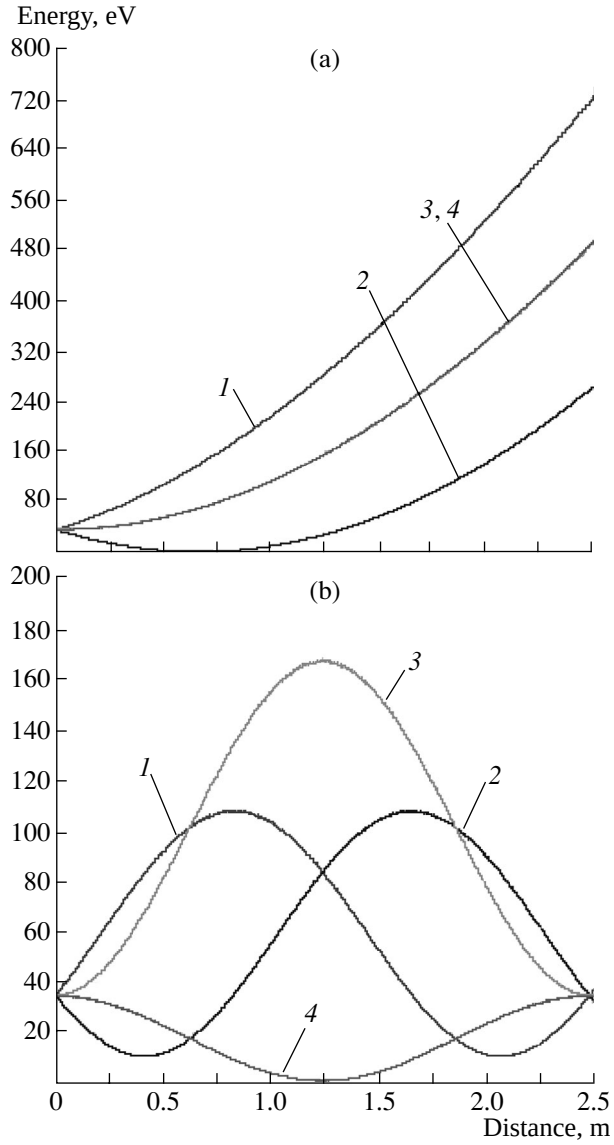

Fig. 7. Change in the transverse energies of (a) resonant ^{157}Gd ions and (b) nonresonant ^{158}Gd ions moving at optimum longitudinal velocities in a heating region with the length L = 2.5 m along the antenna for B_0 = 3 T, G_a = 5000 V/m^2, W_0 = 35 eV, and r_0 = 0.03 m. The relative phases $\Delta\varphi$ of the ions to the phase of the RF field are (*1*) 0°, (*2*) 180°, (*3*) 90°, and (*4*) 270°.

ions at the exit from the ICR heating region should be much higher than the initial ion energy W_0 (at the entrance to the antenna):

$$W \approx \Delta W N \approx 2qG_a\bar{r}\bar{\rho}A \gg W_0.$$

If the product of the amplitude of a uniform magnetic field and the mean distance from the guiding center of the Larmor orbit to the antenna axis is $B_0\bar{r} \gg \sqrt{W_0 m_a A\pi/(2q^2)}$ (where m_a is the proton mass), then the effect of the ion drift motion is insignificant and the radial displacement of the ion in the heating region is small, $\overline{\Delta r}\, N/\bar{r} \approx \overline{\Delta r}\, A/\bar{r} \ll 1$ (where $\overline{\Delta r}$ is the mean ion displacement per Larmor revolution and the number of Larmor revolutions along the antenna length is $N \sim A$). For ^{157}Gd ions with the initial energy W_0 = 35 eV, the effect of their drift motion on their heating is insignificant at $B_0\bar{r} \gg 10^{-2}$ T m.

Hence, selective ICR heating by a solenoidal antenna is possible only for a wide annular plasma flow in a strong magnetic field. The characteristic ICR heating process for this case is illustrated in Fig. 7 and is seen to be analogous to ICR heating in a uniform RF field of a capacitive antenna [10]. The calculations carried out in [7, 8, 11] for a similar case confirm the above conclusion on the possibility of selective ICR heating by a solenoidal antenna.

3. CONCLUSION

In the case of ICR heating of a narrow ($\rho/r \sim 1$) plasma flow in a weak magnetic field, the use of a solenoidal antenna is decidedly unpromising because of the significant ion drift in the gradient vortex electric field, which results in the mixing of ions in both coordinate and energy spaces and thereby renders the separation of isotopes much less efficient.

Solenoidal antennas can be successfully used for selective ICR heating of the ions in a wide ($\rho/r \ll 1$) plasma flow in a strong magnetic field in which the drift effects are insignificant. In this case, the process of ICR heating is closely analogous to that in a uniform field of a capacitive antenna. However, an increase in the magnetic field and/or the width of the plasma flow requires significant energy expenditure.

The ion drift motion in the gradient RF electric field, which was considered above for the case of a solenoidal antenna, may also be encountered in cases with some other antennas. Thus, for a capacitive antenna, the ion drift in the region of a weaker field can be driven by the spatial inhomogeneities associated, e.g., with the screening of the RF field by the plasma and with the inaccuracy of the assembly. On the other hand, by forming the region of a stronger field near the central plane of the capacitive antenna (a so-called "reversed" solenoidal configuration), it may be possible to improve the direct extraction of resonant ions from the plasma flow [10].

ACKNOWLEDGMENTS

We are grateful to A.V. Timofeev and I.A. Kotel'nikov for useful methodological comments.

REFERENCES

1. J. G. Tracy and W. S. Aaron, Nucl. Instrum. Methods Phys. Res. A **334**, 45 (1993).

2. Yu. A. Muromkin, Itogi Nauki Tekh., Ser. Fiz. Plazmy **12**, 83 (1991).
3. *Isotopes: Properties, Production, Application*, Ed. by V. Yu. Baranov (IzdAT, Moscow, 2000).
4. V. I. Volosov, I. A. Kotel'nikov, I. N. Churkin, *et al.*, At. Énerg. **88**, 370 (2000).
5. A. V. Timofeev, Fiz. Plazmy **25**, 232 (1999) [Plasma Phys. Rep. **25**, 207 (1999)].
6. A. I. Karchevskiĭ, V. S. Laz'ko, Yu. A. Muromkin, *et al.*, Fiz. Plazmy **19**, 411 (1993) [Plasma Phys. Rep. **19**, 214 (1993)].
7. S. G. Kuz'min, Fiz. Plazmy **25**, 1105 (1999) [Plasma Phys. Rep. **25**, 1020 (1999)].
8. V. E. Karlin and I. A. Kotel'nikov, Preprint No. 2001-63 (Budker Institute of Nuclear Physics, Siberian Division, Russian Academy of Sciences, Novosibirsk, 2001).
9. V. I. Volosov, V. V. Demenev, A. G. Steshov, and I. N. Churkin, Preprint No. 2001-50 (Budker Institute of Nuclear Physics, Siberian Division, Russian Academy of Sciences, Novosibirsk, 2001).
10. V. I. Volosov, V. V. Demenev, A. N. Dranichnikov, *et al.*, Preprint No. 2001-48 (Budker Institute of Nuclear Physics, Siberian Division, Russian Academy of Sciences, Novosibirsk, 2001).
11. V. I. Volosov, I. A. Kotel'nikov, and S. G. Kuz'min, Fiz. Plazmy **24**, 517 (1998) [Plasma Phys. Rep. **24**, 474 (1998)].

Translated by I. A. Kalabalyk

Plasma Physics Reports, Vol. 28, No. 7, 2002, pp. 565–571. Translated from Fizika Plazmy, Vol. 28, No. 7, 2002, pp. 611–617.

ISOTOPE SEPARATION

Coefficient of the Extraction of the Target Isotope and Optimum Parameters of a Collector of Heated Ions in the Context of the ICR Method of Isotope Separation

A. I. Karchevskiĭ and E. P. Potanin

Russian Research Centre Kurchatov Institute, pl. Kurchatova 1, Moscow, 123182 Russia

Received December 25, 2001

Abstract—The separation parameters of a collector of heated ions are estimated in the context of the ion cyclotron resonance method of isotope separation. The separation power dU, the coefficient Γ_C of the extraction of the target isotope, and the collector efficiency η are calculated. These parameters are investigated as functions of the repulsive potential U of the collector plates, the half-height a of the front screen, and the distance b between the plates. It is shown that the dependence of the collector efficiency η on the distance b between the plates has a pronounced maximum at $b \approx 2r_L^*$, where r_L^* is the mean ion gyroradius. © *2002 MAIK "Nauka/Interperiodica".*

1. INTRODUCTION

Among the plasma methods for the separation of stable isotopes, the ion cyclotron resonance (ICR) method is now considered to be the most promising. To the best of our knowledge, the ICR method of isotope separation in a plasma was first proposed as early as 1975 by Askar'yan *et al.* [1] and the first verification of the possibility of separating isotopes by this method came from the experiments carried out in 1976 by Dawson *et al.* [2]. The most interesting results on ICR isotope separation were obtained in [3–6]. It is expedient to apply this method to the separation of the isotopes of chemical elements that form no gaseous compounds under normal conditions. The ICR method is based on selective ICR heating of the ions of the target isotope, followed by the extraction of this isotope from the plasma flow under the conditions such that the collisions between particles are negligible. A version of the separator that is most suitable for industrial applications is shown schematically in Fig. 1. A steady plasma flow from the plasma source passes through the region where a solenoid (*1*) creates a uniform magnetic field and where an RF antenna (*2*) producing the heating field is located. A system for collecting the target material is arranged behind the heating region. The ion-collecting system consists of equidistant collector plates (*3*) and a waste plate (*5*). The collector plates, which are parallel to the plasma flow and are protected by front screens (*4*), are intended for extracting the heated ions (with a large gyroradius) of the target isotope (*7*). The waste plate, which is perpendicular to the plasma flow, is aimed at depositing the "cold" (nontarget) ions (*6*). In order to increase the separation efficiency, the collecting plates can be held at a positive repulsing potential U, which substantially reduces the nontarget ion flux. An ICR separator is capable of yielding a considerably larger amount of the target material (in comparison with industrial electromagnetic separators based on ion beams), because the plasma (and, accordingly, the flow of the isotopes to be processed) is free of restrictions associated with the positive space charge of an ion beam. A competitive alternative to ICR separation is the laser isotope separation method [7]. However, it should be noted that the application of the laser method may involve difficulties associated with the loss of selectivity due to the charge exchange of the target ions with the atoms of the nontarget isotope during the ion extraction from a partially ionized plasma. The ICR method is free of this drawback because it implies the use of a fully ionized plasma. Nevertheless, in the above version of an extractor of heated ions in the ICR method (i.e., in an extractor whose main elements are cooled metal plates parallel to the plasma flow), not all of the target ions produced by the source are extracted: some of them miss the collector plates when passing through the collector and reach the waste plate. Below, we will attempt to estimate the efficiency with which the target material is extracted as a function of different characteristics: the geometric parameters of the collector and the repulsive potential of the collector plates.

2. CALCULATION OF THE SEPARATION PARAMETERS OF A COLLECTOR

The efficiency of the extraction of the target isotope is characterized by the extraction coefficient Γ. For

1063-780X/02/2807-0565$22.00 © 2002 MAIK "Nauka/Interperiodica"

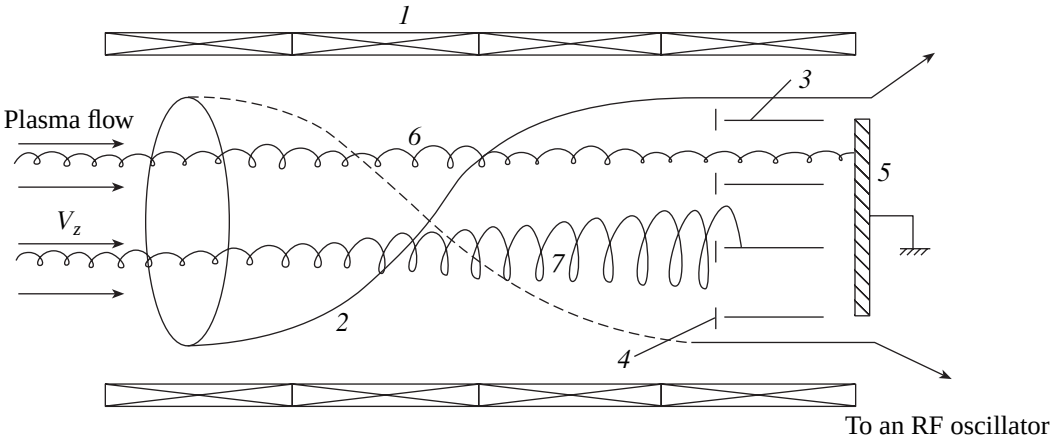

Fig. 1. Schematic diagram of the ICR method of isotope separation: (*1*) solenoid, (*2*) RF antenna, (*3*) collector plates, (*4*) front screens, (*5*) waste plate, (*6*) "cold" ions, and (*7*) target isotope ions.

classical separation schemes, this coefficient is defined by the relationship [8]

$$\Gamma = \frac{C_\tau \tau}{C_g G}, \tag{1}$$

where τ and G are the product and feed fluxes of the separation unit, respectively, and C_τ and C_g are the corresponding partial mole concentrations. For the ICR separation method, the total extraction coefficient should be determined from the relationship

$$\Gamma = \Gamma_S \Gamma_C, \tag{2}$$

where the coefficient Γ_S accounts for the losses of material within the plasma source and the extraction coefficient Γ_C of the collector system is defined as the ratio of the flux of the target isotope deposited on the parallel collector plates to the flux of this isotope at the entrance to the collector. The calculation of the coefficient Γ_S, dependent on the type of source, is a separate task, which is fairly complicated and goes beyond the scope of this paper. Our purpose here is merely to estimate the extraction coefficient Γ_C of the collector. Note that the extraction coefficient, along with the mean separation coefficient $\langle\alpha\rangle$ and the separation power δU [8], is an important parameter governing the economic characteristics of the ICR separation method. Below, we will focus on the calculation of the extraction coefficient in a collector with parallel plates protected by front screens and on the determination of the optimum parameters of an extractor.

We take into account the following circumstance. At the entrance to the collector, the ions of the target isotope move along spiral trajectories; in the plane transverse to the flow, they rotate along the Larmor circles with the gyrofrequency ω_c. We start by obtaining a rough estimate of the extraction coefficient. We assume that, when an ion strikes an infinitely thin plate, it becomes a neutral and remains on the plate surface. In order to simplify the analysis, we also assume that the ions of the target isotope are heated to the same energy $W_{\perp 0}$ (and, accordingly, have the same gyroradius r_L) and there is no repulsive potential. Let the distance between the plates be b, and let the half-height of the front screen be a (Fig. 2). Additionally, we neglect electrostatic field perturbations induced in the plasma by the deposition of the ions in the collector [9]. For $b \le 2r_L$ and $a = 0$, each of the ions eventually reaches one or another of the collector plates and we immediately obtain $\Gamma_C = 1$. In the presence of the front screen ($a \neq 0$), the extraction coefficient is obviously equal to

$$\Gamma_C = \frac{b - 2a}{b}. \tag{3}$$

The front screen has several functions. It protects the collector plates from the plasma flow, thereby making it possible to maintain a positive potential on the plates. It also increases the degree of separation by reducing the flux of cold ions of the nontarget isotope. However, since the screen absorbs some of the target material, it is expedient to decrease its height to the maximum possible extent consistent with the design requirements and the constraints of protecting the collector plates from an electron flux in the operating modes with the repulsive potential. In the limit $a \longrightarrow 0$, the extraction coefficient Γ_C is equal to

$$\Gamma_C = 1 \quad \text{for} \quad 2r_L \ge b, \tag{4}$$

$$\Gamma_C = \frac{2r_L}{b} \quad \text{for} \quad 2r_L < b. \tag{5}$$

Assuming that, initially, the condition $b = 2r_L$ is satisfied, we fix the gyroradius r_L and change the distance b between the collector plates. In the approximation at hand (i.e., under the assumption that the gyroradii of the ions of the target isotope are the same), an increase in b from $b = 2r_L$ to ∞ results in a proportional decrease in the extraction coefficient from $\Gamma_C = 1$ to 0. As b is

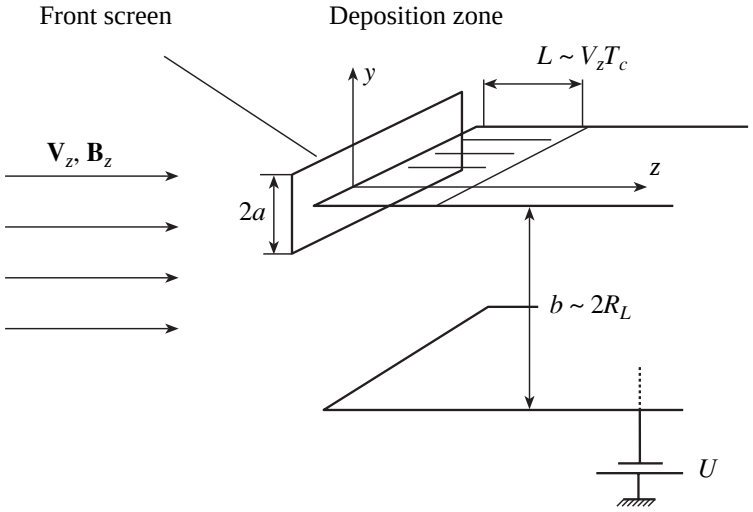

Fig. 2. Magnified fragment of an element of the extractor.

decreased from $2r_L$ to zero, the coefficient Γ_C remains unchanged and equals unity.

In practice, for a number of reasons (first of all, because of the initial longitudinal velocity spread of the ions and the associated distribution over the residence times of the ions within the heating region), the ions deposited on the collector plates have a spread in transverse energies. As a first approximation, we assume that the distribution function of the target ions over their transverse velocities $V_\perp$ is equilibrium:

$$f = n(m/2\pi kT_\perp)\exp\left(-\frac{mV_\perp^2}{2kT_\perp}\right), \qquad (6)$$

where n is the ion density, $T_\perp$ is the effective transverse ion temperature, m is the mass of an ion, and k is Boltzmann's constant. Let us estimate the extraction coefficient, assuming that the plates are separated by the distance $b = 2r_L^*$ (where $r_L^* = \sqrt{\frac{2kT_\perp}{m}}\frac{1}{\omega_c}$ is the mean ion gyroradius) and that there is no repulsive potential ($U = 0$) and no front screen ($a = 0$). In the plasma flow, the fraction of ions whose gyroradii are $r_L > b/2$ ($V_\perp > V_{\perp 1} = (b/2)\omega_c$) and which thus eventually reach the collector plates is equal to

$$q = \int_{V_{\perp 1}}^{\infty}\left(\frac{m}{2\pi kT_\perp}\right)\exp\left(-\left(\frac{mV_\perp^2}{2kT_\perp}\right)\right)2\pi V_\perp dV_\perp$$
$$= \exp\left(-\left(\frac{b^2}{4r_L^{*2}}\right)\right) \simeq 0.37.$$

However, the ions with gyroradii $r_L < b/2$ also reach the plates. In order to obtain a rough estimate of the fraction q_1 of the ions that are additionally deposited on the collector plates, we calculate the mean gyroradius of the ions whose velocities lie within the range from 0 to $b\omega_c/2$:

$$\bar{r}_L\left(0, \frac{b}{2}\omega_c\right) = \frac{\bar{V}_\perp\left(0, \frac{b}{2}\omega_c\right)}{\omega_c} \simeq 0.38\sqrt{\frac{2kT_\perp}{m}}\frac{1}{\omega_c}.$$

In this case, the fraction of the ions that are additionally deposited on the collector plates is

$$q_1 = \frac{2\bar{r}_L\left(0, \frac{b}{2}\omega_c\right)}{b} \simeq 0.38,$$

so that, for Γ_C, we obtain

$$\Gamma_C = q + q_1 \simeq 0.75.$$

For a front screen of finite height ($a \neq 0$), we find, to a first approximation, $\Gamma_C = (q + q_1)(1 - 2a/b)$. Thus, setting $a = 2.5$ mm and $b = 30$ mm yields $\Gamma_C \simeq 0.6$. Note that this is merely a rough estimate. The method providing more precise calculations of the extraction coefficient was first developed by Ustinov [10]. In the present paper, we use a modified calculation procedure described in our earlier paper [11]. We calculate the coefficient Γ_C as the ratio of the flux $j_{\perp 1}$ of the ions of the target isotope deposited on the collector plates to the total longitudinal flux $j_{\parallel 1}$ of these ions at the entrance to the collector:

$$\Gamma_C = \frac{j_{\perp 1}}{j_{\parallel 1}}. \qquad (7)$$

In this way, we assume that the effect of the front screen on the extractor parameters is negligible. We determine

the fluxes of the ion components onto the collector plates by integrating the corresponding distribution functions with different effective transverse temperatures for the allowed values of the coordinates of the guiding centers of the ion trajectories at the entrance to the extractor [11]. The related calculations were carried out for a natural ^{6}Li–^{7}Li isotope mixture and for the following parameters of an ICR separator [6]: the magnetic induction is $B_z = 0.25$ T, the electric field amplitude in the plasma is $E = 50$ V/m, the length of the ICR heating region is $L = 0.8$ m, and the wavelength of the RF field is $\lambda = 0.8$ m, the initial transverse and longitudinal ion temperatures being $T_{\perp 0} = 5$ eV and $T_{\|0} = 10$ eV, respectively. Under these conditions, the calculated transverse temperature of ^{6}Li ions is $T_{\perp 6} \simeq 40$ eV and that of ^{7}Li ions is $T_{\perp 7} \simeq 5$ eV [11]. We assume that the longitudinal velocity distribution function of the ions of the Kth species is "semi-Maxwellian" (no ions move toward the ion source):

$$f_{zK}(V_z) = 2\left(\frac{m_K}{2\pi k T_{\|K}}\right)^{1/2} \exp(-X^2), \tag{8}$$

where $X = V_z(m_K/2kT_{\|K})^{1/2}$ and V_z is the longitudinal ion velocity. The dimensionless ion flux on the upper surface of the collector plate, $J_K = j_K/j_{0K}$ (where $j_{0K} = 2n_K\left(\frac{2kT_{\perp K}}{m_K}\right)^{1/2}\frac{1}{\pi^{3/2}}$, with n_K the density of the ions of the Kth species), is determined by the following expression, which incorporates the repulsive potential U of the collector plate:

$$\begin{aligned} J_K = \exp(-U_K^*)\Bigg\langle & \int_{2X_K^*}^{\infty} dX \Bigg\{ \int_0^{B_1} Y^2\left(1+\cos\frac{\alpha_K}{2}\right)T(X,Y)dY \\ & + \int_{B_1}^{B_2} Y\left[Y\left(1+\cos\frac{\alpha_K}{2}\right) - 2b_{Kp}D_{Kp}\cot\frac{\alpha_K}{2}\right]T(X,Y)dY \\ & + \int_{B_2}^{\infty} Y\left[b_{Kp} + Y\cos\frac{\alpha_K}{2} - b_{Kp}D_{Kp}\cot\frac{\alpha_K}{2}\right]T(X,Y)dY \Bigg\} \\ & + \int_{X_{0K}^*}^{2X_K^*} dX \Bigg[\int_0^{B_2} Y^2\left(1+\cos\frac{\alpha_K}{2}\right)T(X,Y)dY \\ & + \int_{B_2}^{\infty}\left(2b_{Kp} - Y + Y\cos\frac{\alpha_K}{2}\right)YT(X,Y)dY \Bigg] \\ & + \int_{X_K^*}^{X_{0K}^*} dX \left[\int_0^{B_2} Y^2\left(1+\cos\frac{\alpha_K}{2}\right)T(X,Y)dY \right] \Bigg\rangle, \end{aligned} \tag{9}$$

where

$$b_{Kp} = \frac{b\omega_{cK}}{2}\sqrt{\frac{m_K}{2kT_{\perp K}}}, \quad X_{0K}^* = \frac{\omega_{cK}z}{\alpha_0}\sqrt{\frac{m_K}{2kT_{\|K}}},$$

$$X_K^* = \frac{\omega_{cK}z}{2\times 10^3}\sqrt{\frac{m_K}{2kT_{\|K}}}, \quad D_{Kp} = \sqrt{\frac{Y^2\sin^2\frac{\alpha_K}{2}}{b_{Kp}^2} - 1},$$

$$\alpha_0 \simeq 4.18, \quad B_1 = b_{Kp}/\sin\frac{\alpha_K}{2}, \quad B_2 = b_{Kp}/\sin^2\frac{\alpha_K}{2},$$

$$B_3 = b_{Kp}/\sin^2\frac{\alpha_K}{4}, \quad Y = V_\perp\sqrt{\frac{m_K}{2kT_{\perp K}}},$$

$$T(X,Y) = \exp(-(X^2+Y^2)),$$

$\omega_{cK} = eB_z/m_K$ is the cyclotron frequency of the ions of the Kth species, $\alpha_K = \omega_{cK}z/V_z$ is the angle by which the gyrating ions rotate as they fly from the front edge of the plate to the point z at which they strike the plate, and $U_K^* = eU/kT_{\perp K}$.

Note that the ions are deposited on the collector plates mainly over the mean period of their spiral trajectories, $L \approx V_zT_c$, where V_z is the mean longitudinal ion velocity and T_c is the cyclotron period (Fig. 2). In actuality, however, the transverse ion flux density depends on the longitudinal coordinate due to such factors as the longitudinal velocity spread of the ions and the character of their motion before they strike the plate (the ions can strike the upper plate surface only when they fly toward the plate from above and the plate itself does not allow the deposition of some ions over the second half-period of their spiral trajectories; as a result, most of the ions are deposited over the first half-period of the "spirals"). It is for this reason that the separating parameters should be calculated by integrating the corresponding quantities over the z-coordinate. In this case, expression (7) for the coefficient of the extraction of the ions of the Kth species can be rewritten as

$$\Gamma_K = \frac{4}{(b+d)}\int_0^{\infty}\frac{J_K(z)}{\pi}\sqrt{\frac{T_{\perp K}}{T_{\|K}}}dz, \tag{10}$$

where d is the thickness of the collector plate.

Figure 3 shows the dependence of the extraction coefficient for a ^{6}Li target isotope on the repulsive potential U, calculated for a fixed distance between the plates and without allowance for the plate thickness ($d = 0$).

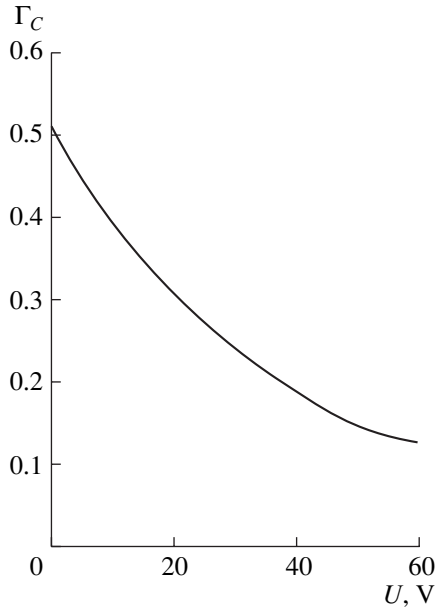

Fig. 3. Dependence of the extraction coefficient Γ_C for a ^{6}Li target isotope on the repulsive potential U for collector plates separated by the distance b = 30 mm ($T_{\perp 6}$ = 40 eV, $T_{\perp 7}$ = 5 eV).

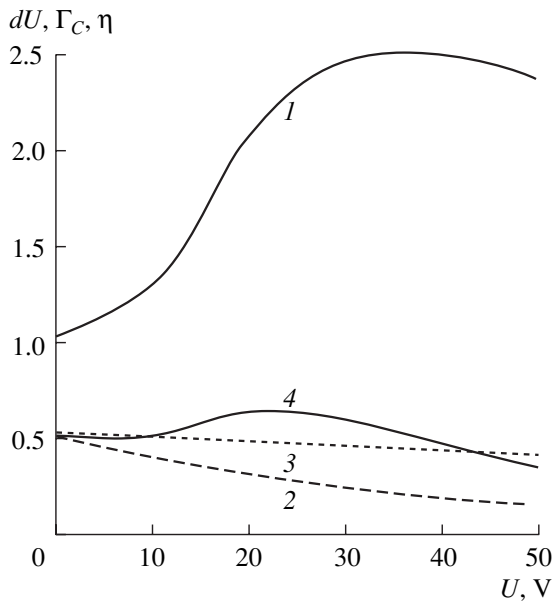

Fig. 4. Dependence of (*1*) the separation power dU, (*2*) the extraction coefficient Γ_C, (*3*) the extraction coefficient calculated in [10], and (*4*) the collector efficiency η on the repulsive potential U for collector plates separated by the distance b = 30 mm.

Let us estimate the separation power δU of one of the sides of the collector plate. To do this, we turn to the expression [8]

$$\delta U = \int_0^\infty \tau_1(z)\frac{(\alpha(z)-1)}{\alpha(z)+1}\ln\alpha(z)\,dz, \qquad (11)$$

where $\tau_1(z)$ is the density of the ion-mixture flux onto one side of the plate per unit length in the direction perpendicular to the main flow velocity at the distance z from the front edge of the plate, $\alpha(z) = \left(\frac{C_6(z)}{C_7(z)}\right)\Big/\left(\frac{C_{60}}{C_{70}}\right)$ is the local separation coefficient, $C_6(z)$ and $C_7(z)$ are the concentrations of ^{6}Li and ^{7}Li isotopes at the plate, and C_{60} and C_{70} are the concentrations of the same isotopes in the plasma flow from the source. In Fig. 4, curve *1* shows the dependence of the dimensionless separation power $dU = \delta U/0.05(n_{60} + n_{70})(2kT_{\perp 6}/m_6)^{1/2}$ (where n_{60} and n_{70} are the corresponding initial ion densities) of one side of the plate on the repulsive potential at a fixed distance between the plates. We can see that there is an optimum value of the separation power in terms of the repulsive potential U. The dashed curve *2* shows the U-dependence of the extraction coefficient Γ_C of the collector, and the dotted curve *3* is for the same coefficient calculated by Ustinov [10]. Figure 5 shows the extraction coefficient Γ_C calculated as a function of the distance b between the plates for different repulsive potentials. As may be seen, the extraction coefficient decreases as b increases, which is associated with an increase in the fraction of ions that do not strike the collector plates. The decrease in Γ_C also results from an increase in the repulsive potential U, which facilitates the reflection of the fraction of ions with such velocities whose projections onto the direction transverse to the plate are small. We introduce the quantity η as the product of the separation power δU and the extraction coefficient Γ_C and call this quantity the "collector efficiency." The dependence of the efficiency η on the repulsive potential U is shown by curve *4* in Fig. 4. Calculations show that the collector efficiency is the highest at repulsive potentials lower than those at which the separation power is maximum. Figure 6 shows the collector efficiency η calculated as a function of the distance b between the plates for different values of the repulsive potential U. We see a very pronounced maximum with respect to the distance b between the plates: the collector efficiency is peaked at approximately $b \approx 2r_L^*$.

The results presented above were obtained without allowance for the effects of the front screen and the finite thickness of collector plates. Note that, in an actual extractor, the collector plates should be intentionally cooled, so that their thickness cannot be arbitrarily small.

Let us analyze the effects of both the thin front screen and the finite thickness of the collector plates on the coefficient of the extraction of the target isotope. For a relatively large distance between the plates ($b \geq$

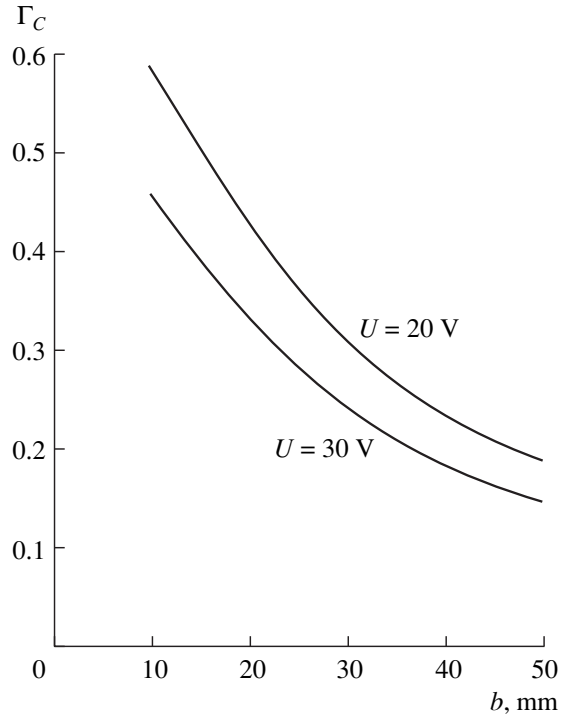

Fig. 5. Extraction coefficient Γ_C vs. distance b between the plates for two values of the repulsive potential U at $T_{\perp 6}$ = 40 eV and $T_{\perp 7}$ = 5 eV.

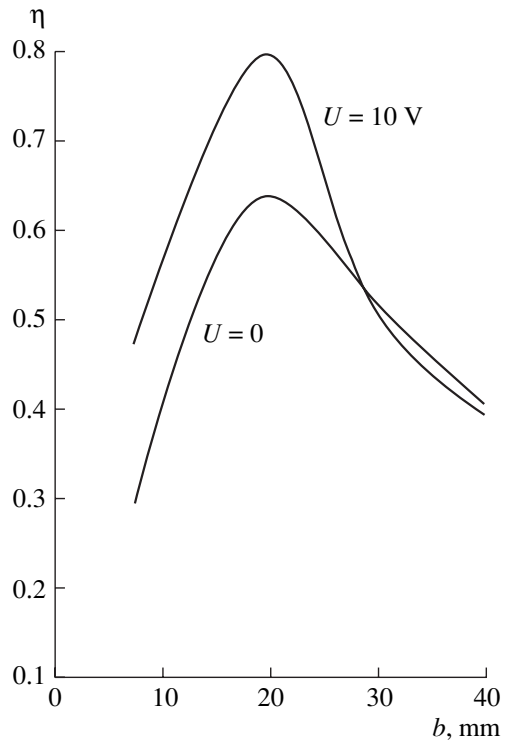

Fig. 6. Collector efficiency η vs. distance b between the plates.

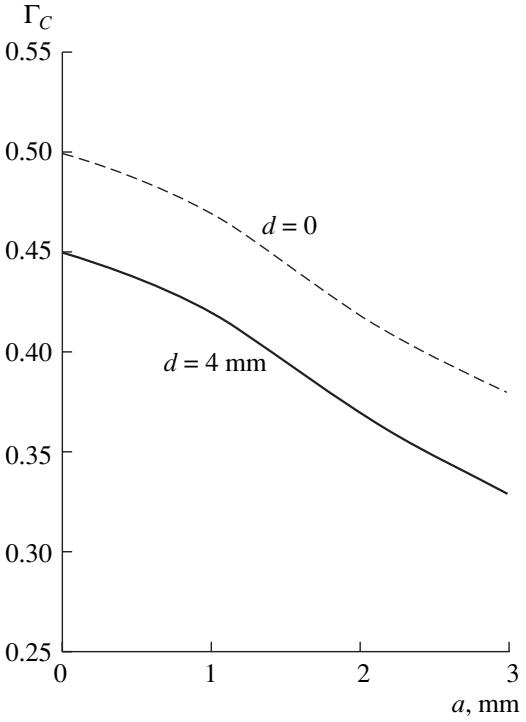

Fig. 7. Extraction coefficient Γ_C vs. half-height a for infinitely thin plates (dashed curve) and for plates with the thickness d = 4 mm (solid curve), the remaining parameters being b = 30 mm, U = 0, $T_{\perp 7}$ = 5 eV, and $T_{\perp 6}$ = 40 eV.

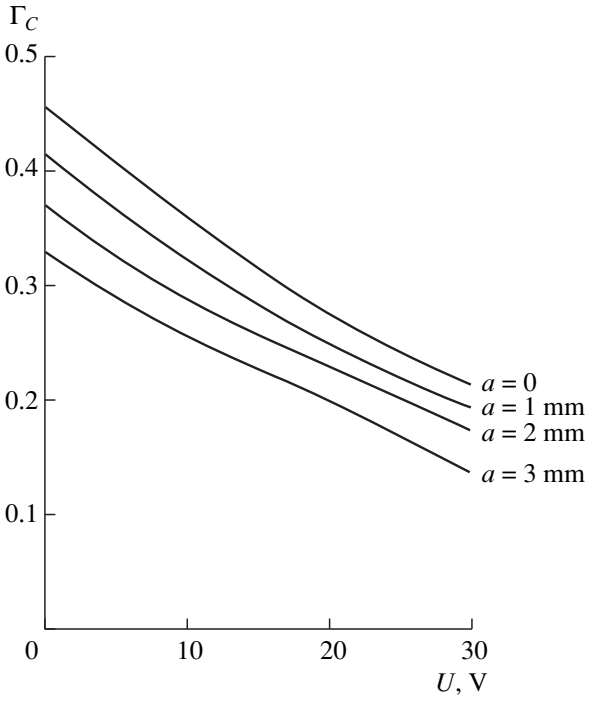

Fig. 8. Extraction coefficient Γ_C vs. repulsive potential U for a front screen with different half-heights a, the remaining parameters being b = 30 mm, d = 4 mm, $T_{\perp 6}$ = 40 eV, and $T_{\perp 7}$ = 5 eV.

r_L^*), the ion fluxes onto the plates can be estimated from the relationships

$$J_K = \exp(-U_K^*) \times \left\{ \int_{2X_K^*}^{\infty} dX \left[\int_{A_1}^{A_2} 2a_K^* \cot(b_K z/X) D_K YT(X, Y) dY + \int_{A_2}^{\infty} (Y - a_K^* + a_K^* \cot(b_K z/X) D_K) YT(X, Y) dY \right] + \int_{X_K^*}^{2X_K^*} dX \int_{A_2}^{\infty} [Y - a_K^* + a_K^* \cot(b_K z/X) D_K] YT(X, Y) dY \right\}, \quad (12)$$

where $a_K^* = \frac{a\omega_{cK}}{2}(m_K/2kT_{\perp K})^{1/2}$, $D_K = (Y^2 \sin^2(b_K z/X)/a_K^{*2} - 1)^{1/2}$, $A_1 = a_K^*/\sin(b_K z/X)$, $A_2 = a_K^*/\sin^2(b_K z/X)$, $X = V_z/(2kT_{\|K}/m_K)^{1/2}$, $X_K^* = (\omega_{cK} z/2000\pi)(m_K/2kT_{\|K})^{1/2}$, $Y = V_\perp/(2kT_{\perp K}/m_K)^{1/2}$, $b_K = X_K^* \pi/z$.

Figure 7 shows the extraction coefficient Γ_C calculated as a function of the half-height a of the front screen for infinitely thin collector plates (dashed curve) and for collector plates with the thickness d = 4 mm (solid curve). The calculations were carried out for a fixed distance between the plates, the repulsive potential being zero. The results of calculations show that, at the plate thickness d = 4 mm (which is the minimum possible thickness for the plates to be water-cooled), the extraction coefficient is smaller by 10 to 30% than that for infinitely thin plates. Figure 8 shows the dependence of the extraction coefficient Γ_C on the repulsive potential U for a front screen with different half-heights a.

ACKNOWLEDGMENTS

We are grateful to Yu.A. Muromkin for useful remarks.

REFERENCES

1. G. A. Askar'yan, V. A. Namiot, and A. A. Rukhadze, Pis'ma Zh. Tekh. Fiz. **1**, 820 (1975) [Sov. Tech. Phys. Lett. **1**, 356 (1975)].
2. J. M. Dawson, H. C. Kim, D. Arnush, *et al.*, Phys. Rev. Lett. **37**, 1547 (1976).
3. M. Mussetto, T. E. Romesser, D. Dixon, *et al.*, in *Abstracts of the IEEE International Conference on Plasma Science, San Diego, 1983*, p. 70.
4. T. E. Romesser, V. Vanek, J. Tang, *et al.* in *Abstracts of the IEEE International Conference on Plasma Science, San Diego, 1983*, p. 71.
5. A. C. La Fontaine and P. Louvet, *Compte rendu des Journees sur les Isotopes Stables, Saclay, France, 1993*, p. 332.
6. A. I. Karchevskiĭ, V. S. Laz'ko, Yu. A. Muromkin, *et al.*, Fiz. Plazmy **19**, 411 (1993) [Plasma Phys. Rep. **19**, 214 (1993)].
7. I. L. Bass, R. E. Bonanno, R. P. Hackel, and R. Hammond, Appl. Opt. **31**, 6993 (1992).
8. A. M. Rozen, *Theory of Isotope Separation in Columns* (Atomizdat, Moscow, 1960).
9. A. I. Karchevskiĭ and E. P. Potanin, Fiz. Plazmy **22**, 1146 (1996) [Plasma Phys. Rep. **22**, 1044 (1996)].
10. A. L. Ustinov, Preprint No. 5354/6, IAÉ (Institute of Atomic Energy, Moscow, 1991).
11. A. I. Karchevskiĭ and E. P. Potanin, Fiz. Plazmy **21**, 416 (1995) [Plasma Phys. Rep. **21**, 394 (1995)].
12. D. A. Dolgolenko, G. E. Zotin, A. I. Karchevskiĭ, *et al.*, in *Proceedings of the 4th All-Russia Conference "Physicochemical Processes Accompanying the Selection of Atoms and Molecules," Zvenigorod, 1999.*

Translated by O. E. Khadin

Plasma Physics Reports, Vol. 28, No. 7, 2002, pp. 572–579. Translated from Fizika Plazmy, Vol. 28, No. 7, 2002, pp. 618–626.

PLASMA OSCILLATIONS AND WAVES

Oscillations of a Magnetized Plasma in a Waveguide of Complicated Shape

A. M. Ignatov

Institute of General Physics, Russian Academy of Sciences, ul. Vavilova 38, Moscow, 117942 Russia

Received January 24, 2002

Abstract—Potential hybrid oscillations in a resonator of arbitrary shape are investigated theoretically. It is shown that, for a periodic waveguide, the frequency dependence of the wavenumber is represented by a fractal curve of the "devil's staircase" type. © *2002 MAIK "Nauka/Interperiodica".*

1. INTRODUCTION

About ten years ago, Lou *et al.* [1] theoretically revealed strange behavior of the spectrum of the Trivelpiece–Gould (TG) waves in a periodic waveguide. Usually, plasma oscillations are either characterized by a certain dependence of the frequency on the wavenumber or do not satisfy any dispersion relation, as is the case, e.g., with Langmuir waves in an inhomogeneous cold plasma or Van Kampen waves [2]. However, the spectra revealed in [1] and called dense spectra had nothing to do with these two types of waves and were represented by a dense (in the mathematical sense) set in the (ω, k) plane.

The arguments of Lou *et al.* [1] apply, in principle, to any type of oscillations; it is only necessary that the oscillation frequency be limited from above by a certain maximum frequency. Thus, consider a uniform waveguide bounded in the transverse direction and filled with a certain medium and assume that the eigenmodes of the waveguide are excited at frequencies $\omega_n(k)$ $(n = 1, 2, \ldots)$ such that $\omega_n(k) < \omega_{\max}$ (Fig. 1a). This property is peculiar to the TG modes, but there are many other examples of such oscillations in physics. In the presence of a weak periodic perturbation (e.g., in a periodic waveguide with a slightly corrugated wall), the wave spectrum in the standard perturbation theory is constructed as follows. First, it is necessary to plot all of the dispersion curves and shift them along the k-axis by the wavenumbers that are multiples of the wavenumber of the perturbation, $k_0 = 2\pi/a$, where a is the period of the perturbation. This results in an infinite set of dispersion curves $\omega = \omega_n(k + lk_0)$ $(l = 0, \pm1, \pm2\ldots)$. Then, it is necessary to take into account the fact that, at the intersection of two curves, there is a Bragg gap (or a stop band); of course, this is possible only if the existence of the gap is allowed by the symmetry properties of the waveguide. For conventional electromagnetic waves in a waveguide, the dispersion curves obtained by this procedure do not exhibit any particularly unusual behavior. But if the oscillations exist only in a certain frequency band (as is shown in Fig. 1a), there are an infinite number of shifted dispersion curves each of which intersects the remaining curves, giving rise to a certain fractal grid that densely covers the entire frequency band $0 < \omega < \omega_{\max}$. Some insight into the grid structure can be gained from Fig. 1b, which shows the first Brillouin zone $(0 < k < \pi/a)$ with several intersections and in which the Bragg gaps are not plotted, for simplicity.

The above procedure for constructing the wave spectrum raises the following two questions. The first question is whether it is, in principle, possible to describe the situation under consideration by perturbation theory. Serious doubts on this possibility were raised by the results obtained by Gusakov and Piliya

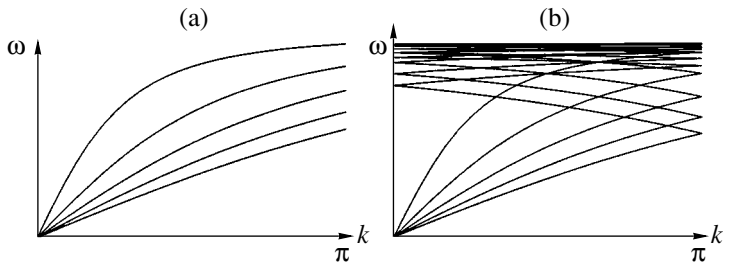

Fig. 1. Formation of a dense spectrum: (a) unperturbed spectrum and (b) perturbed spectrum with the period $a = 1$.

1063-780X/02/2807-0572$22.00 © 2002 MAIK "Nauka/Interperiodica"

[3], who investigated the propagation of a hybrid wave in a periodically nonuniform waveguide in the geometrical-optics approximation and noted that the spatial wave structure is highly singular, which indicates that, even in a slightly corrugated waveguide, the solution describes a large number of spatial modes. The second question is how Fig. 1b can be converted back to Fig. 1a in the limit of a vanishingly small periodic perturbation. In fact, the question is how to understand Fig. 1b: in the sense of reduced or in the sense of extended Brillouin zones (see, e.g., [4]). This understanding can be readily reached for waves with an infinitely broad frequency spectrum, but the situation at hand is far more complicated.

The dense spectra were further investigated in a number of papers. Thus, the author of this paper demonstrated that, under certain restrictions, it is possible to construct an exact solution for TG waves in a planar periodic waveguide of arbitrary shape [5]. The wave spectrum was found to consist of separate oscillation branches analogous to those shown in Fig. 1a. However, each of the branches is rather unusual: the frequency dependence $k(\omega)/k_0$ is a fractal curve, which is called the Cantor's function by mathematicians and the devil's staircase by physicists. This dependence is described by a monotonic function, which is constant in a certain interval if its value is a rational number.[1] The method used in [5], which will be considered in more detail below, makes it possible to determine the main parameters of the devil's staircase and to calculate the field structure explicitly when the ratio k/k_0 is a rational number. The resulting eigenfunctions of a waveguide are highly singular: to approximate them requires a large number of spatial harmonics. If the ratio k/k_0 is irrational, it can only be stated that the eigenfunctions are, on the contrary, smooth, but their shapes cannot be determined analytically and it is, in a sense, impossible to find them numerically.

On the other hand, using a fairly involved algorithm based on the perturbation theory in terms of the waveguide corrugation depth, Zaginaylov *et al.* [7, 8] numerically calculated dispersion curves for the TG waves under essentially the same assumptions as those made in [5]. The main result obtained in [7, 8] is precisely opposite to the conclusions drawn in [5]: for certain rational values of $k(\omega)/k_0$ that are determined by the order of perturbation theory, there are Bragg gaps in the spectrum, while, for intermediate values of $k(\omega)/k_0$, the spectrum is smooth. Nevertheless, papers [5] and [7, 8] do not apparently contradict one another. This point will be discussed at the end of the paper. It is also necessary to mention the paper by Volkov and Krasovitskiĭ [9], who obtained solutions for a cylindrical waveguide but under the model boundary conditions that can hardly be treated as physically meaningful.

[1] It should be noted that analogous spectra are also met in the so-called quasicrystals in solid-state physics [6].

The goal of the present paper is to discuss the spectra of potential hybrid waves in a purely electron plasma in a two-dimensional waveguide of arbitrary shape. The main result obtained in this work is illustrated in Fig. 7, in which the spectra of both the upper and lower hybrid waves are represented by fractal curves of the devil's staircase type. The paper is organized as follows. In Section 2, the basic equations are formulated and the statement of the problem is discussed. Section 3 is aimed at constructing a very general solution for a waveguide of arbitrary shape. In Section 4, a periodic waveguide is considered and corresponding explicit solutions are derived. In Section 5, the calculation of the spectral characteristics is illustrated using a waveguide with a sawtooth-shaped wall as an example.

2. BASIC EQUATIONS

We consider a symmetric planar waveguide oriented along the z-axis and bounded by metal walls at $x = \pm a(z)$ (Fig. 2). At this point, no restrictions (including the periodicity condition) are imposed on the wall shape. Let the region $-a(z) < x < a(z)$ be filled with a cold electron plasma against a neutralizing ion background, and let the magnetic field be directed along the z-axis. The potential hybrid oscillations are described by Poisson's equation

$$\varepsilon_\parallel(\omega)\frac{\partial^2\varphi(z, x)}{\partial z^2} + \varepsilon_\perp(\omega)\frac{\partial^2\varphi(z, x)}{\partial x^2} = 0, \qquad (1)$$

where

$$\varepsilon_\parallel(\omega) = 1 - \frac{\omega_p^2}{\omega^2}, \quad \varepsilon_\perp(\omega) = 1 - \frac{\omega_p^2}{\omega^2 - \Omega^2} \qquad (2)$$

are the longitudinal and transverse dielectric functions of a cold magnetized plasma and ω_p and Ω are the plasma and cyclotron frequencies.

The boundary conditions on Eq. (1) have the form

$$\varphi(z, \pm a(z)) = 0. \qquad (3)$$

Obviously, Eq. (1) with the boundary conditions (3) has nontrivial solutions only when $\varepsilon_\parallel(\omega)$ and $\varepsilon_\perp(\omega)$ have

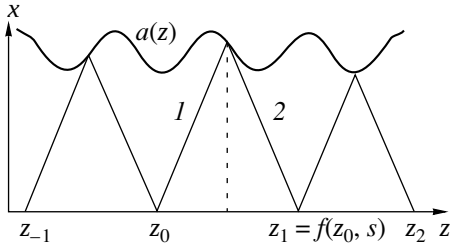

Fig. 2. Mapping that results from the reflection of the wave front from the waveguide wall: $z_0 \longrightarrow z_1 = f(z_0, s)$.

opposite signs. This circumstance is reflected in explicit form by rewriting Eq. (1) as

$$\frac{\partial^2\varphi(z, x)}{\partial z^2} - s^2\frac{\partial^2\varphi(z, x)}{\partial x^2} = 0, \quad (4)$$

where

$$s^2 = -\frac{\varepsilon_\perp(\omega)}{\varepsilon_\parallel(\omega)} = \frac{\omega^2(\omega^2 - \Omega^2 - \omega_p^2)}{(\omega_p^2 - \omega^2)(\omega^2 - \Omega^2)}. \quad (5)$$

An important point here is that Eqs. (1) and (4) are hyperbolic, in which case ω and *s* are spectral parameters. Although the simplest wave equation (4) has been known for several hundred years, it is usually treated in a quite different mathematical sense: the quantity *s* is assumed to be a given constant (such as the speed of sound, the speed of light, etc.). To the best of my knowledge, the spectral problems associated with Eq. (4) have not yet been investigated by mathematicians (at least, I failed to find references to such investigations in the literature). Thus, in the traditional theory of hyperbolic equations, the question of solving equations of the type of Eq. (4) in a region bounded by a closed curve is meaningless: as has been noted in many textbooks, such solutions do not exist. On the other hand, the question about the oscillation spectrum in a finite-size closed resonator filled with a magnetized plasma is quite natural from the physical standpoint. Thus, for a resonator of rectangular cross section, the eigenvalues of Eq. (4) can be determined by elementary methods.

3. OSCILLATIONS IN A WAVEGUIDE OF ARBITRARY SHAPE

In what follows, we restrict ourselves to considering a waveguide unbounded in the longitudinal direction. The general solution to Eq. (4) is well known. The boundary-value problem with conditions (3) at a boundary $a(z)$ of arbitrary shape can be solved by the technique of *h*-conformal mappings [10]. In the case under consideration, reproducing this solution does not require heavy mathematics. Since we are interested in a symmetric waveguide, any solution is either even or odd in *x*. Hence, in the general case, we can write

$$\varphi(z, x) = \Phi(z + x/s) - (-1)^\lambda\Phi(z - x/s), \quad (6)$$

where $\Phi(z)$ is an arbitrary function and odd and even solutions are those with $\lambda = 0$ and $\lambda = 1$, respectively. Substituting representation (6) into boundary conditions (3) yields the following functional equation for $\Phi(z)$:

$$\Phi(z + a(z)/s) = (-1)^\lambda\Phi(z - a(z)/s). \quad (7)$$

This equation can be solved as follows. First, we define the function $f(z, s)$ as

$$z_0 = \zeta - a(\zeta)/s, \quad f(z_0, s) = \zeta + a(\zeta)/s. \quad (8)$$

How to construct this function is illustrated in Fig. 2, in which the wave fronts represented by straight lines *1* and *2* are at angles $\pm\vartheta$ to the *z*-axis, where $\tan\vartheta = s$. The function $f(z, s)$ is clearly defined at all points *z* only when $s > s_0 = \max|a'(z)|$, in which case we have $\partial f(z, s)/\partial z > 0$. In accordance with relationship (5), the condition $s > s_0$ also imposes certain restrictions on the oscillation frequencies. Equation (7) is now written as $\Phi(f(z, s)) = (-1)^\lambda\Phi(z)$, and its solution is looked for in the form

$$\Phi(z) = \exp[i\pi(2m + \lambda)\psi(z)], \quad (9)$$

where *m* is an arbitrary integer. Equation (7) is an identity when

$$\psi(f(z, s)) - \psi(z) = 1. \quad (10)$$

It is significant to note that, if we find a solution satisfying condition (10), we thus obtain a series of waveguide modes with different numbers *m* and λ (or, equivalently, with different spatial structures).

Let us now apply these results to a straight waveguide. Assuming that $a(z) = \text{const}$, we find $f(z, s) = z + 2a/s$, in which case the simplest of solutions satisfying condition (10) is the linear function $\psi(z) = \kappa z$, where $\kappa = s/(2a)$. Then, using formulas (5), (7), and (9), we can readily determine an entire spectrum of waveguide modes similar to that shown in Fig. 1a.

It is also an easy matter to construct a general solution satisfying condition (10) for the boundary $a(z)$ of arbitrary shape. We choose a certain point z_0 and successively calculate the points $z_1 = f(z_0, s)$, $z_2 = f(z_1, s)$, $z_n = f^{(n)}(z_0, s)$, where $f^{(n)}(z, s)$ stands for the *n*th iteration of the function $f(z, s)$ (Fig. 2). Since $f(z, s)$ is a monotonic invertible function of *z* (see above), this sequence is increasing and we have $z_n \longrightarrow \infty$ as $n \longrightarrow \infty$. By iterating the inverse function, we can also construct the sequence z_n for $n < 0$. In this case, the entire *z*-axis is divided into the intervals $I_n = [z_n, z_{n+1})$; moreover, the function $f(z, s)$ induces a one-to-one mapping of any interval onto a neighboring interval, $I_n \longleftrightarrow I_{n+1}$. Now, it is sufficient to arbitrarily specify the phase $\psi(z)$ over the entire interval I_0; below, this phase will be denoted by $\psi_0(z)$. Then, the phase $\psi(z)$ in any interval can be calculated by iterating the function $f(z, s)$ using condition (10): if $z \in I_n$, then $f^{(-n)}(z, s) \in I_0$, so that $\psi(z) = \psi_0(f^{(-n)}(z, s)) + n$. In order for the function $\psi(z)$ to be continuous over the entire axis, it is necessary to require that $\psi_0(z_1) = \psi_0(z_0) + 1$.

Hence, for any $s > s_0$ or, equivalently, for an upper or lower hybrid wave with any frequency lying in the corresponding range, it is possible to construct quite arbitrary solutions to Eq. (4) with boundary conditions (3). In order to reduce the arbitrariness of the solutions, it is necessary to impose additional restrictions. As has been mentioned, for a straight waveguide with $a(z) = \text{const}$, it is convenient (but not necessary) to choose the phase

as a linear function of z. In fact, this choice is based upon the waveguide symmetry. Another kind of restriction is associated with a waveguide of a variable thickness such that $a(z)$ tends to certain finite limiting values as $z \longrightarrow \pm\infty$. Generally, the function $\psi_0(z)$ constructed from an arbitrarily chosen function $\psi(z)$ behaves at infinity in an irregular manner. We may require that the derivative $\psi'(z)$ tends to certain limiting values at infinity. As was proved in [10], this requirement determines the function $\psi_0(z)$ to within a constant. Although it is impossible to construct an explicit solution for this case, the line of reasoning described in [10] may well be adapted to develop a numerical algorithm. Finally, a waveguide with a periodically corrugated wall is of most practical interest. Additional natural constraints on such a waveguide will be discussed in the next section.

4. PERIODIC WAVEGUIDE

Let the function $a(z)$ be periodic. The scale length can be chosen to equate its period to unity, $a(z + 1) = a(z)$. Now, it is natural to require that the solutions to Eq. (4) should satisfy the additional constraint

$$\varphi(z + 1, x) = e^{ik}\varphi(z, x). \tag{11}$$

Although the wavenumbers k and $k + 2\pi$ yield the same solution, in what follows, the value of k may be conveniently regarded as an arbitrary number, in which case we can use the scheme of extended Brillouin zones [4].

For a periodic waveguide, the solution can be obtained in essentially the same way as in the previous section. The only difference is that condition (11), together with condition (10), yields an additional constraint:

$$\psi(z + 1) = \psi(z) + \kappa, \tag{12}$$

where the quantity κ is proportional to the wavenumber, $k = \pi(2m + \lambda)\kappa$. Hence, the task now is to find the solution satisfying both conditions (10) and (12) and to determine the κ values for which the solution exists.

As in the previous section, the construction of the solution reduces to an analysis of the successive iterations of the function $f(z, s)$, defined by relationships (8). By virtue of the periodicity of the boundary $a(z)$, this function possesses the obvious property $f(z + 1, s) = f(z, s) + 1$. Such functions, which are called circle maps, have been investigated in detail (see, e.g., [11]). In physics, they appear in the study of both nonlinear oscillations and transitions to chaos (see, e.g., [12]). Recently, de la Llave and Petrov [13] have applied the theory of circle maps to study the spectrum of an optical resonator with an oscillating wall and have also found that the spectrum is described by Eq. (4).

The character of the sequence $z_n = f^{(n)}(z_0, s)$ depends strongly on the so-called winding number, which is formally defined as the limit $W(s) = \lim_{n\to\infty}(z_n - z_0)/n$. If $W(s)$ is an irrational number, then the sequence $\{z_n\}$ (where $\{a\}$ denotes the fractional part of a number) densely fills the unit interval [0, 1) as n increases. If the winding number is rational, $W(s) = P/Q$, then, in the limit $n \longrightarrow \infty$, the sequence $\{z_n\}$ becomes periodic and consists of the repeating Q values $\alpha_0, \alpha_1, \ldots, \alpha_{Q-1}$, which are called the Q cycle. (More precisely, the cycle length is a multiple of Q, but this point is unimportant for further analysis.)

These considerations may be illustrated by a simple example. We assume that, for a certain integer P, the equation

$$f(z, s) = z + P \tag{13}$$

has a root (the case with $P = 1$ is illustrated in Fig. 3). Clearly, in the unit interval [0, 1), there are at least two such roots. We denote them by α_0^- and α_0^+ and assume that $f_z'(\alpha_0^-, s) < f_z'(\alpha_0^+, s)$. The successive iterations shown as a broken line in Fig. 3 result in the convergent sequence $\{z_n\} \longrightarrow \alpha_0^-$ for any of the initial points z_0 except for $\{z_0\} = \alpha_0^+$. In this case, for $n \gg 1$, we have $z_{n+1} = z_n + P$, so that the winding number is equal to $W(s) = P$. We can also iterate the inverse function $f^{(-1)}(z, s)$ (this corresponds to the motion in the opposite direction along the broken line in Fig. 3), in which case we obtain $\{z_n\}_{n\to-\infty} \longrightarrow \alpha_0^+$ provided that $\{z_0\} \neq \alpha_0^-$.

Now, we insert $z = \alpha_0^-$ into conditions (10) and (12) and obtain

$$\psi(f(\alpha_0^-, s)) = \psi(\alpha_0^-) + 1 = \psi(\alpha_0^- + P) = \psi(\alpha_0^-) + P\kappa. \tag{14}$$

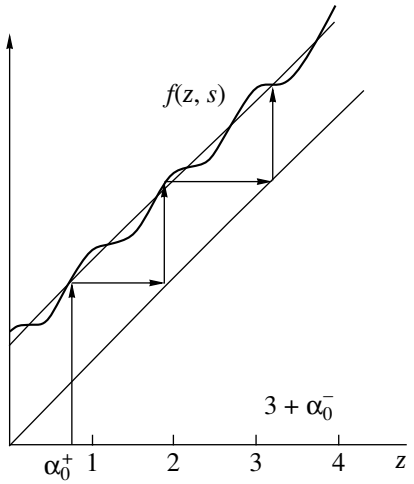

Fig. 3. Successive iterations of the function $f(z, s)$.

This indicates that conditions (10) and (12) are consistent only if $\kappa = 1/P = 1/W(s)$. A slight change in the frequency or, equivalently, in the parameter s causes a small displacement of the curve in Fig. 3 but does not change the number of roots of Eq. (13), so that the quantity κ remains constant in a certain range of variation of the parameter s. Using definition (8), we can easily convince ourselves that Eq. (13) has roots in the range

$$\frac{2\max a(z)}{P} \geq s \geq \frac{2\min a(z)}{P}. \quad (15)$$

We denote this range by $\Delta_{1/P}$. Now, we can readily understand the structure of the solution satisfying conditions (11) and (12). In successive iterations of the function $f(z, s)$, the fractional part of the phase remains unchanged, $\{\psi(z_0)\} = \{\psi(z_n)\}_{n\to\infty} \longrightarrow \psi(\alpha_0^-) = \text{const}$, if $z_0 \neq \alpha_0^+$. Consequently, the phase $\psi(z)$ is a piecewise constant function with discontinuities at the points $\alpha_0^+ + n$. Since $\kappa = 1/P$, the periodicity condition (12) implies that the jumps at the discontinuities are equal to $1/P$.

The second solution can be obtained by iterating the inverse function. Clearly, these iterations again yield the range $\Delta_{1/P}$ and a piecewise constant phase, but the discontinuities now occur at the points $\alpha_0^- + n$.

The solution just constructed describes a wave whose electric field has singularities of the δ-function type at the points at which the phase is discontinuous. In other words, the wave is a superposition of double layers oriented along a periodically continued broken line shown in Fig. 2. Using formulas (6) and (9), we can immediately write out the following explicit expression for the electric field of, e.g., the fundamental even mode ($m = 0$, $\lambda = 1$) at the $x = 0$ axis: $E_z(z) = -2\mathrm{Re}[\exp(-i\omega t)A^\eta(z, s)]$, where

$$A^\eta(z, s) = \sum_{n=-\infty}^{\infty} e^{\frac{in\pi}{P}} \delta(z - \alpha_0^\eta(s) - n), \quad (16)$$

$\eta = \pm$, and ω and s are related by expression (5). To be specific, we assume here that $s > 0$ and note that the wave propagation direction is determined by the sign of ω. Using the familiar Poisson's formula, we can rewrite expression (16) as

$$A^\eta(z, s) = e^{\frac{i\pi(z-\alpha_0^\eta)}{P}} \sum_{n=-\infty}^{\infty} e^{2ni\pi(z-\alpha_0^\eta)}, \quad (17)$$

which shows that, although the position of the double layers does not change with time, the wave phase velocity is nonzero and is equal to $\omega P/\pi$. It may be proved that the functions $A^\eta(z, s)$ with $s \in \Delta_{1/P}$ form a basis in the class of functions satisfying the quasi-periodicity condition $y(z + 1) = e^{i\pi/P}y(z)$, and the expression for the temporal evolution of an arbitrary wave packet is also easy to obtain [5].

Hence, we have shown that, as the parameter s (or, equivalently, the frequency) changes within the range $\Delta_{1/P}$ (15), the wavenumber remains a constant multiple of $1/P$. In the theory of nonlinear oscillations, the same method is used to describe the phenomenon of mode locking (which has been known for several hundred years and underlies the entire scope of radio engineering): two coupled self-excited oscillators tend to tune their frequencies to the same frequency or to frequencies such that one frequency is a multiple of the other; moreover, the oscillator frequencies so tuned remain unchanged when subjected to slight variations in the external parameters. In the situation under discussion, we deal with a reverse (in a sense) phenomenon: we can vary the frequency, in which case, however, the spatial period of the wave remains unchanged.

Consider what happens when the parameter s goes beyond the range $\Delta_{1/P}$. This situation can be understood by analyzing the fixed points of an arbitrary iteration of the above mapping of a circle. In other words, instead of Eq. (13), we must investigate the roots

$$f^{(Q)}(z, s) = z + P, \quad (18)$$

where Q and P are arbitrary integers that have no common divisors. Clearly, after Q iterations, the function $f^{(Q)}(z, s)$ is again a circle map that is analogous to the mapping illustrated in Fig. 3, but now the number of oscillations of this function in the unit interval is larger. Accordingly, there are at least $2Q$ roots (18) in the unit interval, provided that they do exist. Let us assume that there are exactly $2Q$ roots, which is valid if the function $a(z)$ has only one minimum and only one maximum per period. We denote them by $\alpha_0^\pm$, $\alpha_1^\pm$, …, $\alpha_{Q-1}^\pm$ in such a way that $\alpha_i^\pm = \{f(\alpha_{i-1}^\pm, s)\}$ ($i = 1, \ldots, Q - 1$) and $\alpha_0^\pm = \{f(\alpha_{Q-1}^\pm, s)\}$. Then, as $n \longrightarrow \mp\infty$, the fractional part $\{z_n\}$ runs through the sequence of the roots (…, $\alpha_0^\pm$, $\alpha_1^\pm$, …, $\alpha_{Q-1}^\pm$, $\alpha_0^\pm$, …). Performing the same analysis as for the root $Q = 1$ of Eq. (13), we can establish that the winding number is equal to $W(s) = P/Q$ and conditions (10) and (12) are consistent only if the wavenumber is $\kappa = Q/P$. In this way, we again arrive at two solutions satisfying conditions (10) and (12): the solutions turn out to be piecewise constant functions with discontinuities at the points α_i^- and α_i^+, which indicates that there are Q discontinuities in each of the solutions within a unit interval. Between the discontinuities, the phase $\psi(z)$ takes on arbitrary values. In order to satisfy periodicity condition (12), it is sufficient to assume that each jump is equal to $1/P$. An example of this dependence is illustrated in Fig. 5.

Finally, we again see that the number of roots (18) do not change when the parameter s is varied within a

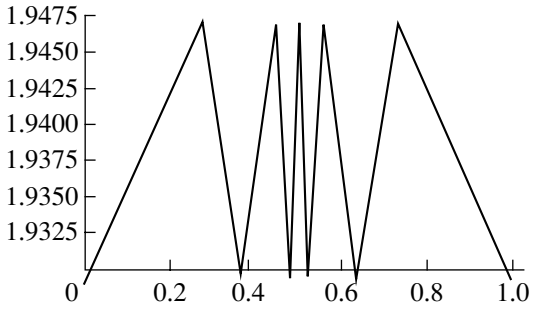

Fig. 4. Function $\sigma_{5/6}(z)$.

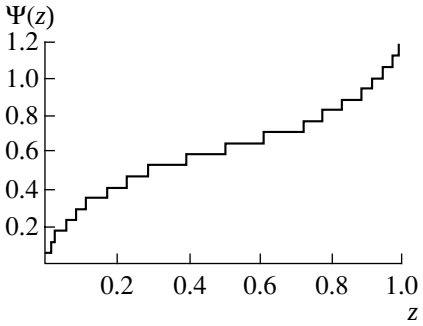

Fig. 5. Coordinate dependence of the wave phase for Q/P = 20/17 and s = 3.12393.

certain range $\Delta_{Q/P}$. However, in contrast to range (15) in the case $Q = 1$, it is now impossible to explicitly find the boundaries of the range $\Delta_{Q/P}$. In numerical calculations, these boundaries can be conveniently determined as follows. We solve Eq. (18) with respect to s and denote the solution obtained by $s = \sigma_{Q/P}(z)$. Clearly, this solution is a periodic function varying in the range $\Delta_{Q/P}$, at the boundaries of which it has a maximum and a minimum. Treating the relationship $s = \sigma_{Q/P}(z)$ as an equation for z, we can obtain all the elements $\alpha_0^{\pm}, \ldots, \alpha_{Q-1}^{\pm}$ of the cycle and thereby determine the phase $\psi(z)$.

If the shape $a(z)$ of the waveguide possesses additional symmetry, some of the ranges $\Delta_{Q/P}$ may shrink to a point. In particular, this is true when $a(z) = a_0 + b(z)$, where $b(z + 1/2) = -b(z)$, e.g., $b(z) \propto (2\pi z)$, in which case, from definition (8), we can readily see that, for $Q = 2$, the function $\sigma_{2/2m+1}(z) \equiv 4a_0/(2m + 1)$ is constant.

Hence, for any rational winding numbers, the wavenumber is equal to $\kappa = 1/W(s)$. Since any irrational number is approximated by a rational number, this equality is also valid for irrational $W(s)$. However, in regard to the phase $\psi(z)$, we can only say that it is a continuous function. Some insight into the character of the function $\psi(z)$ can be provided by considering the limit of large Q and P values such that $\kappa = Q/P \longrightarrow$ const. In this limit, the number of discontinuities in the unit interval increases and the jump at each discontinuity decreases. In this sense, the phase $\psi(z)$ tends to become a continuous function. In the next section, the above analysis will be illustrated by a particular example.

Based on the general theorems on the properties of the circle map (see, e.g., [11]), we can state that the dependence $\kappa(s)$ is a monotonically increasing continuous function. In this case, the range $s > s_0$ is divided into an infinite number of nonoverlapping subranges over each of which the function $\kappa(s)$ is constant. As was mentioned above, such a dependence (which is illustrated, e.g., in Fig. 6) is called the devil's staircase.

In this context, two questions arise. The first is how to go over to a smooth waveguide. For a function $a(z) = a_0 + \epsilon b(z)$, where $b(z)$ is a periodic function, we can see that, as the corrugation depth tends to zero, so does the width of each staircase step, and the centers of all steps tend to lie along a straight line. In other words, we have $\kappa(s) = s/(2a_0) + \Delta\kappa$, where $\Delta\kappa \le \epsilon^Q$.

The second question concerns the total length of the subranges $\Delta_{Q/P}$. Let us calculate the Lebesgue measure (the total length L) of all of the subranges $\Delta_{Q/P}$ inside a certain range $s_1 < s < s_2$. It can be shown that, in the case at hand, $L < s_2 - s_1$; that is to say, the devil's staircase is incomplete. Moreover, if $\epsilon \longrightarrow 0$, then $L \longrightarrow 0$. In other words, for a randomly chosen wave frequency ω, the probability for the corresponding wavenumber to occur at a step of the devil's staircase is always smaller than unity. On the other hand, inside any wave packet with a nonzero frequency spread, there should exist either one step or an infinite number of steps.

As a result, we can see that the evolution of a wave packet is generally very complicated. Thus, it is clear that the traditional notion of the group velocity is inapplicable to such wave packets, because the dependence $\omega(k)$ is nondifferentiable. It also remains unclear how to describe the dispersive spreading of a wave packet when passing to a smooth waveguide.

The above method of constructing the solution is valid if the spectral parameter s is larger than a certain minimum value. But, as $s \longrightarrow s_0$, the first and second derivatives of $f(z, s)$ with respect to z both vanish at a certain point. For most problems in the theory of nonlinear oscillations, this indicates that the inverse function $f^{(-1)}(z, s)$ is non-single-valued. Hence, we have come to the most interesting point—the onset of stochastic oscillations. However, in the case under discussion, the method of constructing the solution becomes invalid: before the broken line in Fig. 2 comes back to the $x = 0$ axis, it may be reflected from the walls several times, in which case the resulting function is not, strictly speaking, a circle map. For reasons related to this, the situation with $s < s_0$ still remains unclear.

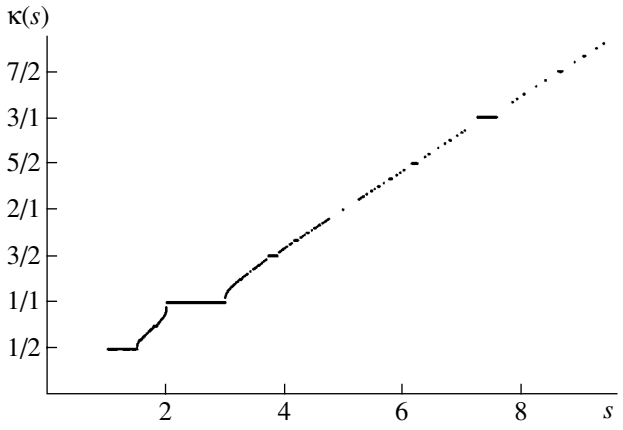

Fig. 6. Dependence $\kappa(s)$ for a $a_0 = 1$ and $s_0 = 1$. Shown are all steps of the devil's staircase that correspond to the rational values of $\kappa = Q/P$ with $Q \le 20$ and $P \le 20$.

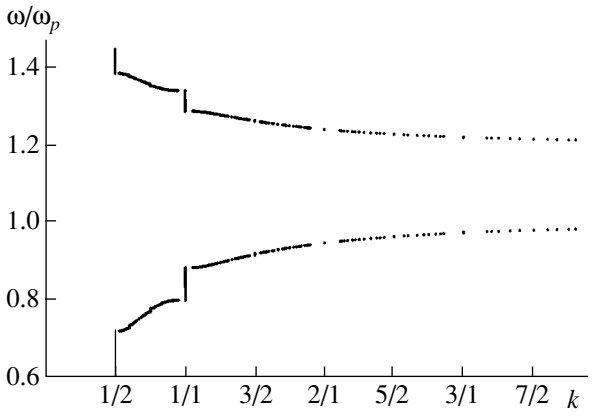

Fig. 7. Spectrum of hybrid waves in a periodic waveguide.

5. AN EXAMPLE

Here, we consider a waveguide with a sawtooth-shaped wall:

$$a(z) = a_0 + s_0|z - n|; \quad |z - n| < \frac{1}{2}, \qquad n = 0, \pm 1, \ldots. \tag{19}$$

For such a waveguide, the function $f(z, s)$ is a piecewise smooth function that can readily be evaluated in explicit form:

$$f(z, s) = \begin{cases} \dfrac{(s + s_0)z + 2a_0}{s - s_0}; & -\dfrac{a_0}{s} < z < -\dfrac{a_0}{s} + \dfrac{s - s_0}{2s} \\ \dfrac{(s - s_0)z + 2a_0}{s + s_0}; & -\dfrac{a_0}{s} - \dfrac{s + s_0}{2s} < z < -\dfrac{a_0}{s}, \end{cases} \tag{20}$$

the periodicity condition being $f(z + 1, s) = f(z, s) + 1$.

Solving Eq. (18) numerically for a certain set of rational numbers Q/P, we can obtain a piecewise-linear function $\sigma_{Q/P}(z)$. An example of this function for $Q/P = 5/6$, $a_0 = 1$, and $s_0 = 1$ is depicted in Fig. 4, which shows, in particular, that the maxima, as well as the minima, of $\sigma_{Q/P}(z)$ are the same in magnitude and that the equation $s = \sigma_{Q/P}(z)$ with respect to z has exactly $2Q$ roots. As was noted earlier, having found these roots, we can determine the coordinate dependence $\psi(z)$. An example of this dependence is displayed in Fig. 5: we can see how the function $\psi(z)$ tends to become a smooth function as Q and P increase.

Taking all rational numbers Q/P with Q and P smaller than a certain large number and determining the maxima and minima of the function $\sigma_{Q/P}(z)$ for each of them, we arrive at a set of steps of the devil's staircase. An example of the devil's staircase $\kappa(s)$ obtained in this way is shown in Fig. 6. The completeness of the staircase is characterized by the ratio of the total length of its steps to the total length of the range of variation of the parameter s; in the case at hand, this ratio is approximately equal to 0.364.

Finally, the entire spectrum of hybrid waves can be constructed from Fig. 6 using relationship (5). A characteristic example of the mode with $m = 0$ and $\lambda = 1$ at $\Omega/\omega_p = 1.2$ is given in Fig. 7.

Of course, the spectral curves constructed above are not dense in the (ω, k) plane. To arrive at a dense spectrum implies the neglect of the spectral classification by the numbers m and λ in formula (9). A dense spectrum can be obtained by constructing the spectral curves for all m values (in analogy with the two curves in Fig. 7), by reducing them to the first Brillouin zone $-\pi < k < \pi$, and by plotting them in the same figure. An approximation to a dense spectrum constructed in this way for $\lambda = 1$ and $m \le 5$ is shown in Fig. 8.

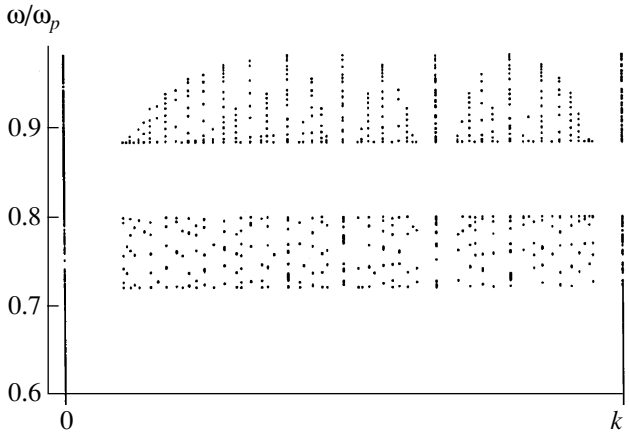

Fig. 8. Formation of a dense spectrum.

6. CONCLUSION

Hence, the main result of the present study is that the spectra of hybrid waves in a periodic waveguide are nowhere differentiable, fractal curves. An analogous result for the TG waves was obtained in my earlier paper [5], where it was shown that, if the wavenumber occurs at one of the steps of the devil's staircase, then it is possible to find explicit solutions to wave equation (1).

On the other hand, Zaginaylov *et al.* [7, 8] solved essentially the same equation (1) by the method of expansion in the waveguide corrugation depth. However, for the same values of the wavenumber, they arrived at solutions that differ from those obtained above; specifically, they obtained stop bands or Bragg gaps in the spectrum. Thus, according to [7, 8], the Bragg gaps should take the place of the vertical lines at $k = \pi$ or $k = \pi/2$ in Fig. 7. It is expedient to discuss the causes of this discrepancy in more detail.

Recall that the solutions constructed above are singular. According to expression (16) or (17), all of the spatial Fourier harmonics have the same amplitude and differ only in phase. Consequently, it seems very likely that the perturbation methods used in [7, 8] do not result in singular solutions. The conclusion that a stop band (or an instability) arises at the intersection of two spectral curves is actually based on the analysis of solutions to a quadratic equation (see, e.g., [14], Section VI). In the system under consideration, every neighborhood of the intersection point of any two spectral curves is crossed by an infinite number of spectral curves, which should also be taken into account. With this circumstance in mind, one cannot expect that it is precisely the stop band that will appear.

In the above analysis, the theory of the circle mapping made it possible to find solutions for a rational normalized wavenumber, $\kappa = Q/P$. Formally, this is enough to say that all possible solutions are found, because irrational numbers, being experimentally nonmeasurable, may be regarded merely as a mathematical abstraction and computer calculations are always carried out with rational numbers. However, the computations based on the above-described algorithm can actually be performed only when the numbers Q and P are not too large (no larger than several thousands). As a result, the relative accuracy of such computations is comparatively low.

On the other hand, the computational scheme used in [7, 8] naturally smoothes out small-scale irregularities and thus makes it possible to efficiently calculate smooth dispersion curves far from resonances with small Q and P numbers. Hence, the approaches developed in the present study and in [7, 8] are not so much contradictory as they are supplementary: solving the problem by different approaches may yield different results, each of which is nevertheless valid.

In conclusion, note that the plasma model adopted here is fairly simple: it does not take into account thermal corrections to the plasma dielectric function. These corrections change Eq. (4), and they are rather difficult to analyze accurately. It may be expected that allowing for thermal corrections will result in some smoothing out of the singular natural waves (the width of the double layers should be on the order of the Debye radius) and of the dispersion curves far from resonances, as well as in an additional damping of oscillations. On the other hand, taking into account the nonpotential character of oscillations is unlikely to change the final results qualitatively.

ACKNOWLEDGMENTS

This work was supported in part by the "Integration" program, project no. A0105-1.

REFERENCES

1. W. R. Lou, Y. Carmel, T. M. Antonsen, *et al.*, Phys. Rev. Lett. **67**, 2481 (1991).
2. B. B. Kadomtsev, *Collective Phenomena in a Plasma* (Nauka, Moscow, 1988).
3. A. Z. Gusakov and A. D. Piliya, Pis'ma Zh. Éksp. Teor. Fiz. **48**, 75 (1988) [JETP Lett. **48**, 75 (1988)].
4. J. M. Ziman, *Principles of the Theory of Solids* (Cambridge Univ. Press, London, 1972; Mir, Moscow, 1974).
5. A. M. Ignatov, Phys. Rev. E **51**, 1391 (1995).
6. M. Quilichini and T. Janssen, Rev. Mod. Phys. **69**, 277 (1997).
7. G. I. Zaginaylov, A. A. Rozhkov, and J.-Y. Raguin, Phys. Rev. E **60**, 7391 (1999).
8. G. I. Zaginaylov, Phys. Rev. E **64**, 016406 (2001).
9. Yu. A. Volkov and V. B. Krasovitskiĭ, Preprint No. 52 (Keldysh Institute of Applied Mathematics, Russian Academy of Sciences, Moscow, 2001).
10. M. A. Lavrent'ev and B. V. Shabat, *Problems in Hydrodynamics and Their Mathematical Models* (Nauka, Moscow, 1977).
11. V. I. Arnol'd, *Supplementary Chapters of the Theory of Ordinary Differential Equations* (Nauka, Moscow, 1978).
12. N. V. Butenin, Yu. I. Neĭmark, and N. A. Fufaev, *Introduction to the Theory of Nonlinear Oscillations* (Nauka, Moscow, 1987).
13. R. de la Llave and N. P. Petrov, Phys. Rev. E **59**, 6637 (1999).
14. E. M. Lifshitz and L. P. Pitaevskiĭ, *Physical Kinetics* (Nauka, Moscow, 1979; Pergamon, Oxford, 1981).

Translated by O. E. Khadin

Plasma Physics Reports, Vol. 28, No. 7, 2002, pp. 580–585. Translated from Fizika Plazmy, Vol. 28, No. 7, 2002, pp. 627–632.

PLASMA DIAGNOSTICS

Theory of Cross-Polarization Scattering at the Upper Hybrid Resonance

E. Z. Gusakov

Ioffe Physicotechnical Institute, Russian Academy of Sciences, Politekhnicheskaya ul. 26, St. Petersburg, 194021 Russia

Received November 29, 2001

Abstract—A study is made of the cross-polarization scattering by magnetic field fluctuations and the resulting conversion of an extraordinary wave into an ordinary wave in the vicinity of the upper hybrid resonance. It is shown that the scattering efficiency increases with decreasing fluctuation wavelength. It is also demonstrated that the accompanying spurious signal from the cross-polarization scattering by density fluctuations is suppressed. © *2002 MAIK "Nauka/Interperiodica".*

1. INTRODUCTION

The development of methods for diagnosing magnetic turbulence in tokamak plasmas is a very important task because this kind of turbulence may play a role in the anomalous energy and particle transport [1]. In most of the modern tokamak experiments, the level of small-scale magnetic field fluctuations is inferred from the lifetime of the runaway electrons; however, the information so derived is averaged over the discharge duration, the cross section of the discharge plasma, and the fluctuation spectrum. On the other hand, the data obtained on the properties of small-scale magnetic turbulence in the plasma core from magnetic measurements by the probes placed in the shadow of a limiter are even less reliable and less direct. Diagnostic methods based on collective scattering of electromagnetic waves are usually efficient in studying plasma turbulence, but they are difficult to apply to magnetic fluctuations because of their relatively low intensity. According to present opinion, the relative level of magnetic fluctuations, $10^{-5} < \delta B/B < 10^{-4}$, is substantially lower than that of density fluctuations, $10^{-3} < \delta n/n < 10^{-2}$, which govern the amplitude of the scattering signal in conventional tokamak experiments. The only possible way to diagnose magnetic fluctuations by a collective scattering technique is that based on the effect of the cross-polarization scattering (CPS) of a probing wave propagating transverse to the external magnetic field [2, 3]. The essence of this method is that plasma density fluctuations in such experiments cause no change in the polarization of the probing wave during the scattering, thereby making it possible in principle to record weaker magnetic fluctuations. However, the implementation of CPS diagnostics runs into serious difficulties associated with the stringent requirements for the transverse propagation of both probing and scattered waves, the mode selectivity of the antenna, and the suppression of a small-angle scattering signal driven by the density fluctuations in the polarization of a probing wave. Thus, if the last requirement is not satisfied because of the imperfect mode selectivity of the receiving antennas, the CPS signal can become indistinguishable from a high-power spurious signal. The method for diagnosing magnetic fluctuations by the CPS technique was already implemented in the TORE SUPRA tokamak, where the receiving antennas were protected by the cutoff surface from the direct action of the extraordinary probing radiation [4].

The level of magnetic fluctuations was for the first time estimated directly in the cited TORE SUPRA experiments, in which the correlation of magnetic turbulence with electron heat transport was also investigated. However, it should be noted that the scheme of CPS experiments adopted in [4] had a number of disadvantages. Thus, the attenuated small-angle scattering signal from the probing extraordinary wave was not completely prevented from reaching the receiving horn after multiple reflections from both the cutoff surface and chamber wall. In addition, the assumption that magnetic fluctuations are localized near the cutoff surface for the probing wave appears questionable, as well as the corresponding estimate of the wave vector of fluctuations.

An alternative scheme for implementing the CPS-based diagnostic method in tokamaks was proposed in recent papers by Bulyiginskiy *et al.* [5, 6]. In this scheme, the plasma is sounded by microwaves under the conditions of electron cyclotron resonance (ECR) for the probing waves within the tokamak chamber. A probing wave with extraordinary polarization is excited in the equatorial plane from the high-field side. When propagating transverse to the external magnetic field, the wave traverses the ECR region, without being subject to a strong absorption in the plasma of the experimental devices ($T_e \le 4$ keV, $R \le 1$ m), and then reaches the upper hybrid resonance (UHR) region,

1063-780X/02/2807-0580$22.00 © 2002 MAIK "Nauka/Interperiodica"

where the projections of its wave vector and its electric field onto the direction of the gradient of the external magnetic field both increase sharply. According to [5, 6], in the UHR region, the probing wave can undergo CPS by short-wavelength fluctuations with a wide wavenumber spectrum ($\omega_{ce}/c < q < \rho_{ce}^{-1}$). The scattered wave is recorded from the low-field side by an antenna that is also placed in the equatorial plane of a tokamak. In this one-dimensional probing scheme, the wave vectors are resolved by either a time-of-flight or a correlation technique [5–7]. An obvious advantage of the proposed scheme is a complete absorption of the probing extraordinary wave and of the waves whose polarization remains unchanged during the scattering after the linear transformation at the UHR. Another advantage is the considerable ECR absorption of a small admixture of an ordinary wave in the probing radiation and of the waves that result from the small-angle scattering of this admixture by density fluctuations. The theoretical analysis carried out below will reveal some other advantages of the proposed scheme.

The paper is organized as follows. In Section 2, the nonlinear current that drives CPS in the vicinity of the UHR is analyzed. It is shown that, in contrast to the accepted views [2, 3, 8], the nonlinearity of the ponderomotive force, $(\mathbf{v}\cdot\nabla)\mathbf{v}$, in the electron cyclotron frequency range is not negligible in comparison with that of the Lorentz force. Moreover, the vicinity of the UHR is dominated by the effects associated with the nonlinearity of the ponderomotive force, so that CPS is more likely to be associated with the fluctuations of the longitudinal current rather than with the magnetic field fluctuations. In Section 3, the CPS signal from the UHR region is calculated using the plane-stratified plasma model under the assumption that the directional patterns of the emitting and receiving antennas are narrow. Expressions are obtained both for the actual signal from the CPS by magnetic fluctuations and (in Section 3) for the spurious CPS signal, which is driven by the density fluctuations and is associated with a deviation of the propagation direction of the probing wave from the direction transverse to the external magnetic field. In the Conclusion, the advantages of the proposed scheme are summarized.

2. NONLINEAR CURRENT

In the MHD approximation [9], the nonlinear current that drives collective scattering has the form

$$\mathbf{j}_s = eN\mathbf{v}_s + en_i\mathbf{v}_\Omega + en_\Omega\mathbf{v}_i. \tag{1}$$

Here, N is the unperturbed electron density; the subscripts s and i refer to the scattered and probing waves, respectively; the subscript Ω stands for low-frequency fluctuations; n_Ω and v_Ω describe low-frequency perturbations of the electron density and electron velocity, respectively; the oscillatory electron velocity in the field E_i of the probing wave is given by the relationship

$$v_{i\alpha} = \frac{\delta\sigma_{\alpha\beta}(\omega_i)E_\beta}{eN}; \tag{2}$$

and $\delta\sigma_{\alpha\beta}(\omega_i)$ are the partial electron conductivities in linear theory.

The electron density perturbed at the frequency of the probing extraordinary wave has the form

$$n_i = N\frac{\mathbf{k}_i\cdot\mathbf{v}_i}{\omega_i}, \tag{3}$$

where $\mathbf{k}_i$ is the wave vector of the probing wave. In the MHD approximation, the electron velocity perturbation at the frequency of the scattered wave is given by relationship (2) with the subscript i replaced by s and the field E_β replaced by $\bar{E}_\beta$, which is the effective electric field describing the effect of the nonlinear components of the ponderomotive and Lorentz forces on the electron motion:

$$\bar{E}_\beta = -i\frac{m_e}{e}[(\mathbf{v}_\Omega\cdot\mathbf{k}_i)\mathbf{v}_i + (\mathbf{v}_i\cdot\mathbf{k}_\Omega)\mathbf{v}_\Omega]_\beta + \frac{1}{c}[\mathbf{v}_i\times\mathbf{B}_\Omega + \mathbf{v}_\Omega\times\mathbf{B}_i]_\beta + E_{s\beta}. \tag{4}$$

Using relationships (1)–(4), we can readily obtain an expression for the projection of the nonlinear current onto the direction of the external magnetic field—in other words, for the nonlinear current component that leads to CPS when the probing and scattered waves propagate strictly transverse to the external magnetic field:

$$j_{sz} = \frac{eN}{\omega_i}(\mathbf{k}_i + \mathbf{k}_\Omega)\cdot\mathbf{v}_i v_{\Omega z} + \frac{i\omega_{pe}^2}{4\pi\omega_s}\frac{v_{ix}B_{\Omega y} - v_{iy}B_{\Omega x}}{c}. \tag{5}$$

This expression shows that CPS can be associated not merely with the magnetic fluctuations but also with the fluctuations of the longitudinal electron velocity.

In contrast to the assertions made in [2, 3, 8], the contribution of longitudinal velocity fluctuations is not negligible, which can be easily verified by using Ampére's law for low-frequency fluctuations. In fact, neglecting the displacement current, we have $\mathbf{v}_\Omega = \frac{c}{4\pi eN}\mathbf{k}_\Omega\times\mathbf{B}_\Omega$. Using this expression and the Bragg relationship $\mathbf{k}_s = \mathbf{k}_i + \mathbf{k}_\Omega$, we can readily obtain the relationship

$$j_{sz} = i\frac{\mathbf{k}_s\mathbf{v}_i}{\omega_s}\frac{c}{4\pi}[\mathbf{k}_\Omega\times\mathbf{B}_\Omega]_z + \frac{i\omega_{pe}^2}{4\pi\omega_i}\frac{[\mathbf{v}_i\times\mathbf{B}_\Omega]_z}{c}, \tag{6}$$

which shows that the only contribution of the longitudinal velocity fluctuations that can be neglected is the contribution of long-wavelength fluctuations such that $k_\Omega c/\omega_{pe} < \omega_{pe}/\omega_i$. Note that relationship (4) fails to hold

for the experimental conditions of [4] and even more so for the scattering at the UHR, which can only be driven by fluctuations satisfying the condition $k_\Omega c/\omega_i \gg 1$. In the latter case, the inequality $k_\Omega c/\omega_{pe} \gg \omega_{pe}/\omega_i$ is satisfied by a large margin, so that the nonlinear current is dominated by the ponderomotive force.

It should be stressed that the MHD expressions (5) and (6) for the nonlinear current are, strictly speaking, valid only when all of the three interacting waves are fast; i.e., when they satisfy the conditions $k_{\|\alpha} v_{Te}/\omega_\alpha \ll 1$, $k_{\perp\alpha} v_{Te}/\omega_{ce} \ll 1$, and $k_{\|\alpha} v_{Te}/(\omega_\alpha \pm \omega_{ce}) \ll 1$. On the other hand, as was shown in a recent paper by Bindslev [10], MHD expressions that are closely analogous to those presented in this section are also valid when only two of the three interacting waves, specifically, the probing and scattered waves, are fast. It is this situation that usually holds in experiments on collective scattering.

3. CALCULATION OF A CPS SIGNAL FROM THE UHR REGION

According to the reciprocity theorem [11], the CPS signal with ordinary polarization that is recorded by the receiving antenna placed on the low-field side can be expressed as

$$A_{cps} = \frac{1}{4}\int \mathbf{j}_s \mathbf{E}_s^+ d^3 r, \tag{7}$$

where the nonlinear current j_s is given by relationship (1) and E_s^+ is the field distribution of the receiving antenna, which operates as an emitting antenna in a reversed constant external magnetic field. The field E_s^+ is normalized in such a way that the incident power is equal to unity, and the CPS signal is normalized so that $\langle A_s(\omega_s) A_s^*(\omega_s')\rangle = 2\pi P_s(\omega_s)\delta(\omega_s - \omega_s')$.

In the plane-stratified plasma model, the expression for the field E_s^+ of the receiving antenna can be written in the geometrical-optics approximation, which adequately describes the behavior of the refractive index of the plasma along the ray trajectory in the case of probing in the equatorial plane. In the paraxial approximation, the main component of the electric field of an ordinary wave has the form

$$E_{sz}^+ = \sqrt{\frac{\omega_s}{ck_0}}\int \frac{dk_{sy}dk_{sz}}{(2\pi)^2} \times \exp\left\{ i\int_{R_0+a}^{R}\left[-k_0 + \left(\frac{c}{\omega}\right)^2 (k_{sy}^2\kappa_{0y} + k_{sz}^2\kappa_{0z})\right]dR' + i(k_{sy}y + k_{sz}z)\right\} f(k_{sy}, k_{sz}), \tag{8}$$

where $k_0 = (\omega_s/c)\sqrt{1 - \omega_{pe}^2(R)/\omega_s^2}$, the x coordinate is directed along the tokamak major radius, y is a poloidal coordinate, $R = R_0 + a$ is the radial position of the receiving antenna, $\kappa_{0y} = \omega_i^2/2k_0c^2$ and $\kappa_{0z} = k_0/2$. The beams of radiation from the emitting and receiving antennas are both assumed to be Gaussian near the horn; this assumption corresponds to the directional pattern $f(k_y, k_z) = 4\pi\rho\exp[-\rho^2(k_y^2 + k_z^2)/4]$.

Expression (8) is written in the plane-stratified plasma model, which implies that k_{sy} is constant along the tokamak major radius. This model is well suited for describing the wave propagation in a vertically elongated plasma and can be generalized to a plasma with a circular cross section by introducing the quantity $\kappa_{0y} = (\omega_s a)^2/2k_0(cr)^2$, which takes into account the relationship $k_y \sim 1/r$. In order to calculate the nonlinear current, it is necessary to know the field of an extraordinary wave in the vicinity of the UHR. According to [12], this field is described by the following expressions:

$$E_{ix}^+ = \int \frac{dk_{iy}dk_{iz}}{(2\pi)^2} D(k_{iy}, k_{iz})\int_0^\infty \exp\{i\Psi(t,\xi)\}dt, \tag{9a}$$

$$E_{iy}^+ = \int \frac{dk_{iy}dk_{iz}}{(2\pi)^2}\frac{D(k_{iy}, k_{iz})}{lk_c^2} \times \int_0^\infty \left[k_{iy} - i\left|\frac{\omega}{\omega_{ce}}\right|\frac{1}{tl}\right]\exp\{i\Psi(t,\xi)\}dt, \tag{9b}$$

$$E_{iz}^+ = \int \frac{dk_{iy}dk_{iz}}{(2\pi)^2}\frac{k_{iz}D(k_{iy}, k_{iz})}{lk_c^2}\int_0^\infty \exp\{i\Psi(t,\xi)\}\frac{dt}{t}, \tag{9c}$$

where $\Psi(t,\xi) = \frac{\kappa t^3}{3} - \frac{1}{t} + \xi t$, $\xi = (R - R_{UH} + i\varepsilon^{im} l) l k_c^2$ is the dimensionless coordinate, $l = (\partial\varepsilon/\partial R)^{-1}_{R = R_{UH}}$, $\varepsilon = 1 - \omega_{pe}^2/(\omega^2 - \omega_{ce}^2) + i\varepsilon''$, $k_c = \omega_{ce}(R_{UH})/c$, $\kappa = l^4 l_T^2 k_c^6$, and $l_T^2 = 3v_{Te}^2/(3\omega_{ce}^2 - \omega_{pe}^2)$. The factor $D(k_{iy}, k_{iz})$ is determined by the directional pattern of the emitting antenna and the wave propagation far from the UHR. The assumption that the plasma is homogeneous only along the major radius (which provides an adequate description of the propagation of an extraordinary wave in the equatorial plane of a tokamak) allows us to calculate this factor in explicit form:

$$D = \frac{(lk_c)^{3/2}}{\sqrt{\pi}}\sqrt{\frac{|\omega_{ce}|}{\omega}}P_i \times \exp\{i[\phi_e + k_{iy}y + k_{iz}z - 3\pi/4]\} f(k_{iy}, k_{iz}), \tag{10}$$

where $\phi_e = \int_{R_0-a}^{R_{UH}} \left[k_e - \left(\frac{c}{\omega}\right)^2 (k_{iy}^2 \kappa_{ey} + k_{iz}^2 \kappa_{ez}) \right] dR'$, $k_e = \sqrt{\frac{\varepsilon^2 - g^2}{\varepsilon}} \frac{\omega_i}{c}$ is the wave vector of a transversely propagating extraordinary wave, $g = \frac{|\omega_{ce}|}{\omega_i} \frac{\omega_{pe}^2}{\omega_i^2 - \omega_{ce}^2}$, $\kappa_{ey} = \omega_i^2 / 2k_e c^2$, $\kappa_{ez} = \left[1 + \frac{\omega_i^2 - \omega_{pe}^2}{2(\varepsilon^2 - g^2)} \frac{\omega_{ce}^2 \omega_{pe}^2}{(\omega_i^2 - \omega_{ce}^2)\omega_i^4} \frac{ck_e}{\omega_i} \right] \frac{\omega_i}{c}$, $R_0 - a$ is the position of the emitting horn, and P_i is the power of the probing wave.

Substituting expression (8) for the field of the receiving antenna and expression (6) for the nonlinear current into representation (7) for the scattered signal and using expression (2) for the oscillatory electron velocity and expressions (9) and (10) for the field of the probing wave, we can integrate over the spatial coordinates and thus obtain the spectral density of the scattered signal as a function of the spectrum of magnetic fluctuations:

$$P_{S\Omega} = \frac{\omega_{ce}^4}{\omega_{pe}^4} \frac{\pi \ell k_c P_i e^{-\tau}}{\sqrt{[1 + 4(X_{ey} - X_{0y})^2][1 + 4(X_{ez} - X_{0z})^2]}} \times \int \frac{d^3\mathbf{q}}{(2\pi)^3} S_1(\mathbf{q}) \exp\left\{ -2\varepsilon''(q_x - k_c)\ell - \frac{q_y^2 \rho^2}{4} \frac{1 + 8[(X_{0y})^2 + (X_{ey})^2]}{1 + 4[X_{ey} - X_{0y}]^2} - \frac{q_z^2 \rho^2}{4} \frac{1 + 8[(X_{0z})^2 + (X_{ez})^2]}{1 + 4[X_{ez} - X_{0z}]^2} \right\}, \quad (11)$$

with

$$S_1(\mathbf{q}) = |b_{y\mathbf{q},\Omega}|^2 \left(\frac{q_x}{k_c} - \frac{\omega_{pe}^2}{k_c^2 c^2} \right)^2 + |b_{x\mathbf{q},\Omega}|^2 \frac{\omega_{pe}^4}{\omega_{ce}^2 \omega_i^2}. \quad (12)$$

In formula (11), the magnetic fluctuations responsible for CPS are expanded in a Fourier integral,

$$\frac{\mathbf{B}_\Omega}{B_0} = \int \frac{d^3\mathbf{q}}{(2\pi)^3} \mathbf{b}_{\mathbf{q},\Omega} e^{-i\mathbf{qr}}, \quad (13)$$

under the assumption that they are statistically uniform and steady, $\langle \mathbf{b}_{\mathbf{q}\Omega} \cdot \mathbf{b}^*_{\mathbf{q}'\Omega'} \rangle = |\mathbf{b}_{\mathbf{q}\Omega}|^2 (2\pi)^4 \delta(\mathbf{q} - \mathbf{q}') \delta(\Omega - \Omega')$. Also, in formula (11), the following notation is introduced: τ is the optical thickness of the ECR layer for an extraordinary wave, $X_{0\alpha} = \left(\frac{c}{\omega_s \rho}\right)^2 \int_{R_0+a}^{R_{UH}} \kappa_{0\alpha} dR'$ and $X_{e\alpha} = \left(\frac{c}{\omega_i \rho}\right)^2 \int_{R_0-a}^{R_{UH}} \kappa_{e\alpha} dR'$.

An important feature of expression (11) for the spectral density of the CPS signal in the UHR region is that it contains the factor $(q_x/k_c)^2$, which accounts for the contribution of the short-wavelength fluctuations ($q_x \gg k_c$) to the scattering process and is associated with the contribution of the fluctuations of the longitudinal electron velocity to the nonlinear current. It is this factor that facilitates the observation of short-wavelength magnetic fluctuations and, in particular, electron-temperature-gradient (ETG) driven modes.

Note that, when deriving representation (11), the contribution of the density fluctuations to the CPS signal was neglected. This simplifying assumption is valid for a probing wave propagating strictly transverse to the external magnetic field, but it has yet to be justified for the case of an obliquely propagating probing wave. Since obliquely propagating waves are always present in the actual directional pattern of an emitting antenna, it is necessary to estimate the contribution of their scattering by density fluctuations to the total CPS signal. The CPS by density fluctuations is driven by the nonlinear current component $\mathbf{j}_s = en_\Omega \mathbf{v}_i$. The CPS signal associated with this component can be calculated from relationship (7) even with allowance for the contribution of the field components E_{iz}, E_{sx}, and E_{sy}, which are given by expressions (9c) and (14) and are small for the case of nearly transverse propagation:

$$E_{sx}^+ = \frac{ck_{sz}\omega_{ce}}{\omega^2} E_{sz}^+, \quad E_{sy}^+ = -i\frac{ck_{sz}}{\omega} E_{sz}^+. \quad (14)$$

As a result, we obtain that the spectral density of the CPS signal driven by the plasma density fluctuations is described by expression (11), in which the function $S_1(\mathbf{q})$ is replaced with

$$S_2(\mathbf{q}) = \frac{\omega_{pe}^8}{\omega_{ce}^6 \omega_i^2} |\delta n_{\mathbf{q},\Omega}|^2 \left| \left[\frac{\tilde{k}_{iz}}{q_x - k_c} - \frac{(q_z - \tilde{k}_{iz})k_c}{(q_x - k_c)^2} \right] \right|^2, \quad (15)$$

where the notation $\tilde{k}_{iz} = \frac{q_z}{2} \frac{1 + 4iX_{0z}}{1 + 2i[X_{ez} + X_{0z}]}$ is introduced and it is assumed that $\langle n_{\mathbf{q}\Omega} n^*_{\mathbf{q}_\Omega} / N^2 \rangle = (2\pi)^4 |\delta n_{\mathbf{q}\Omega}|^2 \delta(\Omega - \Omega') \delta(\mathbf{q} - \mathbf{q}')$.

Note that, although the level of density fluctuations in a tokamak discharge is relatively high, the signal of the CPS driven by them in the UHR region is suppressed to a significant extent. This suppression is described by both the factor $\omega_{pe}^8 / \omega_{ce}^8$ (which is small for conventional tokamaks) and the factor $[q_z/(q_x - k_c)]^2$

(which is extremely small for the drift turbulence). The latter factor can be estimated from the expression $q_x = m/R(n/m - \mu)$, where m and n are the poloidal and toroidal mode numbers, and μ is the reciprocal of the safety factor. To do this, it is necessary to take into account the fact that the characteristic width of the region where the drift mode is localized in the vicinity of the resonant magnetic surface is on the order of the ion gyroradius ρ_{ci}. In this way, one can readily obtain the relationship $\frac{q_z}{q_x} = \frac{a}{R}\frac{\omega}{cq_x}\frac{\rho_{ci}}{r_s}\mu$, in which the shear length $r_s = |\mu/\mu'|^{-1}$ is introduced and the fact that the CPS diagnostics makes it possible to observe fluctuations with the poloidal numbers $m \le a/\rho$ is taken into account. We can see that the parameter q_z/q_x is represented as the product of four factors, each of which is either smaller or much smaller than unity, thereby explaining a substantial suppression of the signal from the CPS driven by the density fluctuations in the UHR region. Note that such a significant suppression occurs only when the directional patterns of the antennas are symmetric with respect to the direction of the external magnetic field. In the case of asymmetric directional patterns characterized by the mean wavenumber $\bar{k}_{iz} \gg q_z$, the factor $[q_z/(q_x - k_0)]^2$ in expression (15) should be replaced with the factor $[\bar{k}_{iz}/(q_x - k_0)]^2$, which also leads to the suppression of the spurious signal of the CPS associated with density fluctuations. The smaller the radial scale of the fluctuations (i.e., the smaller the deviation of the propagation direction of the probing wave from the direction transverse to the external magnetic field in the UHR region), the more significant the suppression. This effect is associated with an increasingly small deviation of the propagation direction of the probing wave from the direction transverse to the external magnetic field in the UHR region.

Recall that, in the plane-stratified plasma model, the poloidal asymmetry of the directional patterns of antennas does not enhance the spurious CPS signal. This is, however, not the case for a true toroidal geometry. The reason is that, in a nonuniform tokamak magnetic field, the UHR surface is not a magnetic surface, so that the projection of the increasing wave vector component perpendicular to the UHR surface onto the poloidal direction may be finite and even large.

In this case, the projection of the wave vector onto the magnetic field direction is described by the expression $q_z = 4\alpha\frac{\omega_{ce}^2}{\omega_{pe}^2}\frac{L_n}{R}\frac{c\bar{k}_y}{\omega}\frac{H_\theta}{H_\phi}q_x$. Here, L_n is the scale on which the plasma density varies; $\bar{k}_y$ is the mean poloidal wavenumber of the directional pattern of an antenna; α is a factor of order unity, which is determined by the propagation of a probing wave far from the UHR; and H_θ and H_ϕ are, respectively, the poloidal and toroidal components of the magnetic field. Note that, in this situation, the attenuation coefficient for the spurious CPS signal is also much smaller than unity.

It should be emphasized that, although the above expressions for the CPS signal were derived for the scattering process in which an extraordinary wave is converted into an ordinary wave, the symmetry of the nonlinear matrix elements and of the overall pattern of the propagation of waves also makes it possible to use expression (11) to describe the opposite CPS process, in which an ordinary wave excited from the low-field side is converted into an extraordinary wave.

4. CONCLUSION

In conclusion, let us summarize the advantages of the proposed scheme for diagnosing magnetic fluctuations by the CPS technique:

(i) Localization of the signal from the CPS driven by short-wavelength fluctuations in the UHR region.

(ii) Possibility of investigating a wide wavenumber spectrum of fluctuations by a simple one-dimensional probing technique.

(iii) Resolution of the wave vectors by a time-of-flight or a correlation technique [5–7].

(iv) Increasing the CPS efficiency due to the contribution of the fluctuations of the longitudinal electron velocity in the UHR region.

(v) Suppression of the signal from the CPS by density fluctuations in the UHR region because of the strictly transverse propagation of a probing wave near the UHR.

(vi) Absorption of the small-angle scattering radiation with extraordinary polarization in the UHR region.

(vii) ECR absorption of an admixture of an ordinary wave in the probing radiation and of the waves that result from the small-angle scattering of this admixture by density fluctuations.

ACKNOWLEDGMENTS

This work was supported in part by the Russian Foundation for Basic Research (project nos. 01-02-17926 and 00-15-96762), INTAS (grant no. 97-11018), and the Netherlands Organization for Scientific Research (project no. NWO-047.009.009).

REFERENCES

1. A. B. Rechester and M. N. Rosenbluth, Phys. Rev. Lett. **40**, 38 (1978).
2. T. Lehner, D. Gresillon, X. L. Zou, *et al.*, in *Proceedings of the 12th EPS Conference on Controlled Fusion and Plasma Physics, Budapest, 1985*, ECA, Vol. 9F, p. 664.
3. T. Lehner, J. M. Rax, and X. L. Zou, Europhys. Lett. **8**, 759 (1989).

4. X. L. Zou, M. Paume, J. M. Chareau, *et al.*, in *Proceedings of the 20th European Conference on Controlled Fusion and Plasma Physics, Lisbon, 1993*, ECA, Vol. 17C, Part III, p. 1091.
5. D. G. Bulyiginskiy, A. D. Gurchenko, E. Z. Gusakov, *et al.*, in *Proceedings of the 25th EPS Conference on Controlled Fusion and Plasma Physics, Prague, 1998*, ECA, Vol. 22C, p. 1546.
6. D. G. Bulyiginskiy, A. D. Gurchenko, E. Z. Gusakov, *et al.*, Phys. Plasmas **8**, 2224 (2001).
7. A. D. Gurchenko, E. Z. Gusakov, M. M. Larionov, *et al.*, in *Proceedings of the 27th EPS Conference on Controlled Fusion and Plasma Physics, Budapest, 2000*, ECA, Vol. 24B, p. 416.
8. L. Vahala, G. Vahala, and N. Bretz, Phys. Fluids B **4**, 619 (1992).
9. A. G. Sitenko, *Fluctuations and Nonlinear Wave Interactions in Plasmas* (Academic, New York, 1982).
10. H. Bindslev, Plasma Phys. Controlled Fusion **37**, 169 (1995).
11. K. M. Novik and A. D. Piliya, Plasma Phys. Controlled Fusion **36**, 357 (1994).
12. B. Bruesehaber, E. Z. Gusakov, M. Kraemer, and A. D. Piliya, Plasma Phys. Controlled Fusion **36**, 997 (1994).

Translated by O. E. Khadin

Plasma Physics Reports, Vol. 28, No. 7, 2002, pp. 586–591. Translated from Fizika Plazmy, Vol. 28, No. 7, 2002, pp. 633–638.

IONOSPHERIC PLASMA

Nonlinear Planetary Electromagnetic Vortex Structures in the Ionospheric F-Layer

G. D. Aburjaniya, A. G. Khantadze, and O. A. Kharshiladze

Dzhavakhishvili State University of Tbilisi, pr. Chavchavadze 3, Tbilisi, 380028 Georgia

Received October 17, 2001; in final form, December 4, 2001

Abstract—A study is made of the dynamics of planetary-scale electromagnetic waves in the F-layer of the ionosphere. It is shown that, in this layer, a new branch of large-scale magneto-ionospheric wave perturbations is generated under the action of the latitudinal variations of the geomagnetic field, which are a constant property of the ionosphere. The waves propagate along the parallels with phase velocities of tens to hundreds of km/s. The pulsations of the geomagnetic field in the waves can be as strong as several tens of nT. A possible self-localization effect is revealed: these waves may form nonlinear localized solitary vortices moving either westward or eastward along the parallels with velocities much higher than the phase velocities of the linear waves. The characteristic dimension of a vortex is about 10^4 km or even larger. The magnetic fields generated by vortex structures are one order of magnitude stronger than those in linear waves. The vortices are long-lived formations and may be regarded as elements of strong structural turbulence in the ionosphere. The properties of the wave structures under investigation are very similar to those of ultralow-frequency perturbations observed experimentally in the ionosphere at middle latitudes. © *2002 MAIK "Nauka/Interperiodica".*

1. INTRODUCTION

Large-scale wave structures play an important role in the energy balance and in circulations of the atmosphere and oceans. Numerous observations show that planetary-scale perturbations of an electromagnetic nature are always present in the ionosphere in the form of background wave perturbations [1–4]. Of particular interest among these perturbations are so-called large-scale ionospheric perturbations propagating around the Earth along the parallel at a fixed latitude [4]. They are especially pronounced during geomagnetic storms and substorms [5], earthquakes [6, 7], major artificial explosions, military operations [8, 9], etc. Observations also revealed so-called magneto-ionospheric wave perturbations (MIWP) propagating in the F-layer along the parallels at middle latitudes [4, 6]. The amplitudes of the geomagnetic pulsations in such waves may vary from a few to several tens of nT.

In planetary atmospheres, the wave perturbations are actually generated in the tropo- and stratosphere and can hardly penetrate to the ionospheric F-layer because of the strong screening effect of stable zonal winds in the ionosphere (especially in summer) [10]. That is why MIWP should be excited just inside the ionospheric F-layer. One of us [11] showed, first, that a possible mechanism for generating MIWP may be associated with the latitudinal variations of the geomagnetic field (a permanent fundamental factor in planetary-scale processes in the ionosphere) and, second, that MIWP generated by this mechanism are a new branch of natural oscillations in the F-layer.

In nature, these perturbations manifest themselves as background oscillations. Observations show that forced oscillations of this type occur in the ionosphere under the pulsed action from above (geomagnetic storms [5]) or from below (earthquakes, volcanic eruptions, and major artificial explosions [4, 6, 8, 12]). In the latter case, the perturbations exist in the form of localized solitary wave structures.

In this paper, we continue a theoretical investigation of the properties of MIWP. We demonstrate the possibility of a self-localization effect: these wave perturbations may form nonlinear localized solitary vortices in the ionosphere.

2. FORMULATION OF THE PROBLEM AND BASIC EQUATIONS

When studying the dynamics of large-scale ($L \sim 10^4$ km) waves in the F-layer of the ionosphere, it is necessary to take into account the fact that the Hall conductivity depends on the sign of the charge; i.e., the electron and ion contributions to the Hall conductivity have opposite signs. Calculations show that, at altitudes above about 150 km, these contributions cancel one another, so that the Hall conductivity vanishes. Since large-scale waves are damped by turbulent and molecular viscosities only slightly, the Reynolds number for such wave motions is high [13]. For planetary-scale perturbations in the F-layer, the magnetic Reynolds number $R_{em} = \omega L^2/\nu_\perp$ (where $\nu_\perp = c^2/(4\pi\sigma_\perp)$, ω is the characteristic perturbation frequency, $\sigma_\perp$ is the transverse conductivity, and L is the characteristic perturba-

1063-780X/02/2807-0586$22.00 © 2002 MAIK "Nauka/Interperiodica"

tion scale length) is about 10^2, so that, in a first approximation, the damping by ions can also be neglected. This is justified by the observations [4, 10]: in the F-layer, planetary-scale electromagnetic waves propagate over very large distances without being significantly damped. Additionally, the dimensionless Maxwell's equation $R_{\mathrm{em}}\bar{\mathbf{J}} = \bar{\nabla} \times \bar{\mathbf{h}}$ (where the superior bar indicates the dimensionless character of the quantities and of the operator) implies that, even when the current **J** in the ionosphere is low, the magnetic field **h** induced by it should play an important role in planetary-scale processes. In this case, the problem of the dynamics of large-scale low-frequency electromagnetic perturbations in the ionosphere is solved in the so-called induction approximation ($R_{\mathrm{em}} \gg 1$) on the basis of the MHD equations for the ionosphere. In the case $R_{\mathrm{em}} \ll 1$, no waves of electromagnetic nature can exist [13, 14]. In this approximation, the magnetic field is assumed to be prescribed and is set equal to the external geomagnetic field $\mathbf{H}_0$, whose effect on the motions in the ionospheric F-layer reduces to the inductive damping of Rossby waves [13, 15, 16] (however, as was noted in the Introduction, these waves can hardly reach the F-layer).

With the above analysis in mind, we consider the problem in the induction approximation ($R_{\mathrm{em}} \gg 1$), which *a priori* implies the existence of electromagnetic waves, and investigate the possible generation of planetary-scale electromagnetic wave structures in the F-layer by such permanent factors as the latitudinal gradients of the geomagnetic field and of the angular velocity of the Earth's rotation. Taking into account the fact that large-scale flows do not seriously perturb the particle densities [13, 17], we can exclude acoustic-gravitational waves from consideration and use the MHD equations and the generalized Ohm's law to obtain the following set of equations:

$$\frac{\partial \mathbf{\Omega}}{\partial t} - \nabla \times (\mathbf{V} \times (\mathbf{\Omega} + 2\mathbf{\Omega}_0)) - \frac{1}{4\pi\rho}\nabla \times ((\nabla \times \mathbf{H}) \times \mathbf{H}) = 0, \tag{1}$$

$$\frac{\partial \mathbf{H}}{\partial t} + (\mathbf{V} \cdot \nabla)\mathbf{H} - (\mathbf{H} \cdot \nabla)\mathbf{V} = 0, \quad \nabla \cdot \mathbf{V} = 0, \quad \nabla \cdot \mathbf{H} = 0. \tag{2}$$

Here, $\mathbf{\Omega} = \nabla \times \mathbf{V}$, $\mathbf{\Omega}_0(0, \Omega_0 \sin\theta, \Omega_0 \cos\theta)$ is the vector of the angular velocity of the Earth's rotation; θ is the colatitude, i.e., the complement of the latitude φ' ($\theta = \pi/2 - \varphi'$); $\mathbf{H} = \mathbf{H}_0 + \mathbf{h}$, $\mathbf{H}_0$ is the geomagnetic field strength; **h** is the induced magnetic field; **V** is the vector of the perturbed hydrodynamic velocity; $\rho = MN_n$ is the density of neutrals; N_n is their concentration; and M is the mass of a neutral (and an ion).

Equation (2) implies that, in the F-layer, the total magnetic field **H** is frozen in the ionospheric plasma. According to the experimental data [18, 13], at altitudes of about 200 km in the F-layer, the ratio of the characteristic vertical velocity v_v to the horizontal velocity v_h is small, $v_v/v_h \le L_v/L_h < 10^{-2}$, where L_v and L_h are, respectively, the vertical and horizontal scales of the perturbation. Hence, large-scale motions in the F-layer are nearly horizontal.

That is why we restrict ourselves to investigating a horizontal incompressible flow in the β-plane approximation [17], using a standard coordinate system in which the x-axis is directed eastward along the parallel, the y-axis is directed northward along the meridian, and the vertical z-axis is directed outward from the Earth's surface. We assume that the vertical velocity component is zero, $V_z = 0$, and that $V_{x,y} = V_{x,y}(x, y, t)$. For simplicity, we also assume that the geomagnetic field has only the vertical component (i.e., we consider middle and temperate latitudes), $H_{0z} = -H_p \cos\theta$, where $H_p = 5 \times 10^{-5}$ T is the geomagnetic field strength at the pole. In the linear approximation, the horizontal component of the field $\mathbf{H}_0$ was taken into account in [11]. From a dynamic point of view, the motions in question are affected primarily by the angular velocity component that is perpendicular to the Earth's surface, $\Omega_{0z} = \Omega_0 \cos\theta$. We thus take into account the latitude variations of both the geomagnetic field and the angular velocity of the Earth's rotation. In what follows, we will be interested only in the perturbation $h_z(x, y, t)$ of the geomagnetic field H_{0z}, in which case the quantities $(\mathbf{H}_0 \cdot \nabla)\mathbf{V}$ and $(2\mathbf{\Omega} \cdot \nabla)\mathbf{V}$ vanish identically and Alfvén, magnetoacoustic, and inertial waves as well as helicons are all excluded from consideration. We introduce the stream function ψ through the relationship $\mathbf{V} = \nabla\psi \times \mathbf{e}_z$ (where $\mathbf{e}_z$ is the unit vector along the vertical axis) and write Eqs. (1) and (2) in the form

$$\frac{\partial \Delta\psi}{\partial t} + \beta\frac{\partial \psi}{\partial x} + C_H\frac{\partial h}{\partial x} = J(\psi, \Delta\psi), \tag{3}$$

$$\frac{\partial h}{\partial t} - \beta_H\frac{\partial \psi}{\partial x} = J(\psi, h). \tag{4}$$

Here, R is the Earth's radius; θ_0 is a certain mean colatitude, in the vicinity of which we are considering the motions in the medium; N is the density of the charged particles; c is the speed of light; e is the elementary charge; and the following notation is introduced:

$$\beta = \frac{\partial 2\Omega_{0z}}{\partial y} = -\frac{1}{R}\frac{\partial}{\partial\theta}(2\Omega_{0z}) = \frac{2\Omega_0 \sin\theta_0}{R},$$

$$C_H = \frac{c}{4\pi eN}\frac{\partial H_{0z}}{\partial y} = -\frac{cH_p}{4\pi eNR}\sin\theta_0 < 0,$$

$$h = \frac{eN}{N_n Mc}h_z, \quad \beta_H = \frac{eN}{\rho c}\frac{\partial H_{0z}}{\partial y} = -\frac{N}{N_n}\frac{eH_p}{MRc}\sin\theta_0 < 0, \tag{5}$$

$$\Delta = \frac{\partial^2}{\partial x^2} + \frac{\partial^2}{\partial y^2}, \quad J(a, b) = \frac{\partial a}{\partial x}\frac{\partial b}{\partial y} - \frac{\partial a}{\partial y}\frac{\partial b}{\partial x}.$$

When writing Eqs. (3) and (4), we also neglected the difference between the geographic and geomagnetic latitudes.

From these equations, we obtain the conservation laws for the energy E,

$$\frac{\partial E}{\partial t} = 0, \quad E = \frac{1}{2}\int\left[(\nabla\psi)^2 + \frac{h^2}{k_0^2}\right]dxdy \qquad (6)$$

and for the potential enstrophy K,

$$\frac{\partial K}{\partial t} = 0, \quad K = \frac{1}{2}\int\left[(\Delta\psi)^2 + \frac{(\nabla h)^2}{k_0^2}\right]dxdy. \qquad (7)$$

Here, $k_0^2 = N\omega_{pi}^2/(N_n c^2)$, $\omega_{pi}^2 = 4\pi e^2 N/M$, and ∇ is the two-dimensional nabla operator in the horizontal plane. The energy of the wave perturbation under consideration is the sum of the hydrodynamic (kinetic) energy and the electromagnetic energy.

3. PLANETARY-SCALE WAVE STRUCTURES

Here, we investigate Eqs. (3) and (4). We start by analyzing the linear stage, i.e., the case of small-amplitude motions. We seek a solution in the form of a plane wave $\psi, h \sim \exp\{i(\mathbf{k}\cdot\mathbf{r} - \omega t)\}$ (where $\mathbf{k}$ is the wave vector and ω is the perturbation frequency) and assume that $k \gg k_0$ (the wavelength corresponding to k_0 is much larger than the Earth's radius $\lambda_0 = 2\pi/k_0 \sim 10^3 R$). From Eqs. (3) and (4), we obtain the dispersion relation

$$\omega^2 - \omega_p\omega - \omega_n^2 = 0, \qquad (8)$$

where

$$\omega_p = -\frac{k_x}{k^2}\beta \ll \omega_n,$$

$$\omega_n^2 = \frac{k_x^2}{k^2}\beta_H C_H = \frac{k_x^2}{k^2}\frac{1}{4\pi M N_n}\left(\frac{\partial H_{0z}}{\partial y}\right)^2.$$

In the absence of planetary-scale Rossby waves in the ionospheric F-layer (i.e., when $\beta = 0$, $\omega_p = 0$, and the penetration of Rossby waves to the ionosphere is hindered by the screening effect of stable zonal winds), the dispersion relation (8) yields the eigenfrequency

$$\omega = \omega_n = \pm\frac{k_x}{kR}\frac{H_p\sin\theta_0}{\sqrt{4\pi M N_n}}. \qquad (9)$$

We can see that, in contrast to the one-dimensional case analyzed in [11], a two-dimensional wave with the eigenfrequency ω_n has dispersion. In the F-layer, this wave can propagate either westward or eastward along the parallels. According to expression (8), the presence of a Rossby wave such that $V_{ph}^2 = C_n^2/(1 - \omega_p/\omega)$ (where $V_{ph} = \omega/k$ and $C_n = \omega_n/k$) produces an additional dispersion of the wave with the eigenfrequency ω_n.

Since, at altitudes from 150 to 500 km, the density N_n of neutral particles decreases substantially with increasing altitude (from 3.8×10^{16} to 2.2×10^{12} m^{-3} [13]), the eigenfrequency ω_n of the zonal oscillations changes over a wide range. The eigenfrequency ω_n is a new (eighth) eigenfrequency for the ionospheric F-layer [11] (the closed set of MHD equations for the ionosphere is eight-order in time [13]).

The physical mechanism for generating these free zonal wave perturbations in the F-layer can be readily understood from the following equations, which are a simplified version of Eqs. (3) and (4):

$$\omega k^2\psi \approx -k_x C_H h, \quad \omega h = -k_x\beta_H\psi. \qquad (10)$$

Introducing the displacement $V_y = d\xi_y/dt = \partial\psi/\partial x = -i\omega\xi_y$ and the quasi-elastic force density $f = -\omega_n^2\xi_y \equiv -æ\xi_y/\rho$, we obtain from Eqs. (10) the following equation for free oscillations of a linear oscillator:

$$\frac{d^2\xi_y}{dt^2} + \omega_n^2\xi_y = 0. \qquad (11)$$

The second of equations (10), which is the frozen-in equation $h = \beta_H\xi_y$ or, equivalently, $h = H_{0z}\xi_y/R$, implies that, owing to collisional processes, a transverse displacement ξ_y of a neutral particle in the ionospheric plasma in the F-layer gives rise to the tension of the lines of the geomagnetic field H_{0z}. As a result, the geomagnetic field acquires the h_z-component, which is proportional to ξ_y and generates a quasi-elastic force with the density $f = -\kappa\xi_y/\rho$. The quantity $\kappa = \rho\omega_n^2$ can be referred to as the electromagnetic elasticity of a unit volume of the ionospheric plasma.

Now, we solve the nonlinear equations (3) and (4). We seek a solution in the form of steady regular waves, $\psi = \psi(\eta, y)$ and $h = h(\eta, y)$, propagating along the parallels with a constant velocity (u = const) without changing their shape ($\eta = x - ut$). Following [19], we introduce the polar coordinates on the Earth's surface, $r = (\eta^2 + y^2)^{1/2}$ and $\tan\varphi = y/\eta$, and also a circle of radius a, on which the corresponding internal and external solutions are to be matched. We require that the functions $\psi(r, \varphi, t)$ and $h(r, \varphi, t)$ tend to zero exponentially as $r \longrightarrow \infty$ and be twice continuously differentiable everywhere (in particular, at the circle with the radius $r = a$) with respect to each of their arguments. Then, Eqs. (3) and (4) have the exact solution

$$\psi(r, \varphi, t) = -\frac{u}{\beta_H}h(r, \varphi, t) = auF(r, t)\sin\varphi, \qquad (12)$$

where

$$F(r,t) = \begin{cases} -(p/\chi)^2 J_1(\chi r)/J_1(\chi a) + (\chi^2 + p^2)/(a\chi^2), \\ r < a \\ K_1(pr)/K_1(pa), \quad r \geq a; \end{cases} \tag{13}$$

the parameters p and χ are related by the dispersion relation

$$pJ_2(\chi a)K_1(pa) = -\chi J_1(\chi a)K_2(pa),$$
$$p^2 = \frac{u\beta - C_H\beta_H}{u^2} > 0, \tag{14}$$

J_n are Bessel functions of the first kind, and K_n are modified Bessel functions of the second kind (n = 1, 2).

Since we are constructing a solution that decreases exponentially to zero at infinity, the parameter p^2 should be positive. This requirement impose a restriction on the possible phase velocities u of the nonlinear wave structures. A nonlinear wave described by solution (12) can propagate either westward ($u > 0$) or eastward ($u < 0$) along the parallels with the velocity $u < k^2\omega_n^2/(k_x^2\beta)$. In this case, the velocity u of a vortex is much higher than the phase velocity of a linear wave: $|u/V_{ph}| = |k^3\omega_n/(k_x^2\beta)| \gg 1$.

An important point here is that the phase velocity of the nonlinear structures in question cannot take on values lying within the range of all possible phase velocities of the corresponding linear periodic waves. As a consequence, no energy of the vortices is expended on generating linear waves, so that the vortices themselves are long-lived structures.

With allowance for the dispersion relation (14), solution (12) contain two free parameters, u and a, although the range of their values is limited by the above inequalities. As $r \longrightarrow \infty$, solution (12) has the asymptotic behavior ψ, $h \sim r^{1/2}\exp(-pr)$, thereby indicating that the wave is localized along the Earth's surface (η, y). Since the pattern of isolines of the stream function is dipole in character, such structures exist in the form of a pair of vortices (a cyclone and an anticyclone) that rotate in opposite directions, have the same intensities, and move along the parallels against the background of a mean zonal flow.

In the nonlinear structures described by solution (12), the vorticity of the particle motion is nonzero: $\nabla \times \mathbf{V} = -\Delta\psi\mathbf{e}_z \neq 0$; this indicates that the particles in a vortex rotate at a velocity of $u_c \sim u$. The vortex entrains a group of particles in circulation. The number of these particles is approximately equal to the number of transit particles. These particles circulate inside the vortex and migrate together with it. The characteristic dimension d of the vortex is about $d \sim a \sim p^{-1} \approx \alpha\omega_n/\beta$ ($\alpha < 1$).

4. DISCUSSION OF THE RESULTS

We have established that, in the ionospheric F-layer, linear and nonlinear planetary-scale wave structures may be generated as a result of the latitudinal variations of the geomagnetic field. The parameters of the structures (such as the amplitude of the geomagnetic pulsations, phase velocity, and period) have been calculated numerically using the familiar models of the ionosphere and neutral atmosphere [20–22]. Calculations show that, for the wavelength λ = 2000 km and exospheric temperature T_{ex} = 600° at the mean colatitude θ_0 = 45°, the phase velocity $V_{ph} = \omega_n/k$ of the linear waves changes from 20 to 1400 km s^{-1} at altitudes of 200 to 500 km and, for T_{ex} = 2600°, it changes from 10 to 50 km s^{-1} at the same altitudes. The phase velocity V_{ph} increases in linear proportion to the wavelength λ. The wave period T_n is independent of the wavelength and changes from 105 to 3 s for T_{ex} = 600° and from 210 to 40 s for T_{ex} = 2600°. For displacements ξ_y equal to 0.1 and 1 km at θ_0 = 45°, the amplitude $h_z \simeq H_{0z}\xi_y/R$ of the geomagnetic pulsations driven by the waves under consideration is 8 and 80 nT, respectively. The strong dependence of the parameters V_{ph} and T_n on the exospheric temperature (in particular, a decrease in V_{ph} and an increase in T_n with increasing exospheric temperature) can be explained as being due to the inflation of the atmosphere and the generation of the ascending flows transporting heavy particles to the F-layer from the lower ionospheric layers. The wave phase velocity increases with increasing altitude and latitude θ_0.

The linear waves can propagate either westward or eastward along the parallels.

By solving the nonlinear dynamic equations (3) and (4) analytically, we have established a self-localization effect: large-scale waves may form nonlinear localized solitary vortex structures moving either westward or eastward along the parallels with a constant velocity $|u| < k^2\omega_n^2/(k_x^2\beta)$, which is much higher than the phase velocity of the corresponding linear waves, $|u/V_{ph}| \simeq |k^3\omega_n/(k_x^2\beta)| \sim 10^7 \gg 1$. It is because of the large difference in phase velocities that no energy of the nonlinear structures is expended on generating linear waves, so that the structures themselves may be fairly long-lived formations. The nonlinear structures consist of a pair of vortices (a cyclone and an anticyclone) that rotate in opposite directions, entrain the particles of the medium in circulation, and transport them to the ionosphere. The characteristic dimension of a vortex is about $d \sim \alpha\omega_n/\beta \simeq 10^4$ km.

Being long-lived objects, nonlinear planetary-scale electromagnetic vortex structures may play an important role in transporting matter, heat, and energy, and also in driving the macroturbulence of the ionosphere [23].

In particular, vortex structures that play the role of "turbulization agents" can be treated as elements of the horizontal macroscopic turbulent exchanges in global circulation processes in the ionospheric F-layer. The coefficient of the horizontal turbulent exchange can be estimated from the Obukhov formula [24]: $k_T \simeq 10^{-2} d^{4/3}$ m^2 s^{-1}. Thus, for vortices with dimensions of about $d \sim 10^3$ km at latitudes of about $\varphi' \simeq 50°$–$55°$, we obtain $k_T \simeq 3 \times 10^6$ m^2 s^{-1}. This estimate (which can be regarded as an upper one) shows that, in the global exchange processes between high and low latitudes, the meridional heat transport from north to south in the ionospheric F-layer should be of the nature of a macroturbulence (recall that, in the ionosphere, the polar regions are warmer than the equatorial region). This question requires a separate analysis and is the subject of an ongoing investigation.

Using solution (12), we can determine the amplitude h_{zb} of the magnetic field generated by nonlinear vortex structures. With allowance for the relationship $d \sim a \simeq \alpha\omega_n/\beta$ ($\alpha < 1$), we obtain from solution (12) the estimate

$$h_{zb} = \alpha \frac{N_n}{N} \frac{\beta_H}{\beta} \frac{\omega_n}{\omega_{ci}} H_p,$$

where $\omega_{ci} = eH_p/(Mc)$. From the parameter values characteristic of the F-layer, namely, $\omega_{ci} \simeq 10^2$ s^{-1}, $N_n \simeq 3 \times 10^{14}$ m^{-3}, $N = 3 \times 10^{11}$ m^{-3}, $\beta_H = 5.4 \times 10^{-11}$ m^{-1} s^{-1}, $\beta = 1.3 \times 10^{-11}$ m^{-1} s^{-1}, $\alpha = 0.1$, and $\omega_n = 2\pi/T_n$ with $T_n \simeq 100$ s, we find $h_{zb} \simeq 200$ nT. Presumably, the generation of such strong geomagnetic field perturbations is associated with the following intrinsic feature of the large-scale nonlinear structures under consideration. On the one hand, the vortices drive particles (in particular, charged particles) in circulation. On the other hand, the geomagnetic field in the F-layer is frozen in the ionospheric plasma. As a result, the formation of vortex structures is accompanied by the compression of the magnetic field lines and, accordingly, by the growth of magnetic perturbations within the structures.

The above theoretical estimates for the parameters of the wave structures in question agree fairly well with the experimentally deduced values of the parameters of fast large-scale MIWPs [1–9], which provides evidence for the actual existence of mechanisms for the generation of intrinsic (background) planetary-scale electromagnetic wave structures in the ionospheric F-layer. These mechanisms may involve the latitudinal variations of both the geomagnetic field and the angular velocity of the Earth's rotation.

The above wave structures are associated with the excitation of the internal degrees of freedom of the ionospheric F-layer. They occur on planetary scales and can be recorded at all latitudes in the Earth's ionosphere. The MIWPs observed at mid-latitudes in the ionospheric F-layer are manifestations of these natural oscillations in the upper atmosphere. When the ionosphere is affected from above (e.g., by geomagnetic substorms) or from below (by earthquakes, major artificial explosions, etc.), the first to be generated and/or amplified are precisely the wave structures at the MIWP modes [25]. That latitudinal geomagnetic-field variations with a certain amplitude are capable of generating solitary vortices [19] is confirmed by observations [8, 26–28].

REFERENCES

1. A. G. Khantadze and Z. S. Sharadze, *Wave Disturbances in Atmosphere* (Nauka, Alma-Ata, 1980), p. 143.
2. Z. S. Sharadze and A. G. Khantadze, Soobshch. Akad. Nauk Gruz. SSR **94** (1), 69 (1979).
3. Z. S. Sharadze, Ionos. Issled., No. 29, 29 (1979).
4. Z. S. Sharadze, *Phenomena in Middle-Latitude Ionosphere Concerned with Atmospheric Waves* (IZMIRAN, Moscow, 1991).
5. L. A. Haykowicz, Planet. Space Sci. **39**, 583 (1991).
6. V. A. Liperovskiĭ, O. A. Pokhotelov, and S. A. Shalimov, *Ionospheric Precursors of Earthquakes* (Nauka, Moscow, 1992).
7. Z. S. Sharadze, G. A. Dzhaparidze, E. G. Matiashvili, *et al.*, Izv. Akad. Nauk SSSR, Fiz. Zemli, No. 1, 20 (1989).
8. V. I. Drobzheev, G. R. Molotoev, Z. S. Sharadze, *et al.*, Ionos. Issled., No. 39, 61 (1986).
9. O. A. Pokhotelov, V. A. Liperovskiĭ, Yu. P. Fomichev, *et al.*, Dokl. Akad. Nauk SSSR **321**, 1168 (1991).
10. A. G. Khantadze, Z. S. Sharadze, and Z. L. Kobaladze, *Research of Dynamic Processes in the Upper Atmosphere* (Gidrometizdat, Moscow, 1988), p. 110.
11. A. Khantadze, J. Georgian Geophys. Soc. B **4**, 125 (1999).
12. K. Cheng and Y.-N. Huang, J. Geophys. Res. **97**, 16995 (1992).
13. A. G. Khantadze, *Some Problems of the Dynamics of Conductive Atmosphere* (Metsniereba, Tbilisi, 1973), p. 193.
14. S. I. Syrovatskiĭ, Usp. Fiz. Nauk **3**, 247 (1957).
15. V. P. Dokuchaev, Izv. Vyssh. Uchebn. Zaved., Radiofiz., No. 4, 5 (1961).
16. T. D. Kaladze, L. V. Keshelashvili, and L. V. Tsamalashvili, Fiz. Plazmy **25**, 683 (1999) [Plasma Phys. Rep. **25**, 625 (1999)]; Phys. Lett. A **232**, 269 (1997).
17. E. E. Gossard and W. H. Hooke, *Waves in the Atmosphere* (Elsevier, Amsterdam, 1975; Mir, Moscow, 1978).
18. É. S. Kazimirovskiĭ and V. D. Kokourov, *Motions in the Ionosphere* (Nauka, Novosibirsk, 1979).
19. G. D. Aburjaniya, Fiz. Plazmy **22**, 954 (1996) [Plasma Phys. Rep. **22**, 864 (1996)].
20. L. G. Jachia, SAO Spec. Rep., No. 332, 114 (1971); No. 313 (1970).

21. T. I. Zelenova, A. D. Legenka, and M. N. Fatkullin, in *Physics and Empirical Simulations of the Ionosphere* (Nauka, Moscow, 1975), p. 7; *Physics and Empirical Simulations of the Ionosphere* (Nauka, Moscow, 1978), p. 40.
22. *Reference Model of the Ionosphere-83*, Ed. by Yu. K. Chasovitin (IÉM GK SSSR GMKPS, Obninsk, 1983).
23. G. D. Aburjaniya, Fiz. Plazmy **16**, 70 (1990) [Sov. J. Plasma Phys. **16**, 40 (1990)].
24. L. S. Gandin, D. L. Laĭkhtman, L. T. Matveev, and M. I. Yudin, *Foundations of Dynamic Meteorology* (Gidrometizdat, Leningrad, 1955), p. 633.
25. G. D. Aburjania and G. Z. Machabeli, J. Geophys. Res. **103**, 9441 (1998).
26. V. I. Petviashvili and O. A. Pokhotelov, *Solitary Waves in Plasmas and in the Atmosphere* (Énergoatomizdat, Moscow, 1989; Gordon and Breach, Reading, 1992).
27. M. V. Nezlin and E. N. Snezhkin, *Rossby Vortices, Spiral Structures, and Solitons* (Nauka, Moscow, 1990; Springer-Verlag, Heldeiberg, 1993).
28. V. N. Chmyrev, V. A. Marchenko, O. A. Pokhotelov, *et al.*, Planet. Space Sci. **39**, 1025 (1991).

Translated by O. E. Khadin

Plasma Physics Reports, Vol. 28, No. 7, 2002, pp. 592–602. Translated from Fizika Plazmy, Vol. 28, No. 7, 2002, pp. 639–650.

CHARGED PARTICLE MOTION

Trapping and Scattering of a Relativistic Charged Particle by Resonance in a Magnetic Field and an Electromagnetic Wave

A. P. Itin

Institute for Space Research, Russian Academy of Sciences, Profsoyuznaya ul. 84/32, Moscow, 117810 Russia

Received December 18, 2001

Abstract—A study is made of the dynamics of a relativistic charged particle in an electromagnetic wave (with an electrostatic component) in a constant uniform magnetic field. A system with a high-frequency wave is a Hamiltonian system with two degrees of freedom and with fast and slow variables. The trapping of a particle into resonance and its scattering on resonance in such a system is described. *© 2002 MAIK "Nauka/Interperiodica".*

1. INTRODUCTION

This paper is aimed at investigating the problem of the interaction between a charged particle and a high-frequency electromagnetic wave with an electrostatic component in a magnetic field. Similar problems often arise in studying the phenomena that occur in magnetic confinement systems and accelerators, as well as in planetary magnetospheres and cosmic rays. In the case of a constant magnetic field and a plane electromagnetic or electrostatic wave, the problem reduces to that of investigating a Hamiltonian system with two degrees of freedom; under certain condition, such a system can be examined by the methods of perturbation theory [1–8].

Previously, this problem was studied by Chernikov *et al.* [8], who obtained the conditions for particle trapping into a resonance. In the present paper, the dynamics of the system is analyzed in more detail. The purposes here are to describe the structure of the phase space of the system, to investigate the conditions for particle trapping and detrapping and also for particle scattering on a resonance, and to give examples of different types of particle motion. On the whole, the system is examined in the same way as was done in [1] for a system with a purely electrostatic wave. The problem is studied by using a scheme for analyzing resonance phenomena in Hamiltonian systems with two degrees of freedom: this scheme, which was described by Neishtadt [9], is a Hamiltonian version of a more general approach [10, 11].

The wave phase at the position of a particle is a "fast" variable. In what follows, the term "resonance" means that the time derivative of this phase vanishes. Physically, this indicates that the projection of the particle velocity onto the propagation direction of the wave coincides with the wave phase velocity (Cherenkov resonance). In the space of slow variables, resonance points form a so-called resonant surface. The particle dynamics far from resonance can be described by the method of averaging over the fast variable. The variable that is canonically conjugate to the fast variable is an integral of motion (an adiabatic invariant) of the system so averaged. However, in the vicinity of resonance, where this averaging method is inapplicable, the adiabatic invariant may change by a large amount. The particle dynamics in this region is described by the procedure proposed in [9]. The original system is modeled by a system analogous to a nonlinear pendulum under the action of a constant torque. The parameters of the pendulum depend on the slow variables of the original system. This slow time dependence makes possible transitions of a phase point from the regions of rotational motion in the phase space of the pendulum to the regions of oscillatory motion. These transitions correspond to particle trapping into resonance. During a trapping event, the particle leaves the adiabatic trajectory and continues to move along a resonant trajectory, which is the intersection of an isoenergetic surface and a resonant surface. As a result, the adiabatic invariant changes significantly, so that, under certain additional conditions, the particle may be accelerated without bound.

The trapping into resonance is a probabilistic phenomenon. The probabilistic approach to studying the behavior of dynamic systems was described in [12, 13] (see also [9, 11]). The trapping probability is estimated by the method described in [9]. If the particle passes through resonance without being trapped, then it is scattered on resonance, in which case the adiabatic invariant undergoes a jump on the order of $\sqrt{\varepsilon}$ [14] (the small parameter ε of the perturbation characterizes the typical ratio between the velocities of slow and fast motions). The accumulation of such jumps due to multiple passages through resonance destroys the adiabatic

1063-780X/02/2807-0592$22.00

invariance; as a result, the particle motion becomes stochastic.

The paper is organized as follows. In Section 2, the Hamiltonian equations of motion are derived and the particle motion far from resonance is described. In Section 3, particle motion in the immediate vicinity of the resonance is investigated and the Hamiltonian is reduced to that of a nonlinear pendulum. In Section 4, the properties of the nonlinear pendulum are used to study the particle trapping into resonance, to estimate the trapping probability, and to consider the conditions for unbounded acceleration of the particles. In Section 5, the particle scattering on resonance is investigated and diffusion-like statistical changes in the adiabatic invariant are estimated.

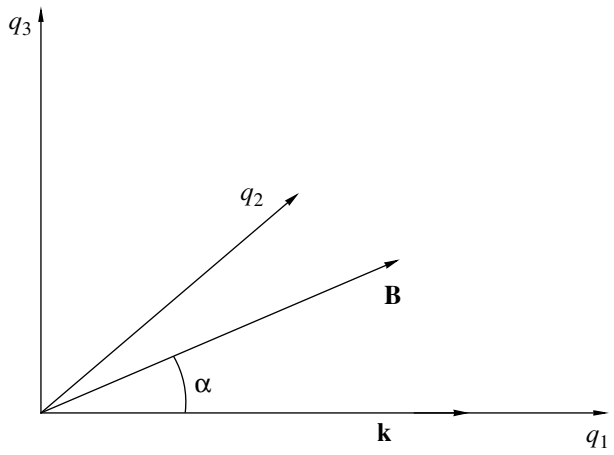

Fig. 1. Configuration of the fields.

2. HAMILTONIAN EQUATIONS OF MOTION

We consider the motion of a relativistic particle with charge e and rest mass m in an elliptically polarized plane electromagnetic wave with an electrostatic component under the action of a constant magnetic field **B**. The wave frequency is assumed to be much higher than the cyclotron frequency of the particle. We introduce the orthogonal coordinate system (q_1, q_2, q_3) such that, first, the vector **B** lies in the (q_1, q_3) plane and is directed at an angle α to the q_1-axis and, second, an electromagnetic wave propagates along the q_1-axis, in which case the components of its electric field are $E_2 = b_1\cos(kq_1 - \omega t)$ and $E_3 = b_2\sin(kq_1 - \omega t)$ (Fig. 1). In these coordinates, the vector potential of the wave electromagnetic field can be chosen to be

$$\mathbf{A} = \{A_1, A_2, A_3\} = \left\{0, B_0 q_1 \sin\alpha + \frac{cb_1}{\omega}\sin(kq_1 - \omega t), \right. \\ \left. B_0 q_2 \cos\alpha - \frac{cb_2}{\omega}\cos(kq_1 - \omega t)\right\}, \quad (1)$$

so that the Hamiltonian H of the particle has the form

$$H = \left[m^2c^4 + c^2p_1^2 \right. \\ + \left(c\mathcal{P}_2 - eB_0q_1\sin\alpha - \frac{ceb_1}{\omega}\sin(kq_1 - \omega t)\right)^2 \\ \left. + \left(c\mathcal{P}_3 - eB_0q_2\cos\alpha - \frac{ceb_2}{\omega}\cos(kq_1 - \omega t)\right)^2\right]^{1/2} \\ + e\Phi_0\cos(kq_1 - \omega t), \quad (2)$$

where c is the speed of light, $\mathcal{P}_2 = p_2 + eA_2/c$, $\mathcal{P}_3 = p_3 + eA_3/c$, and $p = (p_1, p_2, p_3)$ is the particle momentum. The variables p_1, $\mathcal{P}_2$, and $\mathcal{P}_3$ are canonically conjugate to the variables q_1, q_2, and q_3. Since Hamiltonian (2) is independent of q_3, the quantity $\mathcal{P}_3$ is an integral of motion, which can be driven to zero, $\mathcal{P}_3 = 0$, by shifting the q_2-axis. We introduce the notation

$$\omega_c = \frac{eB_0}{mc}, \quad b = \sqrt{b_1^2 + b_2^2}, \\ \varepsilon = \frac{eb}{m\omega c}, \quad \kappa_{1,2} = b_{1,2}/b, \quad \varepsilon\mu = e\frac{\Phi_0}{mc^2}, \quad (3)$$

where ω_c is the cyclotron frequency, and specify the parameter range in which the problem is to be treated: $\omega/(kc) \sim 1$, $\varepsilon \ll 1$, $\omega_c/\omega \sim \varepsilon$, and $\varepsilon\mu \ll 1$.

We also introduce the new dimensionless variables and parameters

$$\tilde{\mathcal{P}}_{2,3} = \mathcal{P}_{2,3}/mc, \quad \tilde{p}_1 = p_1/mc, \quad \tilde{q}_{1,2} = \frac{\omega_c q_{1,2}}{\varepsilon c}, \\ v = \omega/kc, \quad \tilde{k} = kc\varepsilon/\omega_c, \quad \tilde{t} = \omega_c t/\varepsilon, \\ \tilde{\omega} = \varepsilon\omega/\omega_c, \quad \tilde{H} = H/mc^2 \quad (4)$$

and, omitting the tildes, write the dimensionless Hamiltonian

$$H = \sqrt{1 + p_1^2} + (\varepsilon q_2\cos\alpha - \varepsilon\kappa_2\cos(kq_1 - \omega t))^2 + (\mathcal{P}_2 - \varepsilon q_1\sin\alpha - \varepsilon\kappa_1\sin(kq_1 - \omega t))^2 + \varepsilon\mu\cos(kq_1 - \omega t). \quad (5)$$

Then, we make a canonical transformation to a new set of variables, $(q_1, p_1, q_2, \mathcal{P}_2) \longrightarrow (q, p, \phi, I)$, using the generating function $W(q_1, q_2, I, p, t) = (kq_1 - \omega t)I/k + q_2(p + \varepsilon q_1\sin\alpha)$.

In terms of the new variables, the Hamiltonian becomes

$$\mathcal{H} = -\nu I + \sqrt{1 + (I + \varepsilon q\sin\alpha)^2 + (\varepsilon q\cos\alpha - \varepsilon\kappa_2\cos k\phi)^2 + (p - \varepsilon\kappa_1\sin k\phi)^2} + \varepsilon\mu\cos k\phi. \quad (6)$$

Now, we introduce the new coordinate $\tilde{q} = \varepsilon q$ and, again omitting the tilde, write the Hamiltonian in the form

$$\mathcal{H} = -\nu I + \sqrt{1 + I^2 + p^2 + q^2 + 2Iq\sin\alpha - 2\varepsilon(q\kappa_2\cos\alpha\cos k\phi + p\kappa_1\sin k\phi) + O(\varepsilon^2)} + \varepsilon\mu\cos k\phi, \quad (7)$$

where the canonically conjugate pairs of variables are $(p, \varepsilon^{-1}q)$ and (ϕ, I). Additionally, we introduce the unperturbed Hamiltonian

$$\mathcal{H}_0 = -\nu I + \sqrt{1 + I^2 + p^2 + q^2 + 2Iq\sin\alpha} \quad (8)$$

and the perturbation $\varepsilon\mathcal{H}_1 = \mathcal{H} - \mathcal{H}_0$, which can be rewritten as

$$\varepsilon\mathcal{H}_1 = -\varepsilon\frac{q\kappa_2\cos\alpha\cos k\phi + p\kappa_1\sin k\phi}{\sqrt{1 + I^2 + q^2 + p^2 + 2Iq\sin\alpha}} + \varepsilon\mu\cos k\phi + O(\varepsilon^2). \quad (9)$$

In the (I, p, q) space, the equation $\mathcal{H}_0 = \text{const}$ determines the second-order isoenergetic surface, such that the moving particle always remains within its ε-vicinity. The isoenergetic surface may have different shapes, depending on the ratio between $\mathcal{H}_0$, ν, and α.

Hamiltonian (7) leads to the following equations of motion:

$$\dot{I} = -\frac{\partial\mathcal{H}}{\partial\phi} = \varepsilon k\frac{p\kappa_1\cos k\phi - q\kappa_2\cos\alpha\sin k\phi}{\sqrt{1 + I^2 + q^2 + p^2 + 2Iq\sin\alpha}} + \varepsilon k\mu\sin k\phi + O(\varepsilon^2),$$

$$\dot{\phi} = \frac{\partial\mathcal{H}}{\partial I} = -\nu + \frac{I + q\sin\alpha}{\sqrt{1 + I^2 + q^2 + p^2 + 2Iq\sin\alpha}} + O(\varepsilon), \quad (10)$$

$$\dot{p} = -\varepsilon\frac{\partial\mathcal{H}}{\partial q} = -\varepsilon\frac{q + I\sin\alpha}{\sqrt{1 + I^2 + q^2 + p^2 + 2Iq\sin\alpha}} + O(\varepsilon^2),$$

$$\dot{q} = \varepsilon\frac{\partial\mathcal{H}}{\partial p} = \varepsilon\frac{p}{\sqrt{1 + I^2 + q^2 + p^2 + 2Iq\sin\alpha}} + O(\varepsilon^2).$$

We can readily see that these equations describe particle motion on short and long time scales: the variable ϕ is fast, while the remaining variables are slow. Therefore, if $\dot{\phi} \neq 0$, the dynamics of the system can be investigated by using the averaging method [15]. Thus, averaging Eqs. (10) over the fast variable ϕ yields $I = \text{const}$. Consequently, in this approximation, the particle trajectory in the (I, p, q) coordinates is the intersection of the isoenergetic surface $\mathcal{H}_0 = \text{const}$ and the plane $I = \text{const}$. We call this trajectory the adiabatic trajectory. The adiabatic trajectory is an ellipse corresponding to Larmor gyration of the particle. Actually, the particle momentum I along the trajectory is conserved accurate to ε on time scales of about $1/\varepsilon$.

However, the averaging method is inapplicable in the vicinities of the resonances where $\partial\mathcal{H}_0/\partial I = 0$. Along a trajectory passing through resonance, the change in I may be large. The phenomena occurring near resonance will be considered below.

3. REDUCTION OF THE HAMILTONIAN IN THE VICINITY OF THE RESONANCE

In the (I, p, q) space, the resonant condition $\partial\mathcal{H}_0/\partial I = 0$ determines the surface $I = I_{\text{res}}(p, q)$, which is called the resonance surface. If the resonant and isoenergetic surfaces intersect, their intersection is a second-order plane curve [1]. We call this curve the resonant curve. For $\nu = \cos\alpha$, the resonant curve is a parabola, and, for $\nu > \cos\alpha$ and $\nu < \cos\alpha$, it is a hyperbola and an ellipse, respectively. The projection of the resonant curve onto the (p, q) plane is described by the equation

$$q^2(\cos^2\alpha - \nu^2) + (1 - \nu^2)p^2 + 2q\nu\mathcal{H}_0\sin\alpha + 1 - \nu^2 - \mathcal{H}_0^2 = 0. \quad (11)$$

It is easy to see that isoenergetic and resonant surfaces, as well as adiabatic (Larmor) trajectories, are symmetric about the $p = 0$ plane. Each adiabatic trajectory either does not intersect the resonant surface or intersects it at two points, which are symmetric with respect to the $p = 0$ plane.

Particle motion in the vicinity of the resonant surface cannot be investigated by the averaging method. Let us consider the phenomena that occur at the intersection of the phase trajectory of the particle and the resonant surface. Near the resonant surface (in its vicinity with a width on the order of $\sqrt{\varepsilon}$), the Hamiltonian $\mathcal{H}$ can be represented as

$$\mathcal{H} = \Lambda(p, q) + \frac{1}{2}g(p, q)(I - I_{\text{res}}(p, q))^2 + \varepsilon\mathcal{H}_1 + O(|I - I_{\text{res}}|^3), \quad (12)$$

where Λ and g are the values of $\mathcal{H}_0$ and $\partial^2\mathcal{H}_0/\partial I^2$ at the resonant surface.

Let us introduce the new momentum $K = I - I_{res}(p, q) + O(\varepsilon)$. To do this, we make a canonical transformation to a new set of variables, $(K, \bar{\phi}, \bar{p}, \bar{q})$, using the generating function

$$W_1 = \bar{p}\varepsilon^{-1}q + (K + I_{res}(\bar{p}, q))\phi. \quad (13)$$

We omit the bar over the new variables and write the new Hamiltonian as

$$\mathcal{H} = \Lambda(p, q) + \frac{1}{2}g(p, q)K^2 + \varepsilon d(p, q)\cos(k\phi + \beta) + \varepsilon b(p, q)\phi + O(K^3) + O(\varepsilon K\phi) + O((\varepsilon\phi)^2), \quad (14)$$
$$b = \{I_{res}, \Lambda\},$$

where $\{\cdot, \cdot\}$ is the Poisson bracket in terms of the variables p and q. It is an easy matter to obtain the following relationships:

$$\Lambda = qv\sin\alpha + \sqrt{(1 - v^2)(1 + p^2 + q^2\cos^2\alpha)},$$
$$b = -\frac{\sin\alpha}{\sqrt{1 - v^2}}\frac{p}{\sqrt{1 + p^2 + q^2\cos^2\alpha}},$$
$$g = \frac{(1 - v^2)^{3/2}}{\sqrt{1 + p^2 + q^2\cos^2\alpha}}, \quad (15)$$
$$d = \left\{\frac{(1 - v^2)}{1 + p^2 + q^2\cos^2\alpha}\right.$$
$$\left.\times\left[p^2\kappa_1^2 + \left(q\kappa_2\cos\alpha - \mu\sqrt{\frac{1 + p^2 + q^2\cos^2\alpha}{1 - v^2}}\right)^2\right]\right\}^{1/2},$$
$$\beta = \arctan\left(\frac{p\kappa_1}{-q\kappa_2\cos\alpha + \mu\sqrt{\frac{1 + p^2 + q^2\cos^2\alpha}{1 - v^2}}}\right).$$

We consider the motion in the region in which b is on the order of unity. In this region, the new momentum changes by $K = O(\sqrt{\varepsilon})$ and the phase ϕ changes by an amount of $O(1)$ on a time scale of about $O(1/\varepsilon)$. Consequently, we have

$$\mathcal{H} = \Lambda(p, q) + \frac{1}{2}g(p, q)K^2 + \varepsilon d(p, q)\cos(k\phi + \beta) + \varepsilon b(p, q)\phi + O(\varepsilon^{3/2}). \quad (16)$$

Then, we introduce the momentum $P = K/\sqrt{\varepsilon} = O(1)$ and the new time $\theta = t\sqrt{\varepsilon}$. In order to keep the canonical Hamiltonian form of the system, we also introduce the new Hamiltonian $F = \mathcal{H}/\varepsilon$ and switch to the new canonically conjugate pairs of variables, (P, ϕ) and $(p, \varepsilon^{-3/2}q)$. The new Hamiltonian F has the form

$$F = \varepsilon^{-1}\Lambda(p, q) + F_0(P, \phi, p, q) + O(\sqrt{\varepsilon}),$$
$$F_0 = \frac{1}{2}gP^2 + d\cos(k\phi + \beta) + b\phi. \quad (17)$$

Particle motion in the vicinity of the resonant surface can be approximately described by Hamiltonian (17) in which the terms $O(\sqrt{\varepsilon})$ are omitted. In this case, we obtain the following equations of motion:

$$p' = -\sqrt{\varepsilon}\frac{\partial\Lambda}{\partial q}, \quad q' = \sqrt{\varepsilon}\frac{\partial\Lambda}{\partial p},$$
$$P' = -\frac{\partial F_0}{\partial\phi}, \quad \phi' = \frac{\partial F_0}{\partial P}, \quad (18)$$

where the prime denotes the derivative with respect to θ. In these equations, (p, q) are slow variables and (P, ϕ) are fast variables. The evolution of p and q is determined by the Hamiltonian $\sqrt{\varepsilon}\Lambda$, which defines a flux at the resonant surface (the "resonant" flux). The evolution of the variables P and ϕ is described by Eqs. (18) with the Hamiltonian $F_0(P, \phi, p, q)$, which depends on the slow variables (p, q). Equations (18) approximately describe the motion in the resonance region, i.e., at short distances from the resonant surface (on the order of $\sqrt{\varepsilon}$ or shorter).

4. PARTICLE TRAPPING INTO RESONANCE

At fixed values of p and q, Eqs. (18) for the variables P and ϕ refer to a Hamiltonian subsystem with one degree of freedom. The Hamiltonian F_0 describes a nonlinear pendulum under the action of a constant torque b. Similar systems always arise in solving the problems of passage through the resonance [10] and are characterized by two types of phase portraits: with and without the region of oscillatory motion. For $|b| < |dk|$, the region of oscillatory motion is present in the phase portrait (Fig. 2a), and, for $|b| > |dk|$, this region is absent (Fig. 2b). For brevity, we will call this region the "oscillatory" region. In Fig. 2a, the motion within the oscillatory region corresponds to the motion of the phase point trapped into a resonance. The motion outside this region corresponds to the phase points that cross the resonance region without being trapped.

The area S of the oscillatory region is important for further analysis. This area is a function of the coordinates on the resonant surface. Since there is a one-to-one correspondence between the points of the resonant curve and the points of its projection onto the (p, q) plane, the quantity S can be regarded as a function of the variables p and q: $S = S(p, q)$. We take into account the slow change in the parameters p and q along the res-

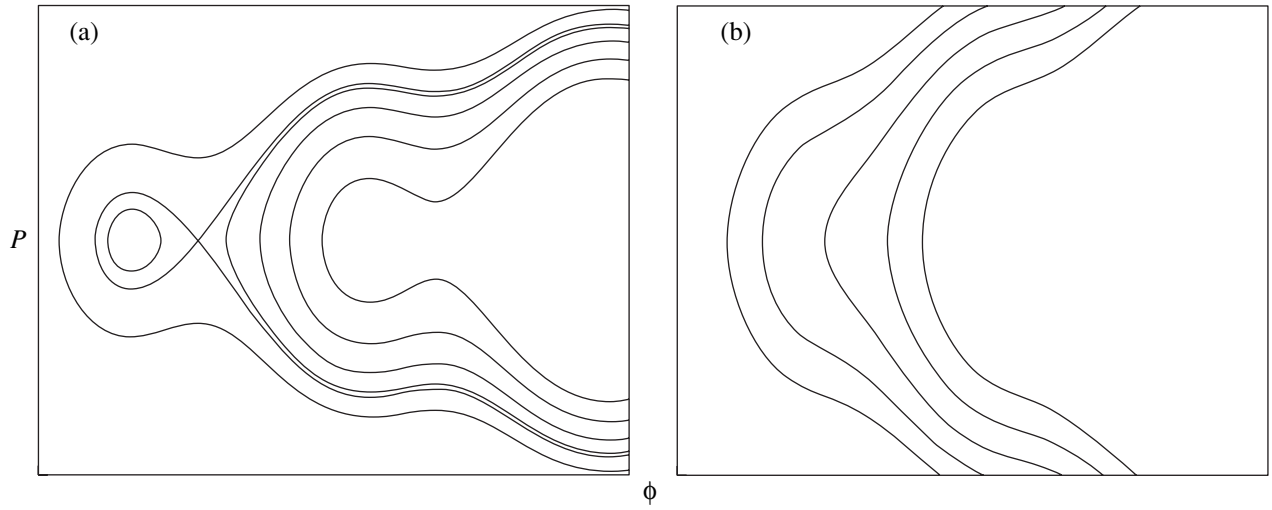

Fig. 2. Phase portrait of a pendulum system for (a) $|b| < |dk|$ and (b) $|b| > |dk|$.

onant flux in the subsystem described by Eqs. (18) and assume that the area S increases along this flux. In this case, an additional space appears within the oscillatory region. Since Hamiltonian systems preserve phase volume, this space is not occupied by phase points that were previously trapped into the resonance. Consequently, the phase points of subsystem (18) cross the separatrix and change from the passing to the oscillatory state. This indicates that the phase points are trapped into the resonance. The trapped phase point of system (10) leaves the vicinity of the curve (I = const, $\mathcal{H}_0$ = const) and continues to move near the resonant curve. The area of the region enclosed by the trajectory of the phase point in the (P, ϕ) plane is also an adiabatic invariant, which is called the "internal" adiabatic invariant [9]. This invariant is approximately conserved along the trajectory of the trapped point. Consequently, if the area S of the oscillatory region decreases along the resonant flux, some of the phase points leave the oscillatory region and then they also leave the resonance region. This corresponds to detrapping of the phase point from the resonance. Note that, if the area S always increases along the resonant flux, then neither of the phase points can escape from the oscillatory region, so that detrapping is impossible.

If ε is small, the initial conditions for the phase points trapped into the resonance and those for the phase points passing through the resonance region without being trapped are mixed in phase space. Even a small (on the order of ε) variation in the initial conditions may considerably change the state of motion. That is why it is expedient to treat trapping as a random event and, accordingly, to analyze the trapping probability. This approach to studying systems in which there are crossings of a separatrix was proposed by Lifshits *et al.* [12]. A rigorous definition of the trapping probability was given by Arnol'd [13] (see also [1]).

Following [9], we find that this probability is described by the expressions

$$\begin{aligned} \Pr(M_0) &= \sqrt{\varepsilon}\frac{\{S, \Lambda\}_*}{2\pi|b_*|} \quad \text{for} \quad \{S, \Lambda\}_* > 0, \\ \Pr(M_0) &= 0 \quad \text{for} \quad \{S, \Lambda\}_* < 0, \end{aligned} \tag{19}$$

where the asterisk indicates that the value should be calculated at the point at which an adiabatic trajectory with the initial conditions M_0 intersects the resonant surface.

The trapped phase point moves along the resonant curve, which is the intersection of the resonant and isoenergetic surfaces. As was mentioned in the previous section, depending on the ratio between v and $\cos\alpha$, the resonant curve is an ellipse, a hyperbola, or a parabola.

The probabilities of trapping into the resonance and detrapping from resonance depend on the behavior of the function $S(p, q)$ along the phase trajectory. Two reliefs of this function are shown in Fig. 3. The function $S(p, q)$ in Fig. 3a does not vanish at any point in the (p, q) plane; i.e., the separatrix is always present in the phase portrait of the corresponding pendulum. This indicates that, in Hamiltonian (17), we have $|b| < |dk|$ regardless of the p and q values.

In Fig. 3b, the function $S(p, q)$ vanishes in a certain region in the (p, q) plane; i.e., there is no separatrix in this region ($|b| > |dk|$).

In a system with a purely electrostatic wave, the boundary of the region $\{S = 0\}$ is a hyperbola [1]:

$$p^2\left(\frac{\sin^2\alpha}{1-v^2} - k^2\mu^2\right) - k^2\mu^2q^2\cos^2\alpha - k^2\mu^2 = 0. \tag{20}$$

Generally, the region $\{S = 0\}$ can be bounded by a second-order plane curve of any type.

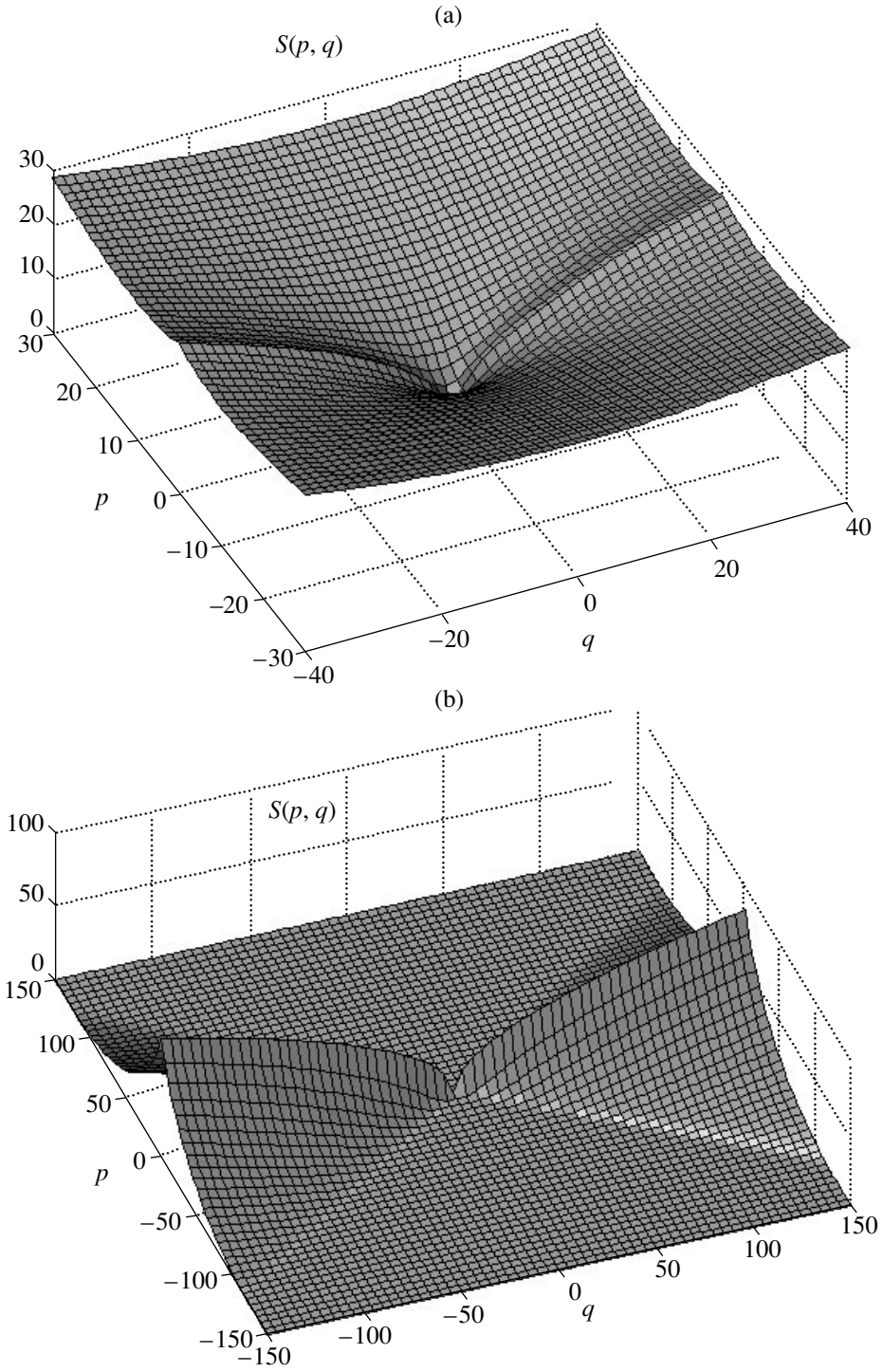

Fig. 3. Reliefs of the function $S(p, q)$ for (a) $k = 1.3$, $\alpha = \pi/4$, $\nu = 0.4$, $\kappa_1 = 0.8$, and $\mu = 0$ and (b) $k = 1.3$, $\alpha = \pi/4$, $\nu = 0.72$, $\kappa_1 = 0.8$, and $\mu = 0$.

Let us consider particle motion under the condition $|b| < |dk|$. Figure 4a shows the isolines of $S(p, q)$ for the same parameters as in Fig. 3a. Also shown in Fig. 4a is the projection of a resonant curve (an ellipse) onto the (p, q) plane. The particle moves along the adiabatic trajectory, which is the intersection of the isoenergetic surface $\mathcal{H}_0 = \text{const}$ and the plane $I = \text{const}$. For certain values of I, this trajectory intersects the resonant curve at two points, which are symmetric with respect to the $p = 0$ plane. At one of these points (point A in Fig. 4a),

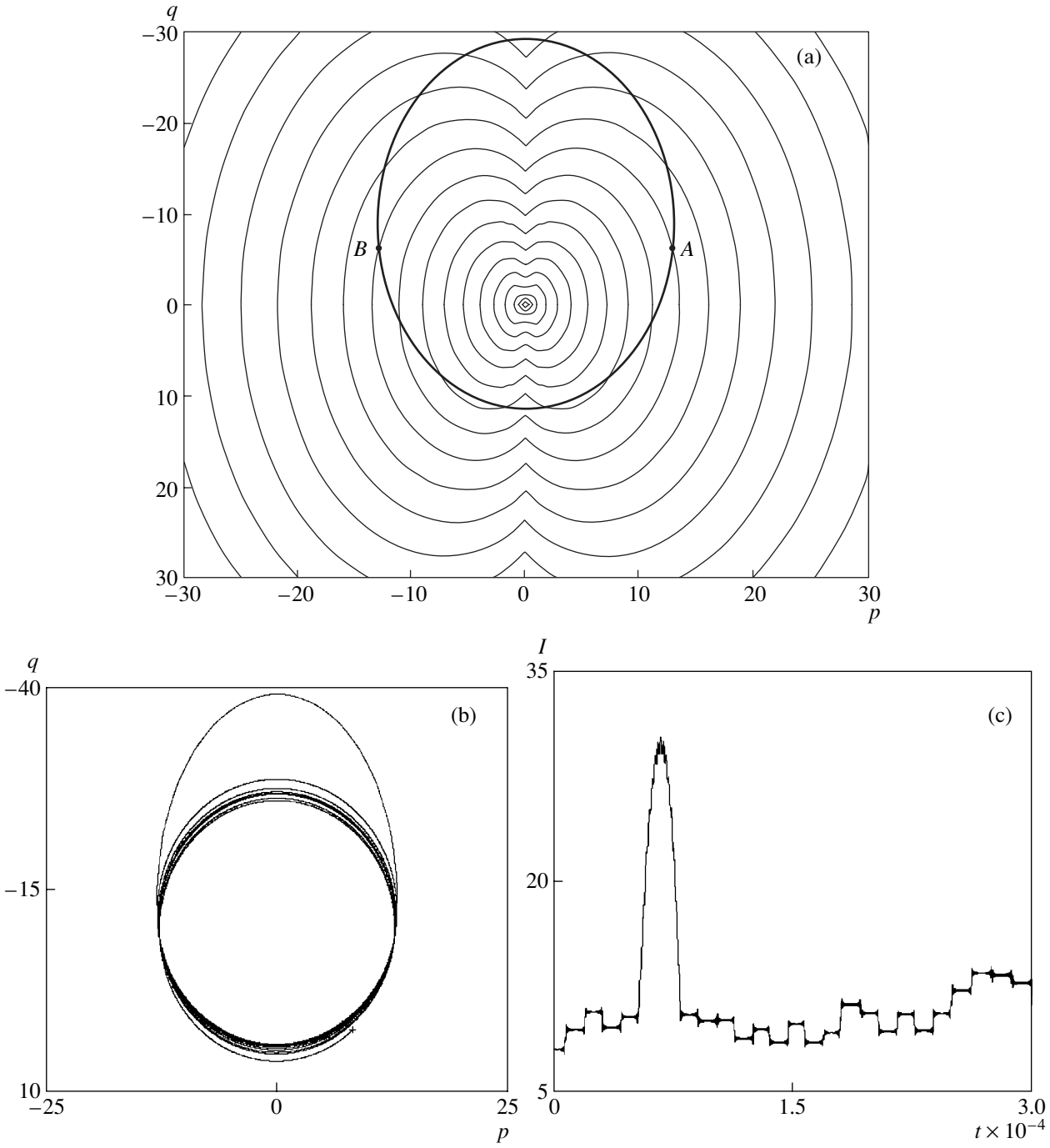

Fig. 4. (a) Isolines of $S(p, q)$ for $k = 1.3$, $\alpha = \pi/4$, $\nu = 0.4$, $\kappa_1 = 0.8$, and $\mu = 0$ and the projection of the resonance curve (the ellipse) onto the (p, q) plane for $\mathcal{H}_0 = 10.71$. (b) Phase trajectory of a particle that becomes trapped into the resonance for $\mathcal{H}_0 = 10.71$ and $\varepsilon = 0.04$. (c) Time evolution of the adiabatic invariant.

the area S increases along the resonant flux, so that we have $\{S, \Lambda\} > 0$. At the other point (point B), this area decreases, so that $\{S, \Lambda\} < 0$. Consequently, when the adiabatic trajectory intersects the resonant curve at point A, the particle can be trapped into the resonance. Then, the particle continues to move along the resonant curve up to point B, at which it becomes untrapped.

The results of numerical investigations involving a solution of the exact equations of motion generated by Hamiltonian (7) are illustrated in Fig. 4b, which shows

the projection of the particle trajectory onto the (p, q) plane. After many Larmor revolutions (smaller ellipses), the particle is trapped into the resonance and moves along the resonant curve (larger ellipse). At the point that is symmetric with respect to the trapping point about the $p = 0$ plane, the particle becomes untrapped (i.e., it leaves the resonance region). Note that, in Fig. 4b, the smaller ellipses (the parts of the trajectory of a gyrating particle) are somewhat different. The reason is that the adiabatic invariant undergoes a small jump every time the particle trajectory intersects the resonant surface. This phenomenon will be discussed in the next section. The time evolution of I is shown in Fig. 4c. For a long time, the particle moves along the adiabatic trajectory and its adiabatic invariant I changes insignificantly. Then, the phase point is trapped into the resonance, in which case the adiabatic invariant I changes considerably. After the particle becomes untrapped, it continues to move at approximately the same value of I. If the resonant curve is a hyperbola or a parabola, the particle may go to infinity, in which case the particle energy H becomes arbitrarily high [see expression (2)] and the particle velocity approaches the speed of light. As a result, the particle is accelerated without bound (this effect is called the surfatron acceleration and was studied for the first time by Katsouleas and Dawson [7] for the case of a wave propagating transverse to the magnetic field). The particle is accelerated along the wave front by a magnetic field in such a way that the projection of its velocity onto the wave vector remains approximately equal to the wave phase velocity. The condition for unbounded acceleration can be obtained as follows. Since $(p^2 + q^2) \longrightarrow \infty$ along the resonant curve, expressions (11) and (15) yield

$$\left(\frac{p}{q}\right)^2 \longrightarrow \frac{v^2 - \cos^2\alpha}{1 - v^2}, \quad b \longrightarrow -\sqrt{\frac{v^2 - \cos^2\alpha}{v^2(1 - v^2)}},$$
$$d \longrightarrow \frac{\sqrt{(1 - v^2)(v^2 - \cos^2\alpha)}}{v\sin\alpha} \times \sqrt{\kappa_1^2 + \kappa_2^2\frac{\cos^2\alpha(1 - v^2)}{v^2 - \cos^2\alpha}}, \quad g \longrightarrow 0. \tag{21}$$

Consequently, for $|b| < |dk|$, i.e., for

$$\frac{\sin\alpha}{1 - v^2} < k\sqrt{\kappa_1^2 + \left(\kappa_2\cos\alpha\sqrt{\frac{1 - v^2}{v^2 - \cos^2\alpha}} - \frac{\mu v\sin\alpha}{\sqrt{(1 - v^2)(v^2 - \cos^2\alpha)}}\right)^2}, \tag{22}$$

the area S of the oscillatory region increases monotonically to infinity along the resonant curve, thereby indicating that the acceleration is unbounded. If inequality (22) fails to hold, then the unbounded acceleration is impossible. Let us introduce the following notation: B_1 and B_2 are the amplitudes of the y- and z-components of the magnetic field of an electromagnetic wave and $E_\parallel$ is the amplitude of the electric field of the electrostatic wave. Then, condition (22) can be rewritten as

$$\frac{B_0\sin\alpha}{1 - v^2} < \sqrt{B_2^2 + \left(B_1\cos\alpha\sqrt{\frac{1 - v^2}{v^2 - \cos^2\alpha}} - E_\parallel\frac{v\sin\alpha}{\sqrt{(1 - v^2)(v^2 - \cos^2\alpha)}}\right)^2}. \tag{23}$$

One can readily see that condition (23) coincides with condition (20) from [8], which was obtained in a quite different way. For a purely electrostatic wave, condition (23) coincides with condition (25) from [1].

In the case illustrated in Fig. 5a, which was obtained for the function $S(p, q)$ shown in Fig. 3a, the resonant curve is a hyperbola. If the trapping occurs at $p > 0$, the area S increases along the resonance curve, so that the particle may be accelerated without bound. However, Fig. 5a implies that the particle can also be trapped at $p < 0$, in which case, however, the trapped particle becomes untrapped at a certain point at which $p > 0$. Figure 5b shows the phase trajectory of a particle that is trapped into resonance and moves to infinity along the resonant curve. The related time evolution of I is displayed in Fig. 5c.

Now, we consider the case in which the inequality $|b| < |dk|$ holds for some but not all values of p and q. Figure 6 shows the isolines of S and the projections of the resonant curves onto the (p, q) plane. The resonant curve in Fig. 6a is an ellipse, and the resonant curves in

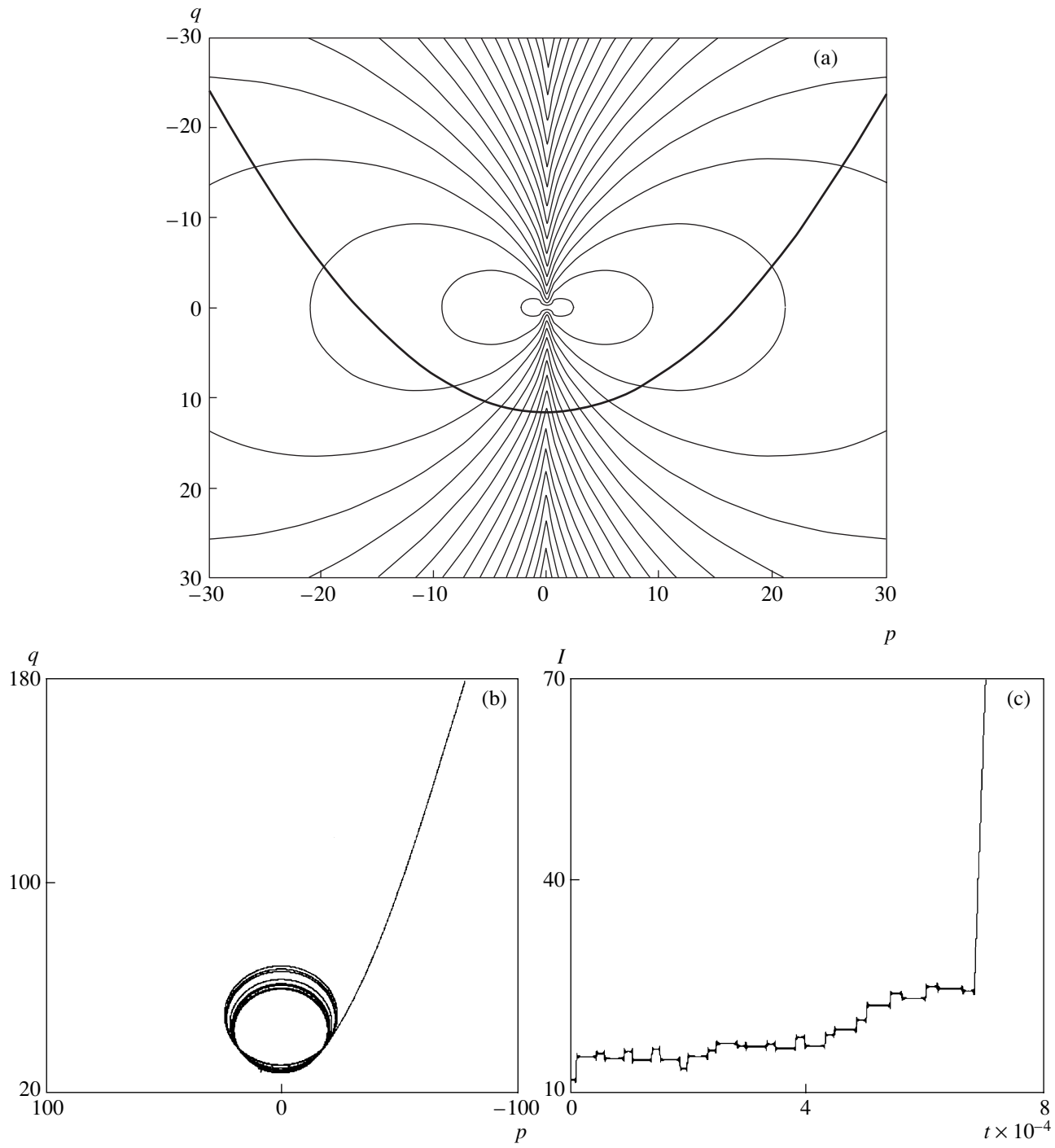

Fig. 5. (a) Isolines of $S(p, q)$ for $k = 1.3$, $\alpha = \pi/4$, $\nu = 0.72$, $\kappa_1 = 0.8$, and $\mu = 0$ and the projection of the resonance curve (the hyperbola) onto the (p, q) plane for $\mathcal{H}_0 = 11.658$. (b) Phase trajectory of a particle that becomes trapped into the resonance (the regime of unbounded acceleration) for $\mathcal{H}_0 = 11.658$ and $\varepsilon = 0.03$. (c) Time evolution of the adiabatic invariant.

Figs. 6b and 6c are hyperbolas. Condition (22) holds for isolines shown in Fig. 6b and is not satisfied for those in Fig. 6c. In the case illustrated by Fig. 6b, the particle can be accelerated without bound.

5. SCATTERING ON RESONANCE

Now, we consider the motion of the phase point that crosses the resonant surface without being trapped into the resonance. This situation will be described in much

the same way as in [1]. Far from the resonant surface, the adiabatic invariant I oscillates along the trajectory with an amplitude $O(\varepsilon)$. When the phase point passes through resonance, the invariant I undergoes a jump $\Delta I \sim \sqrt{\varepsilon}$. This effect is illustrated in Figs. 4c and 5c, as well as in Fig. 7, in which the jumplike change in the adiabatic invariant at the resonance is shown separately.

Let a particle start moving from the point (I_0, ϕ_0, p_0, q_0) at $t = 0$. The adiabatic trajectory with these initial conditions intersects the resonant surface at the point (I_0, p_*, q_*). Let ϕ_* be the ϕ value at the intersection point of the true trajectory with the resonant surface, and let h_* be the value of the Hamiltonian F_0 at the point $(I, \phi, p, q) = (I_0, \phi_*, p_*, q_*)$ in the resonant surface. Hence, we have $h_* = d(p_*, q_*)\cos(k\phi_* + \beta_*) + b(p_*, q_*)\phi_*$. The jump in the adiabatic invariant in the first approximation can be found from the corresponding asymptotic formula [9, 14]:

$$\Delta I = -2s\sqrt{\varepsilon}\int_{-s\cdot\infty}^{\phi_*}\frac{kd\sin(k\phi+\beta)d\phi}{\sqrt{2g(h_*-d\cos(k\phi+\beta)-b\phi)}}, \quad (24)$$

where $s = \mathrm{sgn}(b)$ and the values of g, d, and b are taken at the intersection point of the adiabatic trajectory with the resonant surface. The value ϕ_* depends strongly on the initial conditions: even a small (on the order of ε) variation in these conditions may lead to a large (on the order of unity) change in ϕ_*. Accordingly, the jump ΔI is also highly sensitive to the initial conditions. That is why we can treat ϕ_*, h_*, and ΔI as random quantities. We can determine their probability distributions taking into account the fact that the quantity $\xi = \mathrm{Frac}(h_*/2\pi|b|)$, where Frac is the fractional part of a number, is distributed uniformly over the interval (0, 1) [1, 9].

Using formula (24), we can obtain the probability distribution of ΔI. In particular, the averaged value of ΔI is equal to [9]

$$\langle \Delta I \rangle = -\sqrt{\varepsilon}\frac{s}{2\pi}S(p_*, q_*). \quad (25)$$

Repeated crossings of the resonant surface by the trajectory of the phase point give rise to diffusion-like changes in the adiabatic invariant. During the period, the adiabatic trajectory of a particle intersects the resonant surface at two points, which are symmetric with respect to the $p = 0$ plane. The above analysis shows that, in the lowest order approximation, the averaged jump over the period equals zero.

Let us consider the jumps in the adiabatic invariant at two successive intersections of the resonant surface by the phase trajectory of the particle. Let these inter-

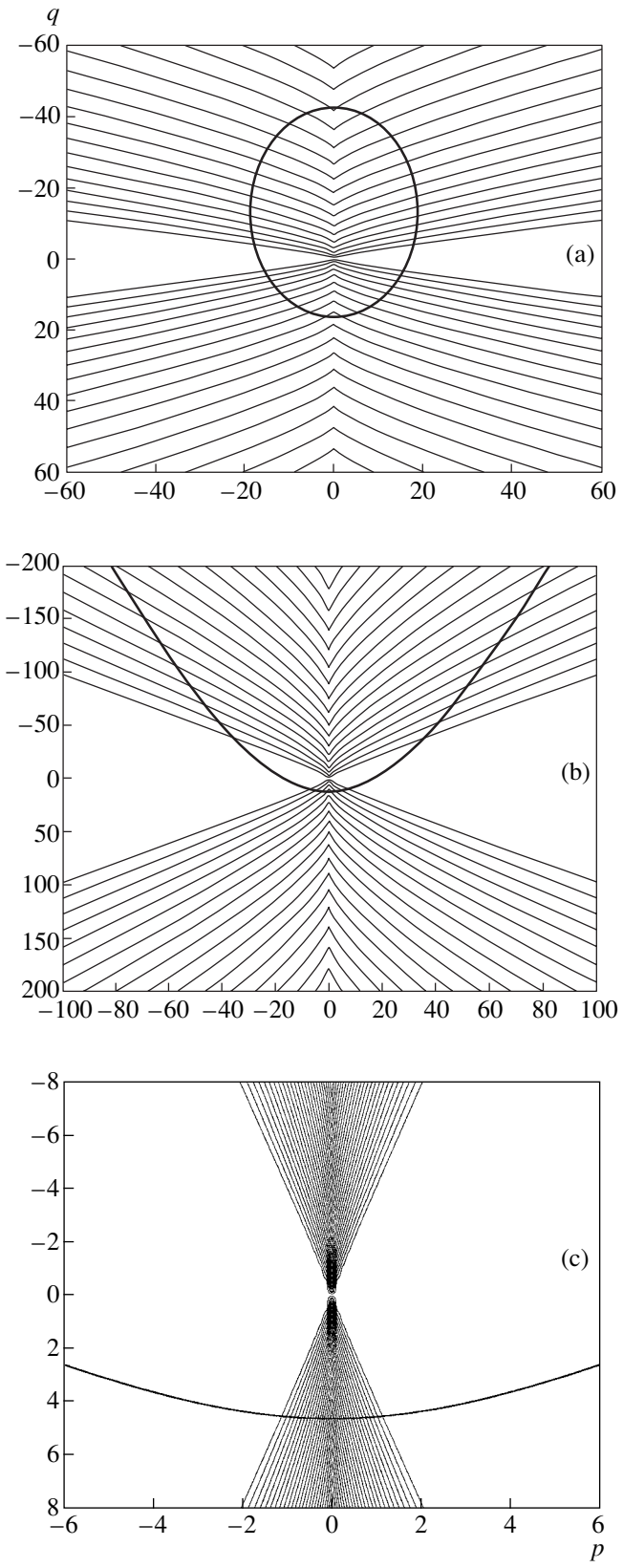

Fig. 6. Isolines of $S(p, q)$ and resonant curves at $\alpha = \pi/4$ and $\mu = 0$ for (a) $k = 1.3$, $\nu = 0.4$, and $\kappa_1 = 0.05$; (b) $k = 1.1$, $\nu = 0.72$, and $\kappa_1 = 0.2$; and (c) $k = 1.3$, $\nu = 0.9$, and $\kappa_1 = 0.4$.

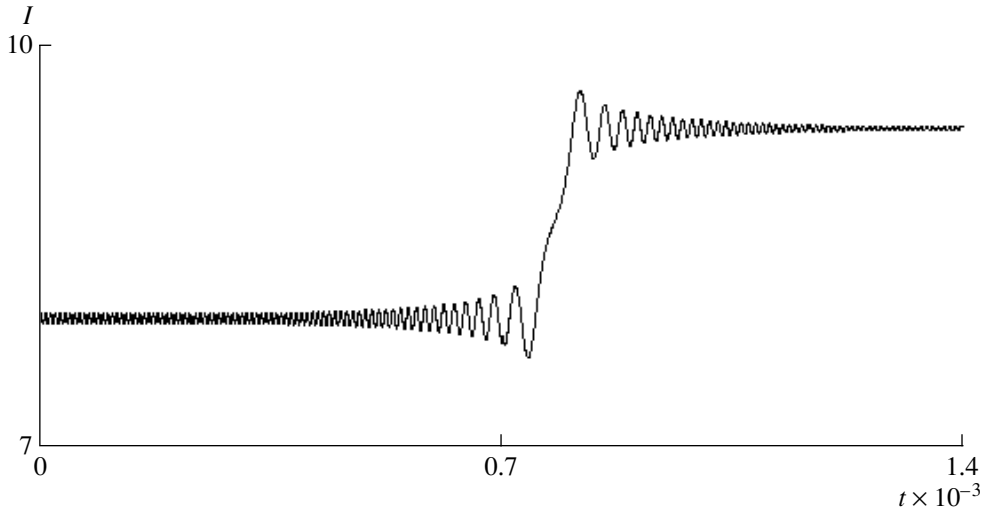

Fig. 7. Jump in the adiabatic invariant at resonance.

sections occur at $\phi_* = \phi_1$ and $\phi_* = \phi_2$, respectively. A small variation $\delta\phi_1$ of the quantity ϕ_1 leads to the following variation of the jump in the adiabatic invariant: $\delta\Delta I \approx \dfrac{\partial}{\partial\phi_*}\Delta I(\phi_*)\delta\phi_1 \sim \sqrt{R}\sqrt{\varepsilon}\,\delta\phi_1$, where R is the characteristic dimension of the adiabatic trajectory and $\Delta I(\phi_*)$ is given by formula (24). As a result, the time of particle motion between two successive passages through the resonant surface changes by $\Delta t \sim \delta\Delta I/\varepsilon$, which produces the variation $\delta\phi_2 \sim \delta\Delta I/\varepsilon$. Therefore, we have $d\phi_2/d\phi_1 \sim \sqrt{R}/\sqrt{\varepsilon} \gg 1$, so that the values ϕ_1 and ϕ_2 can be regarded as independent. Hence, the changes in the adiabatic invariant due to the jumps in it after multiple passages through resonance are of the nature of a diffusion. After the particle has passed through the resonance N times without being trapped, the adiabatic invariant I changes by an amount of about $\sqrt{N}\sqrt{\varepsilon R}$. Consequently, after $N \sim (\varepsilon R)^{-1}$ passages, which occur within a time of about ε^{-2}, the change in I becomes on the order of unity, so that the diffusion coefficient can be estimated as $D \sim \varepsilon^2$.

ACKNOWLEDGMENTS

I am grateful to A.I. Neishtadt for bringing to my attention the problem studied here and for his constant interest in this paper. This work was supported in part by the Russian Foundation for Basic Research (project no. 00-01-00538) and INTAS (grant no. 00-221).

REFERENCES

1. A. P. Itin, A. I. Neishtadt, and A. A. Vasiliev, Physica D (Amsterdam) **141**, 281 (2000).
2. G. R. Smith and A. N. Kaufman, Phys. Fluids **21**, 2230 (1978).
3. C. F. Karney, Phys. Fluids **22**, 2188 (1979).
4. R. Sugihara and Y. Midzuno, J. Phys. Soc. Jpn. **47**, 1290 (1979).
5. G. M. Zaslavskiĭ, A. I. Neishtadt, B. A. Petrovichev, and R. Z. Sagdeev, Fiz. Plazmy **15**, 631 (1989) [Sov. J. Plasma Phys. **15**, 368 (1989)].
6. C. R. Menyuk, A. T. Drobot, K. Papadopoulos, and H. Karimabadi, Phys. Rev. Lett. **58**, 2071 (1987).
7. T. Katsouleas and J. M. Dawson, Phys. Rev. Lett. **51**, 392 (1983).
8. A. A. Chernikov, G. Shmidt, and A. I. Neishtadt, Phys. Rev. Lett. **68**, 1507 (1992).
9. A. I. Neishtadt, *Hamiltonian Systems with Three or More Degrees of Freedom*, Dordrecht: Kluwer, 1999, NATO ASI Ser., Ser. C **533**, 193 (1999).
10. V. I. Arnol'd, V. V. Kozlov, and A. I. Neishtadt, *Mathematical Aspects of Classical and Celestial Mechanics. Dynamic Systems-3* (VINITI, Moscow, 1985).
11. A. I. Neishtadt, Celest. Mech. Dyn. Astron. **65**, 1 (1997).
12. I. M. Lifshits, A. A. Slutskin, and V. M. Nabutovskiĭ, Zh. Éksp. Teor. Fiz. **41**, 939 (1961) [Sov. Phys. JETP **14**, 669 (1961)].
13. V. I. Arnol'd, Usp. Mat. Nauk **18**, 85 (1963).
14. B. V. Chirikov, Dokl. Akad. Nauk SSSR **125**, 1015 (1959).
15. N. N. Bogolyubov and Yu. A. Mitropol'skii, *Asymptotic Methods in the Theory of Nonlinear Oscillations* (Akad. Nauk SSSR, Moscow, 1963; Gordon and Breach, New York, 1962).

Translated by I. A. Kalabalyk

Plasma Physics Reports, Vol. 28, No. 7, 2002, pp. 603–609. Translated from Fizika Plazmy, Vol. 28, No. 7, 2002, pp. 651–658.

PLASMA OPTICS

Moment Aberrations of Magnetoelectrostatic Plasma Lenses

V. I. Butenko and B. I. Ivanov

Kharkov Institute of Physics and Technology, National Science Center, Akademicheskaya ul. 1, Kharkov, 61108 Ukraine

Received November 14, 2001

Abstract—The moment and geometric aberrations of magnetoelectrostatic plasma lenses are studied by computer modeling. Conditions are determined such that these aberrations can be made substantially lower, in which case the cross-sectional area of a focused beam can be reduced by a factor of 10^5 and the ion current density at the focus of a lens can amount to 10^3 A/cm^2. © *2002 MAIK "Nauka/Interperiodica".*

1. INTRODUCTION

The problems associated with the focusing of intense ion beams are important not only for controlled fusion research but also for scientific and engineering fields, such as high-energy physics, acceleration techniques, radiative technology, and implantation metallurgy (see, e.g., [1, 2]). An essential feature of the focusing of intense ion beams is that, in order to prevent the beam ions from expanding, the ion space charge should be neutralized by electrons during both the guiding of a beam and its focusing. For these purposes, it is expedient to use plasma-optic focusing devices (lenses), whose development was initiated by A.I. Morozov *et al.* [3, 4] and, in recent years, has been successfully continued by A.A. Goncharov *et al.* [5–8]. Additional advantages of these lenses are their high focusing power, the possibility of removing geometric aberrations, and the possibility of focusing large-aperture (nonparaxial) beams. At present, the main problems in this area are those of improving such lenses, minimizing aberrations, and maximizing both the focusing efficiency and the focusing power.

The quality of the focusing of charged particles is governed by different types of aberrations. These are geometric aberrations, which depend on the beam radius and the beam injection angle (in [4] and in subsequent papers on the focusing of parallel beams in plasma optics, geometric aberrations are called spherical aberrations or aberrations of finite-width beams); chromatic aberrations, which are associated with the longitudinal momentum of the beam particles; and, in the presence of magnetic fields, aberrations that result from the azimuthal particle motion (in plasma optics, they are called moment aberrations, because they are associated with the particle's angular momentum with respect to the lens axis [4]). It should be noted that, in traditional electron optics (which deals mainly with electron microscopy), the generally accepted terminology is somewhat different [9–11]: chromatic aberrations have the same meaning; the term "moment aberrations" is not used; and geometric aberrations are divided into eight types, notable among which are spherical aberrations (they are independent of the radius of the injected beam and are determined by the beam injection angle with respect to the lens axis) and anisotropic aberrations (these include three types of aberrations that depend on the direction of the magnetic field and its strength).

Moment aberrations in plasma-optic systems were studied theoretically for the case of focusing of compensated ion beams over radial and azimuthal velocities and also for recuperation of such beams [4]. Moment aberrations in electrostatic (or, more precisely, magnetoelectrostatic) plasma lenses were studied experimentally by Goncharov *et al.* [5, 6], who arrived at the following conclusion: in the absence of spherical (geometric) aberrations, a relatively small experimental compression factor of an ion beam (a decrease in the beam radius by a factor of 2–5) can be explained by the moment aberrations that result from the azimuthal rotation of fast ions focused in the magnetic field of a plasma lens and are, in principle, unavoidable.

In the present paper, the moment aberrations in magnetoelectrostatic plasma lenses are considered in more detail by computer simulations with a special-purpose computer program that was devised in order to model a plasma-optics focusing lens. We will be interested in modeling conditions analogous to those under which the experimental data reported in [5–8] were obtained. The computer program presented below, being unable to exactly simulate the experimental lens developed and created in [5–8], makes it possible, however, not only to model the main operating modes of the lens, its focusing properties, and its moment and geometric aberrations but also to give recommendations for the ways of removing these aberrations.

2. FORMULATION OF THE PROBLEM

In our earlier paper [12], a Morozov plasma lens in which the magnetic field is produced by a single current loop was thoroughly investigated through computer

1063-780X/02/2807-0603$22.00

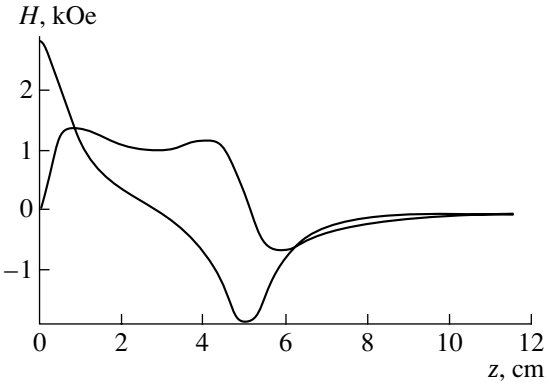

Fig. 1. Longitudinal profiles $H_z(z)$ and $H_r(z)$ calculated at a radius of 5.7 cm in the region around the ring electrodes of the lens with the above parameters and with the current J_c = 10 kA in the central coil.

modeling. In experimental papers [5–8], the reference electrodes (with which the electric potentials were applied to the plasma) were localized near the central plane of a lens by using three short solenoids carrying opposite currents. Here, we model this configuration by three loops with opposite currents. In contrast to [12], we take into account the azimuthal motion of the focused particles, which gives rise to moment aberrations. We consider an axisymmetric lens. Note that Morozov plasma lenses are studied theoretically under the assumption that there is no current across the magnetic field and that the magnetic surfaces coincide with the equipotential surfaces of the electric field. In this case, the strength of the electric field and its spatial distribution in a plasma are governed completely by the magnetic field geometry and by the boundary conditions, which are usually imposed on the externally defined electric potential Φ in the form of a continuous function $\Phi(R, z)$, where R is the radius of a cylindrical surface around the plasma. In practice [5–8], the electric potentials Φ_n applied to the plasma are generated by n reference ring electrodes of radius R, which give rise to a set of equipotential surfaces of the electric field in the plasma. Note that, in experimental investigations, it is very desirable to carry out direct measurements in order to control and to correct for the calculated optimum strength and optimum distribution of the electric field in the plasma.

The magnetic field created by the current J in a ring of radius a_c, with its center at the point l on the z-axis, is described by the azimuthal component of the vector potential (see [13], Section 4):

$$A_\varphi = \frac{4J}{ck}\sqrt{\frac{a_c}{r}}\left[\left(1-\frac{k^2}{2}\right)K(k)-E(k)\right],$$
$$k^2 = \frac{4a_c r}{(a_c+r)^2+(z-l)^2}, \quad (1)$$

where c is the speed of light and K and E are complete elliptic integrals of the first and second kind, respectively.

In an axisymmetric lens, the magnetic surfaces satisfy the equation (see [13], Section 3)

$$rA_\varphi = \text{const}. \quad (2)$$

We calculated the magnetic surface topography for different ratios between the opposite currents in the central coil (J_c) and in two side coils (J_s), the center of the central coil and the centers of the side coils being at $z = 0$ and $z = \pm 5$ cm. In this case, the equation for the magnetic surfaces can be written as

$$rA_\varphi(r, z) = rA_{\varphi, c} - rA_{\varphi, l} - rA_{\varphi, r} = \text{const}, \quad (3)$$

where $A_{\varphi, c}$, $A_{\varphi, l}$, and $A_{\varphi, r}$ are the vector potentials of the fields produced by the central, left, and right coils, respectively. The numerical results presented below were obtained for $J_c = -1.5J_s$, in which case the magnetic field line topography is appropriate for our purposes.

Figure 1 shows the longitudinal profiles $H_z(z)$ and $H_r(z)$ calculated at a radius of 5.7 cm in the region around the ring electrodes of the lens with the above parameters and with J_c = 10 kA.

The density and other parameters of the plasma that fills the lens and through which an ion beam propagates are chosen so as to ensure complete neutralization of the beam space charge and to create the required focusing fields (these questions were thoroughly discussed in [3, 4]). In the central region of the lens (–2.8 cm < z < 2.8 cm), i.e., in the region bounded by separatrices (at which the magnetic field vanishes) and by a cylindrical surface of radius R, the optimum (for ion focusing) distribution of the electric potentials over the magnetic surfaces is produced by ring electrodes introduced into the plasma at the radius R. In the region $r > R$, the magnetic surfaces are free of electric charges, which can be ensured, e.g., by placing a special annular insulator at a radial position $R_1 > R$ on the outside of the ring electrodes. Thereby, the electric field of the lens is prevented from being short-circuited to the wall of the vacuum chamber. Instead, it is the magnetic field lines to the left and to the right of the central region that are assumed to be short-circuited to the wall and/or the special electrodes. The topography of the equipotential surfaces of the electric field, calculated for $J_c = -1.5J_s$, is shown in Figs. 2 and 3 (see below).

3. BASIC EQUATIONS

We express the components of the electric and magnetic fields in terms of the so-called magnetic flux function [4]

$$\Psi(r, z) = rA_\varphi(r, z). \quad (4)$$

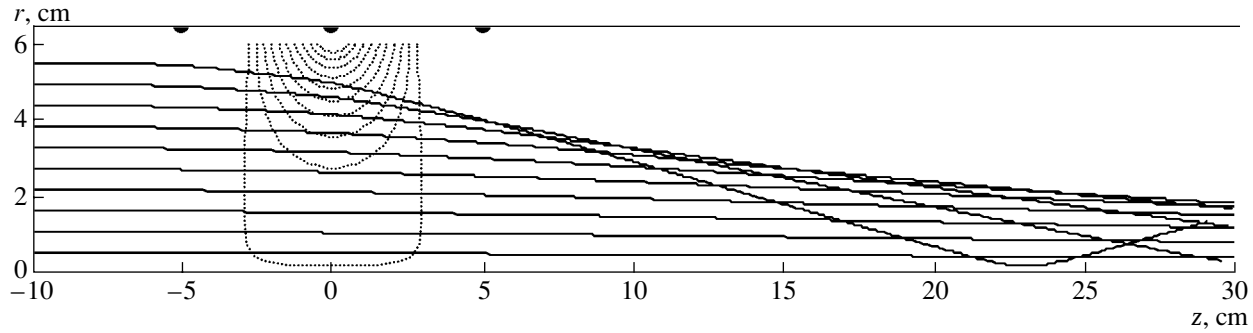

Fig. 2. Trajectories of 20-keV protons in the absence of an electric field. The beam radius is 5.5 cm, J_c = 30 kA, and the coordinate of the proton injector is z_i = –20 cm.

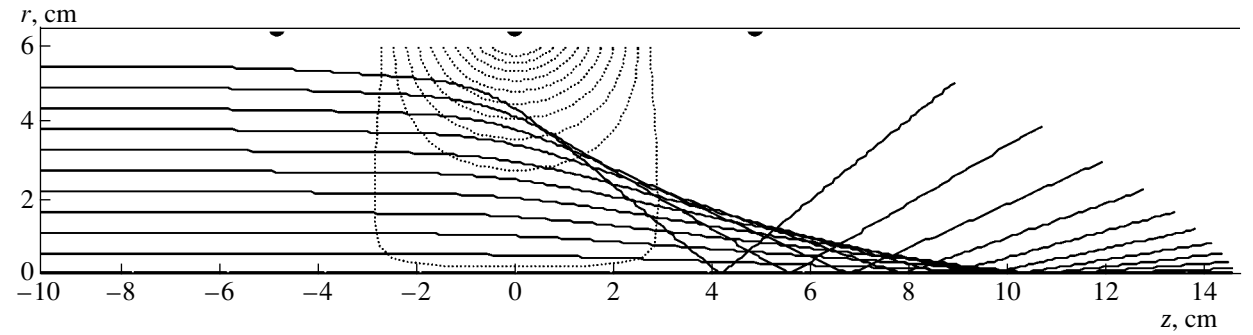

Fig. 3. Proton trajectories for a lens with the parabolic radial potential profile $\Phi = 1.5r^2$ in the cross section $z = 0$ (in the Gauss system of units). The remaining parameters are the same as in Fig. 2.

In the plasma of a Morozov lens, the electric potential Φ is assumed to change in a prescribed manner from one magnetic surface to another. This change is described by the relationship

$$\Phi(r, z) = F(\Psi), \tag{5}$$

in which case the electric- and magnetic-field components can be written as

$$B_r = -\frac{1}{r}\frac{\partial\Psi}{\partial z}, \quad B_z = \frac{1}{r}\frac{\partial\Psi}{\partial r}, \tag{6}$$

$$E_r = -\frac{\partial\Phi}{\partial r} = -\frac{dF}{d\Psi}\frac{\partial\Psi}{\partial r} = -r\frac{dF}{d\Psi}B_z, \tag{7}$$

$$E_z = -\frac{\partial\Phi}{\partial z} = -\frac{dF}{d\Psi}\frac{\partial\Psi}{\partial z} = r\frac{dF}{d\Psi}B_r. \tag{8}$$

The equations of motion in cylindrical coordinates have the form

$$\frac{dV_r}{dt} = \frac{q}{M}E_r + \frac{q}{Mc}V_\varphi B_z + \frac{V_\varphi^2}{r}, \tag{9}$$

$$\frac{dV_z}{dt} = \frac{q}{M}E_z - \frac{q}{Mc}V_\varphi B_r, \tag{10}$$

$$\frac{dV_\varphi}{dt} = \frac{q}{Mc}(V_z B_r - V_r B_z) - \frac{V_r V_\varphi}{r}. \tag{11}$$

Substituting the expressions for the electric- and magnetic-field components into these equations, we obtain

$$\frac{dV_r}{dt} = \frac{q}{M}E_r + \frac{q}{Mc}V_\varphi B_z + \frac{V_\varphi^2}{r}, \tag{12}$$

$$\frac{dV_z}{dt} = \frac{q}{M}B_r\left(r\frac{dF}{d\Psi} - \frac{1}{c}V_\varphi\right), \tag{13}$$

$$\frac{dV_\varphi}{dt} = \frac{q}{Mcr}\left(-V_z\frac{\partial\Psi}{\partial z} - V_r\frac{\partial\Psi}{\partial r}\right) - \frac{V_r V_\varphi}{r}, \tag{14}$$

where q and M are the charge and mass of an ion and V is its velocity (the calculations described in this paper were carried out for protons).

For a homogeneous monoenergetic ion beam injected parallel to the lens axis, the initial conditions (at $t = 0$) have the form

$$V_z = V_0, \quad V_r = V_\varphi = 0, \quad z = z_i \quad (z_i < 0), \quad r = r_i, \tag{15}$$

where z_i is the coordinate of the end of the injector and the radius r_i at which an ion is injected is varied from

zero to a value somewhat smaller than the radius R of the reference electrodes, which, in turn, is smaller than the radius a_c of the current-carrying coils.

The boundary conditions are imposed by specifying the radial profile $\Phi(r, 0)$ of the electric potential in the plane of the central coil:

$$\Phi = B_1 r^2 + B_2 r^4 + B_3 r^6 + \ldots. \quad (16)$$

The profile was optimized by choosing the dimensional coefficients B_n so as to minimize the geometric aberrations [see profiles (17) and (18) below]. If necessary, the optimized profile was recalculated into the potential distribution $\Phi(R, z)$ over a cylindrical surface. (It is precisely the boundary conditions that are expected to be the principle cause of a discrepancy between the lens modeled theoretically and the actual one. It seems that this discrepancy may be resolved by using adequate methods for measuring the strength of the electric fields and their spatial distribution in the plasma.)

From the standpoint of computational mathematics [14], Eqs. (12)–(14) with the initial and boundary conditions (15) and (16) may themselves be regarded as a solution to the problem as formulated in our model. Thus, the corresponding first integrals of the problem reflect the laws of conservation of the total energy and the moment of the generalized momentum (see, e.g., [15]). We calculated the trajectories of the ions and their velocities by integrating Eqs. (12)–(14) directly and by checking the calculated results against these conservation laws. As will be shown below, it is possible in this way to establish a relation between the moment aberrations and the law of conservation of the moment of the generalized momentum of an ion with respect to the z-axis.

Formulas (1)–(16) served as the basis for devising a special-purpose program—a computer model of a plasma-optics focusing device, which was used to trace ion trajectories in a plasma lens and to investigate the dependence of momentum and geometric aberrations on the parameters of the lens and of the ion injector. The images displayed on the screen of a conventional personal computer allowed us to observe the ion focusing dynamics over a time of about ten seconds and correct it rapidly (in a time as short as several minutes).

4. ION FOCUSING BY BOTH ELECTRIC AND MAGNETIC FIELDS IN A MOROZOV LENS

As a rule, aberrations are calculated by the method of perturbations of the trajectories of paraxial ions [4, 9–11]. Computer modeling makes it possible to investigate the focusing of large-aperture (nonparaxial) beams in strong magnetic fields, in which case moment and geometric aberrations of a lens are significant. In such simulations, a Morozov lens should be assumed to be magnetoelectrostatic, because the ions are focused both by the electric field and, to a lesser extent, by the magnetic field, which, in addition, gives rise to moment aberrations. As an example, we consider ion focusing in a Morozov plasma lens with the following parameters: the radius of a proton beam is 5.5 cm, the radius of the current-carrying coils is 6.5 cm, the current in the central coil is 30 kA (this corresponds to 3×10^4 ampere-turns of an equivalent short solenoid), and the coordinate of the proton injector is $z_i = -20$ cm. Figure 2 shows the trajectories of protons focused by a purely magnetic lens (with the electric field switched off). In this case, the influence of moment aberrations can be seen in the fact that azimuthally moving protons do not pass through the lens axis. We also simulated proton trajectories under the same conditions but for $z_i = -50$ cm and found that moment aberrations practically disappear, whereas geometric aberrations do not. As will be shown below, this effect can be explained in terms of the conservation law for the moment of the generalized momentum of a charged particle.

Figure 3 shows proton trajectories calculated for the above conditions but in the presence of an electric field whose potential has a parabolic profile in the plane of the central coil (such a profile is regarded as being nearly optimum [7]):

$$\Phi = 1.5r^2. \quad (17)$$

We can see that the electric field potential with profile (17) ensures the focusing of paraxial protons, while the nonparaxial character of the beam is the source of significant geometric aberrations, which, in turn, can be reduced by invoking the next-order terms in polynomial (16). Figure 4a shows (on an enlarged scale) proton trajectories in the focal region in the presence of an electric field that is optimized by choosing the coefficients of polynomial (16) so as to minimize geometric aberrations and whose potential has the following radial profile in the plane of the central coil:

$$\Phi = 1.5r^2 - 0.015r^4 - 0.00033r^6. \quad (18)$$

This profile was adjusted to fit the focusing by both electrostatic and magnetic fields. The corresponding radial profile of the proton current density is shown in Fig. 4b. In a stronger (or weaker) magnetic field, the focusing is appreciably worse. Hence, in the case in question, a Morozov plasma lens is to be regarded as a magnetoelectrostatic lens with intrinsic moment and geometric aberrations.

5. DEPENDENCE OF MOMENT ABERRATIONS ON THE FOCUSING CONDITIONS AND LENS PARAMETERS

Different types of aberrations can be treated as being independent of each other provided that they are sufficiently low (see [11], Section 5.7). Hence, having minimized geometric aberrations, we can switch to the investigation of moment aberrations. Let us consider how they depend on the focusing conditions in a lens

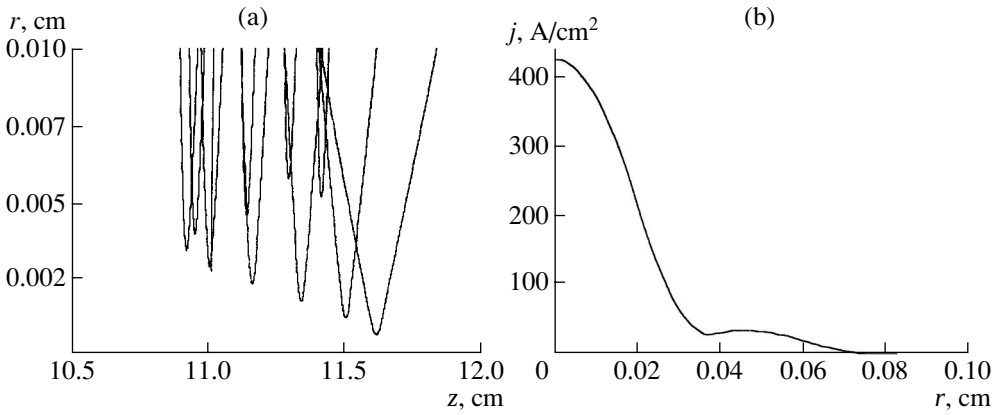

Fig. 4. (a) Proton trajectories and (b) radial proton current density profile in the focal region for $z_i = -20$ cm, $J_c = 30$ kA, a beam radius of 5.5 cm, and the optimized radial profile (18) of the potential Φ (in the Gauss system of units). The spread of protons in the radial and longitudinal coordinates is governed by the moment and geometric aberrations, respectively.

with the parameters adopted in the previous section. Figure 5 shows the dependence of the minimum radius r of a proton trajectory in the focal region on both the radius r_i at which the proton is injected and the coordinate z_i of the injector. The calculations were carried out for a fixed current in the central coil ($J_c = 30$ kA). As may be seen, the moment aberrations increase as the injection radius increases and as the injector is displaced toward the region of stronger longitudinal magnetic field created by the current loops of a lens. As the injector is moved farther away from the current loops, the moment aberrations fall to zero.

In order to investigate the dependence of moment aberrations on the magnetic field in a Morozov lens, we carried out a series of computations for the following conditions: the beam radius was 3.5 cm, the radius of the reference electrodes was 3.7 cm, the coordinate of the injector was $z_i = -15$ cm, and the radial potential profile was

$$\Phi = 1.5r^2 - 0.017r^4. \quad (19)$$

We numerically traced proton trajectories in magnetic fields of different strengths by increasing the current J_c in the central coil from 1 to 30 kA, in which case, the current density at the focus of a lens decreased from 2600 to 10 A/cm^2 as a result of moment aberrations. Figure 6 shows the dependence of the minimum radius r of a proton trajectory in the focal region on both the radius r_i at which the proton is injected and the magnetic field of a lens (or, equivalently, the current J_c in the central coil).

According to our computer modeling, the moment aberrations increase as the beam injection radius and the magnetic field of a lens increase and as the ion injector is displaced toward the lens. Along the calculated ion trajectories, the conservation law for the moment of the generalized momentum,

$$P_\varphi = r\left(MV_\varphi + \frac{q}{c}A_\varphi\right) = \text{const} \quad (20)$$

(in electronics, an analogous relationship is known as the Busch theorem), and the conservation law for the total energy are both satisfied to within five significant decimal digits.

An important point to note is that the ion gyroradius is not small in comparison with the characteristic dimensions of the lens under investigation. The gyrora-

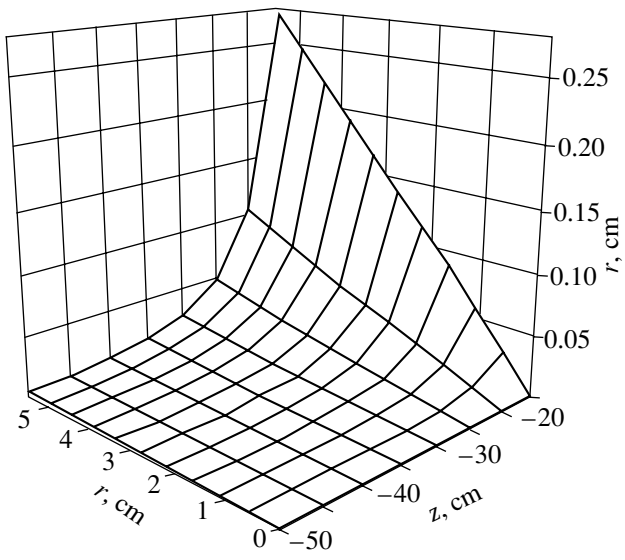

Fig. 5. Dependence of the minimum radius of a proton trajectory in the focal region on the radius at which the proton is injected and on the coordinate of the injector for a fixed current in the central coil ($J_c = 30$ kA).

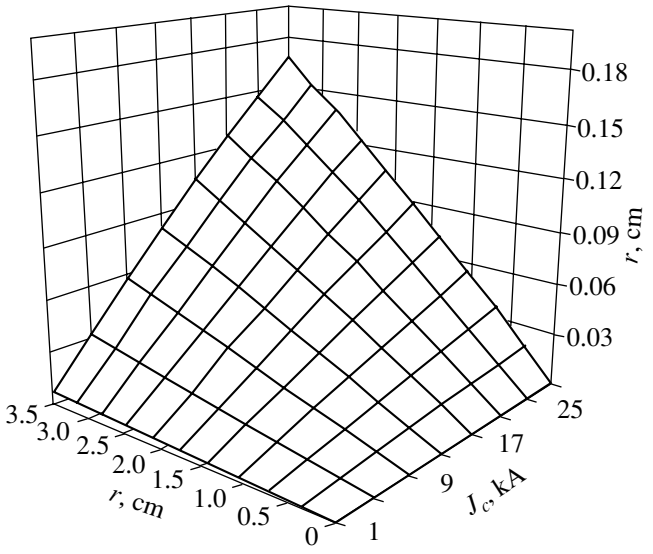

Fig. 6. Dependence of the minimum radius of a proton trajectory in the focal region on the radius at which the proton is injected and on the current in the central coil. The beam radius is 3.5 cm, the radius of the reference electrodes is 3.7 cm, the coordinate of the injector is $z_i = -15$ cm, and the electric potential profile is $\Phi = 1.5r^2 - 0.017r^4$ (in the Gauss system of units).

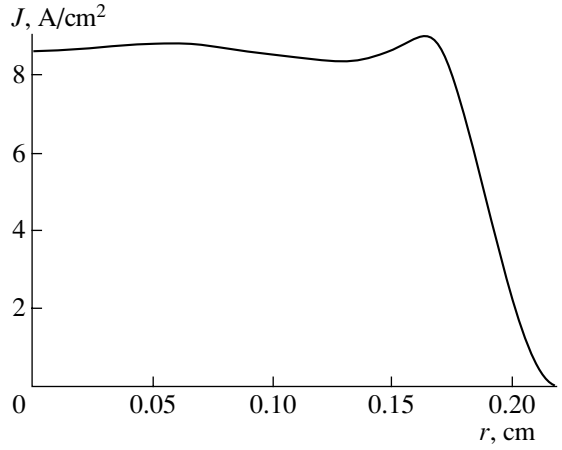

Fig. 7. Steplike radial profile of the ion current density in the focal plane for a beam radius of 3.5 cm, the remaining parameters being $z_i = -20$ cm, $J_c = 30$ kA, and $\Phi = 1.5r^2 - 0.023r^4$ (in the Gauss system of units).

dius of the plasma electrons, in contrast, is fairly small (for the characteristic lens parameters, it is about 0.1 mm). The electrons drift in the azimuthal direction in crossed electric and magnetic fields, in which case their guiding centers move along the corresponding magnetic surface (see [15], Section 3).

The conservation law (20) implies that, in order for a parallel particle beam to be focused into the focal point of a lens, it suffices that the initial azimuthal velocities of the particles be zero and that the magnetic field vanish in the injection region and in the focal plane. The lenses used in the experiments of [5–8] satisfy all these conditions. Consequently, the reasons for an insufficient focusing of the ion beams in [5–8] lie not in the moment aberrations but in other effects. Preliminary results from computer modeling show that one of the reasons for this may be an insufficient optimization of the focusing fields over the lens volume.

Of course, ordinary vacuum magnetic lenses are also not devoid of moment aberrations (see Fig. 2 as an example). However, it should be noted that monographs [9–11] on traditional electron and ion optics contain no information about investigations of the aberrations under discussion.

6. PLASMA LENSES AND ENGINEERING APPLICATIONS OF ION BEAMS

The above results show that, in magnetoelectrostatic plasma lenses, moment aberrations can readily be removed by placing an ion injector in a region of a zero magnetic field, while geometric aberrations can be appreciably reduced by choosing an optimum distribution of the radial electric field $E_r(r, z)$ over the lens volume. Under the above assumptions, the ion current density at the focus is calculated to be as high as $\sim 10^3$ A/cm^2 for an injection current of 1 A, and the cross-sectional area of a focused beam can be reduced by a factor of about $\sim 10^5$. In the experiments of [5–8], the beam's cross-sectional area was reduced by a factor of about 30 and the achievable ion current density was about 0.1 A/cm^2 for an injection current of 0.1–1 A. For high-dose ion implantation, the aim is to achieve a compression factor of about $\sim 10^3$ [8]. Our investigations show that the results from computer modeling of experimental devices by using special-purpose computer programs may be helpful in making the ion focusing substantially stronger. We stress that, in order to reduce the cross-sectional area of a focused beam to the maximum possible extent, the accuracy with which the prescribed optimum distribution $E_r(r, z)$ is maintained should be sufficiently high [see formulas (18), (19)].

As for moment aberrations, they can be effectively employed for a uniform exposition of samples with finite area (fractions of a square centimeter). By arranging an ion injector in such a way that its exit end occurs either at a certain distance from the lens or within a special solenoid with a controllable longitudinal magnetic field, it is possible to form a steplike radial profile of the ion current density in the focal plane. Figure 7 shows an example of the radial profile $j(r)$ for which the ion current density $j \simeq 10$ A/cm^2 is distributed fairly uniformly over the radial interval from 0 to 0.16 cm and is higher than the initial current density by a factor of approximately 340. Numerical modeling shows that an ion beam focused under these conditions remains laminar

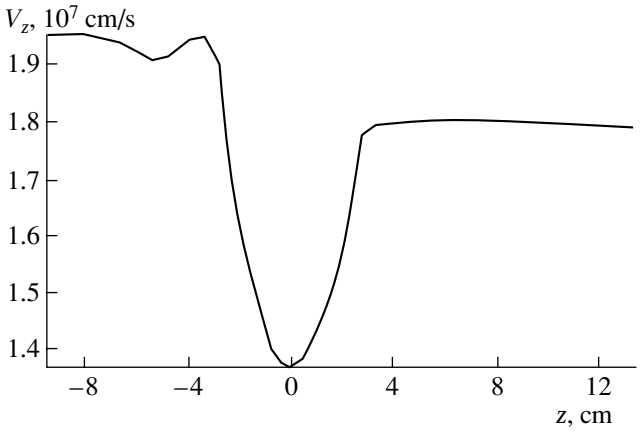

Fig. 8. Change in the longitudinal velocity of protons injected at a radius of 5.5 cm during the focusing. The lens parameters are the same as in Fig. 4.

(i.e., the ion trajectories do not intersect); moreover, the ion beam radius in the focal plane is proportional to the ion beam radius in the injection plane. As the injector is displaced farther away from the lens, the radius of the focal spot decreases, the ion density in the focal plane increases, and the profile $j(r)$ remains close to a steplike profile.

In conclusion, note that the longitudinal ion velocity in the focal plane is fairly nonuniform: it decreases away from the lens axis, at which it is equal to the initial longitudinal velocity ($V_z = V_{z0}$). This decrease is associated, first of all, with the radial focusing ($V_z \approx V_{z0}\cos(\arctan r_i/L_f)$, where L_f is the focal length and r_i is the radius at which an ion is injected) and, to a lesser extent, with the azimuthal ion motion. An example of the calculated velocity $V_z(z)$ is shown in Fig. 8, in which we can see, in particular, how the velocity of the ions changes when they pass through the lens. In order to reduce the longitudinal velocity spread of an ion beam in the region where the sample is placed (e.g., in the case of implantation of separate parallel ion layers), it is necessary to increase the focal length severalfold, in which case it is sufficient to decrease the coefficients of polynomials (18) and (19) for the profile $\Phi(r)$ in the same proportion.

ACKNOWLEDGMENTS

We are grateful to V.I. Karas' for a discussion of the results and useful advice.

REFERENCES

1. M. D. Gabovich, N. V. Pleshivtsev, and N. N. Semashko, *Ion and Atom Beams for Controlled Nuclear Fusion and Processing Purposes* (Énergoatomizdat, Moscow, 1986).
2. G. Hairapetian, AIP Conf. Proc. **335**, 174 (1995).
3. A. I. Morozov, in *Plasma Accelerations and Ionic Injectors* (Nauka, Moscow, 1984), p. 82.
4. A. I. Morozov and S. V. Lebedev, in *Reviews of Plasma Physics*, Ed. by M. A. Leontovich (Atomizdat, Moscow, 1974; Consultants Bureau, New York, 1980), Vol. 8.
5. A. Goncharov, A. Dobrovolskii, I. Litovko, *et al.*, in *Proceedings of the 17th International Symposium on Discharges and Electrical Insulation in Vacuum (ISDEIV), Berkeley, 1996*, Vol. 2, p. 570.
6. A. Goncharov, S. Gubarev, A. Dobrovolskii, *et al.*, in *Proceedings of the 18th International Symposium on Discharges and Electrical Insulation in Vacuum (ISDEIV), Eindhoven, 1998*, p. 625.
7. A. A. Goncharov, A. N. Dobrovol'skiĭ, A. N. Kotsarenko, *et al.*, Fiz. Plazmy **20**, 499 (1994) [Plasma Phys. Rep. **20**, 449 (1994)].
8. A. A. Goncharov, I. M. Protsenko, G. Yu. Yushkov, and I. G. Brown, Appl. Phys. Lett. **75**, 911 (1999).
9. W. Glaser, *Grundlagen der Elektronenoptik* (Springer-Verlag, Vienna, 1952; Gostekhizdat, Moscow, 1957).
10. V. M. Kel'man and S. Ya. Yavor, *Electron Optics* (Nauka, Leningrad, 1988).
11. M. Szilagyi, *Electron and Ion Optics* (Plenum, New York, 1988; Mir, Moscow, 1990).
12. V. I. Butenko and B. I. Ivanov, Fiz. Plazmy **27**, 540 (2001) [Plasma Phys. Rep. **27**, 511 (2001)].
13. A. I. Morozov and L. S. Solov'ev, in *Reviews of Plasma Physics*, Ed. by M. A. Leontovich (Gosatomizdat, Moscow, 1963; Consultants Bureau, New York, 1966), Vol. 2.
14. A. A. Samarskiĭ and Yu. P. Popov, in *Cybernetics: Modern State* (Nauka, Moscow, 1980), p. 89.
15. A. I. Morozov and L. S. Solov'ev, in *Reviews of Plasma Physics*, Ed. by M. A. Leontovich (Gosatomizdat, Moscow, 1963; Consultants Bureau, New York, 1966), Vol. 2.

Translated by I. A. Kalabalyk

Plasma Physics Reports, Vol. 28, No. 7, 2002, pp. 610–614. Translated from Fizika Plazmy, Vol. 28, No. 7, 2002, pp. 659–663.

NONLINEAR PHENOMENA

Plasma Approach to Describing the Electric Dynamics of a Neuron

A. A. Berezin

Oil and Gas Research Institute, Gubkin State Academy of Oil and Gas, Leninskiĭ pr. 65, Moscow, 117917 Russia

Received April 19, 2001; in final form, January 13, 2002

Abstract—The electric excitation of a neuron is interpreted as the formation of a nonlinear solitary ion acoustic wave of the charge density of sodium and hydrogen ions in an electrolytic intracellular fluid, which is treated as a dense plasma. It is shown that such a wave can be described by the coupled sine-Gordon and Korteweg–de Vries equations, having a solution in the form of a soliton whose internal vibrational structure is described by the Fermi–Pasta–Ulam spectrum. It is concluded that a nerve impulse can be interpreted as a low-frequency solitary wave of the charge density of sodium ions with a trapped high-frequency charge density wave of protons. © *2002 MAIK "Nauka/Interperiodica".*

1. INTRODUCTION

Neurons, or nerve cells, are building blocks of the brain. Although their internal structure, as well as genetic and biochemical properties, is analogous to all other cells, they have unique features that differ them from the others. An important property of neurons is their ability to respond to nerve impulses. The internal potential of a neuron with respect to the surrounding medium is equal to –70 mV [1]. This "resting potential" results from the ion gradient created by a "sodium pump" and is also associated with a certain class of permanently open channels that are selectively permeable to potassium ions. The density of potassium ions accumulated in the intracellular fluid by this mechanism is one order of magnitude higher than that in the surrounding medium. As a result, a potential difference of 70 mV is established. Neurons can be excited by ingoing nerve impulses and are capable of generating electric pulses at very different repetition rates: from one pulse to several hundred pulses per second. All of the generated pulses have the same amplitude. Traditionally, the electric activity of an individual neuron is described by the Hodgkin–Huxley model [2]. In this way, according to the Hartley formula, the information capacity of a neuron is equal to $\log_2 2 = 1$ bit. In other words, a neuron is treated as a system with two possible (passive and active) states, and the functioning of the human brain is ascribed to its ability to process enormous amounts of information in parallel. At the same time, in a number of papers [3, 4], it has been reported that there are correlations between the concentrations of both ribonucleic acid (RNA) and some proteins in neurons on the one hand, and the learning process in higher animals on the other hand. In this case, in the context of the amount of information per RNA code triplet (or codon), $\log_2 4 = 2$ bit, a simple estimate of the information capacity of an RNA molecule in a neuron yields a value of 10^{10}–10^{11} bits per neuron [5].

The purpose of this paper is to model an individual neuron in the brain as a generator of solitary ion waves in an intracellular fluid. Being a strong electrolyte, the intracellular fluid within a neuron is treated as a dense plasma, and the neuron itself is treated as an object capable of storing up to 10^{11} bits of information. It is proposed that the role of the main dynamic information carrier is played by the Fermi–Pasta–Ulam (FPU) recurrence [6].

The existing traditional theories of aqueous solutions of electrolytes are valid only for dilute solutions in which the ions do not interact with each other. The higher the electrolyte concentration, the more important the role of ion–ion interaction and the more complicated the situation. Attempts to develop a theory of strong electrolytes have yet been unsuccessful.

It should be noted that aqueous solutions of electrolytes are inherent in all living organisms. Thus, in the human organism, they make up 65–70%, of which two-thirds is an intracellular fluid and the remaining is blood plasma and lymph. The ion content of these aqueous solutions is close to that of sea water [7], which is a strong electrolyte, because the concentration of NaCl in it is about 0.2 mole per liter.

Being strong electrolytes, sea water, blood plasma, and intracellular fluid can all be treated as a dense plasma. This approach makes it possible to describe these three types of fluid in the language of the nonlinear properties of the fourth state of matter.

1063-780X/02/2807-0610$22.00

2. MODEL OF THE FORMATION OF HIGH-FREQUENCY WAVES OF PROTON SPACE CHARGE IN A NEURON

Let us consider a neuron as an object filled with a strong electrolyte of intracellular fluid. The dynamics of ion concentrations in a neuron will be analyzed using the Frank and Wen's cluster model of an electrolyte of sea water [8]. In this model, it is assumed that each sodium ion is surrounded by an ion atmosphere containing four water molecules and that the ion atmosphere around each chlorine ion has two water molecules (see figure). Then, we consider a one-dimensional chain of Na^+ and Cl^- ions near the inner surface of the membrane of a neuron, as is shown in the figure. In what follows, the analysis will be restricted to the vibrations that occur near the membrane.

An electrical activation of a neuron perturbs ion concentrations in the intracellular fluid, in particular, the concentrations of protons and OH^- ions, whose mobilities are almost one order of magnitude higher than those of the remaining ions. The anomalously high mobility of protons and hydroxyl ions is explained in terms of the model developed by Grotthuss [9] in order to describe the nonlinear processes of the "relay-race jump" of a proton between neighboring water molecules. We assume that, as a result of activation of a neuron, a proton jumps in the field of the ion atmospheres of Na and Cl ions (in which case the corresponding OH^- ion jumps in the opposite direction). Then, in accordance with Poisson's equation for a strong electrolyte [9] in the Debye–Hückel theory, the potential φ_H experienced by a proton in the field of the ion atmospheres of Na and Cl ions (the proton is closer to the Cl ion) can be written as a sum of the attractive and repulsive components [8]:

$$\varphi_H = \frac{a}{b}[\exp(-br_n) - 1] + ar_n, \tag{1}$$

where $b = \sqrt{\frac{8\pi n_0}{\varepsilon kT}}$, $a = \frac{e^2}{\varepsilon r_0}\sqrt{\frac{8\pi n_0}{\varepsilon kT}}$, e is the charge of an electron, n_0 is the concentration of sodium ions, ε is the permittivity of water, r_0 is the distance between sodium and chlorine ions in the chain, and $r_n = x_n - x_{n-1}$, x_n being the shift of the nth proton in the chain.

With allowance for representation (1), the equations for the dynamics of a proton in the chain (see figure) can be described by the Toda chain of equations [10]

$$m_H\frac{d^2x_n}{dt^2} = a\{\exp[-b(x_n - x_{n-1})] - \exp[-b(x_{n-1} - x_n)]\}, \tag{2}$$

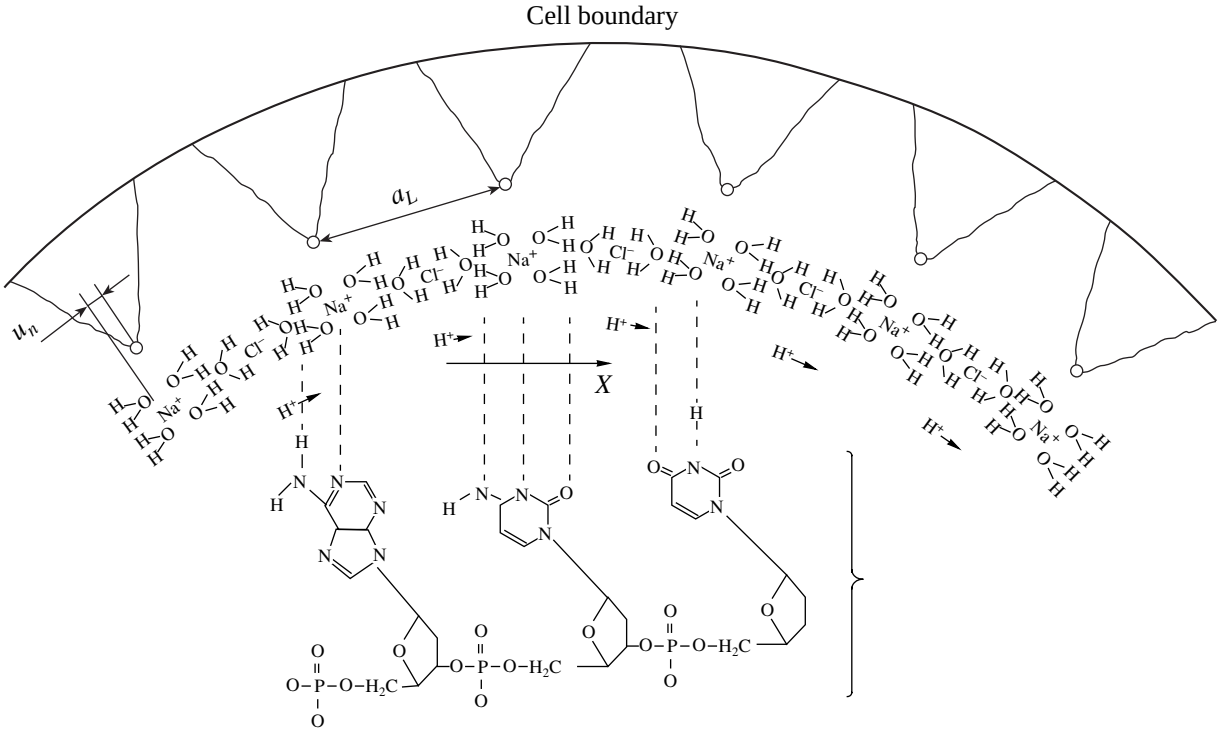

Model dynamics of the ion concentrations in an individual neuron: a_L is the distance between neighboring lipid molecules, u_n is the displacement of a Na^+ ion with respect to a protein molecule in the lower layer of the membrane, $H^+ \longrightarrow$ is the direction of the jumps of protons along a chain of water molecules (the jumps of the corresponding group of OH^- ions in the opposite direction are not shown), and the brace indicates a part of an RNA molecule in a neuron.

where m_H is the mass of a proton. In Eqs. (2), the wavelength is small in comparison with the radius of curvature of the neuron cell body.

Toda [10] showed that, in the long-wavelength limit, Eqs. (2) can be reduced to the Korteweg–de Vries (KdV) equation

$$\frac{\partial u_H}{\partial \tau} - 6u_H\frac{\partial u_H}{\partial \xi} + \frac{\partial^3 u_H}{\partial \xi^3} = 0,$$
$$u_H = 2br_n, \quad \xi = \frac{x - c_H t}{h_t}, \quad h_t = \frac{x}{n}, \tag{3}$$
$$c_H = h_t\sqrt{\frac{ab}{m_H}}, \quad \tau = \frac{c_H t}{24h_t}.$$

The periodic boundary conditions for the charge density wave of protons described by Eq. (3) have the form

$$u_H(\xi, \tau) = u_H(\xi + L_n, \tau), \tag{4}$$

where $L_n = 2\pi R_n$, R_n being the inner radius of the neuron cell body.

Zabusky and Kruskal [11] showed that Eq. (3) with boundary conditions (4) has a solution in the form of the FPU recurrence. In the model proposed in the present paper, the charge density wave of protons in a neuron can be modulated in accordance with the sequence of nitrogen bases in an RNA molecule (see the brace in the figure).

3. MODELING OF A LOW-FREQUENCY CHARGE DENSITY WAVE OF SODIUM IONS IN A NEURON

The next step in the development of the model is a formal description of a high-frequency information signal in the low-frequency component of a nerve impulse. As was shown in [12], charge density waves can be described by the sine-Gordon equation. With this circumstance in mind, we apply the sine-Gordon equation to describe the dynamics of the charge density waves of sodium ions. For this purpose, let us consider the membrane of a neuron as a liquid crystal containing a double layer [13] (see figure). In accordance with the distance between lipid molecules in the membrane and also a distance of 0.47 nm (the distance between sodium ions in an electrolyte) [9, 14], a possible mechanism for the interaction of the high-frequency charge density waves of protons with a low-frequency ion wave of the action potential can be described as follows. Let us denote by u_n the displacement of a Na^+ ion with respect to a protein molecule in the lower layer of the membrane (see figure). In this way, the ion dynamics in a neuron can be analyzed using the approach developed by Frenkel' and Kontorova [15] in order to describe the dynamics of dislocations in crystals.

Let us also denote by $U(u_n)$ the potential exerted by an immobile chain of lipid molecules in the membrane on the nth Na^+ ion (the influence of the membrane mobility on the variations of the ion concentration can be neglected):

$$U(u_n) = U_0\left(1 - \cos\frac{2\pi u_n}{a_L}\right), \tag{5}$$

where a_L is the distance between two neighboring lipid molecules in the membrane and U_0 is the potential of a lipid molecule.

In this notation, the dynamics of a Na^+ ion can be described by the equation

$$m_{Na}\frac{d^2u_n}{dt^2} + \rho(2u_n - u_{n-1} - u_{n+1}) + \frac{\pi U_0}{a_L}\sin\left(\frac{2\pi u_n}{a_L}\right) = 0, \tag{6}$$

where m_{Na} is the mass of a Na^+ ion and the constant ρ characterizes the extent to which the Na^+ ions are resilient to relative displacements.

Switching to the continual approximation $u_n(t) \longrightarrow U(x, t)$ and introducing the function proportional to the modulation of the concentration of Na^+ ions,

$$\varphi(x, t) = \frac{2\pi U(x, t)}{a_L}, \tag{7}$$

we arrive at the sine-Gordon equation

$$\frac{\partial^2\varphi}{\partial x^2} - \frac{1}{c_s^2}\frac{\partial^2\varphi}{\partial t^2} = \frac{1}{\lambda_0^2}\sin\varphi, \tag{8}$$

where $c_s = a_L\sqrt{\frac{\rho}{m_{Na}}}$ is the speed of longitudinal ion acoustic waves in a chain of sodium ions and $\lambda_0 = \frac{a_L^2}{2\pi}\sqrt{\frac{\rho}{U_0}}$ is the scale length on which the potential in the chain varies.

Keeping in mind that the length of the chain is L_n, we can obtain the following breather solution (i.e., a soliton solution with a vibrational degree of freedom) to Eq. (8) [16]:

$$\varphi_s(x, t) = 4\arctan\left\{\frac{c_s k}{\sqrt{2}\omega}\operatorname{sech}(kx)\sin(\omega t)\right\}, \tag{9}$$

where $\omega^2 + c_s^2k^2 = \frac{c_s^2}{\lambda_0^2}$ is the dispersion relation.

Let us draw an analogy with the experimentally revealed phenomenon of the trapping of Langmuir waves by the nascent regions of the depressed plasma density [17]. In terms of this phenomenon, a nerve

impulse can be interpreted as a low-frequency solitary wave of the charge density of sodium ions with a trapped high-frequency wave of the charge density of protons. Let us consider the interaction between these two types of waves.

The jumps of protons along a chain of water molecules (see figure) give rise to periodic variations of their relative positions in the chain and, as a consequence, to a periodic variation of the potential U_0 (5). This modulating action of protons can be described by writing the variation of the potential as $U_0(1 + \beta_1 u_n)$, where the quantity β_1 is inversely proportional to the distance between Na ions and water molecules. The displacement of Na ions along the Wen chain (see figure) leads to a distortion of the exponential shape of the potential φ_H (1) at the expense of periodic variations of the coefficient b in Eqs. (2) in the form $b(1 + \beta_2\varphi)$, where the quantity β_2 is inversely proportional to the distance between Na ions and water molecules in the Wen chain. Hence, the equations describing the interaction between the low-frequency and the high-frequency wave can be written in the form

$$\frac{\partial^2\varphi}{\partial x^2} - \frac{1}{c_s^2}\frac{\partial^2\varphi}{\partial t^2} = \frac{1}{\lambda_0^2}(1 + \beta_1 u_H)\sin\varphi,$$
$$\frac{\partial u_H}{\partial\tau} - 6(1 + \beta_2\varphi)u_H\frac{\partial u_H}{\partial\xi} + \frac{\partial^3 u_H}{\partial\xi^3} = 0. \quad (10)$$

In accordance with the results obtained by Bishop [18], we can reduce Eqs. (10) to a perturbed sine-Gordon equation and, thus, arrive at a breather solution (or a soliton solution with internal vibrational degrees of freedom) [19]:

$$\varphi_B(x, t) = 4\arctan\left\{\frac{c_s k}{\sqrt{2}\omega}\operatorname{sech}(\Delta k x)\sin(\Delta\omega t)\right\}, \quad (11)$$

in which the displacements of the wavenumbers and frequencies, Δk and $\Delta\omega$, are associated with the presence of the FPU recurrence in the chain described above.

We denote the spatial and temporal rates of the FPU recurrence by K_{FPU} and ω_{FPU}, respectively. Estimating these quantities yields $K_{FPU} = 10^{-4}$ and $\omega_{FPU} = 10^{11}$.

Following Bishop [18], we can approximately represent solution (11) in energy form as a sum of the squared amplitudes of the equidistant and non-equidistant modes. In this representation, the sum of the energy of the Fourier harmonics and the energy of a series of non-equidistant modes remains constant, and the reversible regrouping of energy between the equidistant and non-equidistant frequency spectra has the period $T_{FPU} = 2\pi/\omega_{FPU}$ and thus is the FPU recurrence:

$$E_{FPU} = \sum_{i=1}^{\infty} A_i(x)A_i(t)\cos(ik_{FPU}x)\cos(i\omega_{FPU}t)$$
$$+ \sum_{j=1}^{\infty} A_j(x)A_j(t)\cos(k_j x)\cos(\omega_j t) = \text{const}, \quad (12)$$

where E_{FPU} is the total energy of harmonics of the FPU recurrence, in accordance with the description of the FPU recurrence in terms of the Kolmogorov–Arnold–Mozer (KAM) theory [6] of the formation of invariant tori in the phase space of the quasi-integrable system (11).

The dynamics of the spectrum of the FPU recurrence is governed by the properties of the nonlinear dynamics of vibrational processes in a quasi-periodic crystal of an RNA molecule, or, in other words, by the positions of the nitrogen bases along an RNA molecule. In accordance with the properties of the FPU recurrence [12], the dynamic behavior of its spectrum can play the role of the dynamic memory: the parameters of the FPU modes recurrence periodically to their initial conditions, determined by the ordering of nitrogen bases in an RNA molecule.

4. MODEL ESTIMATE OF THE INFORMATION CAPACITY OF A NEURON

Taking into account the fact that the distance between Na and Cl molecules which the proton jumps over is about 0.31 nm [9], we can estimate the excitation frequency ν_c of a nerve impulse from the a and b values: $\nu_c \simeq 10^{13}$ Hz.

Recall that nerve impulses are as short as several milliseconds [20]. With this in mind, we can apply the Kotel'nikov theorem [21] and use the highest excitation frequency to arrive at the following formal estimate for the information capacity of an individual nerve impulse:

$$N_{ic} = 2\nu_c\tau_i = 3.72\times10^{10}\ \text{bits}. \quad (13)$$

5. CONCLUSION

The model developed here provides a piece of evidence in support of the previously proposed hypotheses [3–5] about the capacity of neurons to store a considerable amount of information (about 10^{10}–10^{11} bits per neuron). The role of the storing mechanism is played by repeated periodic returns of the frequency distribution in the spectrum of charge density waves in an electrolytic intracellular fluid of a neuron to the original distribution. Every time the neuron is excited electrically, a significant part of the stored information can be incorporated into the internal high-frequency structure of the

action potential and then transferred to other neurons. It should be noted that the high-frequency component of a nerve impulse has not as yet been measured.

Hence, the model proposed here extends the notion of a neuron as a system with two possible states to a system with numerous possible states.

ACKNOWLEDGMENTS

I would like to express my sincere gratitude to A.M. Ignatov for valuable remarks and fruitful discussions, which stimulated further development of the model.

REFERENCES

1. C. Stephens, in *The Brain* (W. H. Freeman, San Francisco, 1979; Mir, Moscow, 1982).
2. A. L. Hodgkin and A. F. Huxley, J. Physiol. (London) **117**, 318 (1952).
3. H. Hyden and E. Egyhazi, Proc. Natl. Acad. Sci. USA **52**, 720 (1964).
4. H. Hyden, in *The Human Mind* (North-Holland, Amsterdam, 1967), p. 157.
5. B. M. Mednikov, *DNA Structure and Position of Organisms in System* (Nauka, Moscow, 1972), p. 320.
6. L. E. Fermi, *The Fermi-Pasta-Ulam Problem Revised* (Rockefeller Univ. Press, New York, 1998).
7. T. T. Berezov and B. F. Korovkin, *Biological Chemistry* (Meditsina, Moscow, 1983).
8. H. C. Frank and W. Y. Wen, Discuss. Faraday Soc. **24**, 133 (1957).
9. V. V. Skorcheletti, *Theoretical Electrochemistry* (Goskhimizdat, Leningrad, 1963).
10. M. Toda, J. Phys. Soc. Jpn. **22**, 431 (1967).
11. N. J. Zabusky and N. D. Kruskal, Phys. Rev. Lett. **15**, 240 (1965).
12. R. D. Parmentier, in *Solitons in Action*, Ed. by K. Lonngren and A. Scott (Academic, New York, 1978; Mir, Moscow, 1981).
13. F. S. Barnes and J. Hu. Chia-lun, in *Nonlinear Electromagnetics*, Ed. by P. L. E. Uslenghi (Academic, New York, 1980), p. 312.
14. A. S. Pasynkov and A. V. Alekseev, Biofizika **31**, 639 (1986).
15. Ya. I. Frenkel' and T. A. Kontorova, Zh. Éksp. Teor. Fiz. **8**, 89 (1938).
16. E. N. Pelinovskiĭ, Radiofizika **19**, 883 (1976).
17. H. Ikezi, in *Solitons in Action*, Ed. by K. Lonngren and A. Scott (Academic, New York, 1978; Mir, Moscow, 1981).
18. A. R. Bishop, in *Solitons in Action*, Ed. by K. Lonngren and A. Scott (Academic, New York, 1978; Mir, Moscow, 1981).
19. J. Weiland and H. Wilhelmsson, *Coherent Nonlinear Interaction of Waves in Plasmas* (Pergamon, Oxford, 1976; Énergoizdat, Moscow, 1981).
20. A. C. Damask, *Medical Physics* (Academic, New York, 1978), Vol. 1.
21. I. S. Gonorovskiĭ, *Wireless Circuits and Signals* (Sov. Radio, Moscow, 1967), Vol. 1.

Translated by G. V. Shepekina

Plasma Physics Reports, Vol. 28, No. 7, 2002, pp. 615–622. Translated from Fizika Plazmy, Vol. 28, No. 7, 2002, pp. 664–672.

LOW-TEMPERATURE PLASMA

Spatial Structure of the Branching Streamer Channels in a Corona Discharge

N. A. Popov

Skobeltsyn Institute of Nuclear Physics, Moscow State University, Vorob'evy gory, Moscow, 119899 Russia

Received December 5, 2001

Abstract—The dendritic structure of streamer channels in a corona discharge is described by using fractal theory. It is found that, for a needle–plane discharge, the fractal dimension of the plasma structure is $D = 2.16 \pm 0.05$. The computed spatial distributions of the branching ratios are compared with the available experimental data. The influence of the branching processes on the distribution of chemically active radicals in streamer corona discharges is studied. © *2002 MAIK "Nauka/Interperiodica".*

1. Interest in studies of streamer corona discharges stems from their applications in ozone synthesis, the cleaning of flue gases, the removal of organic impurities, etc. [1–3]. An advantage of the devices based on streamer corona discharges as compared to those based on conventional barrier discharges is their simplicity and reliability, as well as a relatively high energy efficiency.

The excitation and ionization of the gas in pulsed corona discharges occurs in streamer channels that form near the corona electrode and, then, propagate into the discharge gap. The chemically active radicals ($O(^3P)$, H, OH, etc.) are produced in the active region with a high electric field at the streamer head. Then, these radicals participate in reactions resulting in both the decomposition of harmful impurities and the cleaning of the gas flowing through the region occupied by the streamer channels. The volume of this region is determined by the channel length and the cross size of the streamer zone. The latter depends on the streamer branching ratio, i.e., the number of channels produced from a primary streamer starting from the electrode. The problem of the enlargement of the streamer zone is of primary importance for passing over from moderate-size research facilities to large industrial reactors [4].

Up to now, theoretical studies have been devoted mainly to describing the dynamics of solitary straight-line streamers [5–8], because taking into account the trajectory bending and branching requires three-dimensional numerical simulations. However, in experiments, in most of cases that are of practical interest, plasma channels are crooked and highly branching.

The simplest method to account for branching was used in [9], where the number of corona discharge streamers was multiplied by a constant factor equal to the ratio of the measured current amplitude to the corresponding calculated value obtained for a solitary streamer. However, it was not taken into account that, generally, the total current in the system of branching channels is not equal to the sum of the currents in individual streamers [8]. Moreover, the branching ratio can change significantly (by a factor of several tens) with distance from the corona electrode [10–14], which was not incorporated in this approach.

In [15], the formation of two effective avalanches with an angle between them exceeding a certain critical angle θ_{cr} was taken as a criterion for streamer branching. The probability of the formation of these avalanches is determined by the distribution of the secondary photoelectron density in front of the streamer head. For $\theta_{cr} \simeq 60°$, it is possible to achieve an agreement between the experimental data and calculations by the model proposed. In [16], a model of branching related to the formation of secondary streamers moving along the plasma channel of the primary streamer and catching up with it was proposed. According to [16], the interaction between the charges of the primary and secondary streamer heads determines the probability of streamer channel branching. However, this model fails to explain a number of the experimentally observed phenomena, e.g., a significant decrease in the branching ratio in streamer discharges in nitrogen–oxygen mixtures as compared to discharges in pure nitrogen [11, 17].

In [18], the influence of the interacting streamer channels starting simultaneously from the corona electrode on the characteristics of an individual streamer was studied and the development of several parallel streamers in a wire–plane electrode configuration under the experimental conditions [13] was simulated. The results of calculations with allowance for the multiplicity of the streamer channels are in better agreement with the experimental data than calculations by the solitary streamer model. It was shown that the streamer channels can greatly influence each other; the higher the applied voltage and the lower the distance between the streamers, the stronger the influence.

1063-780X/02/2807-0615$22.00

One of the well-known models describing the spatial structure of branching channels was developed in [19, 20]. In this model, the plasma channels propagate toward the higher electric field, provided that the field exceeds the threshold value E_{cr}. The spatial distribution of the electric field is determined by solving Laplace's equation for the potential with the boundary conditions that account for the existence of conducting channels. All the channels are considered to be identical and the electric field inside the channels is assumed to be constant. The probability P_z of streamer propagation in the z direction is determined by the distribution of the electric field in the vicinity of the streamer head,

$$P_z = \frac{E_z^\gamma - E_{cr}^\gamma}{\sum_k (E_k^\gamma - E_{cr}^\gamma)}, \quad \gamma > 0, \tag{1}$$

where E_k is the field along the k direction and summation is performed over all the possible directions.

This model was employed to describe the Lichtenberg figures that are formed on a glass surface in SF_6 [21], the leader breakdown in atmosphere [22, 23], etc. In [22, 23], Poisson's equation (rather than Laplace's equation) was solved, which enabled one to take into account the influence of the channel space charge on the electric field distribution. However, the most important result obtained with the model proposed in [19, 20] is that the plasma structures allow spatial scaling; i.e. they are self-similar structures or fractals.[1] It was shown in [19] that the fractal dimension D depends only on the dimensionality of space d and the power index γ in formula (1). It should be noted that, in most studies, the parameter γ was chosen by comparing the calculation results with the corresponding experimental data, which indicates an incompleteness of the model.

The purpose of this study is to apply fractal theory to describing the structure of the branching plasma channels in a streamer corona discharge and to investigate the influence of branching on the spatial distribution of the chemically active radicals produced.

2. According to present-day knowledge, the streamer propagates due to the formation of new electron avalanches (originating from the secondary electrons produced via photoionization) in the strong electric field of the space charge near the streamer head [24, 25]. The propagation direction of these avalanches is determined by the streamer field, rather than the weaker external field. In [15, 26], a model was proposed in which many individual avalanches were replaced with one avalanche that had an equivalent charge and propagated along the maximum field. The interaction between the individual avalanches is such that the weaker avalanches (i.e., those propagating in a weaker field) lag behind the stronger avalanches and, on approaching the streamer head, are absorbed by them. Thus, the main avalanche, which determines the subsequent streamer motion, is formed along the force line of the maximum field. Hence, the probability of streamer propagation in a given direction is determined by the spatial distribution of a certain function $f(E)$ of the electric field near the streamer head [in formula (1), $f(E) \propto E^\gamma$]. Quantitatively, the growth of the electron avalanches is determined by the function $\nu_{ion}(E) - \nu_{att}(E)$, where ν_{ion} and ν_{att} are the ionization and electron attachment frequencies. Note that $\nu_{ion}(E_{cr}) - \nu_{att}(E_{cr}) = 0$. Thus, the avalanche grows only if $E > E_{cr}$. Here, we assume that

$$f(E) = \nu_{ion}(E) - \nu_{att}(E) \propto E^\gamma. \tag{2}$$

As was mentioned above, if the probability of the plasma channel propagation is determined by formula (1) and the electric field in the channel is constant (which holds for streamer channels; see, e.g. [7, 8]), then, according to [19], the plasma structure is a fractal. The fractal dimension D of this structure (at a given space dimensionality d) is determined by the power index γ in formula (1). It should be noted that, in spite of the simplicity of the streamer channel model proposed in [19, 20], the distribution of the probability P_z (1) in the vicinity of the channel head can be determined quite exactly. Indeed, for comparable channel lengths, the potentials of the heads of the neighbor streamers are close to each other. Therefore, the electric field distribution near a given head is mainly determined by the spatial configuration of the neighbor heads. This configuration and, hence, the electric field distribution that determines the propagation direction for the given channel are fairly well described by the model proposed in [19, 20].

Under assumptions (2), the power index γ is

$$\gamma(\xi) = \left.\frac{\partial[\ln(\nu_{ion} - \nu_{att})]}{\partial(\ln E)}\right|_{E=\xi}. \tag{3}$$

For a given gas species, it is entirely determined by the reduced electric field E/N, where N is the density of gas molecules. At high E/N values typical of the streamer head, we have $\nu_{ion} \gg \nu_{att}$; hence, $f(E) = \nu_{ion}(E) - \nu_{att}(E) \simeq \nu_{ion}(E)$.

Figure 1 presents an example of the dependence $\gamma(E/N)$ for air in the range E/N = 150–1500 Td (1 Td = 10^{-17} V cm^2). The data on the ionization and attachment frequencies, $\nu_{ion}(E/N)$ and $\nu_{att}(E/N)$, were taken from [27, 28]. The fractal dimension of the plasma structures versus E/N (under the assumption that the maximum electric field in the streamer head is constant and equal to E) is also shown in Fig. 1. For $D(\gamma)$, we used the results of calculations for the three-dimensional

[1] Before introducing the term fractal, mathematics dealt with the so-called Hausdorff–Besikovitch dimension, which could acquire any value. This justified the conception of fractional dimension. Now, it is clear that the fractal structure and dimension serve as the main characteristic of a variety of physical processes [20].

Laplace field at $d = 3$ [29]. Note that, for most of flue gases, the ionization frequency $\nu_{ion}(E/N)$ is almost the same as for air [28]; hence, the dependences presented in Fig. 1 are also relevant for these gases.

Thus, if the system of plasma channels in a corona discharge is a fractal, then, to determine the fractal dimension, it is necessary to evaluate the maximum reduced electric field in the streamer head and, then, to use the calculated $D(E/N)$ values for the gas under consideration.

The results of two-dimensional calculations of streamer propagation in highly nonuniform [5–7] and weakly nonuniform [30] electric fields show that the maximum field at the streamer head changes slightly and, for air at atmospheric pressure, amounts to E_{max} = 160–180 kV/cm (i.e., E_{max}/N = 640–720 Td). Based on these results, it was assumed that, in the streamer head, where the branching probability is maximum, the parameter E/N attains 640–720 Td. It is seen in Fig. 1 that, in this case, the fractal dimension of the branching plasma channels (in air and most of flue gases) should be

$$D = 2.16 \pm 0.05. \quad (4)$$

According to fractal theory, the total length of streamer channels inside a surface of radius R can be written in the form [19, 20]

$$L \propto R^D, \quad (5)$$

and the number of streamers crossing this surface is

$$N(R) = \frac{dL}{dR} = \left(\frac{R}{R_0}\right)^{D-1}, \quad (6)$$

where D is the fractal dimension and R_0 is the characteristic distance within which streamer branching occurs. The quantity R_0 cannot be determined within the fractal theory and is the parameter of the problem.

3. To verify the assumptions underlying the method for determining the fractal dimension D, the calculated values of the streamer branching ratio (6) were compared with the available experimental data. Most of the data on the streamer channel branching were obtained in the following way (see monographs [11, 12]). A thin dielectric plate covered with photoemulsion was placed in the discharge gap normally to the external electric field. The streamers crossing the plate initiate surface microdischarges, whose glow, similar to Lichtenberg figures, is recorded on a photoplate. One of these patterns, borrowed from review [12], is shown in Fig. 2. Based on the number of microdischarges, the number $N(R)$ of streamer channels at a given distance from the corona electrode is determined. The scatter in branching ratios determined in this way is 20–30% [10, 11].

However, it is not clear how the dielectric plate inserted into the discharge gap affects the discharge characteristics. The charges of the streamer heads are deposited onto the photoplate, thereby perturbing the electric field distribution and the streamer trajectories near the plate. The angles at which the peripheral streamer branches approach the plate are smaller than the corresponding angles for the streamers near dis-

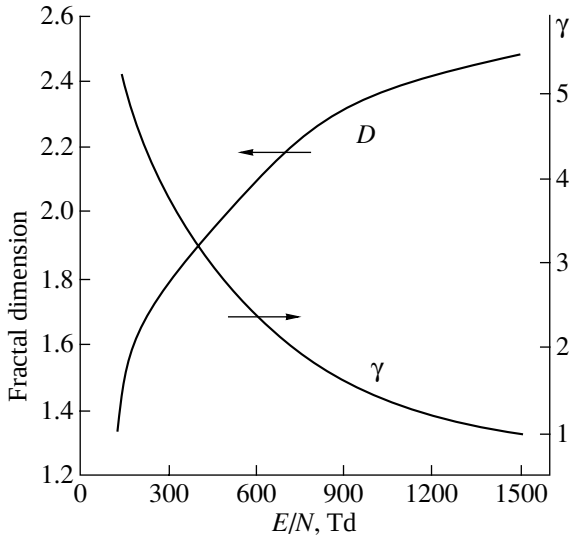

Fig. 1. Parameter γ and the fractal dimension D of a streamer discharge in air as functions of the reduced electric field E/N for $d = 3$.

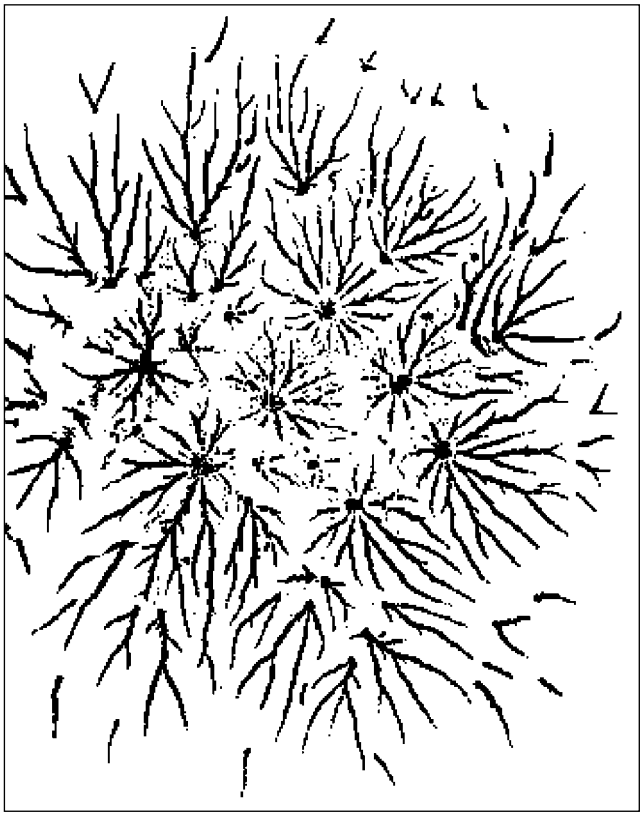

Fig. 2. Pattern of a system of microdischarges crossing a dielectric photoplate for $U = 30$ kV and $R = 2$ cm [12].

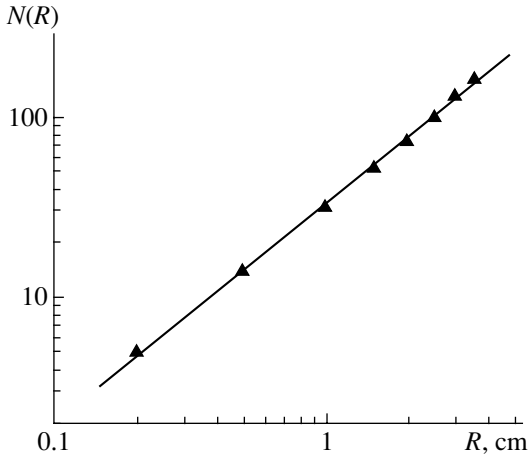

Fig. 3. Streamers branching ratio $N(R)$ vs. distance R to the needle for $U = 36$ kV and $R_h = 4$ cm [10]. The slope of the straight line is $D - 1 \simeq 1.18$.

charge axis. Thus, the trajectories of the peripheral channels change so that they may not cross the plate. The lower the potential at the streamer head and the velocity of the streamers approaching the plate, the higher the probability for the streamer channel to pass by the plate. Hence, the significant distortion of the discharge spatial picture can be expected only at distances comparable with the maximum (under given conditions) channel propagation length. In the remainder of the discharge region, the influence of the photoplate on the measurements of the branching ratios seems to be insignificant [10, 11].

The regime in which the streamer parameters change slightly during streamer propagation is optimum for testing the branching models. On applying an additional steady electric field $E_{add} \geq 4.6$ kV/cm, streamers can propagate in steady-state regime over very long distances [31]. The main streamer parameters, such as the radius, the propagation velocity, and the maximum electric field E_{max} at the streamer head, arrive at their steady-state values [30, 32]. Hence, the fractal dimension of the streamer structure should also be approximately constant at sufficiently long distances from the corona electrode.

The branching of the steady-state streamers was studied in [33] for a discharge in the needle–plane geometry with a combined power supply. The dc voltage was applied to two plane-parallel electrodes, and the pulsed voltage ($U = +35$ kV) was applied to the needle placed in an opening in the plane anode. The needle apex radius was $R_a = 0.05$ cm, the opening radius was 0.5 cm, and the additional electric field was $E_{add} = 4.7$ kV/cm. In [33], the electric field distribution was such that the size of the region with an enhanced field was $R_\varnothing \simeq 0.3$ cm. The calculated branching ratios $N(R)$ adequately describe the corresponding experimental data from [33] at $D = 2.16$ and $R_0 = R_\varnothing = 0.3$ cm (see table).

Measured and calculated streamer branching ratios, N_{exp} and N_{cal}, vs. distance to the anode in a needle–plane discharge with a combined power supply [33]

R, cm	1.0	2.5	4.0	6.0
N_{exp}	4.0	9.0	20.0	–
N_{cal}	4.04	9.03	20.18	32.3

In [10], a needle–plane discharge in air at atmospheric pressure was studied. The voltage amplitude U was from +30 to +40 kV, the pulse duration was $\tau = 1$ ms, the pulse rise time was $\tau_f = 50$ ns, the needle apex radius was $R_a = 0.05$ cm, and the interelectrode distance was $R_m = 3$–10 cm. The measured streamer branching ratios are shown in Fig. 3 for $U = 36$ kV and $R_m = 4$ cm. The function $N(R)$ shown on a double logarithmic scale is a straight line with a slope of $D - 1 \simeq 1.18$. This value agrees with the theoretical prediction (4). The fact that the fractal dimension D and, consequently, the power index γ remain unchanged while the streamers cross the discharge gap indicates that the E_{max} field at the streamer head changes slightly. In this case, inaccuracy in determining D (with allowance for an uncertainty in the data on $N(R)$) is rather low, $D = 2.18 \pm 0.02$. Taking into account the dependence $D(E_{max})$ (Fig. 1), this corresponds to the field $E_{max}/N \simeq 700 \pm 20$ Td. These results confirm the assumption (see, e.g., [7, 8, 34]) that, for a given gas, a more or less constant maximum field E_{max} is established in the streamer head.

When the length of the interelectrode gap R_h exceeds the mean distance that can be passed by streamers at a given applied voltage U, the dependence $N(R)$ changes (Fig. 4). In this case, the branching ratio has a maximum $N_{max}(R_m)$ at the point R_m. At $R < R_m$, the experimental data are adequately described by formula (6) with $D = 2.16$ and $R_0 = R_a = 0.05$ cm (the solid line in Fig. 4). At $R \geq R_m$, the dependence $N(R)$ can no longer be described within fractal theory. This fact agrees with both simulation results and experimental data [21]. The reason for the decrease in the branching ratio at $R \geq R_m$ is the reduction in the potential of the channel head, which becomes lower than the critical value U_{cr}. As a result, either the streamers stop or their trajectories change so strongly that they do not cross the plate. According to measurements [10, 11], the peripheral branches with the maximum length "die" first. Assuming that, at $R < R_m$, the angle of deflection of the outer branches from the axial direction is nearly constant [10], we have

$$R_m \propto R_{max} \simeq \frac{U}{E_c}, \qquad (7)$$

where R_{max} is the maximum distance to which streamers propagate, E_c is the average electric field in the

channel (in air at atmospheric pressure, this field amounts to 5 kV/cm [8]), and R_m is the parameter determining the maximum branching ratio $N_{\max} = (R_m/R_0)^{D-1}$ and the size of the region where fractal theory is applicable.

Based on the available experimental data on the streamer branching ratios in corona discharges [10, 12], one can analyze the dependence of $E_{\max}$ on the applied voltage. In a number of studies (see, e.g., [13, 14]), it was asserted that the branching ratio increases with applied voltage. The dependences $N(R)$ measured for the maximum voltages U_m = 30 and 36 kV [10] are shown in Fig. 4. It is seen that the shape of the $N(R)$ dependence does not change as U_m increases, which is in agreement with similar measurements in [12]. However, the maximum streamer branching ratio $N_{\max}$ increases with the voltage U_m. As was mentioned above, simulations at a constant value of D (solid line in Fig. 4) adequately describe the experimental data within the range of applicability of fractal theory. Hence, the maximum electric field $E_{\max}$ in the streamer head changes slightly. The experimentally observed increase in $E_{\max} = (R_m/R_0)^{D-1}$ with applied voltage is related to the extension of the range of applicability of fractal theory [according to (7), R_m increases proportionally to U], rather than to an increase in the fractal dimension D.

The conclusion about the weak dependence of D on voltage is important because it allows one to compare the fractal dimensions of the streamer structures in different gases in which the breakdown electric fields and, consequently, the applied voltages can differ greatly. Moreover, it follows from here that the change in the voltage growth rate dU/dt should not significantly influence the fractal dimension D, although it does affect the $N_{\max}$ value.

In [35], it was noted that the streamer branching ratio increases with the degree of electric field inhomogeneity (i.e., with R_a/R_h). The data from [10] indicate that changing the discharge gap length R_h only slightly affects the branching ratio.

To evaluate the degree to which the description of the streamer corona structure within fractal theory is universal, it is of interest to compare the $N(R)$ dependences in nitrogen–oxygen mixtures with different oxygen content. In recent study [17], evidence for a significant increase in the streamer branching ratio with decreasing oxygen content in the mixture was obtained. In the region where the electric field is high, $E/N \geq$ 600 Td, the dependences $\nu_{\text{ion}}(E/N)$ for nitrogen–oxygen mixtures with different oxygen content differ slightly [27]. Hence, according to our model, the difference in the parameter γ and the fractal dimension D in the plasma structures also should not be large.

In [11], the streamer branching ratios in $N_2 : O_2$ mixtures at atmospheric pressure were measured in a facility similar to that used in [10]. The voltage amplitude

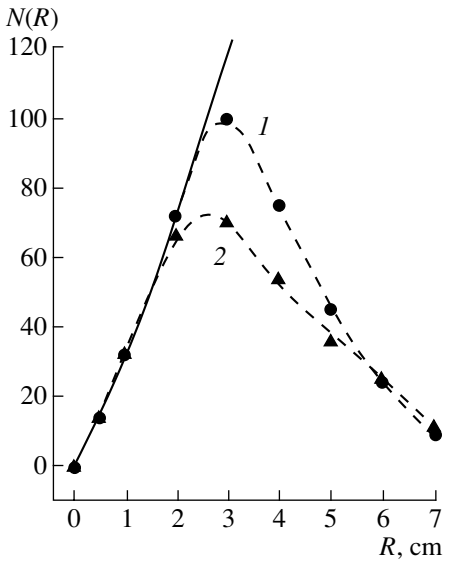

Fig. 4. Streamers branching ratio $N(R)$ vs. distance R to the needle for R_a = 0.05 cm, R_h = 8 cm, and U_m = (*1*) 36 and (*2*) 30 kV [10]. The solid line shows the computation results for D = 2.16 and $R_0 = R_a$ = 0.05 cm ($N_2 : O_2$ = 4 : 1).

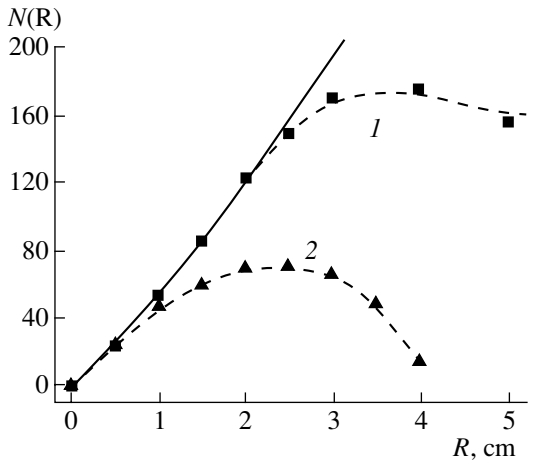

Fig. 5. Streamers branching ratio $N(R)$ vs. distance R to the needle for discharges in (*1*) N_2 + 10%O_2 and (*2*) N_2 + 36%O_2 mixtures; the discharge parameters are R_a = 0.05 cm, R_h = 8 cm, and U = 32.5 kV [11]. The solid line shows the computation results for D = 2.15 and R_0 = 0.031 cm.

was U = +32.5 kV, the pulse duration was τ = 1 ms, and the interelectrode distance was R_h = 8 cm. The oxygen percentage δ in the mixture was varied from 10 to 75%. Figure 5 presents the measured streamer branching ratios [11] for the N_2 + 10%O_2 and N_2 + 36%O_2 mixtures and the results of calculations by formula (6) for D = 2.15 and R_0 = 0.031 cm. It is seen that, in the applicability region of fractal theory, the difference between the simulation and experimental results does not exceed

the measurement error. It was experimentally observed that the maximum branching ratio $N_{\max}$ significantly increased with decreasing oxygen content. The reason is that, according to [14], the decrease in the O_2 concentration results in a decrease in the average electric field E_c in the streamer channel. As a result, both the streamer propagation length and the size R_m of the region where fractal theory is applicable increase [see (7)], which leads to the increase in $N_{\max} = (R_m/R_0)^{D-1}$.

Thus, we can conclude that the system of branching plasma channels in a streamer corona discharge is a fractal. The fractal dimension D and the characteristic distance R_0 over which streamer branching occurs change slightly with changing the applied voltage and oxygen content in the mixture (in the range δ = 10–70%). The latter fact seems to be important because, as δ changes, both the photoelectron density in front of the streamer head and the width of the ionization wave front also change [17]. This, according to [17], is the main reason for an increase in the branching ratio with decreasing δ (a possible influence of photoionization on streamer branching was also discussed in [36, 37]). The fact that the characteristic length of branching R_0 does not depend on the oxygen content in the mixture apparently indicates the insignificant influence of photoionization on streamer branching.

4. Many applications of streamer corona discharges are related to the efficient production of chemically active radicals [1–3]. As was mentioned above, these radicals are produced in the streamer channels; hence, the spatial distribution and the volume-averaged concentrations of active particles depend strongly on the spatial structure of the discharge.

As an example, we consider the distribution of chemically active radicals in a wire–plane streamer corona discharge. The active particles are mainly produced in the streamer head, where the electric field is high. The two-dimensional simulations [5–7] showed that the quantities $E_{\max}$ and $N_e^{\max}$, as well as the maximum concentration of radicals N_R^m in the plasma channel, change slightly along the streamer trajectory. The total number of radicals produced per one pulse in a cylindrical volume of unit length with radius R is

$$\int_{R_a}^{R} N_R(r) \times 2\pi r dr = \pi R_c^2 N_R^m N_c L(R), \qquad (8)$$

where N_c is the number of streamers per unit length of the electrode (this number depends on the applied voltage and amounts to 5–7 cm^{-1} [13, 14][2]), R_c is the radius of the streamer channel, and $L(R)$ is the total length of all the streamer branches inside a cylindrical volume of radius R [see formula (5)].

According to Eqs. (6) and (8), the radial profile of the radical concentration $N_R(R)$ can be written in the form

$$N_R(R) = N_R^m \frac{R_c^2 N_c R^{D-2}}{2R_0^{D-1}} \qquad (9)$$

or

$$N_R(R) = N_R^m (R_c/R_D)^2,$$

where

$$R_D = \sqrt{\frac{2R_0^{D-1}}{N_c R^{D-2}}}. \qquad (10)$$

The quantity R_D has a meaning of the limiting size of the diffusion broadening of the streamer track before the interaction with the tracks of the neighbor channels, i.e., the average distance between the streamers. It is seen from formula (10) that, at $D \simeq 2$, the average distance between the streamers changes slightly with R (within the streamer zone, in which expressions (9) and (10) are valid).

In a wire–cylinder electrode configuration, a lot of streamers can simultaneously start from the corona electrode ($N_c \geq 5$ cm^{-1}). The streamer systems initiated by the streamers starting from the corona electrode begin to interact with each other already at a distance of $R_w = N_c^{-1}\theta/2\pi \simeq N_c^{-1}/6 \ll R_m$ [14], where θ is the average angle of the lateral expansion of the streamer system. At $R > R_w$, the effective dimensionality of space decreases from $d = 3$ to $d = 2$ due to the strong interaction between the streamer systems. This, in turn, should decrease the fractal dimension of the plasma structure. At a maximum reduced electric field in the streamer head of $E_{\max}/N$ = 650–720 Td (according to Fig. 1, this corresponds to $\gamma \simeq 2$) and $d = 2$, the fractal dimension is $D \simeq 1.83$ [29]. Later, this value of D was used to estimate the parameters of the spatial structure in the wire–cylinder electrode configuration.

The production of chemically active radicals is only the first stage of plasmochemical gas cleaning. Then, these radicals participate in reactions that result in the decomposition of harmful agents. The volume-averaged concentration of the particles removed in one pulse is determined by both the concentration of radicals produced in the streamer channels and the relation between the reactor volume V_0 and the volume V_c occupied by the streamers. The latter amounts to

$$V_c = \pi R_c^2 L(R_m) N_c Z_0,$$

where R_m is the maximum radius of the streamer zone and Z_0 is the reactor length.

[2] In many discharge devices, special points are made on the corona wire in order to increase the number of streamers starting from it. Since the streamers start mainly from these points, the streamer number N_c is a known fixed value.

Defining the radius of the cylindrical reactor as R_h, we have

$$F_0 = \frac{V_c}{V_0} = \left(\frac{R_c}{R_h}\right)^2 N_c \frac{R_m^D}{R_0^{D-1}}. \quad (11)$$

In [38], the removal of impurities and the production of ozone in a pulsed corona discharge with a wire–cylinder electrode configuration were numerically simulated under conditions of [39, 40] (R_a = 0.07 cm and R_h = 10 cm). The maximum distance to which streamers propagate did not exceed R_m = 5 cm. The streamer channel radius was assumed to be R_c = 0.025 cm. In [38], the quantity $F_0 = V_c/V_0$, which was a parameter of the problem, was determined by fitting the simulation results to the experimental data. The results of simulations of ozone production and the removal of NO_x and SO_2 impurities can be fitted to the corresponding experimental data from [39, 40] at $F_0 \simeq (6–7) \times 10^{-3}$. Under these conditions, the calculations by formula (11) at $N_c = 6$ cm^{-1}, $D = 1.83$, and $R_0 = R_a = 0.07$ cm give $F_0 = 6.5 \times 10^{-3}$.

5. Thus, we can conclude that fractal theory can be used to describe the spatial structure of the branching plasma channels in streamer corona discharges. The fractal dimension D and the characteristic distance R_0 over which the channel branching occurs remain constant within the range of applicability of fractal theory. This confirms the concept repeatedly discussed in the literature that, for a given gas species, a certain fixed maximum electric field E_{max} is established at the streamer head.

As was mentioned above, fractal theory does not allow one to determine the characteristic length of the streamer branching R_0. This parameter is to be determined based on the branching criterion, which has not yet been formulated. The results of our study show that the quantity R_0 does not change in the range of applicability of fractal theory and is independent of the applied voltage, the radius of the corona electrode, and the mixture composition (for $N_2 : O_2$ mixtures). These results should be taken into account in developing the streamer branching models.

It should be noted that, up to now, all the studies of the streamer branching ratio have been carried out in the needle–plane geometry. To evaluate the degree to which the fractal model of the streamer corona structure is universal, it is of interest to carry out experiments under conditions in which one can expect the change in the fractal dimension D (e.g., due to the reduction of the dimensionality of space where the streamers propagate). One of the possible approaches to this problem is to use wire–plane or wire–cylinder electrode configurations, which, as was noted above, allow one to reduce the fractal dimension of the plasma structures produced. The experimental studies of the branching ratio $N(R)$ in various gas mixtures are also of interest.

ACKNOWLEDGMENTS

I am grateful to É.M. Bazelyan for helpful discussions. This work was supported by the Russian Foundation for Basic Research, project no. 00-15-96554.

REFERENCES

1. S. Masuda, Pure Appl. Chem. **60**, 723 (1988).
2. A. A. Valuev, A. S. Kaklyugin, G. É. Norman, *et al.*, Teplofiz. Vys. Temp. **28**, 995 (1990).
3. *Non-Thermal Plasma Techniques for Pollution Control*, Ed. by B. Penetrante and S. Schulthesis (Springer-Verlag, Berlin, 1993), NATO ASI Series, Vol. 34A.
4. A. Z. Ponizovskiĭ, in *Proceedings of the VIII Conference on Gas Discharge Physics, Ryazan', 1996*, Part 2, p. 35.
5. P. A. Vitello, B. M. Penetrante, and J. N. Bardsley, Phys. Rev. E **49**, 5574 (1994).
6. A. A. Kulikovskiĭ, in *Proceedings of the Conference on Physics of Low-Temperature Plasma, Petrozavodsk, 1995*, p. 352.
7. N. Yu. Badaeva and G. V. Naidis, J. Phys. D **29**, 2423 (1996).
8. E. M. Bazelyan and Yu. P. Raizer, *Spark Discharge* (Mosk. Fiz. Tekh. Inst., Moscow, 1997; CRC, Boca Raton, 1997).
9. A. Bondiou and I. Gallimberti, J. Phys. D **27**, 1252 (1994).
10. E. Nasser and L. B. Loeb, J. Appl. Phys. **34**, 3340 (1963).
11. L. B. Loeb, *Electrical Coronas: Their Basic Physical Mechanisms* (Univ. of California Press, Berkeley, 1965).
12. E. Nasser, *Fundamentals of Gaseous Ionization and Plasma Electronics* (Wiley, New York, 1971).
13. Y. L. Creyghton, E. M. van Veldhuizen, and W. R. Rutgers, in *Non-Thermal Plasma Techniques for Pollution Control*, Ed. by B. Penetrante and S. Schulthesis (Springer-Verlag, Berlin, 1993), NATO ASI Series, Vol. 34A, p. 205.
14. Y. L. Creyghton, PhD Thesis (Eindhoven, 1994).
15. S. Badaloni and I. Gallimberti, in *Proceedings of the XI International Conference on Phenomena in Ionized Gases, Prague, 1973*, p. 196.
16. M. V. Sokolova and A. G. Temnikov, Vestn. MÉI, Fiz., No. 4, 34 (1998).
17. W. J. Yi, B. J. Hankla, and P. F. Williams, IEEE Trans. Plasma Sci. **24**, 93 (1996).
18. G. V. Naidis, J. Phys. D **29**, 779 (1996).
19. L. Niemeyer, L. Pietronero, and H. J. Wiesmann, Phys. Rev. Lett. **52**, 1033 (1984).
20. H. J. Wiesmann and L. Pietronero, in *Fractals in Physics*, Ed. by L. Pietronero and E. Tosatti (North Holland, Amsterdam, 1986; Mir, Moscow, 1988).
21. N. Femia, L. Niemeyer, and V. Tucci, J. Phys. D **26**, 619 (1993).
22. V. Lopatin, M. Noskov, and O. Pleshkov, in *Proceedings of the XII International Conference on Gas Discharge and Their Applications, Greifswald, 1997*, Vol. 2, p. 432.

23. N. I. Petrov and G. N. Petrova, Zh. Tekh. Fiz. **65** (5), 41 (1995) [Tech. Phys. **40**, 427 (1995)].
24. L. B. Loeb, *Fundamental Processes of Electrical Discharges in Gases* (Wiley, New York, 1939; Gostekhizdat, Moscow, 1950).
25. Yu. P. Raizer, *Gas Discharge Physics* (Nauka, Moscow, 1987; Springer-Verlag, Berlin, 1991).
26. I. Gallimberti, J. Phys. D **5**, 2179 (1972).
27. A. W. Ali, Laser Part. Beams **6**, 105 (1988).
28. B. M. Penetrante, in *Non-Thermal Plasma Techniques for Pollution Control*, Ed. by B. Penetrante and S. Schulthesis (Springer-Verlag, Berlin, 1993), NATO ASI Series, Vol. 34A, p. 65.
29. S. Satpathy, in *Fractals in Physics*, Ed. by L. Pietronero and E. Tosatti (North Holland, Amsterdam, 1986; Mir, Moscow, 1988).
30. N. Yu. Babaeva and G. V. Naidis, Phys. Lett. A **215**, 187 (1996).
31. N. L. Allen and A. Graffar, J. Phys. D **28**, 331 (1995).
32. N. L. Aleksandrov and E. M. Bazelyan, J. Phys. D **29**, 740 (1996).
33. T. M. Tang, PhD Thesis (UMIST, Manchester, 1982).
34. M. I. D'yakonov and V. Yu. Kachorovskiĭ, Zh. Éksp. Teor. Fiz. **94**, 321 (1988) [Sov. Phys. JETP **67**, 1049 (1988)].
35. E. M. Bazelyan and I. M. Razhanskiĭ, *Spark Discharge in Air* (Nauka, Moscow, 1988).
36. A. A. Kulikovsky, J. Phys. D **33**, 1514 (2000).
37. S. V. Pancheshnyi and A. Yu. Starikovskii, J. Phys. D **34**, 248 (2001).
38. R. Kh. Amirov, I. S. Samoĭlov, and A. V. Shelepin, Preprint No. 1-372 (Institute for High Temperatures, Russian Academy of Sciences, Moscow, 1994).
39. R. Kh. Amirov, M. B. Zheleznyak, and E. A. Filimonova, Preprint No. 1-403 (Institute for High Temperatures, Russian Academy of Sciences, Moscow, 1997).
40. J. O. Chae, Yu. N. Desiaterik, and R. H. Amirov, in *Proceedings of the V International Symposium on High-Pressure Low-Temperature Plasma Chemistry, Milovy, Czech Republic, 1996*, p. 155.

Translated by N. N. Ustinovskiĭ